THE UNIVERSITY *of* EDINBURGH

Unsteady velocities of energetic tidal currents: An investigation into dynamic flow effects on lifting surfaces at field and experimental scale

Samuel Frederick Harding

A thesis submitted for the degree of Doctor of Philosophy

The University of Edinburgh

May 2013

To my grandfather,

Fred Harding

Abstract

The generation of electricity from tidal currents is an emerging industry with the potential to contribute to the UK energy supply in a predictable and sustainable way. The development of the technology requires the cost effective subsea installation of energy conversion systems in an energetic and challenging marine environment. One concept developed for the fastening of tidal energy converters to the seabed is the Active Gravity Base (AGB), which offers potential reductions in installation cost and time, relative to existing fastening methods. The performance of this concept in response to unsteady flow conditions is explored within this thesis.

The dynamic behaviour of a tidal current is driven by a range of factors from gravitational forces of celestial bodies to high-frequency fluctuations of turbulent eddies. The response of the AGB concept to the unsteadiness of tidal currents is herein considered under the two broad time-scales; the directionality of the mean semi-diurnal cycle and the high frequency variations from a given mean flow velocity.

The correlation between the direction and velocity of the tidal flow was assessed using hourly averaged data provided by the Admiralty Charts in the northern UK waters. The resulting directionality model was used to predict the performance of the AGB under a range of quasi-steady flow conditions.

High frequency velocity measurements of a potential tidal energy site were obtained through collaboration with the University of Washington and the Pacific Northwest National Laboratory. This data was used to estimate the maximum perturbation from the mean velocity that can be expected on an annual basis.

An experimental facility was developed within the re-circulating water flume at the University of Edinburgh to examine the dynamic loads generated by controllable two-dimensional flow perturbations. This was successfully achieved using a configuration of twin pitching foils with independent motion control. A relationship between the foil pitch angle and velocity perturbation time series was predicted using a vortex model of the foil wakes. This configuration was shown to be able to generate significant flow fluctuations within the range of reduced frequencies $0.06 \leq k \leq 1.9$, with a peak gust intensity of $I_g = 0.5$. The numerical solution was validated against experimental results.

Declaration of Originality

I hereby declare that this thesis has been composed by myself and that the work contained herein is entirely my own except where explicitly stated.

I also declare that this work has not been submitted for any other degree or professional qualification except as specified.

Samuel Harding

Acknowledgements

I would like to thank the following people for their involvement, contribution and support throughout the course of this research:

- Professor Ian Bryden and Professor Gareth Harrison for their supervision of the project.
- Emeritus Professor Stephen Salter for technical advice and access to his workshop
- Edward Barbour, Thomas Chabanne, David Forehand, Gareth Gretton, Rémy Pascal, Grégory Payne, Brian Sellar, Duncan Sutherland and Jamie Taylor for making the office a positive and enjoyable place, as well as their technical assistance throughout the project.
- Jim Thomson and Brian Polagye of the Northwest National Marine Renewable Energy Center, University of Washington, and Marshall Richmond and Vibhav Durgesh of the Pacific Northwest National Laboratory for the acquisition and processing of the tidal stream velocity data used in this thesis.
- My family: Murray, Jan and Tom Harding and Lucy Revell for their encouragement from around the world.
- The Dunn family for their hospitality and friendship throughout the project.

This research was funded by the Top Achiever Scholarship awarded by the Tertiary Education Commission of New Zealand.

Contents

List of Figures

List of Tables

List of Symbols and Nomenclature

Symbols

a_0	Location of pitch axis of lifting surface
$\hat{a}$	Amplitude of Gaussian distribution
b	Semi-chord of lifting surface, $c/2$
$\hat{b}$	Horizontal translation of Gaussian distribution
c	Chord length of lifting surface
$\hat{c}$	Spread of Gaussian distribution
$\hat{d}$	Vertical translation of Gaussian distribution
d_c	Length of cable sensor used to measure angular position of fixed wing
e	Efficiency factor of lifting surface
f	Frequency
f_i	Internal sampling frequency of the ADV
f_s	Sample frequency setting of acoustic Doppler instrument
h	Depth of water column
k	Reduced frequency
k_n	Number of exceedances of threshold used in POT analysis
l	Pareto distribution log-likelihood
m	Gradient of linear regression analysis
m_r	Number of observations per return period
n_y	Number of observations per year
p	Declustering threshold
q_r	Radial component of induced velocity
q_θ	Tangential component of induced velocity
r	Declustering run length
s	Reduced time
t	Time
u	Instantaneous flow speed in principal flow direction
u'	Instantaneous perturbation from mean flow speed in principal flow direction
$\tilde{u}$	Normalised longitudinal flow perturbation, u'/U
u_1	Instantaneous flow speed in West-East direction
u_2	Instantaneous flow speed in South-North direction

u_R	Resultant instantaneous flow speed in horizontal plane
v	Instantaneous flow speed in transverse flow direction
v'	Instantaneous perturbation from mean flow speed in transverse flow direction
$\tilde{v}$	Normalised transverse flow perturbation, v'/U
v_b	Flow velocity in direction of acoustic beam
w	Instantaneous flow speed in vertical flow direction
w'	Instantaneous perturbation from mean flow speed in vertical flow direction
$\tilde{w}$	Normalised vertical flow perturbation, w'/U
w'_0	Amplitude of the induced vertical velocity fluctuations
x_t	GPD threshold
x	Return level in statistical analysis of extreme values
y	Threshold excesses used in extreme value analysis
z	Distance from the seabed
A	Planform area of lifting surface
A_s	Frontal area of the turbine fastening structure
B	Buoyancy force
C	Correlation coefficient of acoustic Doppler instrument
C_{ij}	Covariance components of PCA
C_D	Drag coefficient
C_L	Lift coefficient
C_T	Thrust coefficient
C_θ	Torque coefficient
D	Drag Force
F_N	Normal force
F_T	Cable tension force
F_W	Weight force
F_x	Measured force aligned with x-axis
F_z	Measured force aligned with z-axis
G	Cumulative distribution function of Generalized Extreme Value distribution
H	Cumulative distribution function of Generalized Pareto distribution
$\tilde{H}$	Empirical distribution function
I_g	Gust intensity
L	Lift force
L_a	Averaging length scale
N	Number of point vortices used in the wake vortex model

N_p	Number of acoustic pings per averaging ensemble
N_r	Return period of extreme value analysis
M	Number of induced velocity locations in vortex model
P	Power density
P^+, P^-	High/low pressure
R	Distance from point vortex to point of influence
$\hat{R}$	Radius of axial flow turbine
T	Period of oscillation
T_a	Temporal averaging period
TI	Turbulence intensity
U_0	Flow velocity in principal axis direction at surface of water column
U	Mean flow velocity in principal direction
V	Mean flow velocity in transverse direction
W	Mean flow velocity in vertical direction
α	Angle of attack
α_a	Actual geometric angle of attack
α_e	Effective angle of attack
α_0	Amplitude of geometric angle of attack
β	Power law exponent
δ	Thickness of boundary layer in the flume
ζ	Exceedance probability
θ	Direction of point of influence relative from a point vortex
θ_P	Direction of principal axis from W-E direction
θ_R	Direction of flow direction from principal axis
ϵ	Effectiveness of lifting surface
λ	Wavelength
λ_a	Acceleration threshold filter constant
λ_1	Eigenvalue of major principal direction
λ_2	Eigenvalue of minor principal direction
$\tilde{\lambda}$	Normalised ratio of eigenvalues
μ	Coefficient of static friction
ξ	Shape factor of probability distribution
ρ	Density of sea water
σ	Scale factor of probability distribution
φ	Phase difference between pitch motion of Foil A and Foil B

φ_T	Angle of tension force relative to seabed
ϕ	Eigenvectors of PCA
ω	Angular frequency
Λ	Aspect ratio of lifting surfaces
Γ	Circulation of point vortex
Γ_b	Instantaneous bound circulation per unit span
Γ_w	Total circulation in the wake of oscillating lifting surface
τ	Time interval of integration in the Duhamel integral

Subscripts

e	Experimental value
ps	Phase-space
qs	Quasi-steady
t	Theoretical value

Abbreviations

ADCP	Acoustic Doppler Current Profiler
AGB	Active Gravity Base
EMEC	European Marine Energy Centre
FPGA	Field-Programmable Gate Array
OEF	Empirical Orthogonal Function
PCA	Principal Component Analysis
PGB	Passive Gravity Base
POT	Peak Over Threshold
PSD	Power Spectral Density
RMS	Root Mean Squared
SC	Screen Configuration
TTT	Tidal Turbulence Tripod

Chapter 1
Introduction

1.1 Research motivation

The Active Gravity Base (AGB) is a sub-sea support platform under development in response to the time consuming, expensive, labour intensive techniques more commonly considered for the fastening of tidal turbine prototypes to the seabed. The AGB device utilises the motion of the tidal flow itself to generate enhanced gravitational down force using fixed hydrofoils. This allows the dry weight of the device to be reduced relative to conventional gravity based designs, with a significantly reduced installation time and cost relative to other anchoring or drilled pile techniques.

While this concept has been shown to work effectively in 1/7th scale tests as well as in the deployment of the full scale prototype in Orkney, the underlying assumption that the tidal flow was purely one-dimensional was applied in the initial numerical modelling of the device. That is, the performance of the device was calculated for the idealised case where the tidal flow reversed through 180° in a bi-directional flood-ebb cycle. The velocity of real tidal currents has three-dimensional variations and irregularities over a number of orders of magnitudes. This presents an uncertainty in the performance of the device over extended periods of time which has not been explored to date.

This thesis advances the understanding of the three-dimensional nature of energetic tidal flows with a focus on the application of the AGB. In achieving this, such research also constitutes a contribution to the understanding of dynamic loading conditions on existing turbine fastening concepts, as well as turbine blades.

1.2 The increasing importance of renewable energies

The available extraction of the global resource of fossil fuels, which constitutes 63% of fuel sources for OECD electricity production (IEA, 2012), is inevitabley finite. Furthermore, the combustion of such fuels has been strongly linked with a global destabilisation of the climate (Stern, 2006). In response, many governments have introduced targets for increased energy

Table 1.1: Comparison of tidal and wind energy converter operating environments

	Flow Velocity U (m/s)	Fluid Density ρ (kg/m^3)	Kinetic Energy Density $\frac{1}{2}\rho U^2$ (J/m^3)	Power Density $\frac{1}{2}\rho U^3$ (W/m^2)
Tidal	2-4	1025	2050 - 8200	4100 - 32800
Wind	10-20	1.2	60 - 240	600 - 4800
Tidal : Wind	0.2	854	34	7

production using renewable sources (e.g. Climate Change Act (2008)). One such energy source is the astronomically driven tidal current energy, which is the focus of this thesis.

1.3 Benefits and challenges of tidal current energy capture

The primary advantage of extracting energy from tidal currents is the predictability of the energy resource (Pugh, 1987; Boon, 2004). Interestingly, the first recordings of the high and low water levels were probably collected at around 150BC in the Persian Gulf (Strabo, 1969). With the understanding of the driving forces of the tides, and the improved prediction of the motion of these celestial tidal drivers, the harmonic method of tidal predictions was developed by Lord Kelvin. The result is the ability to predict the tidal heights and mean flow velocities years in advance. While the available energy in the tidal stream can be shown to vary harmonically, the predictability is a key advantage over the alternatives of wind and wave energy which are driven by the less predictable meteorological effects.

While the operation of some tidal stream energy converters is modelled on the increasingly common three-bladed horizontal axis wind turbine, the operating environment of the two technologies is significantly different. The flow speeds of energetic tidal sites are approximately 20% of the equivalent site selected for wind energy extraction, and the density of seawater is 854 times greater than air. The result is a greater power density available in the tides for conversion to electricity, and therefore the size of the turbine is able to be greatly reduced. A summary of expected energy and power densities in representative sites for tidal and wind energy conversion is presented in Table 1.1.

The inherent need for tidal turbines to be submerged within the water column has the potential to reduce the visual impact of the installation. While some designs are surface piercing, others are completely submerged to offer little or no obstruction to the present appearance and surface

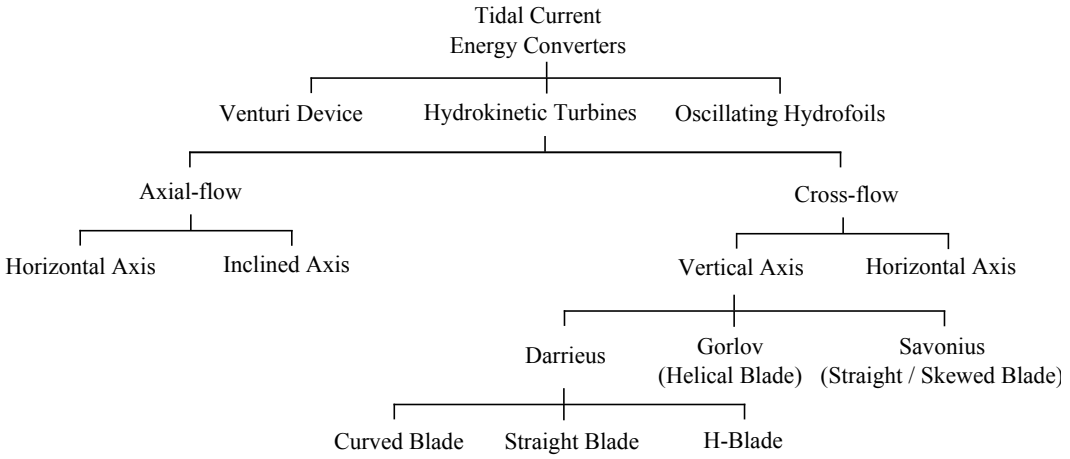

Figure 1.1: Summary of tidal power conversion device concepts. Adapted from Khan *et al.* (2009) and Bryden (2006).

users of the site. The operational noise, often audible from wind turbines, is also reduced by locating the device underwater. This may be viewed as advantageous by humans, however the effect of the operational noise of the submerged devices on the marine environment is an area of important and ongoing research (Basset *et al.*, 2011; Willis *et al.*, 2013).

1.4 Introduction to tidal current energy converters

Faced with the challenge of making tidal power an economically viable prospect, inventors are drawing heavily on the more established wind power industry for inspiration from a proven technology. While an understanding of aerodynamic loading on the blades can be superficially translated to hydrodynamics in energetic tidal streams, and generator technologies can be marinised for sub-sea applications, the operating conditions of the devices are vastly different. Three-bladed axial flow tidal turbine designs are becoming increasingly dominant, the arguments which favoured axial flow turbines to vertical axis configurations in the wind industry do not all directly translated to the tidal power sector (Gretton, 2009). This has resulted in a wide range of power conversion device concepts, summarized in Figure 1.1.

The first level of the flow chart of Figure 1.1 is included to demonstrate the diversity of concepts being considered for energy extraction from tidal streams, however the concept which is primarily addressed in this thesis is the family of hydro-kinetic turbines. As such, the principle designs currently considered by developers are briefly introduced in this section.

1.4.1 Axial flow turbines

Axial flow turbines generate torque about an axis parallel to the tidal stream direction. While this design is similar to that of most modern wind turbines, the convergence towards a three-bladed horizontal axis device experienced in wind is not yet evident in tidal developments.

One of the first axial flow tidal turbine prototypes was that tested by IT Power in Loch Linnhe, Scotland, in 1994. Rated at 10kW, this 3.5m diameter two-bladed design was suspended below a floating raft in the Corran Narrows, and produced a maximum power output of 15kW at the shaft (Ainsworth and Thake, 2006).

Marine Current Turbines Ltd (MCT) was established to commercialize the early research done by IT Power, and was the forerunner of axial flow turbine development at turn of the 21st century. In 2003, the 300kW *Seaflow* turbine was installed at Lynmouth, England (Thake, 2005). The turbine was mounted on a monopile foundation which allowed the 11m diameter turbine to be raised out of the water for maintenance. The electricity generated by *Seaflow* was dissipated by heat sinks. One novel, and now patented, aspect of the design was the ability for the turbine blades to pitch through 360°, allowing the rotational direction of the turbine to be constant through both yaw and ebb tides, and therefore permitting the use of a uni-directional gearbox.

Many attributes of *Seaflow* were then incorporated into MCT's *Seagen*, which was installed in Stangford Narrows, Northern Ireland, in 2008. The key development of this design was the cantilevered positioning of two 600MW turbines on either side of the pile support on a horizontal arm structure (Ainsworth and Thake, 2006). This allowed two turbines to be deployed in a single installation, as well as the removal of blades from the detrimental effects of the pile wake. With limited access to necessary installation vessels, the *Seagen* device was fastened to the seabed using a jacket foundation with four 1m diameter steel pins drilled to a embedment depth of 9m (Fraenkel, 2009).

More recently, a range of devices with a rated power target of up to 1MW are undergoing prototype scaled testing facilitated by the European Marine Energy Centre (EMEC) at Orkney, Scotland. Though similar in generation capacity, the variations within the designs of such large scale turbines is still diverse. In an effort to reduce complexity, OpenHydro Group Ltd have developed a axial flow turbine which operates using drag-based rotor blades, rather than the lift-based blades used by MCT. The power take-off (PTO) is also located circumferentially rather than axially. Though scaled testing has been carried out using twin-piled foundations (Figure 1.2a), the commercial deployments will be fastened to the seabed with a gravity base

(a) OpenHydro EMEC test facility (OpenHydro Group Ltd, 2012b)

(b) Atlantis Resources *AK-1000* turbine (BBC, 2010)

(c) TGL *DEEPGen III* turbine (Tidal Generation Ltd, 2010b)

Figure 1.2: Axial flow turbine prototypes in EMEC

(OpenHydro Group Ltd, 2012a). Atlantis Resources have developed a 1MW *AK Series* device with two co-axial contra-rotating turbines and fixed pitch blades, shown in (Figure 1.2b). With a blade diameter of 18m, this device is currently the largest of its type (BBC, 2010). Tidal Generation Ltd (TGL) is presently constructing a 1MW turbine called *DEEPGen IV* following scaled tests using the 500kW *DEEPGen III* (Figure 1.2c). These devices have the ability to yaw into the incident flow to maximize energy capture and minimize transverse loading on the turbine structure (Tidal Generation Ltd, 2010a).

1.4.2 Cross-flow turbines

Cross-flow turbines operate by generating a torque about an axis perpendicular to the flow direction. These configurations have become less popular in the wind industry compared with axial flow devices, however the reasons for the dominance of axial flow turbines in the wind industry are not directly transferable to the tidal current case.

Gretton (2009) identified two disadvantages of cross-flow wind turbines relative to axial flow wind turbines. Firstly, fixed pitch cross-flow wind turbines operate at a lower optimum tip speed ratio than the axial flow equivalent, leading to increased blade area and gearbox costs. Also, the aerodynamic loading on the blades of a fixed pitch vertical axis device vary throughout one rotation, resulting in a fluctuating torque at the shaft known as 'torque ripple'. The tip speed ratio of tidal turbines is likely to be limited to relatively low values by the onset of cavitation (Salter, 1998), which favours the optimum operating conditions of the cross-flow device. Such low tip speed ratios in the marinised cross-flow turbine require higher solidities than the wind

(a) ORPC *TidGen* Turbine (Walsh, 2012)

(b) *Neptune Proteus* Turbine (Neptune Renewable Energy Ltd, 2012)

Figure 1.3: Cross-flow turbine prototypes

equivalent. One way that this can be achieved is through increasing the number of blades. This will act to reduce the fluctuations in the shaft torque.

Though the principal direction of rotation is in the same plane, cross-flow turbines are perhaps even more diverse than axial flow actuators, with a wide range of blade shapes and configurations as demonstrated in Figure 1.1.

The earliest formally documented project which used cross-flow turbines submerged in moving water was carried out by the Intermediate Technology Development Group from 1976-1984 (Thake, 2005; Khan *et al.*, 2008). As part of this initiative, a Darrius-type rotor was fastened to a floating rig in a 1m/s current of the Nile River in Juda, Sudan, where it was used to pump irrigation water through a head of 5m at a rate of 2000L/hour (Thake, 2005).

Since these beginnings, many cross-flow turbines have been proposed for use in tidal currents, though fewer have progressed to testing phases past laboratory experiments. In 2012, Ocean Renewable Power Company installed the first tidal stream turbine deployed in American waters with the horizontal-axis cross-flow turbine *TidGen* in Cobscook Bay, Maine, shown in Figure 1.3a (Walsh, 2012). Based on the Gorlov turbine design, this 30m long device is expected to generate up to 150kW in the 3m/s flow (ORPC, 2011). Another example of a cross-flow device to reach a similar stage of development is the *Neptune Proteus* device developed by Neptune Renewable Energy Ltd (presently in liquidation), shown in Figure 1.3b, which uses a Venturi duct to accelerate the tidal flow onto a $\varnothing$6m $\times$ 6m vertical axis turbine. The flow is further augmented by automated vertical shutters to optimize the device performance (Neptune Renewable Energy Ltd, 2012).

Table 1.2: Estimated levelised cost of energy components for tidal energy converter farms, and modeled cost reductions between 10MW and 200MW cumulative installed capacity

Cost component	Levelised cost of energy components for tidal current energy		
	Present values		200MW installed capacity prediction
	(Carbon Trust, 2011)	(LCICG, 2012)	(Carbon Trust, 2011)
Installation	33%	35%	31%
O&M	18%	15%	14%
Station keeping	15%	10%	11%
Structure	14%	15%	13%
Power take-off	11%	10%	16%
Grid connection	9%	15%	15%
Total	100%	100%	100%

1.5 Introduction to tidal turbine fastenings

The primary role of the turbine fastening is to maintain the position of the installation on the seabed. To achieve this, the large drag forces generated by the structure and the thrust force generated by the turbine must be withstood. Also, in order for a torque to be generated in a tidal turbine during the power conversion process, an equal and opposite reaction torque must be available. As such, securely fastening a tidal turbine to the seabed is of paramount importance to the performance of the device. However the strong tidal currents which the developers desire have shown to create a design environment with as much energy available for destruction as for conversion.

The importance of the fastening design is also very relevant to the financial viability of tidal stream conversion projects and indeed the potential resulting industry. The levelised cost estimates of the key components of a tidal energy deployment are presented in Table 1.2. If the design of the sea-bed fastening is taken as affecting the cost of both installation and station keeping, this comprises 40-48% of the total installation cost of the device. The cost of the device structure itself could also be influenced by the fastening method used.

Furthermore, the Carbon Trust (2011) have modelled the cost reduction which can be expected from the development of tidal energy deployments from the installed capacity of 10MW to 200MW. This study indicates that the total costs could be expected to decrease by approximately 45%. However when the costs are broken down into levelised values, it can be seen that the relative importance of the cost components influenced by the fastening design remain similar.

1.5.1 Design objectives of tidal turbine fastenings

A variety of technical standards pertaining to the installation and station-keeping of offshore structures have been given by authorities such as API (2005) and DNV (2011). The tightest regulations have been developed for the oil and gas industry due to the risk to human life and high environmental impact of a failure. Offshore marine energy converters, however, are usually unmanned, with the primary consequence of failure being largely financial (Harris *et al.*, 2004). As such, it can be argued that the standards applied to the oil and gas industry are not directly transferable to the fledging tidal energy industry. However the key elements of the regulations for the design of offshore steel structures given by DNV (2011) summarise the general aims of the foundation structure, stating that the design must be able to:

i) Withstand loads which occur during installation, operating and extreme conditions,
ii) Maintain acceptable safety for personnel and environment,
iii) Demonstrate adequate longevity against deterioration throughout the design life.

1.5.2 Obstacles

A range of challenges lie in the way of achieving the specified objectives of the fastening concept. The most significant considerations to be acknowledged at each stage of the design phase are introduced in this subsection.

Cost

As previously discussed, the cost of installations must be reduced in order for the marine renewable energy to develop from a research sector into an economically viable industry. At present, the installation costs represent a significant proportion of the investment required to deploy a marine power device. The key cost drivers can be separated into the following categories:

- Manufacturing
- Transportation
- Deployment
- Operation and maintenance
- Decommissioning

Structural footprint

The projected area of the fastening onto the seabed must also be minimised. In sites where the bathymetry is rapidly changing, a large fastening footprint can be detrimental to the stability of

the installation as it spans areas of the seabed with varying surface heights. In the future, the footprint size of the fastening may become important as developers deploy a number of devices in an array, or 'farm'. If the high impedance of the tidal current through channels is considered, Salter (2009) argues that the energy available for extraction can be increased by close packing of the devices. The device footprint must be limited to facilitate this.

Fatigue

Tidal turbine deployments in energetic flows are subjected to a range of dynamic loading conditions. The resulting fatigue loading is an important consideration in designing for reliability of an installation. These forces are a result of the unsteady flow speeds inherent in submerged offshore environments, and vary over a large range of frequencies and velocity magnitudes. The key velocity fluctuations include ambient turbulence, vortex induced vibration, wave induced velocity oscillations and cyclic tidal constituents.

Extreme events

Marine power installations must be designed to withstand extreme storm loading conditions. The magnitude of the extreme event for which the installation is specified to withstand is often quantified as the statistical frequency for an event of such magnitude occurring. That is, an 'N_r-year storm' is the storm conditions which could statistically be expected once every N_r years. It is often difficult to quantify the magnitude of extreme events due to the limited length of data available at the specific installation site.

Speed of installation

By their nature, marine energy converters are required to be installed in sites of high energy density. For tidal turbines, this means installation in highly energetic flows, often within very shorts slack tide periods. For example, the flow conditions at Strangford Loch were such that a slack tide period of less than 10 minutes was available for the MCT installation.

The meteorological conditions also have an important role in the requirement of rapid installation techniques, as the available installation period is often limited by weather conditions which are suitable for deployment, referred to as weather windows.

Installation orientation

The orientation of the marine energy converter can often be significant with regard to the performance characteristics of the device. This can prove challenging for slack moored devices, which are aligned by the drag of the device itself. In simultaneous wave, tidal and wind condi-

tions, the orientation of the device may be altered to become sub-optimal as a consequence of the combined forcing conditions.

Marine growth

Because many devices are designed to be deployed for a period of years, marine growth is likely to be an important consideration (Orme *et al.*, 2001). While the extent of marine growth is site specific, it is often seen to be increased nearer the surface and in warmer water temperatures. The additional growth on the structure increases both the drag coefficient and the effective area of the host structure. Efforts to minimize marine growth include the use of copper plating which prevents the organisms from attaching to the surface. Anti-fouling paints are available, but often with a limited useful life.

Decommissioning

As with the initial installation, the decommissioning process must also be considered in the design so that this can be carried out in energetic environments within the time constraints of weather windows and low tidal flows.

1.6 Existing technologies for tidal turbine fastenings

The requirements of the support structure of a tidal turbine can be decomposed into the three components of the foundation, load transmitting structure and sub-sea connection (Orme and Masters, 2006). This thesis is specifically concerned with the foundation component of the support structure.

The range of available designs for turbine operation continue into the diverse concepts for fastening the devices in position. The success of a particular fastening concept is highly site-specific, depending on such parameters as the water depth, maximum flow velocity, tidal directionality, accessibility to harbours, bathymetry and the geo-technical structure of the ocean floor. The resulting range of configurations for fastening tidal current energy converters to the seabed can be grouped into the following four broad categories:

- Gravity base
- Mono-pile
- Jacketed pile
- Floating/moored

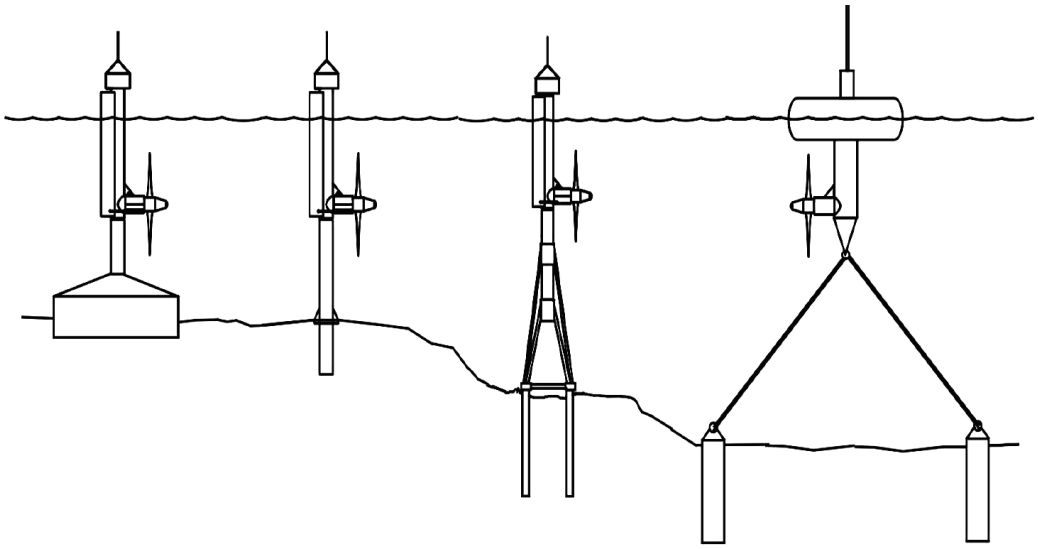

Figure 1.4: Schematics of fastening methods proposed for the installation of tidal turbines. Adapted from Fraenkel (2006).

Schematics of these fastening methods are presented in Figure 1.4. Note that this figure depicts each mooring method fastening a horizontal axis turbine in a surface piercing arrangement. However, each concept can be utilized for the installation of a variety of turbine designs in a range of sub-sea applications.

The following subsections systematically present the key tidal stream turbine fastening categories devised to date, describing their respective benefits and weaknesses.

1.6.1 Gravity base foundations

Gravity based fastening methods rely on the mass of the foundation under the influence of gravity to position the tidal turbine on the seabed. The weight of the structure is such that no tensile loading condition exists between the base and the seabed. The normal force on the seabed must create sufficient friction to overcome the drag force on the structure. Also, the weight distribution of the base must be able to counter the overturning moment generated by the net drag force being located above the seabed connection. While such a fastening method is intuitively simple in concept, the implementation of gravity bases can be challenging.

Transportation and handling

Conceptually, the simplicity of the installation of a gravity based platform is the greatest attrac-

tion to the concept, which allows rapid deployment to the seabed with minimal post-deployment adjustments. While the design of gravity bases is relatively simple, the significant weight of the base, particularly out of the water can lead to high transportation costs. With the combination of dynamic loading conditions on the base, as well as an effective reduction in downforce due to the effect of buoyancy, the required dry weight of a gravity base can be extremely heavy. Quantitatively, if the gravity base was assumed to be manufactured from concrete, the dry weight of the foundation must be increased by a factor of approximately 1.6 to account for this buoyancy effect of sea water. A further safety factor is required to be applied to account for the varying combined loading of tidal current and oceanic swell on the foundation, further increasing the weight of the gravity base. The Rotech Tidal Turbine (RTT2000 Mark II) has a calculated required ballast of 615 tonnes, in addition to 513 tonnes of structural steel, highlighting the true significance of the mass required in the use of gravity base fastening (Previsic, 2006).

One solution to the excessive dry weight of gravity bases is to separate the total mass of the gravity base into smaller units. This method can be seen in the Hammerfest Strom device which separates a total of 200 tonnes of ballast onto the three sea floor contact points (Mraz, 2004).

Another design consideration to improve the ease of installation is to introduce the ballast post-installation. By installing the device with empty ballast chambers and then filling these with silt and gravel in situ, sufficient downforce can be achieved without exceeding dry weight limitations.

Seabed preparation

In order to distribute the weight of the foundation to counter the overturning moment, as well as reduce the bearing load on the supporting seabed, the 'footprint' of the foundation must cover a large area. This is complicated by the fact that the seabed is commonly not a flat surface as thus requires potentially significant seabed preparation to allow the device to be positioned level. Sites with relatively flat, rock sea beds could require little or no seabed preparation measures, but this restricts the number of suitable locations.

Water depth

The overturning moment on the device is proportional to the distance of the turbine from the seabed. As such, the position of the turbine is limited to the lower flow speeds that occur closer to the seabed if the foundation is to be kept at a viable size and weight. It could therefore be argued that gravity bases are better suited to shallower channel depths, in order to operate as close as possible to the desired mid-column location.

The velocity profile of the water column is often approximated using a power relation, such that the mean stream-wise velocity at distance from the seabed, z, follows an exponential vertical profile through the water column. This profile is described by Equation 1.1 where h is the depth of the water channel, U_0 is the flow velocity at the surface, and β is the denominator of the power law exponent.

$$U(z)/U_0 = \left(\frac{z}{h}\right)^{1/\beta} \tag{1.1}$$

While it is often assumed that $\beta = 7$, Gooch *et al.* (2009) have experimentally measured sites in the Puget Sound with values ranging from $2 \leq \beta \leq 12$. The normalised velocity given by Equation 1.1 was plotted for this range of power law exponents for a location of $z = 10m$ for channel depths in the range of 30m $\leq$ h $\leq$ 60m, with the results shown in Figure 1.5. It can be seen that the relative mean stream-wise velocity at this location is relatively insensitive to channel depth, particularly at the higher possible values of β. However, due to the exponential relationship, the values for relative flow velocities are shown to be very sensitive to the value of β used. This parameter is site specific, and so highlights the value of resource characterization studies is the selection of installation methods in order to determine the kinetic energy flux at the installation depth.

Because the installation depth of a gravity base fastening is not limited by the complex operations required in the installation of seafloor-penetrating fastening methods (explained in the following subsections), the feasible depth of installation is superior to other fastening techniques. This is a distinct benefit when it is considered that 63% of extractable tidal resources are found at sites that are deeper than 40m (Black & Veatch Limited, 2005).

Operation and maintenance

Scouring behind offshore wind turbine supports has been found to be most sensitive when gravity bases are used, with the potential to cause a destabilising effect on the supporting seabed (Harland and Wolff Licences Ltd, 2001). Scour is the local removal of seabed sediment by increased hydrodynamic forces owing to the increase in speed and turbulence of the tidal current around an obstructing body (Hoffmans and Pilarczyk, 1995). However, a fundamental difference between the installation of offshore wind turbines and tidal turbines is that tidal turbines are, by necessity, located where the tidal current has significant velocity. As a result, the seabed in desirable sites for tidal power capture is often swept free of sedimentary deposits to expose a solid rock base (Salter, 2009). This is likely to reduce the need for the costly scour prevention techniques utilised by the offshore wind power industry and allow a secure fastening to be

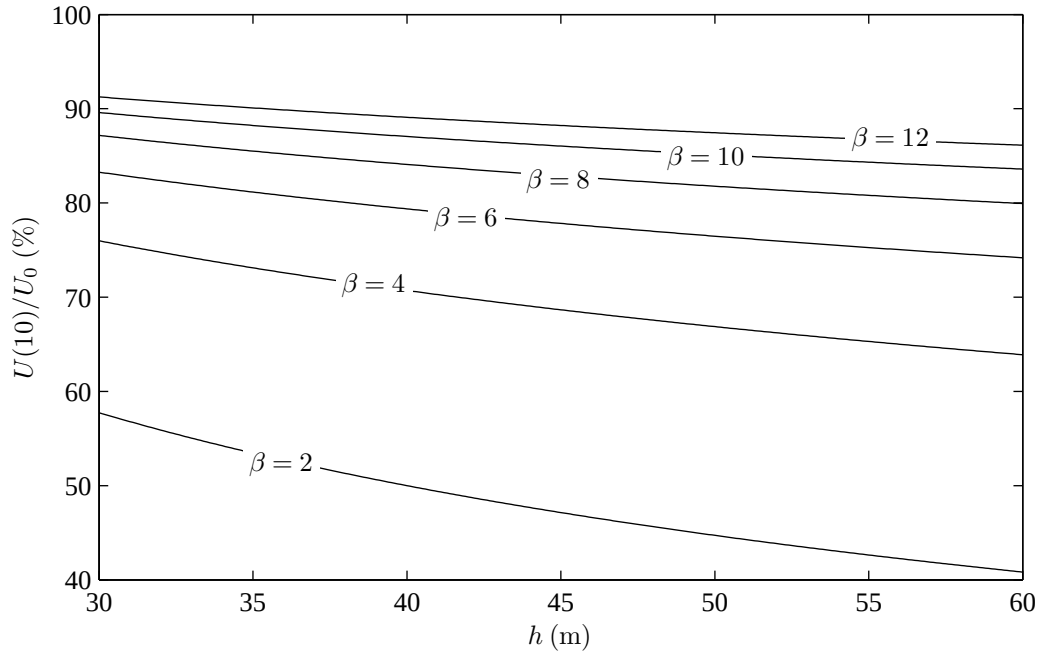

Figure 1.5: Relative velocity at z = 10m in channels with a depth of 30m $< h <$ 60m and vertical profiles following power laws represented by $2 < \beta < 12$.

achieved with minimal maintenance of the seabed connection.

The accessibility of the tidal turbine is an important consideration as the turbine will inevitably require maintenance during its operational life. Gravity based anchors are likely to prevent the use of self-raising techniques to present the turbine above the water surface, due to the excessive overturning moment that would result from drag forces at an increased distance from the seabed as the turbine is raised. One solution to accessing the turbine for maintenance is to allow the turbine and generator components to be detachable from the gravity base, thus reducing the cranage requirements for device removal. Variations of this technique have been incorporated into the turbine designs by such companies as Hammerfest Strom and TGL (Mraz, 2004; Tidal Generation Ltd, 2010a). Inherent challenges exist regarding the attachment of lifting lines to the device, and detachment of the turbines from the gravity bases.

Decommissioning

The decommissioning processes of all tidal power installations, in keeping with the ethos of renewable energy, should be as environmentally benign as possible.

In principle, the decommissioning of the gravity base design is simply the reverse of the installation process. The cranage requirements can be reduced by taking the same measures as

installation; that is, separating the gravity base into a number of lighter discrete masses, or displacing the ballast material in the base with sea water prior to lifting help to reduce the required lifting force. Allowances for a greater lifting load than for installation should be made to overcome the suction effects caused by any sediment transport and embedment in the vicinity of the base.

All decommissioning plans of installations in Great Britain waters must be in accordance with the Energy Act (2004).

1.6.2 Monopile fastenings

Developed in such applications as bridges, oil rigs and offshore wind turbines, the use of a monopole fastening is an established method of seabed fastening. Borrowing from these industries, the use of monopiles as a means of seabed fastening can be divided into two groups based on their interaction with the seabed; those that deeply penetrate the seabed, and those which utilise a pressure differential at the base in the implementation of 'suction piles' (Previsic, 2006; Bang *et al.*, 2000). The former group can be further subdivided by the means by which the pile is inserted into the seabed. This subsection addresses the two predominant penetration methods of hydraulic pile driving and the grouting of a deep penetrating pile into a pre-drilled hole.

The tidal power industry will inherently involve piles with limited lengths in response to the complexities of installation and operation in rapid tidal flows. Detailed standards recommend best engineering practices based on experience with the construction of offshore platforms within the context of the oil industry. One commonly referenced example specifying a design criterion for a 100 year storm is the API RP-2A (American Petroleum Institute, 2000).

Deep penetrating monopiles

The axial compression load on the pile under the weight of the turbine and pile itself is resisted by the skin friction on the outer surface of the pile. For an uncapped hollow driven pile, significant skin friction can also be generated on the inner surface. A capped pile also contributes to opposing the axial compression through bearing loads generated at the closed end. The skin friction on the outer surface on the pile is highly dependent such factors as the ratio of pre-drilled hole diameter to pile diameter, the use of jetting and the use of additional material such as grout which may be inserted between the pile-seabed interface.

In the instance that the pile comes under tensile loading, foreseeable only in decommissioning, the skin friction and weight of the pile provide the opposing force. In the unplugged pile case,

the weight of the internal slug of soil can also contribute significantly to required lifting force.

The influences of transverse loads on the monopile are of particular interest at sites with significant tidal energy. Due to the ability for pilings to protrude a significant distance from the seabed into the flow (potentially spanning the entire water column), the moment generated at the supported end is likely to be more significant with this method of fastenings and the engineering challenges are increased when the dynamic cyclic nature of the loading is considered. The magnitude of the bending moment and subsequent pile stresses is influenced heavily by the pile-soil interface. An increase in wall thickness in the form of a sleeve at the seabed-pile interface is one common technique to reduce the vulnerability for failure in this region.

The analysis of a laterally loaded pile is typically quantified using '$P-y$' curves which account for the soil resistance against load P being a function of its deformation, y, at each level below the seabed. These empirical 'Matlock-Reese' $P-y$ curves can be modified to account for both soil and pile mechanical properties through adaptations of this work, such as in the theoretical solution of the strain wedge model (Ashour and Norris, 2000).

Driven monopile

The use of hydraulic, diesel and steam powered hammers has been successfully used in the oil industry, favoured for the speed of installation relative to the pre-drilling alternative. The operating principle of the hammer is governed by the soil properties; from vibratory mode for loose sands and gravels, to impact driving through more solid strata with energies of 1800kJ with each stroke (Gerwick, 1999). In impact driving, the driving head imparts a transverse wave in the top end of the pile, which travels the length at the speed of sound and is dissipated in the resisting soil at the bottom tip.

A common lubricating technique often used in conjunction with pile driving into softer soils is known as 'jetting'. This process involves directing a jet of water in the vicinity of the pile to loosen the sediment.

It is critical that the pile is designed with dynamic driving loads being fully considered. Fabrication of the pile using spiral welding techniques has historically led to failure in shear along the welded seams under the shock loads of impact driving, though improvements in manufacturing technologies has acted to reduce this risk in recent years (Gerwick, 1999).

Drilled monopile

In circumstances where the seabed has sufficient strength, a self-supporting hole can be drilled to locate the monopile, later fastened with grout. When the seabed is less stable, a socket is

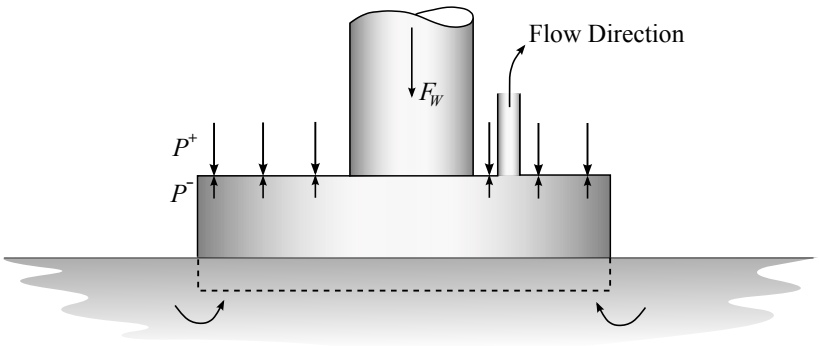

Figure 1.6: Schematic of suction caisson operation. Adapted from Previsic (2005).

created by lining the hole with a casing to prevent collapse.

The drilling and jetting processes can have a detrimental effect on the hole walls. The exposure to moisture of some soils such as shale or serpentine, and also the accumulation of softer sedimentary soils between the pile and rock can lead to a marked decrease in the reactive force offered by the soil on the pile (Gerwick, 1999). The latter issue is remedied by grouting the pile in place, to ensure a positive interface between the soil and pile is made. This technique is able to generate much higher friction coefficients between the pile and underlying strata where softer sediments are present. In some instances, the combination of driving a pile into an under-sized pre-drilled hole may be used to increase the surface friction along the pile wall.

Suction based monopiles

What began as a novel fastening method has now been shown to avoid a number of challenges associated with piled fastenings; reducing the installation cost and complexity relative to seabed penetrating pile installations particular at significant depths (Aubeny and Murff, 2005). Also referred to as 'suction piles', 'skirt foundations' and 'bucket foundations', suction caissons penetrate soft seabed sediments under the gravitational downforce of the pile to form a seal around orifice of the caisson 'bucket'. A valve on the top face of the caisson allows the enclosed water to drain from inside caisson as the foundation settles into the seabed. A pump is then used to extract the seawater from inside the caisson to create a differential pressure which effectively sucks the device to the seabed.

Suction anchors utilise the same principal of differential pressure but differ from suction caissons primarily by requiring the permanent pumping to maintain the suction force (Iskander *et al.*, 2002). Both of these foundations require sediment conditions which allow seabed penetration in order to fully or partially seal the bottom face of the suction drum. However, due

to the energetic flows which define suitable areas for tidal power installations, sediments are typically removed by the currents making suction caissons and anchors unsuitable for use in the majority of cases (Previsic, 2005).

Installation

The most suitable pile installation technique is highly site and device specific, and depth of the pile penetration into the seabed requires an in-depth localised knowledge of the installation site. Thake (2005) recommends that core sampling should be carried out to the maximum potential depth of the monopole; a process requiring jack-up barges with capacity close to that required for the drilling of the final monopole hole, and associated costs are likely to be quite substantial.

The initial attempted installation of *SeaFlow* had to be aborted due to the seabed properties being softer than the values interpolated from nearby bores and existing data in the vicinity of the site. As a result, subsequent core samples were taken at the proposed location of *SeaFlow* to ensure that monopole fastening could be implemented (Thake, 2005).

Transportation and handling

The most suitable method of pile transportation is also highly installation-dependant, influenced by such factors as pile dimensions, the number of installations to be carried out and the distance from port to the offshore site. For long distance transportation of a number of piles, shipping or towed barge is often the most practical method, as is often used in offshore wind farm units. An alternative method of pile transportation is to seal the open ends of the pile to allow the pile to float under its own buoyancy. The raising of the horizontal floating pile to the vertical orientation for installation can create significant bending moments which must be incorporated into design calculations (Gerwick, 1999).

For more rapid installations, transportation of the pile in the vertical orientation is achievable through the use of the cranes on board the jack up barge. For the application of tidal power installations, the time available for the pile to be secured below the waterline is often restricted by slack tide windows in the order of minutes. This makes transportation of the pile in the upright position advantageous, though not without its associated costs and complex restraining considerations.

Water depth

The presence of energetic currents synonymous with locations considered for tidal turbine installation introduces a number of fresh challenges to monopile installation. Though GPS navigation in conjunction with positioning thrusters are able to locate a barge accurately above

the installation site with relative accuracy, several-stage installation processes require greater accuracy which can only be achieved by locating the installation rig through contact with the seabed itself. For this reason, jack-up barges are often used for monopile installations.

In the installation of MCT's 300kW *SeaFlow* device, the same barge (Seacore's *Deep Diver*) was able to perform both the drilling and craning tasks, however for the larger 1.2MW *SeaGen* installation, a separate craning jack-up barge *RAMBIZ* was required to transport the pylon structure (Thake, 2005).

In energetic tidal flow, the legs of the jack-up barge are exposed to highly fluctuating drag forces with the potential to cause significant bending of the legs and slipping at the seabed connection. The flow over the cylindrical legs creates a situation for cyclic vortex shedding, potentially subjecting the legs to high amplitude resonant vibration. The legs of the *Deep Diver* jack-up barge were fitted with custom fairings to prevent such vortex shedding while also reducing the drag loads (Thake, 2005). Fraenkel (2006) suggests that the maximum installation depth able to be achieved using jack-up barges is approximately 50m.

Operation and maintenance

If the underlying stratum has sufficient strength, the monopile arrangement can lend itself to protruding a significant distance from the seabed. In sufficiently shallow tidal channels, this leads to the prospect of surface piercing designs. The effect of having a portion of the structure above the water surface introduces a number of loading conditions and operating considerations which would not influence a submerged design that gravity bases are likely to be limited to. These include the greater influence of meteorological forces such as wind and surface waves, the increased risk of collision with other users of the surrounding waters, in conjunction with enhanced corrosive effect of exposure to oxygen in the air.

The obvious benefit of surface piercing designs is the ability for the turbine to be raised and lowered between the operating position and maintenance position. The option of being able to remove the turbine from the underwater loading conditions may prove invaluable, particularly during the establishing years of the tidal industry.

The challenge of corrosion has been encountered for many years in the maintenance of such semi-submerged structures as ships, piers, and offshore platforms. In the case of the latter, the rate of corrosion has been shown to be a function of water salinity, flow velocity, the concentration of abrasive suspended particulate matter, and turbulence. In a surface and seabed piercing arrangement, it is proposed that the corrosion rate decreases by a factor of two between the splash zone and the permanently submerged zone, and again from the permanently

submerged zone to the length of pile which is under the seabed (Gerwick, 1999). Passively, a corrosion allowance of an increased pipe wall thickness is often incorporated into the design, while sacrificial anodes and protective surface coatings are also essential measures.

Decommissioning

The underlying goal of decommissioning is to return the seabed to a state that can be deemed environmentally benign. Under this criterion, the decommissioning of a pile-fastened installation does not necessarily require the complete removal of the pile. As with the oil industry, deep sea cutting technology is available for the truncation of the pile at the seabed. Such an operation requires close monitoring of the release of potentially harmful waste products.

1.6.3 Jacketed pile fastenings

Jacketed pile fastenings can be seen as an extension of monopile fastenings, as many of the subseabed design considerations are parallel. The primary difference between the two is that jacketed pile fastening includes more than one connection point between the pile and the seabed. This allows the loads to be shared over a number of connection points, as well as providing a wider base from which to counter the moments generated by the drag on the turbine, ultimately allowing the pile to be installed at greater water depths.

As more connection points, or 'pins', are fastened to the seabed, each pin can be designed with a much smaller diameter than that of the pile, thus requiring significantly smaller drilling equipment. However, while the cost of drilling decreases with fastening hole size, it increases with the number of holes in such a way that the net cost of jacketed pile fastening is greater than that of monopile fastening (Fraenkel, 2006). Ensuring that each foot of the jacketed pile base is level adds another degree of complexity to the installation.

As with seabed penetrating monopile installations, the transverse load is resisted by the interaction of the underground pins with the surrounding soil. The use of jacket pile fasting allows for the use of 'batter' piles, which are installed at an angle to vertical, usually in pairs. Such an arrangement allows a component of the transverse force to be resisted axially by the pin, rather than just shear and bending in the vertical case, and hence is more suited to support greater moments created by long piles (Kavazanjian Jr., 2006). Accurate installation of batter piles is intrinsically more demanding than the vertical alternative.

In the case of the MCT's *SeaGen* device shown in Figure 1.7, four 1.0m diameter vertical pins were used with a penetration of 9m (Fraenkel, 2009).

Figure 1.7: Installation of MCT *SeaGen* jacketed pile foundation (Maritime Journal, 2008)

1.6.4 Floating support fastenings

A fastening configuration for midstream turbines with inherently less structural material requirements is the floating support, or slack moored fastening method. This fastening system is made up of a buoyant turbine mounting that is attached by moorings to the seabed. The flexible connection between the turbine and the seabed allows the device to continuously align itself with the tidal current throughout the tidal cycle. The simplicity and size of this fastening methodology are its greatest advantages in both manufacturing and transport.

In order for the turbine to create the torque which drives the generator, an equal and opposite reaction torque must be provided by the fastening. The use of a contra-rotating blade pair has been explored for this purpose, whereby two turbines generate a reaction torque against each other so that the tethers must only restrain the device against the buoyancy and drag forces. Examples of such configurations to be used in conjunction with this fastening method are shown in Figure 1.8.

Transportation and handling

The transportation of slack moored devices can be expected to be less bulky than rigid gravity based anchors and significantly more manoeuvrable than monopile installations. The key components can be separated into the turbine nacelle, flexible mooring lines, and the seabed connection mechanism.

(a) *TidEL* turbine prototype (BWEA, 2007)

(b) *CoRMaT* turbine sea trials (Clarke *et al.*, 2008)

Figure 1.8: Tidal stream turbine designs with floating support systems.

Seabed preparation

The seabed preparation required for a slack moored installation is dependent on the method of fastening to the seabed. Commonly considered connection methods include gravity bases and rock bolts (Owen, 2007).

The requirements of the gravity base are different when used in conjunction with slack moorings as the overturning moment created in the rigid design does not feature. The transverse drag force on the turbine must still be overcome by the frictional resistance between the base and seabed. Also unlike the rigid configuration discussed previously, the moored design requires the turbine to be buoyant, introducing a positive vertical force component to the seabed fastening. Using the notation of the simplified force balance on a moored turbine configuration shown in Figure 1.9, and assuming that the mooring line is fastened to a gravity base, the required weight of the foundation is given by Equation 1.2.

$$F_W > F_B + F_T \sin(\varphi_T) + \frac{F_T \cos(\varphi_T)}{\mu} \tag{1.2}$$

Rock bolts can be considered as downscaled versions of monopile installations, penetrating into the seabed when the underlying strata is solid rock. In contrast to the gravity base, these require the seabed to be accessed by either divers or installation equipment from the water surface. This requirement becomes somewhat more complicated as the installation depth increases.

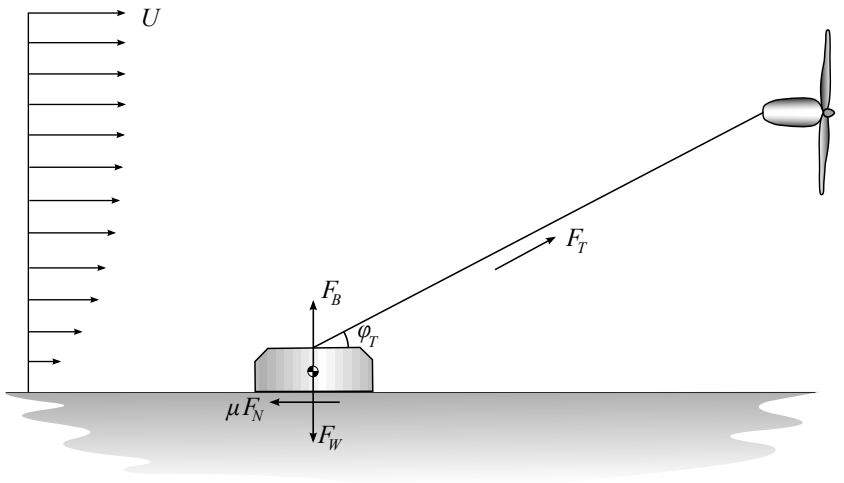

Figure 1.9: Force balance on moored turbine base. Adapted from Owen (2007).

Water depth

Slacked moored designs are typically able to be deployed in greater water depths than methods discussed previously as the overturning moment at the seabed is no longer an issue. While the vertical component of tension in the tethering lines overcomes the buoyancy of the turbine nacelle, the horizontal component of the tension is governed by the turbine geometry and flow speed. The depth of installation is thus primarily limited by the ability to ensure a positive connection is made with the seabed.

Operation and maintenance

In operation, a turbine fastened to the seabed with mooring lines is likely to have more degrees of freedom than rigid fastening designs. Dynamic loading will be introduced if the turbine is sufficiently close to the surface to be influenced by ocean swell. If the turbine motion becomes sufficient, the mooring lines could go slack, inducing 'snatching' loads as they rapidly go taught again. These can be an order of magnitude greater than the operational loads. Multi-catenary configurations can be used to reduce the risk of snatching compared to taut mooring designs.

The variable loading on the moorings due to the tidal cycle, turbulent flow characteristics and oscillating swell motion can prove problematic in the ongoing operation of floating support fastenings. Such loading conditions lead to the rapid fatigue of the moorings, particularly under the harsh operating environment of the deep water current. If chains are used to tether the turbine, particulate matter suspended in the flow increases the friction between links, increasing the rate of wear in areas of contact. Cables are also susceptible to fatigue when operating under

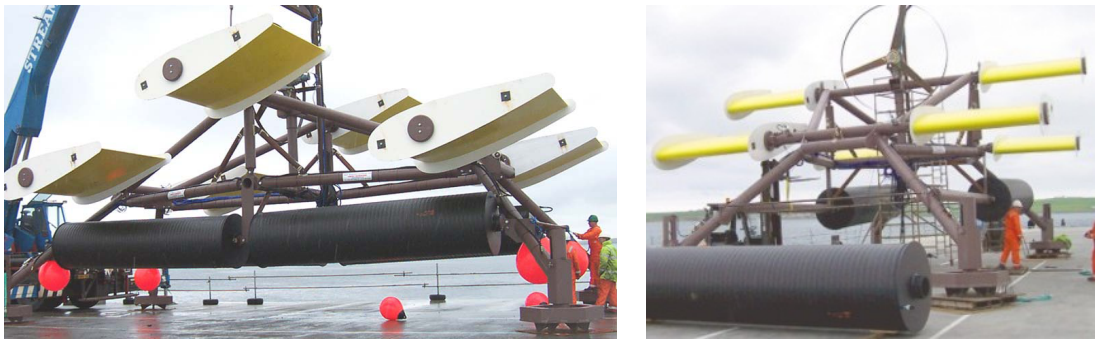

Figure 1.10: Deployment of Active Gravity Base prototype

such conditions. As such the useful life of a floating support fastening can be difficult to predict, especially with respect to the failure of the mooring line.

The flexibility of the mooring lines leads to the requirement of the undersea power cables to also be flexible or compliant. While not expected to carry any of the mechanical loads of the turbine, the motion of the electrical cables can lead to fatigue failure.

In the event of a failure with the turbine, moorings, or power cables, maintenance can prove to be difficult. Maintenance of the turbine is most efficiently performed out of the water, and so for devices fastened on a floating support system, this requires sufficient length of mooring and power cables to enable the device to surface. For more major repairs, part of the device may need to be removed from the water by crane. Maintenance of the tethering line and seabed connection will unavoidably require underwater operations.

1.7 Introduction to Active Gravity Bases

The turbine fastening techniques described in §1.6 represent the predominant concepts being considered in contemporary tidal stream turbine projects. All of these are derived from fastening methods established in related industries including offshore wind power, oil extraction and shipping.

A novel concept has been devised which utilises the hydrodynamic forces created by the flow of the tidal currents over lifting surfaces to generate sufficient down-force to perform as a gravity anchor, without the associated weight issues. This device, referred to in this thesis as an Active Gravity Base (AGB), was conceived by Professor Ian Bryden and developed by Dr. Alan Owen in response to the time consuming, expensive, labour intensive techniques described above to fasten tidal turbines to the seabed. Photographs of the deployment of the prototype are shown

in Figure 1.10 and the key dimensions of the device are shown in Appendix A.

1.7.1 Principle of operation

The underlying development from a conventional or passive gravity base (PGB) which is introduced in the AGB design is the addition of fixed hydrodynamic lifting surfaces at a negative angle of attack to generate an additional down-force component from the tidal current. The primary advantages of this configuration is that the effective weight of the foundation is at its maximum at the peak flow velocities when the forces on the structure are at their maximum. The quasi-static relationship between the additional down-force provided by the lifting surfaces, L, and the flow velocity, U, is shown in Equation 1.3. In this equation, ρ is the density of the seawater, C_L is the lift coefficient of the lifting surface, and A is the planform area of the lifting surface. Note that in this thesis, positive lift is defined in the downwards direction such that the terms 'lift' and 'down-force' are interchangeable.

$$L = \frac{1}{2}\rho U^2 C_L A \tag{1.3}$$

In the design of the original AGB configuration, the lifting surfaces are able to respond to the change in tidal flow direction by rotating about the quarter chord location, in a patented mechanism for generating down-force in bi-directional flows (Owen and Bryden, 2009). This method of providing continuous down-force is facilitated by fabricating the wings with a density less than that off water, so that in a state of zero flow velocity, they freely rotated to an angle of attack of $\alpha = -90°$. When the tidal flow develops from slack water, the drag on the vertical wing passively rotates the lifting surface against a positioning stop to generate the desired negative angle of attack in either flood or ebb direction. This process is shown schematically in Figure 1.11.

1.7.2 Destabilizing flow conditions

While the bulk flow behaviour in a tidal channel is predictable on the hourly scale, the instantaneous flow is influenced by several factors which are the result of random and unpredictable processes. The primary instability of the AGB concept is the sensitivity of the operation to both the changes in water speed and direction which are inherent in energetic tidal currents over a wide range of time scales.

The instantaneous velocity of a tidal flow can be observed to fluctuate in the direction of the

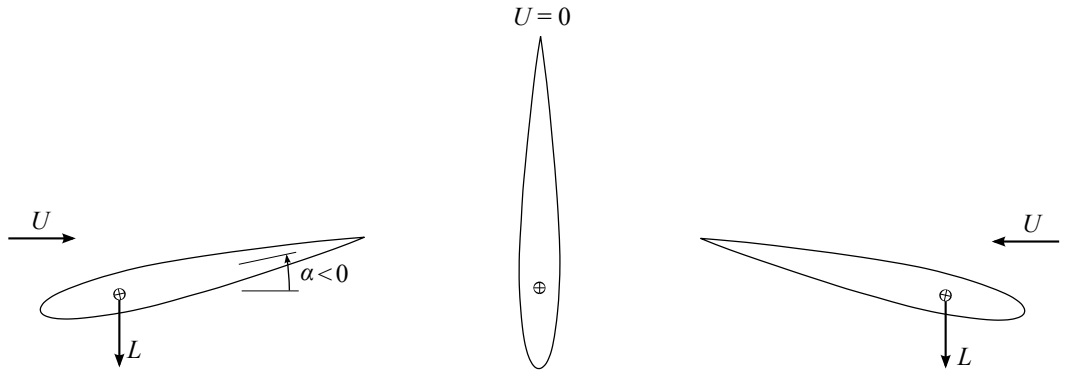

(a) Flood tide (b) Slack tide (c) Ebb tide

Figure 1.11: Rotation of buoyant lifting surface in bi-directional tidal flow. Adapted from Owen and Bryden (2005).

principal axis (x-direction), transverse axis (y-direction), and the vertical axis (z-direction), in time-scales which are not explained by the gravitational pull of the moon and sun. According to convention, in this thesis the instantaneous velocity vectors in the Cartesian coordinate system are defined as (u, v, w) and the mean velocity vectors are defined as (U, V, W). The difference between the instantaneous and mean velocity components in each direction gives the fluctuating velocity components of (u', v', w'). This relationship is shown mathematically in Equation 1.4.

$$u' = u - U, \qquad v' = v - V, \qquad w' = w - W \tag{1.4}$$

Omni-directional currents

Outside of the constraints of local bathymetry and channel boundaries, the flow directional of tidal flows can be attributed to the combination of gravitational forces from the sun and moon (Pugh, 1987; Stanton *et al.*, 2001), as well as the Coriolis Effect in ocean basins (Boon, 2004). This phenomenon of an rotary current results in a flow which rotates from the flood to ebb direction with relatively little change in velocity when compared with the bi-directional case.

Ambient turbulence

The turbulent flow regime inherent in energetic tidal flows causes a chaotic[1] and stochastic[2] instability in the mean flow velocity as the energy from large scale disturbances cascades to smaller perturbations and eventually is dissipated as heat. Turbulence can be identified as a three-dimensional unsteadiness in the flow. Such flows are chaotic in their motion, such that the

[1] A dynamic process which is displays no periodicity in time and space.
[2] A process in which the evolution of a parameter is indeterministic, and can only be described probabilistically.

instantaneous velocity is unable to be predicted. Turbulent fluctuations are able to be observed as rotational 'eddies' in the flow which are at least moderately coherent, though a large eddy structure can be seen to contain smaller eddies within the same region (Pope, 2000). The cascade of energy from the larger eddies result in velocity fluctuations which occur over a wide range of length scales, the extent of which is a function of the Reynolds number (Gretton, 2009).

A common parameter used to quantify the ambient turbulence levels is the turbulence intensity, TI. This is derived as the square root of the mean of the variances in fluctuating velocity components, normalised by a reference mean velocity, as defined by Equation 1.5.

$$TI = \frac{\left[\frac{1}{3}\left(\overline{u'^2} + \overline{v'^2} + \overline{w'^2}\right)\right]^{1/2}}{U_{\text{ref}}} \tag{1.5}$$

The turbulence intensity can be defined for a single direction. For the case of turbulence in the longitudinal flow direction, the directional turbulence intensity is defined by Equation 1.6.

$$TI_u = \frac{\left(\overline{u'^2}\right)^{1/2}}{U} \tag{1.6}$$

Ocean waves and swell

Another cause of unsteady flow conditions which may effect the performance of an AGB are wave and swell conditions. Ocean waves are caused by the shear force of wind acting on the surface water of the ocean and generate out of phase velocity fluctuations in both the horizontal and vertical directions referred to as 'orbitals'. The wavelength of the wave or swell conditions, λ, is of particular importance to structures on the seabed, as a positive relationship exists between wavelength and orbital particle velocity. According to linear wave theory, the relative magnitudes of the horizontal and vertical velocities generated, $|u'/w'|$, increases as a function of λ/h (Sarpkaya and Isaacson, 1981). In ocean waves, such perturbations are present at frequencies of $0.05\text{Hz} \leq f \leq 1.0\text{Hz}$ (Walden, 1961).

In channels of less than 50m depth, the influence of waves results in notable modification of the sea floor friction coefficient, altering the vertical velocity profile of the channel (Prandle, 1997). The resulting profile is highly dependant on the relative directions of wave and current propagation (Zhao *et al.*, 2006).

Storm surges

In channels with a low tidal range, local increases in water level under the influence of a low pressure storm surge can dominate the driving of current flow (Bowditch, 1995). Storm surges are caused by low pressure systems in the atmosphere creating a higher water level than would be expected from the tidal range alone. This head difference has the potential to generate flows in a direction independent of the original tidal flow.

Bathymetric effects

The directional response of the flow in a tidal channel to both astronomical and meteorological forces is strongly effected by the local bathymetry. Furthermore, the bathymetry upstream of a device in the flood tide can significantly modify the flow conditions and direction from that in ebb. In a velocity survey carried out in the Puget Sound, Washington, Gooch *et al.* (2009) recorded sites where the flood and ebb tides demonstrated an asymmetry of up to 58°. In such a site the available energy from an axial flow turbine without yawing capabilities is expected to be significantly decreased (Divett *et al.*, 2009).

1.8 Thesis aims and objectives

The primary aim of this thesis is to provide an analysis of the stability of an Active Gravity Base under the unsteady flow conditions which are inherent in energetic tidal flow. In order to achieve this, a number of prerequisite objectives must be realised.

Firstly, the understanding of the dynamic nature of the incident flow conditions on the device must be improved. Previous design calculations were founded on the assumption that the tidal flow direction is is bidirectional over the tidal cycle. The validity of this assumption will be investigated using qualitative analysis, and the significant of the transverse flow component will be determined using representative tidal data.

While noting the unsteady nature of the tidal flow, existing research has largely ignored the effects of this on the device performance. Owen (2007) uses a quasi-steady analysis in theoretical performance calculations, and a towing tank facility using a constant velocity carriage was used in the final experimentation at $1/7^{th}$ scale. While some tidal sites are sheltered from large waves, the presence of turbulent eddies is unavoidable in such energetic flows, and these will therefore influence the device with relative independence of installation site. The response of the lift force on a hydrofoil exposed to both longitudinal and vertical flow fluctuations will be examined both theoretically and experimentally.

The fastening device is required to survive the most harsh operating conditions which can be expected in the tidal channel. As such, an extreme value analysis of the high frequency flow conditions will be performed. Such an analysis is limited by the availability of velocity measurements of sufficient spatial and temporal resolution; however useful indicators of the magnitude of peak annual velocity fluctuations are expected to be estimated.

To examine the unsteady loads in a controlled manner, an experimental facility capable of generating controllable flow perturbations is required. The present work aims to develop an apparatus to achieve this within the fluids laboratory at the University of Edinburgh. The dynamic loading conditions induced by the velocity fluctuations evident in the tidal flows are of interest for the AGB, as well as other components of generic tidal turbine installations. The final aim of this thesis therefore has wider implications than the application of the novel foundation design on which it was motivated.

1.9 Thesis overview

The present chapter provides an introduction to the present range of fastening techniques currently available for the installation of tidal stream turbines. This overview contextualises the research reported within the thesis which explores the stability of a novel fastening configuration, referred to as an Active Gravity Base.

A review of relevant literature is included on a chapter by chapter basis when appropriate in response to the diverse range of subjects addressed.

The overall structure of the following document is divided into two related research focuses:

i) Understanding the variations in tidal stream velocity, and

ii) Generating two-dimensional velocity fluctuations in laboratory scale tests.

To begin, the relatively low frequency variations in the tidal stream velocity are examined in Chapter 2. A correlation between the flow energy and directionality is developed using measured tidal velocities. This analysis is used as an input to a directional analysis of the AGB performance in response to changes in mean flow conditions.

Chapter 3 advances the understanding of three-dimensional velocities at relatively high frequencies. Again, velocity measurements are used as the basis of this work. The primary output of this chapter is the estimation of maximum velocity perturbations expected over a range of time-scales.

The remainder of the thesis develops ability to generate controllable flow variations in the laboratory to represent the dynamic flow conditions of the tidal stream. This begins by developing a vortex model to compute the two-dimensional flow variations in the wake of two independently pitching hydrofoils in Chapter 4.

The development and fabrication of the velocity perturbation generator for installation in the recirculating flume at the University of Edinburgh is reported in Chapter 5.

Chapter 6 presents the results of the experimental validation of the velocity perturbation generation theory developed in Chapter 3. The dynamic loads experienced by a representative lifting surface subjected to the unsteady flow conditions generated are also examined in this chapter.

The most significant conclusions of the present research and recommendations for further work are presented in Chapter 7.

Chapter 2
Low frequency variations in tidal stream velocity

2.1 Introduction

The directionality of the tidal flow throughout the tidal cycle has important implications for tidal energy capture with respect to turbine performance, capacity factor, and structural loading. There has been a tendency to infer that energetic sites possess near bi-directional flows or that there are sufficient sites with near bi-directional flows such that more omni-directional flow tidal currents can be neglected.

It is common to represent the tidal flow velocities attributed to individual tidal constituents in a graphical form known as a tidal 'ellipse'. Such a plot is named after the elliptical shape formed by plotting the velocity time series attributed to a particular constituent on a Cartesian axis with perpendicular velocity directions. The real tidal flow is the summation of the various constituents of the harmonic analysis, and is therefore not necessarily elliptical itself, as shown in the illustrative case of Figure 2.1.

Many designs for tidal current energy conversion systems do not have the ability to actively respond to changes in current direction. Such devices either depend upon near bi-directional flows, or power conversion systems which are relatively insensitive to small directional deviations from bi-directionality. For fixed axis horizontal axis tidal turbine designs, deviations from bidirectional flow can have a significant impact on turbine performance (Bahaj *et al.*, 2007; Divett *et al.*, 2009). While commercial interest has focused on horizontal axis tidal turbines, it is worth noting that vertical axis tidal turbines are largely insensitive to the incident tidal flow direction.

Mechanical systems such as tidal stream turbines respond to the local flow velocity. Therefore, in this analysis it was considered appropriate to consider the available sites in terms of kinetic energy flux density at representative hub height location.

In the analysis presented in this chapter the resultant velocity magnitude, u_R, and the flow direction measured from the direction of the principle axis, θ_R, are calculated using Equation 2.1

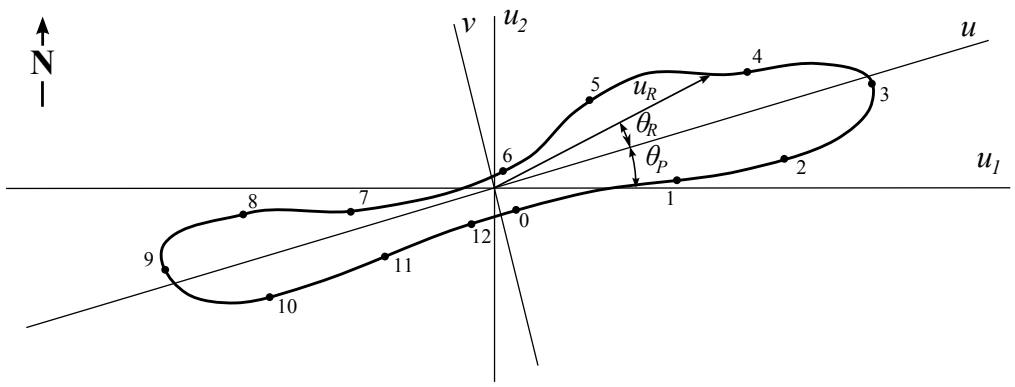

Figure 2.1: Illustrative mean time series of tidal flow over a semi-diurnal cycle, showing cardinal axes (u_1,u_2) and rotated axes system to the principal and secondary axes of (u,v) aligned with the longitudinal and lateral flow directions, respectively. Representative hours from slack tide are indicated with a black dot.

and Equation 2.2 respectively.

$$|u_R(t)| = \sqrt{u(t)^2 + v(t)^2} \tag{2.1}$$

$$\theta_R(t) = \tan^{-1}\left(\frac{v(t)}{u(t)}\right) \tag{2.2}$$

The time-mean power density in the flow, P, over a temporal averaging period of T_a is determined by Equation 2.3, and has the unit of $\mathrm{W/m^2}$ (Bryden, 2006).

$$P = \frac{1}{T_a} \cdot \frac{\rho}{2} \int_0^{T_a} |u_R(t)|^3 \, \mathrm{d}t \tag{2.3}$$

There has been a tendency to infer that energetic sites possess near bi-directional flows or that there are sufficient sites with near bi-directional flows such that more omni-directional flow tidal currents can be neglected. However, the variation in energy flux over the tidal cycle will be reduced in more omni-directional flows. In response to this hypothesis, it was considered whether it is possible to find sites that have comparatively low peak speeds but with overall energy flux densities comparable with sites that might superficially appear more attractive. This would have the implications of decreasing the peak loading requirements of the device and fastening and improving the capacity factor with a more consistent power output. To achieve this the method of power take-off is required to be directionally insensitive, either through yaw

capabilities or by being of the cross-flow type.

Equation 2.3 suggests that a 'circular' tidal ellipse with a constant speed of $u_R = 1.5\text{m/s}$ would have the same net energy flux as a sinusoidally varying bidirectional flow with a peak speed of 2.0m/s. This analysis demonstrates that the available power in the current is most heavily influenced by greater flow speeds owing to the u_R^3 term in the calculation of incident flow energy.

The following analysis on the directionality of tidal sites in the Northern United Kingdom was published in the Journal of Renewable Energy (Harding and Bryden, 2012b).

2.2 Acquisition of tidal current data

Tidal flow information was extracted from the United Kingdom Hydrographic Office's Admiralty Chart data in Northern UK waters, at the locations shown in Figure 2.2a. The available data from these Admiralty Charts provided mean velocity magnitudes and directions at hourly intervals from six hours before high water to six hours after high water. These measurements were presented in two data sets, one for average spring velocities and the other for average neap velocities. This data was amalgamated by Dr Thomas Boehme to form a digital data base, which was used in this analysis.

This directionality analysis has been restricted to spring tides. Although it is appreciated that the ratio between spring and neap peak speeds is not a constant, it is assumed here that appropriate sites for development can be identified, at least in the first instance, by consideration of their average spring conditions.

Data was also received from Acoustic Doppler Current Profilers (ADCPs) deployed in the Fall of Warness by the European Marine Energy Centre (EMEC). This data was recorded at different sample rates for each site, ranging from every 30 seconds to every 20 minutes. The data of each site was recorded for periods of between 16.0 days to 40.7 days, thus incorporating at least one neap-spring cycle at each position. The details of the EMEC data sets used are presented in Table 2.1. For data collected over a time period greater than half a lunar month, all recorded spring cycles were used in the analysis for comparison with the average spring velocity data provided by Admiralty Charts.

The locations of EMEC data readings used are shown in Figure 2.2b. Mid-depth velocity measurements were used, in accordance with previously established conventions (Gooch *et al.*, 2009). The available Admiralty Chart data does not in fact represent the hub depth but has been used for parameterization purposes.

Table 2.1: Summary of EMEC data

EMEC Survey Reference Number	Position	Sample duration (days)	Ensemble Period (s)
6a	59°8.040′N, 2°48.440′W	16.0	1200
6b	59°8.040′N, 2°48.440′W	16.4	20
7	59°8.443′N, 2°48.996′W	33.2	600
10	59°9.323′N, 2°49.515′W	40.7	1200
11	59°9.430′N, 2°49.540′W	27.0	1200
13	59°8.147′N, 2°48.391′W	32.0	30

2.3 Quantification of directionality metric

In order to compare the directionality of sites it is necessary to reduce the velocity time series data to a metric which describes the directional variability with a single value. This process is often called Principal Component Analysis (PCA) or the Empirical Orthogonal Function (EOF) in oceanography.

By convention, the instantaneous velocity components aligned with the West-East direction are denoted as u_1, and the component aligned in the South-North direction as u_2 (Emery and Thomson, 1998). After removing the mean velocity components of $\overline{u_1}$ and $\overline{u_2}$ over the entire duration of the data set, the fluctuating components are denoted as u_1' and u_2' respectively, such that $u_1' = u_1 - \overline{u_1}$ and $u_2' = u_2 - \overline{u_2}$ (Emery and Thomson, 1998).

For two dimensional velocity time series, the covariance components, eigenvectors and eigenvalues are related by Equation 2.4.

$$\begin{vmatrix} C_{11} & C_{21} \\ C_{12} & C_{22} \end{vmatrix} \begin{vmatrix} \phi_1 \\ \phi_2 \end{vmatrix} = \begin{vmatrix} \lambda & 0 \\ 0 & \lambda \end{vmatrix} \begin{vmatrix} \phi_1 \\ \phi_2 \end{vmatrix} \tag{2.4}$$

By setting the determinant of the covariance matrix equation above to zero, and recognizing that $C_{ii} = \overline{u_i'^2}$ and $C_{ij} = \overline{u_i' u_j'}$, the eigenvalues of the rotated data set can be calculated by Equation 2.5 (Emery and Thomson, 1998).

$$\left.\begin{matrix} \lambda_1 \\ \lambda_2 \end{matrix}\right\} = \frac{1}{2}\left\{\left(\overline{u_1'^2} + \overline{u_2'^2}\right) \pm \left[\left(\overline{u_1'^2} - \overline{u_2'^2}\right)^2 + 4\left(\overline{u_1' u_2'}\right)^2\right]^{1/2}\right\} \tag{2.5}$$

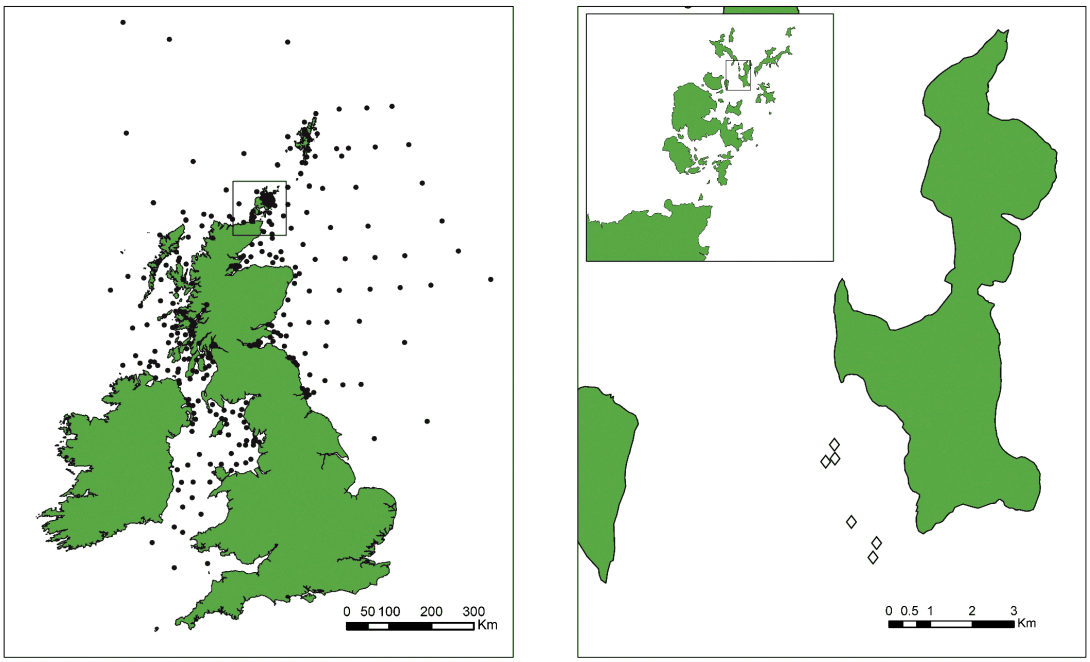

(a) Admiralty Chart data locations

(b) EMEC data locations

Figure 2.2: Locations of tidal current measurements analyzed

The eigenvalues for the longitudinal and transverse flow directions are denoted as λ_1 and λ_2, respectively. These parameters correspond to the variances of the velocity components along the major and minor principal axis directions in a semi-diurnal tidal cycle.

The directionality of a site can then be expressed by a single value, defined using a normalized ratio between the maximum and minimum variances, which is referred to in this document as the eigenvalue ratio, $\tilde{\lambda}$. This metric is defined mathematically by Equation 2.6.

$$\tilde{\lambda} = \frac{\lambda_1 - \lambda_2}{\lambda_1} \tag{2.6}$$

The eigenvalue ratio gives a value of unity for perfectly bi-directional tidal data, and a value of zero for totally omni-directional situations.

The direction of the principal axis, as defined in Figure 2.1, is found using Equation 2.7 (Emery and Thomson, 1998). Again the overline is used to represent the mean over the entire data set.

$$\theta_P = \frac{1}{2}\tan^{-1}\left(\frac{2\overline{u_1' u_2'}}{\overline{u_1'^2} - \overline{u_2'^2}}\right) \tag{2.7}$$

This angle represents the direction along with the maximum flow energy is aligned.

2.4 Correlation of directionality with flow energy density

The correlation between the directionality of the tidal current and the resource energy was observed by plotting the two parameters on a scatter plot. This was performed using two measures of flow energy: the power density, P, and the maximum flow speed, $u_{R,max}$. The graphical results of the directionality analysis are depicted in Figure 2.3.

Figure 2.4 shows the polar plots for three representative sites, corresponding to the points indicated in Figure 2.3a.

While Figure 2.3 indicates that indeed the most directional tidal currents tend to have the highest incident flow energy, it is also useful in demonstrating that all tides have some inherent degree of deviation from bi-directionality. This is particularly evident from analysis of the EMEC data, where a higher sample rate and greater velocity measurement accuracy is available.

2.5 Directionality of energetic sites

Further analysis was performed to quantify the directionality of the flow power density as a function of incident flow angle relative to the principal axis. Considering that first generation tidal energy devices require relatively high flow speeds, this has been carried out using only data from the 36 Admiralty Chart tidal sites with maximum spring velocities greater than 2.0 m/s. A cumulative density plot of flow energy incident from the direction of $|\theta_R| = 30^\circ$ to the principal flow direction, $|\theta_R| = 0^\circ$, is shown in Figure 2.5. The plot shows the cumulative power density for three separate data groups: the 711 Admiralty Chart tidal sites available, the 36 sites with peak flow speeds exceeding 2.0m/s, and the 675 sites with peak flows less than 2.0m/s.

First observing the energetic sites with peak flow speeds greater than 2.0m/s, it is seen that 82.2% of available flow power, as defined by Equation 2.3, flows at an angle of incident $\pm 10^\circ$ either side of the principle axis direction. Conversely, only 0.6% is found at angles of incidence greater than $\pm 30^\circ$ either side of the principle axis direction. This would appear to support the implicit assumptions which the development sector has made in their design philosophies.

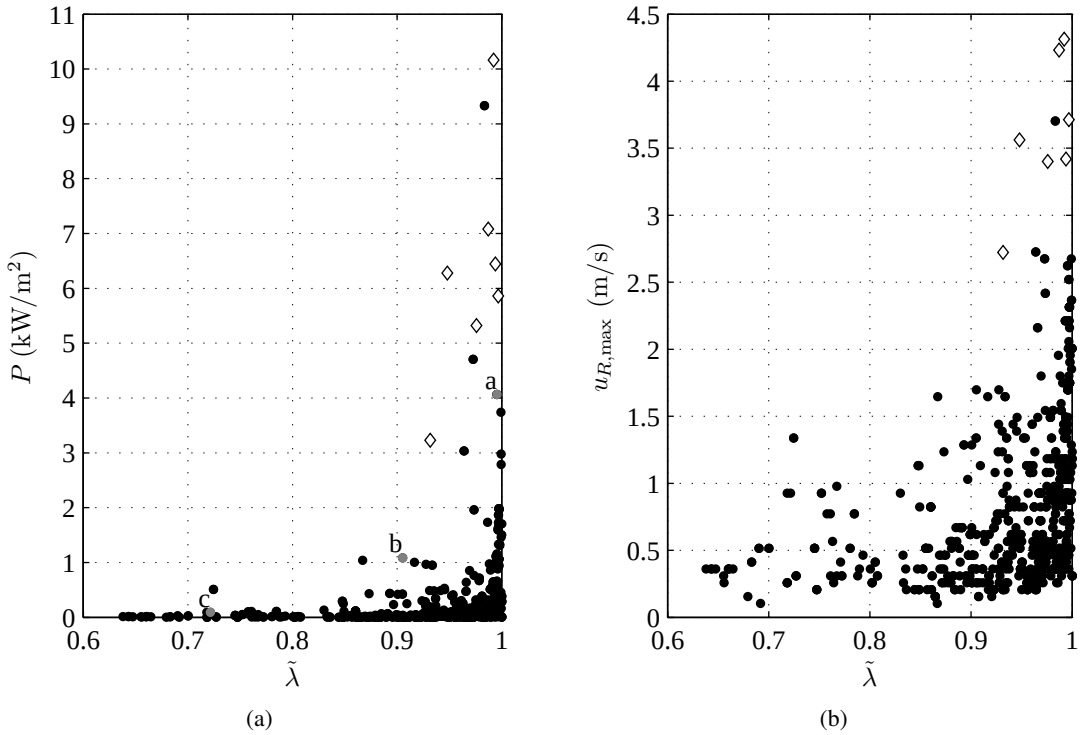

(a) (b)

Figure 2.3: Directionality scatter plots of the eigenvalue ratio against a) flow power density and b) maximum flow speed. Dots are used to represent Admiralty Chart data and diamonds indicate EMEC data.

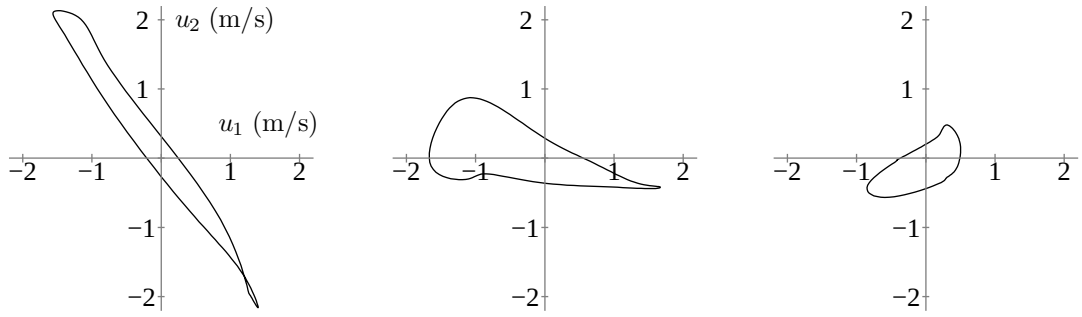

(a) 59°11'N 2°52'W (UKHO, 1993)

(b) 58°44'N 3°23'W (UKHO, 1990)

(c) 58°40'N 3°29'W (UKHO, 1998)

Figure 2.4: Time series of representative tidal flow velocities indicated in Figure 2.3a

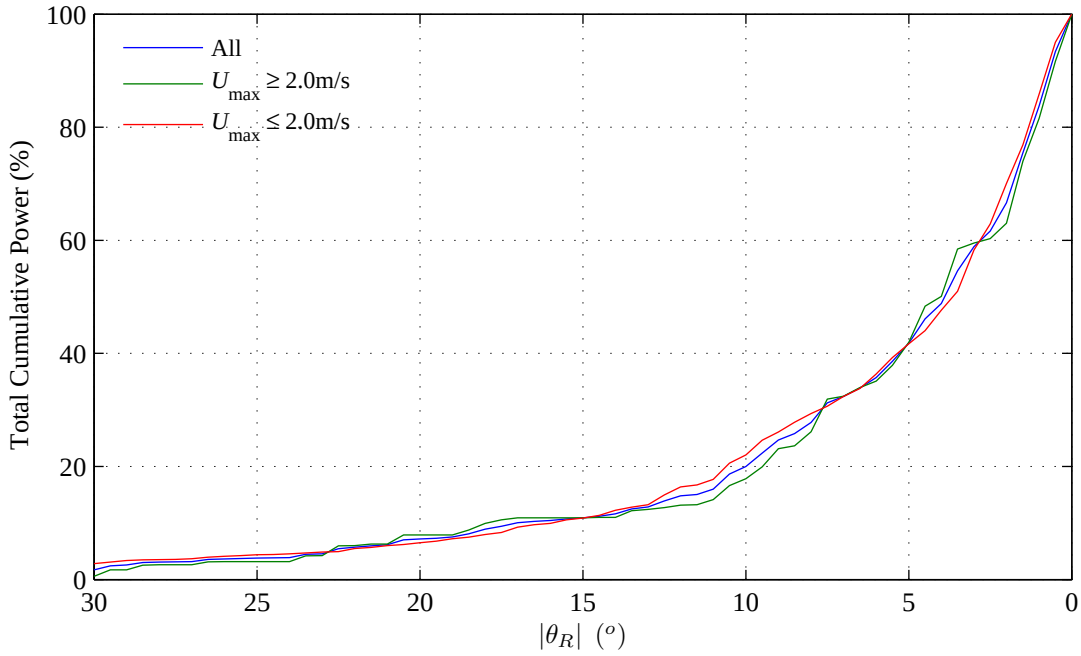

Figure 2.5: Cumulative density plot of available power as a function of flow direction from principal axis.

While such a result was expected after observing the scatter plots of Figure 2.3, the cumulative density plots for sites with peak flow speeds less than 2.0m/s, as well as the combined analysis of all 711 Admiralty Chart sites, show surprisingly similar results to the energetic sites.

In order to perform a directional analysis on the existing AGB design, a representative flow magnitude must be specified as a function of the flow direction. A Gaussian distribution was used to match the directionality-velocity relationship observed in the Admiralty Charts tidal sites as shown in Figure 2.6. The distribution used is described mathematically by Equation 2.8 where $\hat{a} = 2.1$, $\hat{b} = 0$, $\hat{c} = 16$ and $\hat{d} = 0.9$, to encompass all observed values.

$$u_R(\theta_R) = \hat{d} + \hat{a} \exp\left(\frac{-(\theta_R - \hat{b})^2}{2\hat{c}^2}\right) \tag{2.8}$$

It has been proposed that a more complete characterization of directionality can be achieved through analysis of the flood and ebb characteristics separately (Legrand, 2009). Taking this approach, suggested metrics to describe the directionality of the tide include the standard deviation from the principal direction using the flood, ebb, and combined statistics, as well as the angular asymmetry between the ebb and flood principal direction (Gooch *et al.*, 2009). It is suggested by the author that, although separate consideration of the flood and ebb is impor-

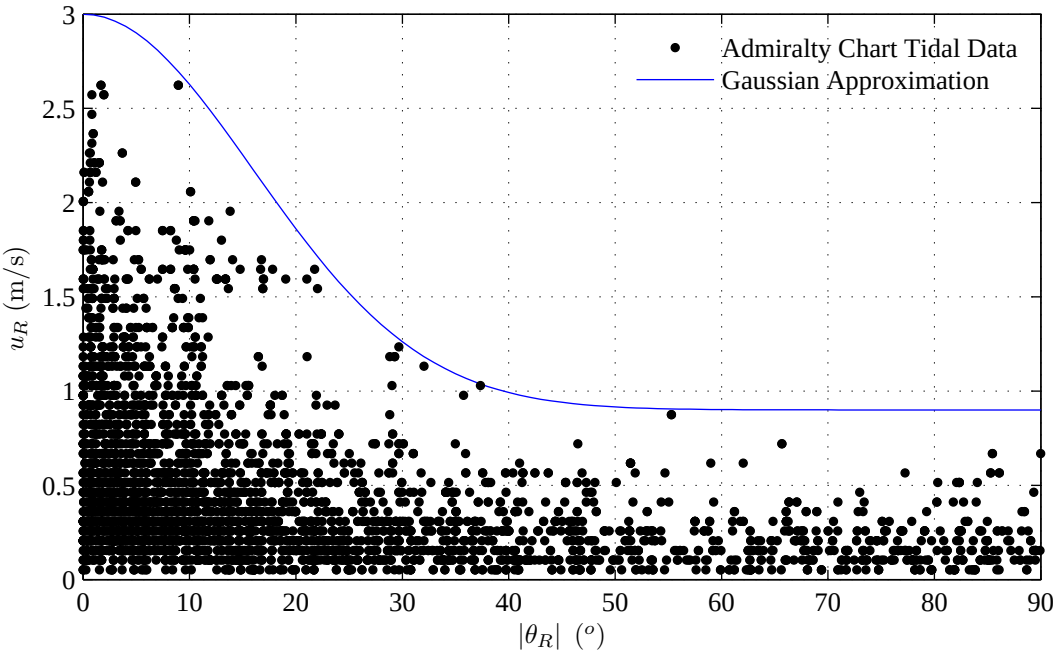

Figure 2.6: Gaussian approximation of velocity magnitude for directionality analysis

tant for detailed analysis of the appropriateness of specific technology for specific sites, most first generation axial flow devices are unable to respond significantly to changes in direction beyond adaptation to flow reversal. Hence, preliminary analysis based on a single predominant direction will prove more immediately useful in site assessment.

In the data considered in this chapter, the directional properties appear very similar in both the spring and neap tide, with only the magnitude being significantly different. This further supports the hypothesis that, for initial analyses at least, examination of directional properties under spring conditions is sufficient. In addition, it can be inferred that the influence of the cubed velocity term in the calculation of power density would make the directionality of the spring tides more significant than the neap for tidal power considerations.

2.6 Performance analysis of Active Gravity Base

The directionality of mean tidal flow velocities has significant implications on the performance of the AGB concept. As previously noted, the hydrodynamic down-force generated by the fixed lifting surface is a function of the longitudinal velocity component. As such, the maximum effective weight of the AGB occurs at the same time as maximum drag loads. However, the transverse velocity component, shown to be inherent in even the most energetic flows, results

in transverse loads during times when the contribution of the lifting surface may be low.

The following section presents a performance analysis of the AGB under mean flow conditions. Initially, the case of pure longitudinal flow conditions on the AGB are explored. The analysis is then developed to incorporate the Gaussian approximation of directionality, addressed in §2.5, to model the combined effects of longitudinal and transverse flows.

2.6.1 Failure mechanisms

The success of a gravity base is determined by the overcoming of both the transverse drag force on the structure and turbine, as well as resisting the overturning moment at $z = 0$ caused by the drag forces acting at the vertical positions of $z > 0$. This section introduces the four failure mechanism which are considered in the performance analysis of the AGB design.

The symbols and locations of the primary forces expected during operation are shown in the free body diagrams of Figure 2.7.

Translational failure

- Longitudinal slip

  When the drag forces exceed the reactive friction force, the fastening structure will translate in the direction of the flow. Given that the available friction force is equal to the product of the normal force of the device on the seabed and the coefficient of static friction at the point of contact, the hydrodynamic lift required to be generated is given in Equation 2.9.

$$\sum_{i=1}^{6} L_i \geq \frac{1}{\mu}\left(\sum_{i=1}^{6} D_{xi} + D_{xT} + D_{xF}\right) - F_W \tag{2.9}$$

- Transverse slip

  While the original AGB concept assumes bi-directional flow, the transverse forces may become important in real tidal flows where this is not achieved. Calculating the required friction force allows the minimum required lift forces to be calculated by Equation 2.10.

$$\sum_{i=1}^{6} L_i \geq \frac{1}{\mu}\left(\sum_{i=1}^{6} D_{yi} + D_{yT} + D_{yF}\right) - F_W \tag{2.10}$$

  Note that the hydrodynamic lift is generated from flow in the longitudinal direction, U,

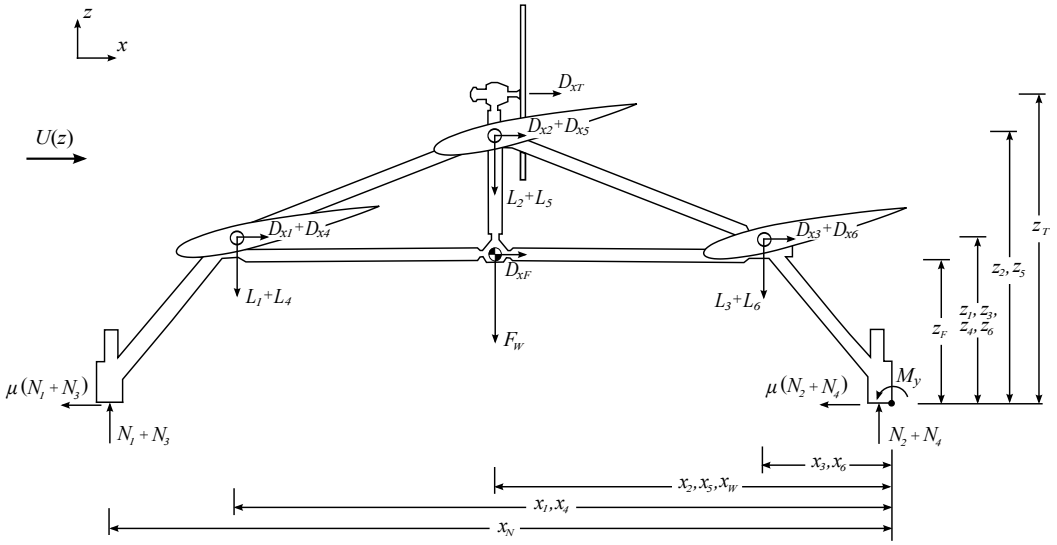

(a) Free body diagram of Active Gravity Base concept operating in axial flow. Adapted from Owen (2007).

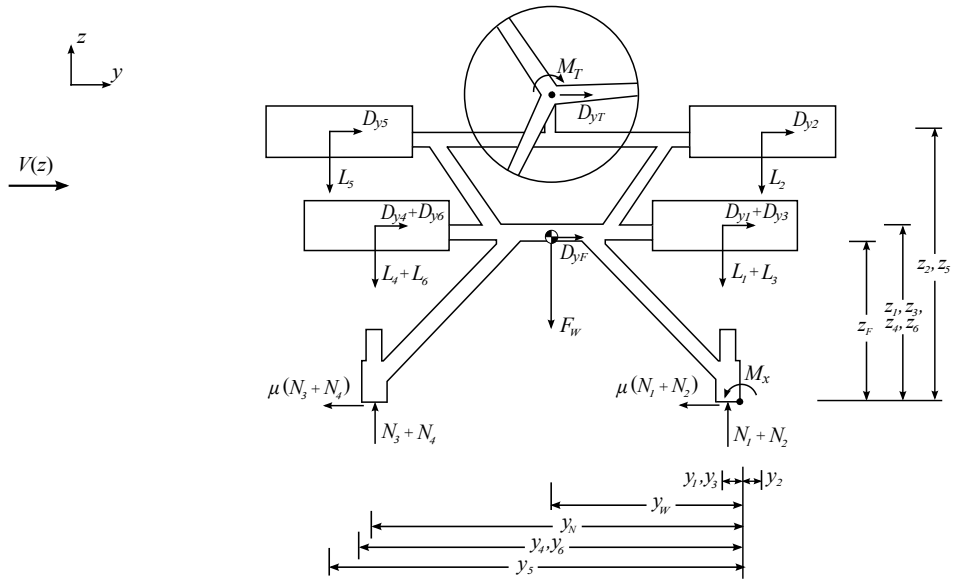

(b) Free body diagram of Active Gravity Base concept operating in tranverse flow.

Figure 2.7: Free body diagrams of Active Gravity Base in operation.

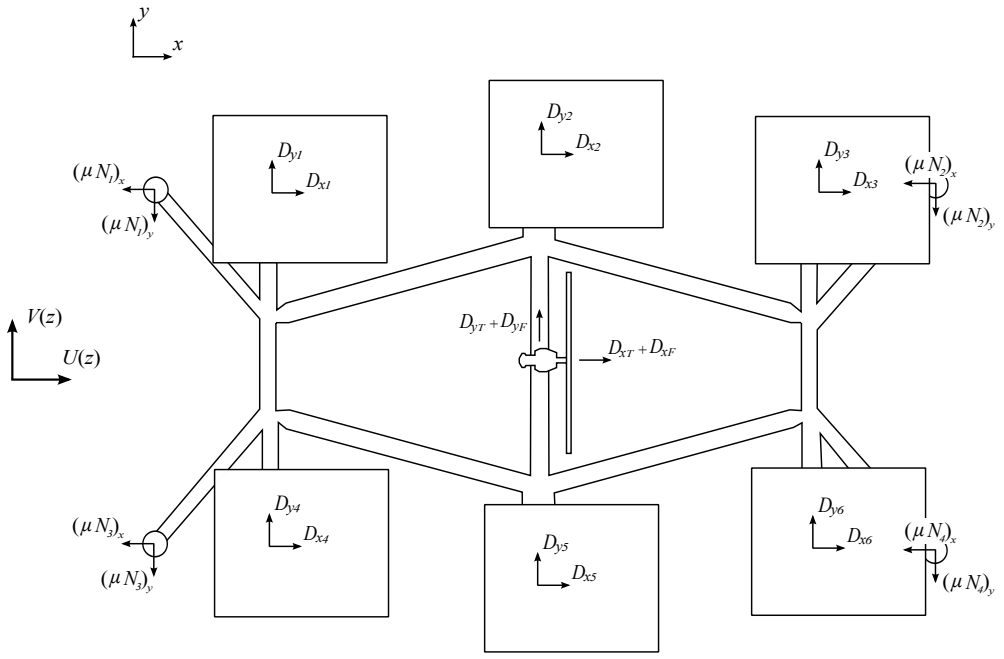

(c) Free body diagram of Active Gravity Base concept operating in combined axial and transverse flow.

Figure 2.7: Free body diagram of Active Gravity Base in operation (continued).

while the drag forces in the transverse direction are the result of the V component of flow velocity.

Rotational failure

- Longitudinal overturning

  The AGB will no longer maintain its static position on the seabed in the case where the overturning moment of the structural drag and generating thrust of the turbine exceed the reacting moment of passive and active gravity components. In this case the structure will rotate about the aft-most point of contact with the seabed. For axial flows, the rotation is about the y-axis such that $N_1 = N_3 = 0$ at the point of failure. Using the force balance presented in Figure 2.7a, the minimum total moment available from the hydrodynamic down-force is calculated by Equation 2.11.

$$\sum_{i=1}^{6} L_i x_i \geq \sum_{i=1}^{6} D_{xi} z_i + D_{xT} z_t + D_{xF} z_F - F_W x_w \tag{2.11}$$

- Transverse overturning

  Again, the response of the foundation to flows which deviate from the principal axis must be considered. While the thrust force of the turbine only acts in the longitudinal direction, the moment generated by the generating torque of an axial flow turbine acts to roll the device about the x-axis. Though the flows and forces in this direction may be expected to be relatively low compared to those in the axial direction, the restoring moment is also smaller in this direction due to the reduced width of the seabed contact points. At the point of failure, $N_3 = N_4 = 0$, and the minimum moment provided by the hydrodynamic lifting surfaces is given by Equation 2.12.

$$\sum_{i=1}^{6} L_i y_i \geq \sum_{i=1}^{6} D_{yi} z_i + D_{yT} z_t + M_T + D_{yF} z_F - F_W y_w \tag{2.12}$$

  Note that the torque generated by the turbine, M_T, is a function of the longitudinal flow velocity, U, while the overturning drag forces are due to the flow in the transverse direction, V. The turbine torque can be quantified by Equation 2.13, where C_θ is the torque coefficient and $\hat{R}$ is the radius of the turbine.

$$M_T = \frac{1}{2}\rho U^2 C_\theta A \hat{R} \tag{2.13}$$

2.6.2 Development of AGB performance model

The performance of the existing AGB configuration was modelled by performing a force balance analysis. The drag contribution of each structural member can be defined as the product of the drag coefficient and frontal area, $C_D A$. The total drag characteristics were calculated as the sum of the drag contributions of the individual components. Similarly, the total moment characteristics were calculated as the sum of the moment contributions of the individual components ($C_D A z$). The total drag force and moments were then calculated as a function of the flow velocity.

The restoring force was calculated as the product of the static friction coefficient, μ, and the submerged normal force, N, using the Coulomb friction approximation. In accordance with this approach the restoring force, which acts in the opposite direction to the net drag force, is proportional to the selected value of the static friction coefficient at the interface of the AGB and seabed. Owen and Bryden (2005) identify that the friction coefficient of the steel/seabed interface is site specific and in the range of $0.7 \leq \mu \leq 0.9$. Given that the feet of the AGB are fabricated with serrated steel teeth, Owen and Bryden (2005) approximated the value of the

static friction coefficient as $\mu = 1.0$. This approach is a significant approximation to the physics of the seabed interaction, however has been adopted in the present analysis for comparability with previous work on the AGB concept (Owen and Bryden, 2005; Owen, 2007).

The key assumptions used in the preliminary performance calculation are as follows:

- The longitudinal flow speed is steady, and the flow speed in all other directions is zero.
- The four feet of the base are rigidly connected, such that one cannot fail independently of the others.
- The performance calculations are given for a site with depth of $h = 30$m and a vertical boundary layer described by Equation 1.1 where $\beta = 7$.
- The thrust coefficient of the axial-flow turbine is assumed to have a constant value of $C_T = 1.0$, as a conservative approximation to published results (Mason-Jones *et al.*, 2012; Bahaj *et al.*, 2007; Gretton *et al.*, 2011).
- The torque coefficient of the axial-flow turbine is assumed to have a constant value of $C_\theta = 0.15$, as a conservative approximation (Mason-Jones *et al.*, 2012; Gretton *et al.*, 2011).
- The lifting surfaces were modelled as being neutrally buoyant such that the operational principle of passive rotation in the flow is still valid, without reducing the effective submerged weight of the structure, taken as 91.9kN (Owen, 2007).
- The lifting surfaces are given an angle of attack of $\alpha = -12°$, with a lift curve slope of $\mathrm{d}C_L/\mathrm{d}\alpha = 0.85\pi\epsilon$. The effectiveness of the lifting surfaces, ϵ, is assumed to decrease from upstream to downstream of the structure due to the interference of the structure with the flow. As such, $\epsilon = 1.0$ for the fore foils, $\epsilon = 0.8$ for the central foils, and $\epsilon = 0.6$ for the aft foils (Owen, 2007).
- The drag coefficient of the low aspect ratio NACA0013 foils in the flow direction, C_D, is calculated as the sum of the base drag coefficient, C_{D_o}, and the induced drag coefficient, C_{D_i}, such that $C_D = C_{D_o} + C_{D_i}$. The base drag coefficient is conservatively assumed to be $C_{D_o} = 0.015$ (Abbott and von Doenhoff, 1959). The induced drag coefficient is calculated as $C_{D_i} = C_L^2/(\pi\Lambda e)$. For the rectangular foils used, the efficiency factor is taken as $e = 0.7$ (NASA, 2010) and the aspect ratio of the rectangular foils is given by $\Lambda = 0.83$.

- The drag coefficient for a cylinder were assumed to be $C_D = 1.2$ in cross-flow direction and $C_D = 0.8$ in the axial flow direction (Hoerner, 1965; Crowe *et al.*, 2005). These coefficients are conservative estimates when $\mathrm{Re} > 10^3$.

- The drag coefficient of lifting surfaces in the cross-flow directions was assumed to be $C_D = 1.5$. This value models the wing sections (with end plates) as a rectangular section with a blunt leading edge and a depth: height ratio of 3:1 (Hoerner, 1965). This drag coefficient was derived from experiments performed with the geometry between two walls, such that no three-dimensional effects are included. However drag data presented for a flat plate with varying height to span ratio indicate that ignoring these three-dimensional effects is an acceptable first approximation (Hoerner, 1965).

This analysis is performed using non-dimensional coefficients which allow the majority of the analysis to be scaled proportionally to the dimensions of the model. However several parameters used in the analysis have been selected to enable a solution to be found and are likely to effect the results. Specifically, the vertical velocity profile has a significant effect on the relative magnitudes of the destabilizing and restoring forces. The lift deficit of the hydrofoils operating in the wake of the upstream structure is also likely to be prone to scale effects.

Furthermore, this analysis has been performed with the simplifying assumption of steady state forces. As such, only the mean flow effects are considered, and high frequency destabilising effects which are present in reality are absent from the model. The use of the Coulomb friction approximation to represent the interface between the structure and the seabed has been adopted from Owen (2007) for comparison with this previous analysis. In reality, the seabed connection is likely to represent a complex interaction between the feet of the AGB and the seabed surface.

2.6.3 AGB performance analysis in longitudinal flow

The drag characteristics of the passive and active gravity bases were calculated as the summation of all the drag coefficients multiplied by the frontal area of the individual structural component. A correction factor was applied to model the vertical shear layer in the tidal flow, following an exponential power law with $\beta = 7$. A comparison of the corrected drag and moment characteristics of the two devices is presented in Table 2.2. The total drag force and overturning moments on the device were calculated using Equation 2.14.

Table 2.2: Longitudinal load characteristics of foundation design, corrected for boundary layer following a 1/7th power law.

Base Configuration	Longitudinal drag characteristics (m^2): $\sum(C_D A_s)_x$	Longitudinal moment characteristics (m^3): $\sum(C_D A_s z)_x$	Down-force characteristics (m^2): $\sum(C_L A)$
Passive	21.2	85.8	-
Active	24.5	98.4	13.8

$$D_x = \frac{1}{2}\rho U^2 \sum (C_D A_s)_x \tag{2.14a}$$

$$M_y = \frac{1}{2}\rho U^2 \sum (C_D A_s z)_x \tag{2.14b}$$

The restoring force of the PGB is attributed to the submerged weight of the installation only. However the restoring force of the AGB has the additional dynamic component of hydrodynamic downforce from the lifting surfaces, calculated by Equation 2.15.

$$L = \frac{1}{2}\rho U^2 \sum (C_L A) \tag{2.15}$$

Note that the value of A_s in Equation 2.14 represents the sum of the frontal area of the structure in the direction given outside the parentheses and the swept area of the turbine, while the value of A in Equation 2.15 corresponds to the planform area of the lifting surfaces.

The magnitude of the drag force and restoring force are compared in Figure 2.8a for the AGB case, and the PGB which results from removing the foils from the AGB. The x-ordinate of the intersection of the drag and restoring force lines represents the flow speed at which longitudinal slip is expected.

Similarly, the magnitude of the overturning moment and the restoring moment are compared in Figure 2.8b and Figure 2.8c for rotation about the y-axis and x-axis, respectively. The flow speed at the intersection of the destabilizing and restoring moment lines for the PGB in Figure 2.8b represents the velocity at which longitudinal overturning is expected. In all other cases, the restoring moments are always shown to exceed the destabilizing moments and therefore failure of the AGB by overturning is not expected at flow speeds <5.0m/s. In purely longitudinal flow conditions, the only destabilising moment about the x-axis is due to the torque of the turbine which is identical for both the PGB and AGB configurations.

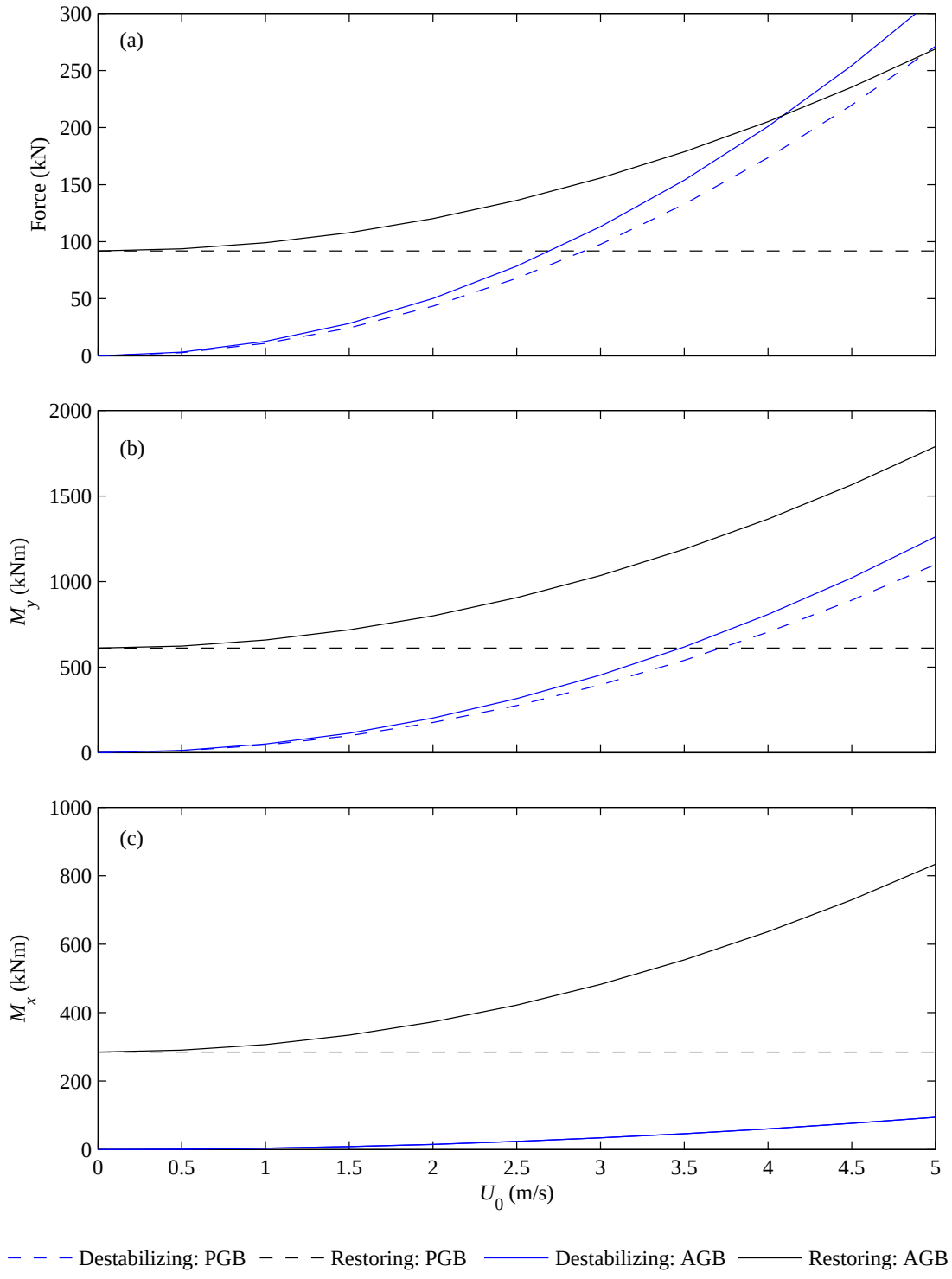

Figure 2.8: Performance of Active Gravity Base in steady longitudinal flow, where a) indicates the translational force analysis, b) indicates the moment analysis about the y-axis and c) indicates the moment analysis about the x-axis.

Table 2.3: Maximum flow speeds for existing AGB prototype and equivalent PGB design

	Passive Gravity Base	Active Gravity Base
Longitudinal Slip	2.9m/s	4.1m/s
Longitudinal Overturning	3.7m/s	$\gg$ 5m/s
Transverse Overturning	$\gg$ 5m/s	$\gg$ 5m/s

The advantages of introducing the active component of the lifting surfaces to the passive gravity base are summarised in Table 2.3 where the maximum flow speeds before each mode of failure are presented. Note that these values do not incorporate any safety factor or consideration of the effects of the destabilising unsteady flows discussed earlier. As such, the results of these calculations are included for comparative purposes only.

The performance of the existing configuration under lateral loading conditions is dependent on the longitudinal flow velocity, U, as well as the transverse flow velocity, V, and is addressed in the following subsection.

2.6.4 Directional performance analysis

A directional analysis was performed on the present design for an Active Gravity Base using the same model assumptions as those specified in §2.6.3. In this analysis the drag coefficient of each structural member of the device was calculated in both the longitudinal and lateral direction. A correction factor was applied to the drag characteristics to account for the vertical location of the member in a shear boundary layer modelled with a power law exponent of 1/7 ($\beta = 7$ in Equation 1.1).

The performance of the AGB design was compared against the same structure excluding the lifting surface, again denoted as the PGB in this analysis. A summary of the drag characteristics in each direction are presented in Table 2.4.

Table 2.4: Longitudinal and lateral drag characteristics of foundation design, corrected for boundary layer following a 1/7th power law.

Base Configuration	$\sum(C_D A)_x$	$\sum(C_D A)_y$	$\sum(C_D Az)_x$	$\sum(C_D Az)_y$	$\sum(C_L A)$
Passive	21.2	22.2	85.8	54.7	-
Active	24.5	32.6	98.4	93.9	13.8

The drag force was calculated in the longitudinal and lateral directions independently using Equation 2.14 and the subsequent resultant drag vector was determined. As in the preliminary longitudinal flow analysis, the reaction force was assumed to be provided by Coulombs friction law, as the product of the normal force on the seabed and the friction coefficient, taken as $\mu = 1.0$ (Owen, 2007). A comparison of the drag forces and restoring forces on the passive and active designs as a function of flow direction is presented in Figure 2.9a.

The overturning failure mode was addressed in the longitudinal and lateral directions independently as the device can be expected to fail either by pivoting over the two aft feet (about the y-axis) or over the two side feet (about the x-axis). A comparison of the destabilizing and restoring moments about the y-axis for both passive and active gravity base designs is presented in Figure 2.9b. The same comparison is presented for the moments about the x-axis in Figure 2.9c.

2.6.5 Discussion of AGB performance analysis

In the case of the PGB, not only are the restoring forces and moments constant when the incident velocity is changing, as shown in Figure 2.8, but they are also constant irrespective of flow direction. For the AGB, the restoring forces and moments are a function of both the velocity magnitude and direction.

For the failure mode of horizontal translation, the drag forces are seen to approach the constant restoring force at flow incidence of $\theta_R = 0^\circ$ for the PGB case. For the directional velocity distribution used, the destabilizing drag force is seen to be greater than the restoring force for the PGB as the peak flow speed in the principal flow direction is 3.0m/s and the maximum longitudinal flow speed has previously been shown to be less than this (Table 2.3). By introducing the lifting surfaces, the AGB configuration responds to provide maximum down force and therefore maximum reaction force when the incident flow is in the direction of the principal axis. In this way Figure 2.9a shows a net restoring force, as the blue and black solid lines respond similarly to the change in flow direction. This demonstrates the advantages of the AGB operation.

At high angles of incidence ($|\theta_R| > 40^\circ$), the destabilizing drag force is significantly reduced. This is in part a result of the turbine thrust not acting in this direction, and also in response to the reduced flow speeds at high angles of incidence. As $|\theta_R| \rightarrow 90^\circ$, the active component of down force reduces to zero, and the reaction force of the AGB approaches that of the PGB. While significantly lower in magnitude than the restoring forces, the drag force of the AGB is greater than that of the PGB at these high incident flow angles as a result of the lateral drag component of the end plates on the lifting surfaces.

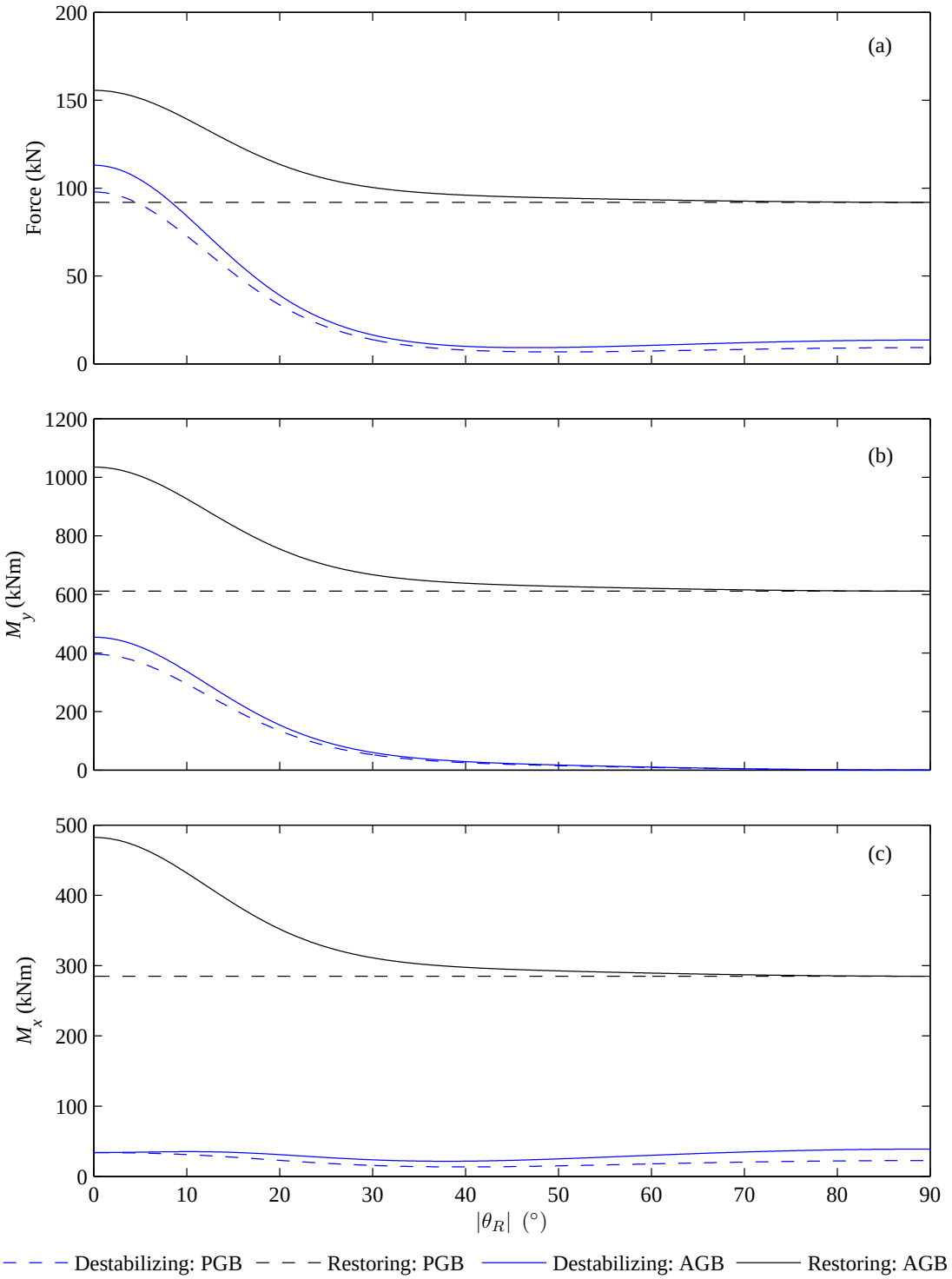

Figure 2.9: Directionality analysis results for the PGB and AGB configurations, where a) indicates the translational force analysis, b) indicates the moment analysis about the y-axis and c) indicates the moment analysis about the x-axis. The Gaussian approximation presented in Figure 2.6 is used to define the flow velocity as a function of the incident flow direction.

The failure mode of overturning about the rear feet shown in Figure 2.9b reflects a similar set of results to the horizontal translation failure mode. Namely, while the restoring moment is constant for the PGB that of the is seen increase in a similar way to that of the overturning drag moment. Again, this is a result of the lift generated by the hydrofoils, which increases with the longitudinal component of velocity. Unlike the translational failure mode where the net drag force reached a minimum value corresponding to the lateral drag component at $\theta_R = 90°$, the moment at this flow angle is equal to zero, as it is only the longitudinal flow speed which generates a destabilizing moment about the y-axis.

Finally, the results of the transverse overturning failure analysis are presented in Figure 2.9c. The maximum moments generated by the structural drag in the transverse direction are both less than half of those generated in the longitudinal direction. This is primarily due to the thrust of the turbine generating a significantly greater overturning moment about the y-axis than the torque of the turbine about the x-axis. The reduction in restoring moments for both the PGB and AGB cases is a result of the reduced spacing of the feet and therefore reduced restoring moment arm about the x-axis. The large difference between the overturning moment and the restoring moment preliminarily indicates that this mode of failure is of less significance than horizontal translation and longitudinal overturning.

Significantly, in all the cases considered, the incident flow angle of $\theta_R = 0°$ represents the situation that is closer to failure. While this preliminary study is considering steady flow conditions only, this result indicates that the future reliability of such a device may not be governed by the performance in transverse flow conditions as suggested in Owen (2007), but that equally the robustness of the design must be better understood under unsteady longitudinal flow conditions.

2.7 Chapter conclusions

It has been shown that high incident kinetic energy in a tidal current can be correlated to the directionality of the tidal flow throughout the tidal cycle. However, even in locations with significant flow energies, it has been shown that deviation from bi-directionality is an intrinsic characteristic of tidal currents. A normalised ratio of eigenvalues, $\tilde{\lambda}$, was introduced as an eccentricity metric for this analysis. This was used to correlate the directionality of a tidal flow with the incident flow energy over a semi-diurnal tidal cycle. In sites with a peak spring tidal current greater than 2.0m/s, it was shown that over 82% of the incident flow energy was aligned within the range of $\pm 10°$ either side of the principal axis.

A Gaussian distribution was then fitted to the real tidal data available from the Admiralty Charts

to characterise the flow velocity magnitude, u_R, as a function of the angle of incidence relative to the principal axis, θ_R. This allowed a directional stability analysis to be performed on the present AGB design, as well as a comparison between the active gravity base and the passive base counterpart without the lifting surfaces. This study demonstrated how the lifting surfaces of the AGB respond to the increase in longitudinal flow in a similar way to the drag, due to the similarity between their governing equations of Equation 2.14 and Equation 2.15, to create a relatively constant net reaction to the drag loads. With the minimum safety factor for the failure modes of lateral translation and longitudinal overturning occurring at $\theta_R = 0°$, and the significant safety factor observed in the transverse overturning case, this study indicates that an improved understanding of the response of the device to unsteady longitudinal flow is of equal, if not greater, benefit to the development of the stability of such a device in the future.

Chapter 3

High frequency variations in tidal stream velocity

3.1 Introduction

The velocity fluctuations in tidal stream velocity exist at frequencies significantly in excess of astronomical effects. These are induced by a range of environmental and meteorological factors which include flow instabilities due to bathymetric effects, ambient turbulence, and subsurface influence of ocean waves and swell. As the physical processes responsible are independent of the bulk flow, the direction of such high frequency effects is generally uncorrelated with that of the mean flow velocity. While the astronomically driven tidal cycles are well understood and can be modelled to predict mean tidal flows, the instantaneous current velocity in the turbulent flow field can be shown to significantly deviate from this (Polagye *et al.*, 2010). This observation has important implications for numerous design considerations, including the dynamic loading conditions on the turbine blades, support structures and seabed connections.

The relative effect of each source of high frequency velocity variation in the tidal flow is site specific. For example, fetch limited sites are often selected for device prototype testing with the advantage of limiting the magnitude of subsurface wave loading . Vortex shedding around islands and headlands in the vicinity of the installation site can also lead to unique flow characteristics (Tang and Chen, 2012).

An apparently unavoidable source of high frequency velocity variation at energetic tidal sites is ambient turbulence. The primary energy source of this flow instability is the shear profile in the mean flow of the marine boundary layer (Tennekes and Lumley, 1999). As such, it can be expected that this source of velocity variation will be influenced by such local effects as seabed roughness and depth which directly influence the shape of the shear profile. However it is interesting to note that at mean velocities greater than 1m/s, the turbulence intensity has been shown to reach a constant value of approximately 10% by Thomson *et al.* (2010) in Puget Sound (USA), as well as McCann *et al.* (2008) using velocity measurements taken in Orkney (UK).

While the metric of turbulence intensity is a useful indicator of the turbulent kinetic energy in the flow, it offers little information on the maximal velocity fluctuations. Such knowledge is an invaluable input for design calculations for both the turbine blades and seabed fastening mechanism.

This chapter presents an analysis of maximum normalised velocity perturbations from the mean flow speed in a tidal stream. The extreme value analysis implements a peak-over-threshold (POT) method to explore the influence of effective duration and length scale of the velocity perturbations on the magnitude of a the maximum perturbation for a one year return period. The author is not aware of any existing extreme value analyses applied to the velocity fluctuations of tidal streams.

The analysis presented herein is an extension of that published by Harding *et al.* (2011).

3.2 Background

Extreme value analyses of meteorological elements such as wind speeds, rainfall, and wave height are often performed when an understanding of 'worst-case' conditions is required, with extensive literature available on the subject (Palutikof *et al.*, 1999). These estimates are often presented in terms of a maximum return value, expected to occur once in the return period of N_r years.

The Generalized Extreme Value (GEV) theory describes how the maximum values of independent and identically distributed random variables can be fitted to a singular distribution, first identified by Fisher and Tippet (1928). This allows their behaviour to be extrapolated into the future in the prediction of extreme events. The shape of this distribution is governed by the inputs of a location factor (μ), scale factor (σ) and shape factor (ξ). The cumulative distribution function of the generalized GEV distribution is of the form expressed in Equation 3.1, where x is the return level (Coles, 2001).

$$G(x) = \exp\left\{-\left[1 + \xi\left(\frac{x-\mu}{\sigma}\right)\right]^{-1/\xi}\right\} \tag{3.1}$$

The shape factor is of particular importance as it governs the bounding behaviour of the distribution. When $\xi = 0$, Equation 3.1 simplifies to the Gumbel distribution family (Gumbel, 1958). When $\xi > 0$ the distribution represents the Fréchet distribution family, and the Weibull distribution results when $\xi < 0$ (Palutikof *et al.*, 1999; Coles, 2001). These distribution families

are often referred to as Type I, Type II and Type III, respectively. The behaviour of the 'tail' of the distribution at the maximal observed values is of primary importance. For Type I and Type II, the return level increases with return period. However for Type III, the distribution reaches an asymptotic limit in return period, where an upper bound in the return level exists.

The challenge remains to estimate these parameters with very limited duration of data, relative to the return period for which the analysis is performed. A key requirement of the GEV theory is that only one value from each observation period (epoch) is used in the model. This is often an inefficient use of data, which becomes particularly significant when the duration of the available historic data is limited. The task of predicting into the future with a restricted data set has been considered in such techniques as the *r*-largest value method (Weissman, 1978) and the method of independent storms (Cook, 1982).

Still another modification of the GEV approach is to consider only the exceedances over a given threshold, as first suggested by Pickands (1975). This 'Peak-Over-Threshold' (POT) method is based on the Generalized Pareto Distribution (GPD) and makes use of each data point above a specified minimum value. In this way, more information can be extracted from the limited data set, than when only the maximum of each epoch is used (Palutikof *et al.*, 1999; Gilli and Këllezi, 2006).

The GPD function describes the conditional probability of exceeding a return level, x, given that the measurements already exceed the threshold level of x_t. Letting X represent a sequence of independent and identically distributed measurements, this distribution is described mathematically by Equation 3.2, where $x > x_t$. The threshold excesses are defined as $y = x - x_t$.

$$\Pr\{X > x \mid X > x_t\} = \left[1 + \xi\left(\frac{x - x_t}{\sigma}\right)\right]^{-1/\xi} \tag{3.2}$$

For a given threshold, the standard approach for selection of the distribution parameters is performed using maximum likelihood estimation. This principle is based on adopting the model parameters which result in the closest fit of the probability distribution to the observed data (Myung, 2003). The profile of the likelihood estimator as a function of the distribution parameter is valuable in providing estimates of the confidence intervals associated with the selected values (Coles, 2001; Royston, 2007).

One of the main challenges with the GPD method relative to the GEV method is the selection of the threshold above which data peaks are considered, x_t. Of primary importance is the sensitivity of the shape and scale factors to the threshold selection. When the threshold is set

very low, the GPD is biased by the values further from the extremes, however setting a very high threshold results in limiting the number of exceedances, leading to excessive error margins in the model. One approach recommended by both Davison and Smith (1990) and Coles (2001) is to use diagnostic methods to assess the appropriateness of the threshold selection. A useful diagnostic is to plot the optimized shape and scale parameters for a range of possible threshold values. In this way, the stability of the distribution parameters with respect to the threshold can be assessed, and selected appropriately.

The implementation of the POT method of estimating maximum values is presented in this chapter for the application of velocity perturbations within a tidal stream. The author is aware that the duration of the available data is significantly less than that used for similar analyses in meteorological and hydrology. However it is important to note that the temporal and spatial resolution of the velocity data set used was unprecedented at the time of the analysis. As such, the results of the analysis enable indicative values of the maximum flow perturbations at the acquisition site to be deduced. Further analysis of longer acquisitions of velocity data of the same quality would be required to improve the confidence results in the future. Such data is expected to become available with the increased instrumentation on device prototypes with communications and power links directly to the shore.

3.3 Data acquisition

In order for an evaluation of the maximum velocity events to be extrapolated with any degree of accuracy, it is of utmost importance that the original measured time series represents the actual flow conditions as closely as possible. This results in the need for highly specialised velocity sensors to be installed in a challenging and dynamic marine environment. As such, the availability of acceptable velocity time series is limited.

The velocity data set used in this analysis was collected in the Puget Sound, Washington, at the location indicated in Figure 3.1a, and was obtained through a collaboration with the University of Washington and the Pacific Northwest National Laboratory. Both an Acoustic Doppler Velocimeter (ADV) and an Acoustic Doppler Current Profiler (ADCP) device were used to simultaneously measure the three-dimensional flow velocity from the Tidal Turbulence Tripod (TTT) shown in Figure 3.1b. The primary purpose of the deployment was to compare the performance of ADCP measurements, which are known to have a higher error at sampling rates of the order of 1Hz, against the ADV measurements which are known to be significantly more accurate at higher sampling frequencies. Mounted on top of the tripod installation, the ADV

Table 3.1: Acquisition settings of ADV and ADCP

	Ensemble Frequency (Hz)	Burst Length (s)	Sampling Interval (min)	Standard Error Velocity (m/s)
ADV	32	64	10	0.04[1]
ADCP	2	64	30	0.195[2]

[1] Taken from Nortek Vector deployment software
[2] Taken from RDI's PlanADCP software

sample volume was located at $z = 4.8$m above the seabed, with the ADCP measuring the adjacent water column in a number of discrete bins. The tidal stream velocity at this site reaches $U = 2$m/s in peak spring conditions and a mean depth of $h = 22$m. More detailed explanations of the instrumentation tripod deployment are given by Thomson *et al.* (2010) and Richmond *et al.* (2011).

In order to compare the measured velocity values, the ADCP bin used in this analysis was centred at 4.7m above the seabed. The operational settings of the two devices are summarised in Table 3.1 and the operating principles of the two devices are described below.

3.3.1 ADV operating principle

The ADV sensor used to measure the velocity data was a Nortek Vector. This acoustic velocimeter is designed for the acquisition of high frequency three-dimensional data velocity in a small sampling volume. The sampling volume can be selected by the user from 0.9cm^3 to 3.5cm^3 (Nortek AS, 2005). This is achieved through the use of the *converging* beam arrangement shown in Figure 3.2a. The transmitted acoustic signal is reflected by particulate matter in the tidal stream, and received by three receiving heads. The velocity in the direction of each of the reflected beams is deduced using Doppler shift in the received signal. The beam velocity components can then be transformed into the commonly used Cartesian coordinate system using a instrument-specific transformation matrix.

Further details on the operating principle of the device are described in more detail in §5.2.

3.3.2 ADCP operating principle

The ADCP device used on the TTT deployment was a Workhorse Sentinel ADCP, manufactured by Teledyne RD Instruments. In contrast to the ADV configuration, the spatial resolution of the velocity measurement is significantly reduced. The bin depth selected for this deployment was 0.5m, and taking the nominal beam diameter as that of the transducer to be 86mm, the sample volume is of the order of 3000cm^3 (RDI, 2002). This calculation neglects the cone angle of the acoustic beam, which causes this sample volume to increase with transmission length in reality.

Again, as with the ADV configuration, the reflected acoustic signals are observed by a number of receivers fixed at different orientation. The Doppler shift is used to deduce the flow velocity in the beam direction. In contrast to the ADV configuration, the beams of the ADCP are characteristically *diverging* as shown in Figure 3.2b. Therefore, in order to apply a transformation from beam velocities to the Cartesian coordinate system, the assumption of homogeneity in the flow must be made. While this may be applicable for the measurement of bulk flow conditions, the validity of this assumption is reduced when calculating instantaneous velocity measurements at the upper limit of the devices output frequencies.

In summary, with increased sample volume and the necessary assumption of homogeneity, the ADCP configuration represents a significant loss of accuracy relative to the ADV for the application of high spatial and temporal resolution velocity measurements.

3.3.3 Preliminary comparison of ADV and ADCP

A sample of the simultaneous longitudinal velocity measurements from the two devices is shown in Figure 3.3, using ensemble data. This plot clearly shows the effect of Doppler noise on the ADCP readings. While the statistical variance can be partially corrected for standard error using methods explained by Thomson *et al.* (2010), the analysis presented in this chapter deals with individual realizations of velocity measurements so this correction cannot be applied. Note that the differences between the ADV and ADCP signals in this figure can be attributed to the difference in sample volume locations as previously discussed, as well as a clock drift of up to 5s per day.

3.4 Data processing

A number of processing stages were applied to the velocity data acquired by both the ADV and ADCP prior to performing the extreme value analysis. These are explained in detail in the

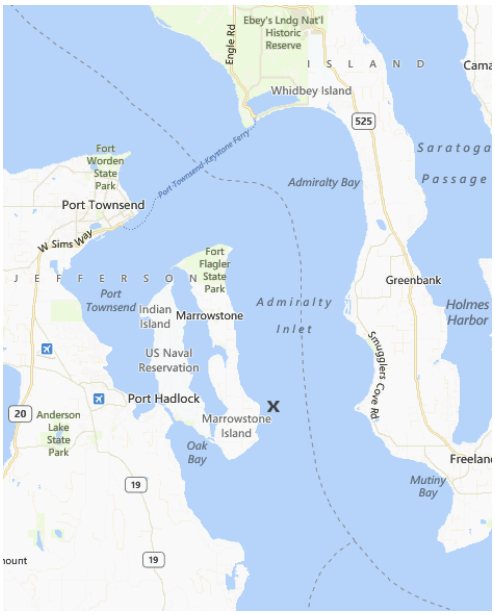

(a) Map of Admiralty Inlet with location of TTT marked with an × (Microsoft Corporation, 2012)

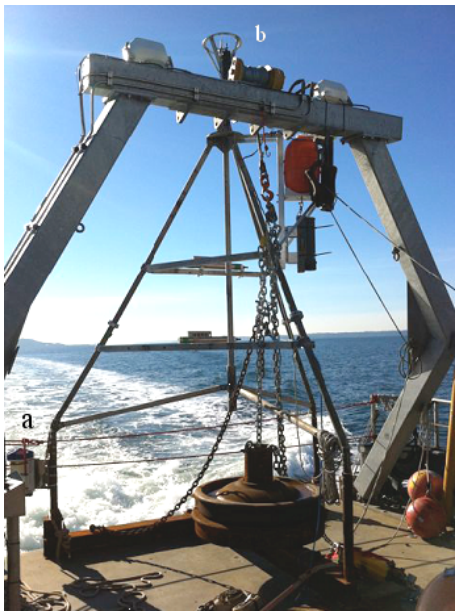

(b) Tidal Turbulence Tripod structure, showing a) ADCP and b) ADV instruments. Adapted from Thomson *et al.* (2010).

Figure 3.1: Tidal Turbulence Tripod installation location and structure

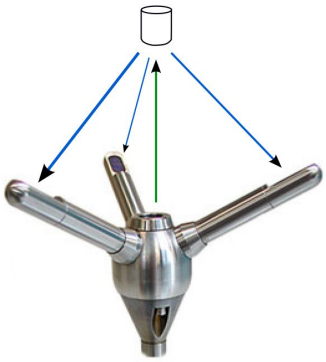

(a) Nortek Vector ADV. Photograph from Nortek USA (2012).

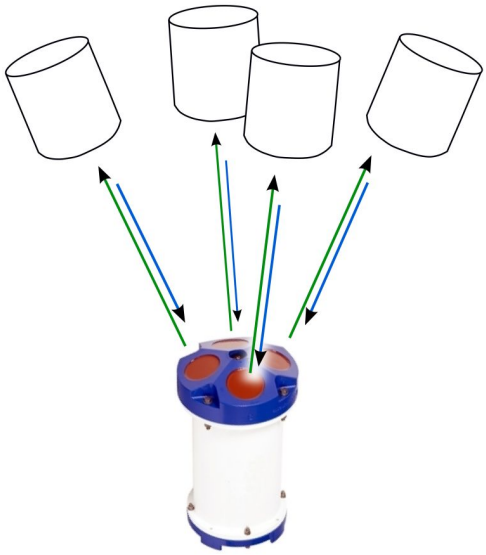

(b) Teledyne RDI Workhorse Sentinel ADCP. Photograph from RDI (2012).

Figure 3.2: Schematic diagram of operating principles and sample volumes of the a) ADV and b) ADCP instruments mounted on the Washington tripod deployment. The green arrows indicate the transmitted acoustic signal, and the blue arrows represent the reflected acoustic signals.

following sections, and summarised in Table 3.2.

Table 3.2: Summary of data processing for extreme value analysis

Process	Reason / Consequence
Rotate velocity data to principal axis	Allows calculation of velocity fluctuations in the longitudinal direction, u, and transverse direction, v
Calculate normalised velocity fluctuations for when $U \geq 1$m/s	Normalised velocity fluctuations follow an approximately stationary distribution as required by the POT method
Detect and replace spurious data points	Remove spikes in velocity data which could bias extreme value analysis
Calculate mean perturbation magnitudes using time-scale and length-scale averaging	Allows extreme value analysis to be carried out using velocity perturbations of varying effective duration and length
Decluster velocity perturbations	Ensure independence of velocity data points used in POT analysis

3.4.1 Orientation of data

To begin, the velocity data from both the ADCP and the ADV were transformed to a Cartesian coordinate system aligned with the principal axis. The principal axis direction is calculated using a least square regression algorithm, to maximize the flow energy along the axis direction.

As we are interested in the deviation from the mean flow velocity, the flow perturbations in each direction are calculated using Equation 1.4. The mean velocity components (U,V,W) are calculated over each acquisition burst length of 64s, using the 32Hz ensembles for the ADV data, and 2Hz ensembles for the ADCP. This allows the use of the maximum amount of points in the averaging calculation for statistical robustness without causing any significant changes in the underlying statistical requirement of stationarity.

Because the perturbation velocities are symmetrically distributed about the mean velocity, only the magnitudes of the perturbations are considered in the extreme value analysis.

3.4.2 Normalisation of velocity fluctuations

In this data set, as well as that presented by McCann *et al.* (2008), it was observed that larger fluctuations occur at the higher flow speeds. The distributions of the velocity perturbations for recorded within mean velocity ranges of 0.5m/s are shown in Figure 3.4. This plot clearly shows

the effect of the significant Doppler noise introduced into the ADCP measurements, discussed further in §3.8.1, by the much wider distribution of fluctuations at all mean flow speeds. The increase in the distribution width as a function of flow speed is also evident within the data set of each instrument.

The statistical methods used in the extreme value analysis require stationarity of the data set, such that both the mean and the variance of the data are independent of time. The mean of the velocity perturbations is zero by definition, however Figure 3.4 indicates that the variance of the instantaneous fluctuations is dependent on the mean flow speed, and consequently on time.

In order to ensure that a stationary distribution is used in the extreme value analysis, the velocity fluctuations were normalised by the mean flow speed. The resulting distribution statistics of the normalised perturbations are shown in Figure 3.5. These plots demonstrate how the distribution of the instantaneous velocity perturbations, indicated using the 25th and 75th percentile values, increases as a function of the mean flow speed. However, when these fluctuations are normalised, the interquartile range is shown to be approximately constant for mean speeds of $U \geq 1\mathrm{m/s}$. As a result of these observations, the data was truncated to only consider the normalised velocity fluctuations when $U \geq 1\mathrm{m/s}$ and all other data entries were discarded. It is interesting to note that this threshold is similar to the cut-in speed off many axial flow turbine prototypes currently being deployed (Polagye *et al.*, 2010; Thomson *et al.*, 2010).

3.5 Velocity data filtering

Though more convenient than alternatives such as Laser Doppler Velocimetry (LDV), the use of acoustic Doppler instruments introduces inherent errors in the measurement of velocity fluctuations, at high frequencies in particular. One significant error source is the 'Doppler' noise floor which can be observed when acquiring data at higher frequencies. Another important source of error common in the use of ADV is the occurrence of spikes in the velocity data. These are caused by the aliasing of the acoustic signal, where the reflected acoustic pulse is received outside the expected range of phase shift relative to the transmitted pulse (Goring and Nikora, 2002).

There are many algorithms available for the detection and replacement of spurious data points of raw velocity data. This process becomes particularly important when the maximum values of the data series are of significance, as in an extreme value analysis. The methods used in this study are briefly described below, and were applied to the ensemble data of both instruments with the respective ensemble frequencies specified in Table 3.1.

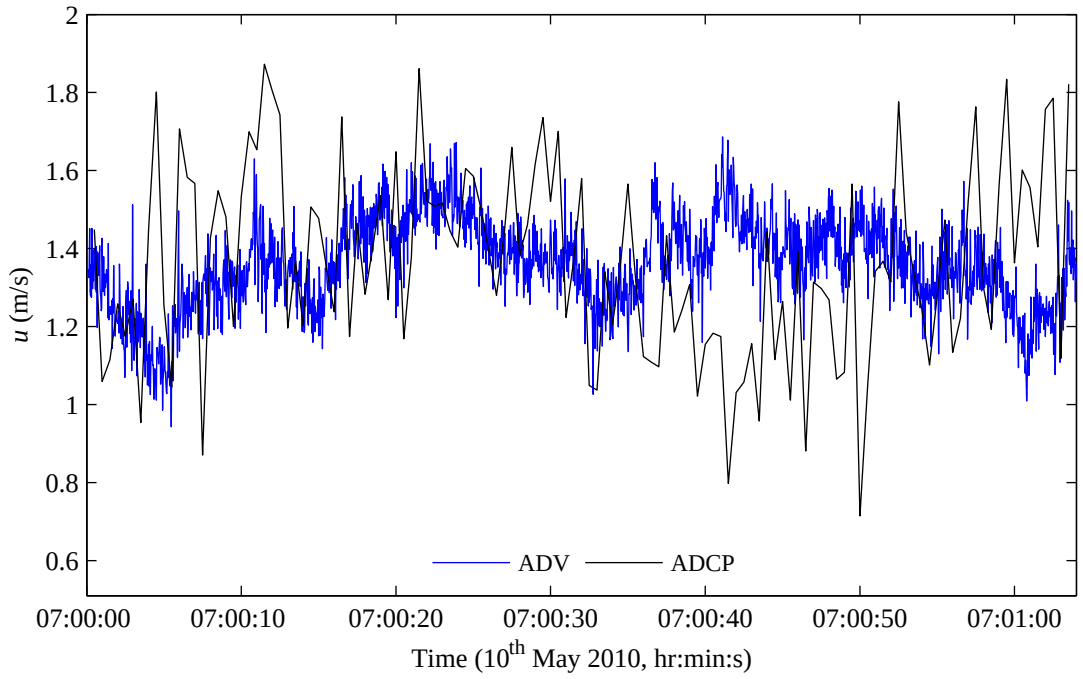

Figure 3.3: Comparison of ADV and ADVP velocity time series in the longitudinal direction

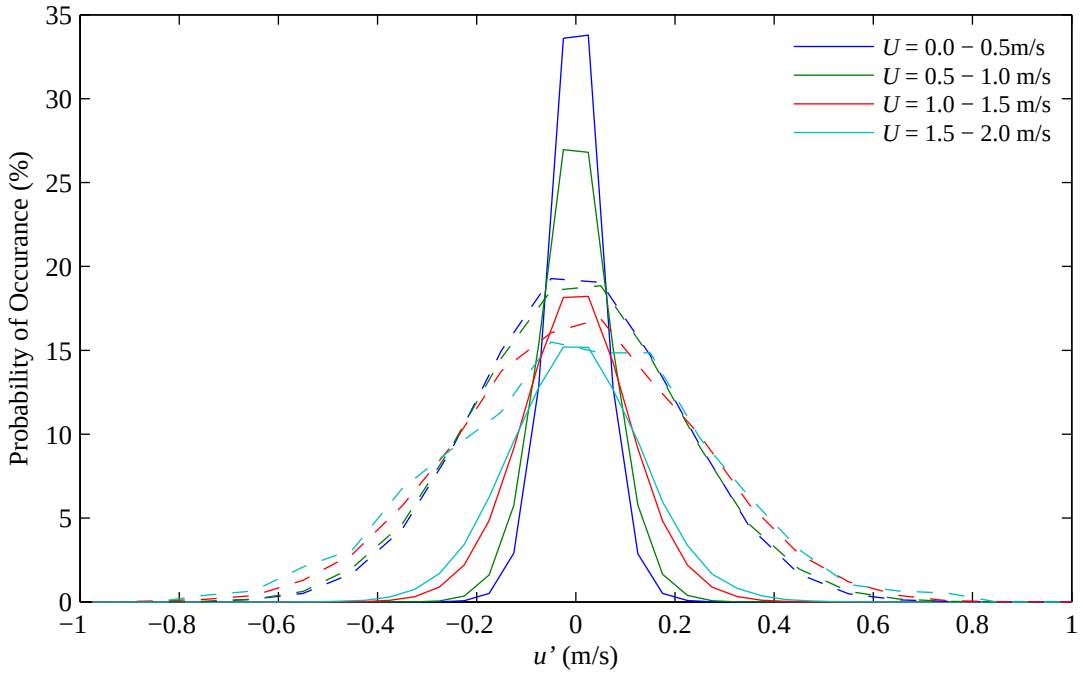

Figure 3.4: Distribution of velocity perturbations for different mean flow speeds. The solid line represents the velocities measured by an ADV, and the dashed line represent the velocities measured by an ADCP.

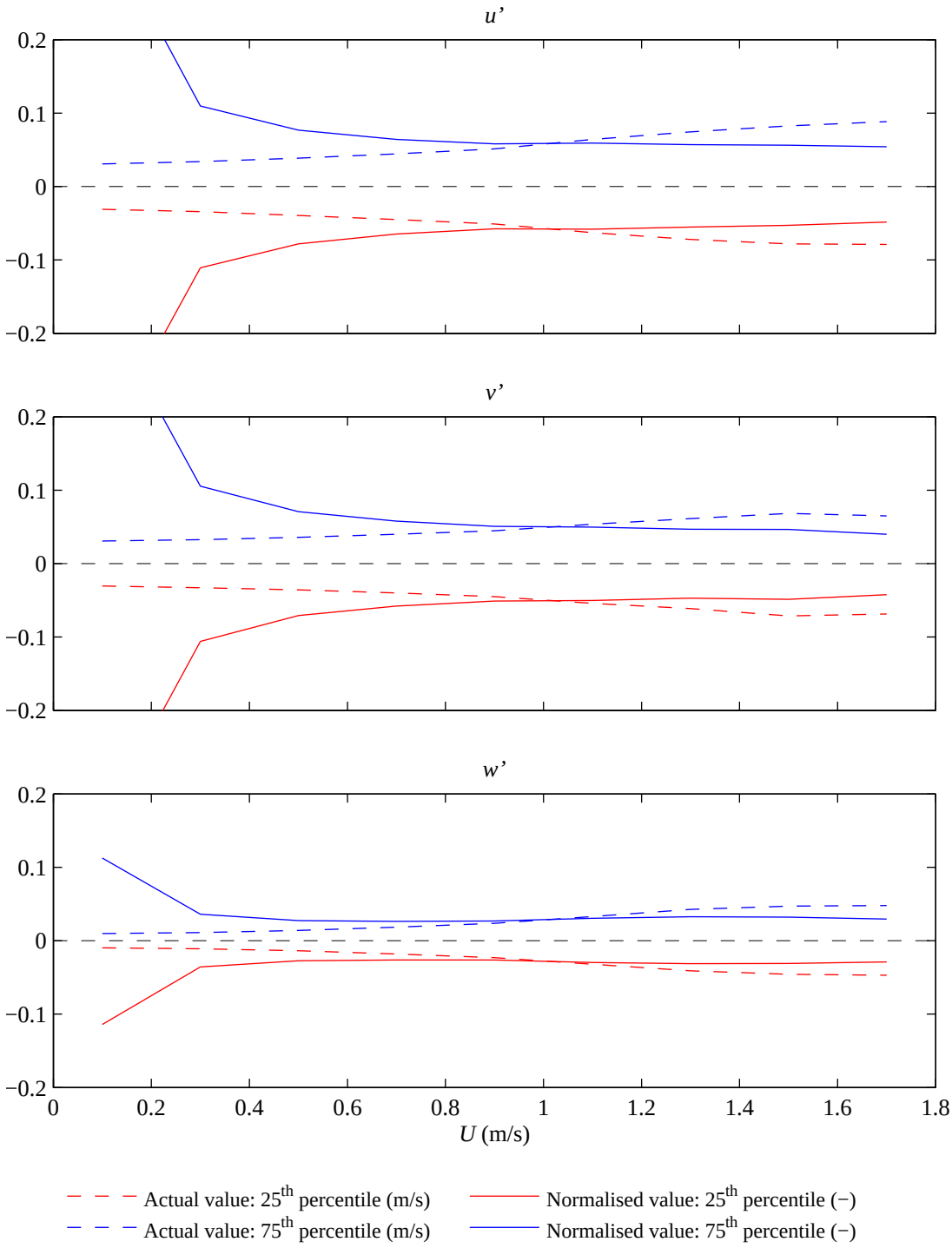

Figure 3.5: Distribution statistics of instantaneous and normalised ADV velocity fluctuations. The lower quartile (25th percentile) is plotted in red, and the upper quartile (75th percentile) is plotted in blue. Dashed lines represent the distribution of the measured velocity perturbations, with the unit of m/s. The solid lines represent that of the measured velocity perturbations normalised by the mean longitudinal flow velocity, and are therefore dimensionless.

3.5.1 Detection methods

Correlation Coefficient Threshold Method

The velocity data from both the ADV and ADCP was quality controlled by removing points of low acoustic correlation. This metric is a useful indicator of data quality, calculated for each data point, and generally increases with the signal-to-noise ratio (SNR) of the measurement (RDI, 1996; Rusello *et al.*, 2006). A correlation threshold of $C = 30 + 40\sqrt{f_s/25}$ was applied to the velocity data, where f_s is the sampling rate in Hz (Elgar and Raubenheimer, 2001). This filtering method was implemented by Thomson *et al.* (2010), prior to disemination of the velocity data set, with a rejection rate of less than 1%. The spurious data points were replaced with a running mean of the velocity time series.

While it is recommended that data with low correlation values be filtered from the time series, it is important to note that high correlation does not always indicate that the flow measurement is valid (Rusello, 2009), so additional filtering methods were employed.

Acceleration threshold method

This method of identifying spikes in the data is based on limiting the measured velocity accelerations below a threshold based on the acceleration due to gravity, g. The acceptance criterion for data point i using this method is described by Equation 3.3 for the longitudinal velocity direction. An equivalent expression can be derived for the transverse and vertical flow directions by modifying the variables used in the numerator.

$$\left|\frac{u_{i+1} - u_i}{t_{i+1} - t_i}\right| < \lambda_a g \tag{3.3}$$

Goring and Nikora (2002) suggest that suitable values of the threshold constant, λ_a, are in the range of $1 \leq \lambda_a \leq 1.5$ for this method, and as such a value of $\lambda_a = 1.5$ has been used in this study. Selecting the threshold constant as the maximum of the suggested range resulted in a more relaxed filtering algorithm. In this way, the selected value of λ_a is expected to result in a conservative estimate of the extreme values of relative velocity. Approximately 0.03% of the data series was identified as spurious using this filter.

Phase-Space threshold method

One of the most efficient algorithms for the removal of spikes in a velocity time series measured using an acoustic Doppler device is the 'phase-space' method. This method is based on a phase-space plot (or Poincaré plot) whereby each velocity data point u_i in the series of n data points is plotted against its derivatives defined by Equation 3.4.

$$\Delta u_i = (u_{i+1} - u_i)/2 \tag{3.4a}$$

$$\Delta^2 u_i = (\Delta u_{i+1} - \Delta u_i)/2 \tag{3.4b}$$

In the original solution, proposed by Goring and Nikora (2002), the algorithm was represented using three projections of two-dimensional coordinate systems: u vs Δu, u vs $\Delta^2 u$ and Δu vs $\Delta^2 u$). The acceptance threshold for each plot was defined by an elliptical boundary.

This method was later developed by Wahl (2003), whereby the algorithm was modified to use a three-dimensional representation of the Poincaré plot, with an ellipsoidal acceptance volume (Mori *et al.*, 2007). The points which appeared outside of this volume were excluded from the data set. As the magnitude of the ellipsoidal threshold is a function of the standard deviation of the data and its derivatives, the process is iterated until all the points are located within the ellipsoidal volume. The geometry of this ellipsoid is a function of the universal criterion, λ_U, defined for a series of n data points by Equation 3.5, and the standard deviation of the velocity data and its two derivatives: σ_u, $\sigma_{\Delta u}$ and $\sigma_{\Delta^2 u}$.

$$\lambda_U = \sqrt{2 \ln (n)} \tag{3.5}$$

The acceptance volume can be defined within the Cartesian coordinate system, (u,Δu,$\Delta^2 u$), using the spherical coordinates with radial distance denoted as ρ, the azimuthal angle θ and the polar angle as ϕ. Using these parameters, the ellipsoid is defined by Equation 3.6.

$$\begin{aligned} \frac{1}{\rho^2} = & \frac{(\sin\phi\cos\theta\cos\alpha + cos\phi\sin\alpha)^2}{a^2} \\ & + \frac{(\sin\phi\cos\theta\sin\alpha - cos\phi\cos\alpha)^2}{b^2} \\ & + \frac{(\sin\phi\sin\theta)^2}{c^2} \end{aligned} \tag{3.6}$$

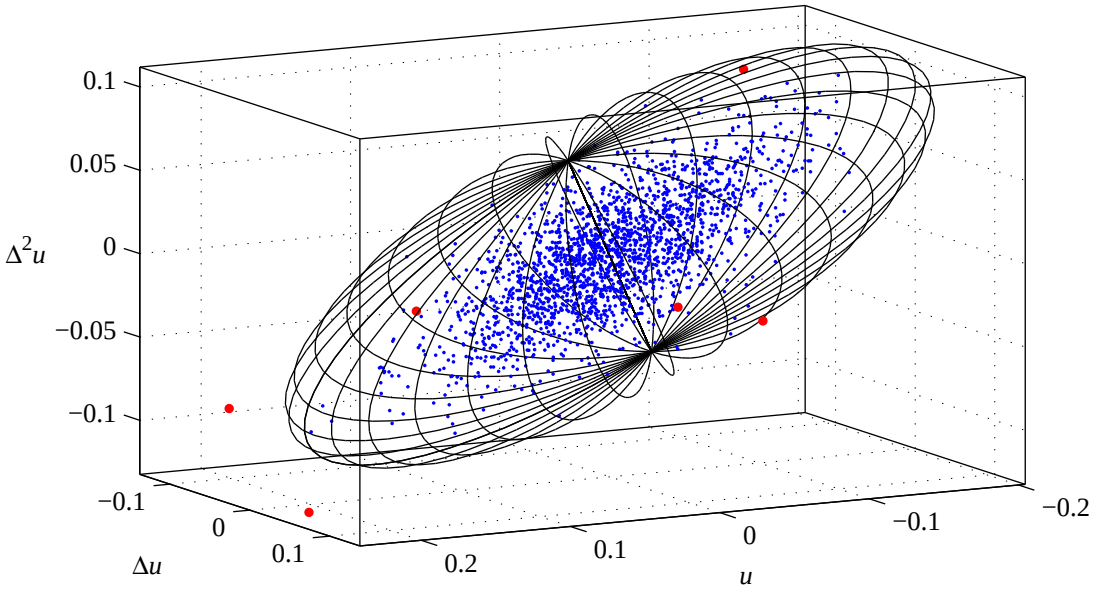

Figure 3.6: Representative three-dimensional threshold of phase space filtering method for ADV velocity measurement in longitudinal direction. The accepted and rejected data are represented by small blue dots and large red dots, respectively.

The constants used in Equation 3.6 are defined in Equation 3.7.

$$(\lambda_U \sigma_u)^2 = a^2 \cos^2 \alpha + b^2 \sin^2 \alpha \tag{3.7a}$$

$$(\lambda_U \sigma_{\Delta^2 u})^2 = a^2 \sin^2 \alpha + b^2 \cos^2 \alpha \tag{3.7b}$$

$$c = \lambda_U \sigma_{\Delta u} \tag{3.7c}$$

$$\alpha = \tan^{-1}\left(\frac{\sum u_i \Delta^2 u_i}{\sum u_i^2}\right) \tag{3.7d}$$

This algorithm was implemented using the despiking functions developed by Mori (2009) as part of the MACE Toolbox for MATLAB. A representative three-dimensional Poincaré plot is shown for the longitudinal velocity data in Figure 3.6. The methodology for this analysis in the transverse and vertical velocity directions is identical. Less than 2% of the data series was excluded through the implementation of this despiking algorithm.

3.5.2 Replacement method

The method of cubic interpolation was recommended by Goring and Nikora (2002) as a useful algorithm to replace spurious data points, and was trialled for this purpose. However this

interpolation method has the ability to interpolate a value greater than the adjacent accepted data points. In this way, a local maximum was introduced to the data set with a value of little physical significance. This is likely to effect the behaviour of the distribution of the maximum points used in the POT analysis.

As a result of these observations using a cubic interpolation, a linear interpolation was used to replace the data points identified as outliers. This algorithm guaranteed that the value of the replacement points would not exceed the local maximum.

3.5.3 Time-scale averaging

Performing an analysis on the raw 32Hz data collected by the ADV would allow the peak fluctuation with an effective time-scale of 0.031s to be deduced, with an equivalent of 0.5s for the ADCP measurements sampled at 2Hz. However the longer the fluctuation time-scale, the more significant the influence on the hydrodynamic performance of an AGB.

Furthermore, instantaneous flow measurements over these minimum time-scales are most susceptible to large contributions of Doppler noise as limited ensemble averaging is applied. It is therefore interesting to understand the magnitude of velocity fluctuations with greater effective durations.

To increase the effective duration of the flow perturbation, the high frequency velocity components were removed from the data series through a low pass filtering process. A central moving average was selected as the filter for this purpose due to its ability to efficiently remove white noise (Smith, 2003).

The moving average filter was implemented with the averaging windows of $T_a = \{0.5\text{s}, 1\text{s}, 2\text{s}, 4\text{s}, 8\text{s}\}$. The effective longitudinal velocity perturbation at time, t, averaged over a temporal window of T_a seconds can be expressed mathematically by Equation 3.8.

$$\langle u'(t, T_a)\rangle = \frac{1}{T_a}\int_{t-T_a/2}^{t+T_a/2} u'(t)\,dt \tag{3.8}$$

A sample of the instantaneous velocity measurements compared with the averaged values with $T_a = 4.0\text{s}$ for the ADV is shown in Figure 3.7.

Because individual points have significant influence on the extreme value analysis, the limits of the data set, which have insufficient points to average over the full averaging window, were discarded (Fuller, 1996). As such, for the example shown in Figure 3.7, the moving average

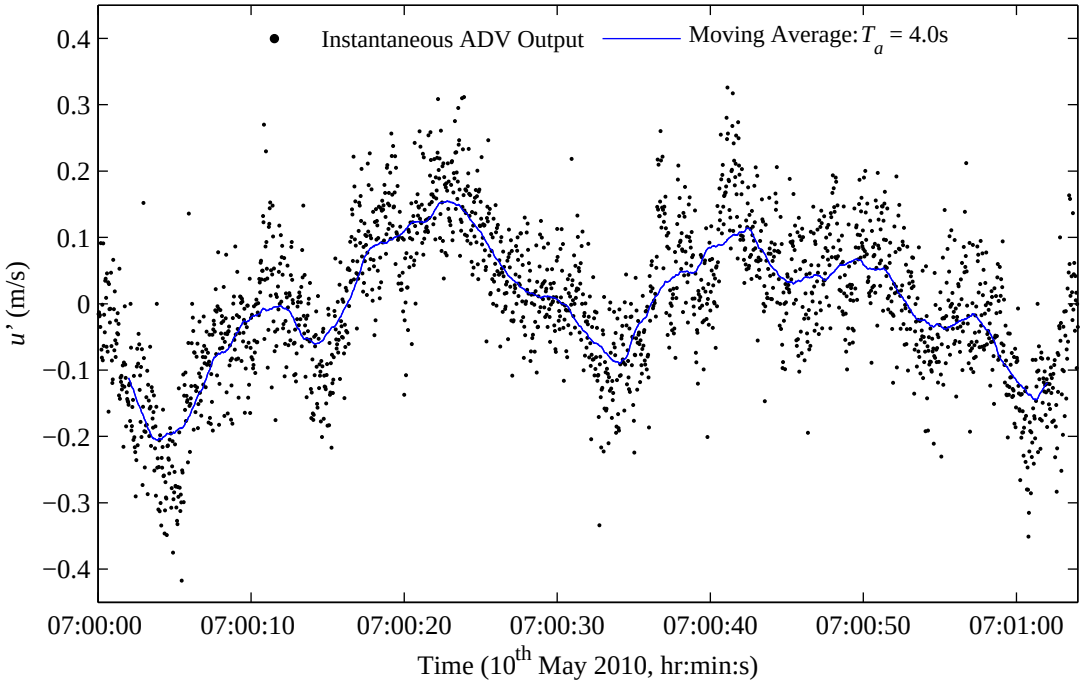

Figure 3.7: Comparison of instantaneous and averaged ADV velocities, using temporal averaging window of T_a = 4.0s.

line does not include the first and last 64 points (two seconds) of each 64s acquisition burst.

3.5.4 Length-scale averaging

In a similar argument to time-scale averaging, the impact of length-scale of the fluctuations is also of interest. Understanding the velocity fluctuations in terms of their effective length is useful when the relative size of the perturbation is important. For example, the effect of unsteady flow conditions on the lifting surfaces of an AGB is a function of the velocity perturbation length-scale relative to the chord length.

Assuming Taylor's hypothesis of frozen turbulence (Taylor, 1938; Pope, 2000), the temporal window for a moving average with a specified length-scale, L, must increase as the advection velocity decreases in accordance to Equation 3.9. The temporal averaging period was calculated for each acquisition burst in response to the continual change in mean longitudinal flow velocity.

$$T_a = L_a / U \tag{3.9}$$

For the longitudinal flow direction, the moving average was calculated over the spacial averag-

ing windows of $L_a = \{1\text{m}, 2\text{m}, 4\text{m}, 8\text{m}\}$. The approximation of Equation 3.9 is only applied for the analysis of flow perturbations in the longitudinal direction.

3.5.5 Declustering

One of the key assumptions made when using the chosen statistical method for the prediction of extreme values is the independence of data in the set (Coles, 2001). Generating a data set using the moving average over a specified time or length scale inherently makes each data point dependent on the surrounding values, therefore invalidating this assumption. In order to overcome this, the data was filtered to obtain a set of independent exceedances of a threshold, in a process known as declustering.

The specific declustering technique used is called 'runs declustering' (Soukissian and Arapi, 2011). Firstly a threshold, p, is defined such that when a data point exceeds this value, a cluster is started. This cluster is terminated when a specified declustering run length of r points fall below the threshold. The maximum absolute value of each cluster is recorded, and all other values are set to zero (Gilleland *et al.*, 2010). The declustering threshold, p, is not to be confused with the threshold value used to define the data used in the POT analysis, x_t.

A representative result of the runs declustering process is shown in Figure 3.8.

3.5.6 Wave induced velocity fluctuations

Waves at the site of the TTT deployment are fetch-limited from all directions and achieve a maximum state of a 1.0m significant wave height and a peak wave period of 4.0s during a large winter storm. This gives a wavelength of $\lambda = 25\text{m}$ using linear theory, which is considered as a deep water wave under the condition of $\lambda/2 < h$. As such, the orbital velocities decay exponentially as a function of depth such that the wave induced velocity fluctuations will be 0.01m/s at the depth of the ADV (Sarpkaya and Isaacson, 1981). This is an order of magnitude less than the turbulent fluctuations measured by the ADV and so no adjustment for the wave induced velocity fluctuations was made in this analysis.

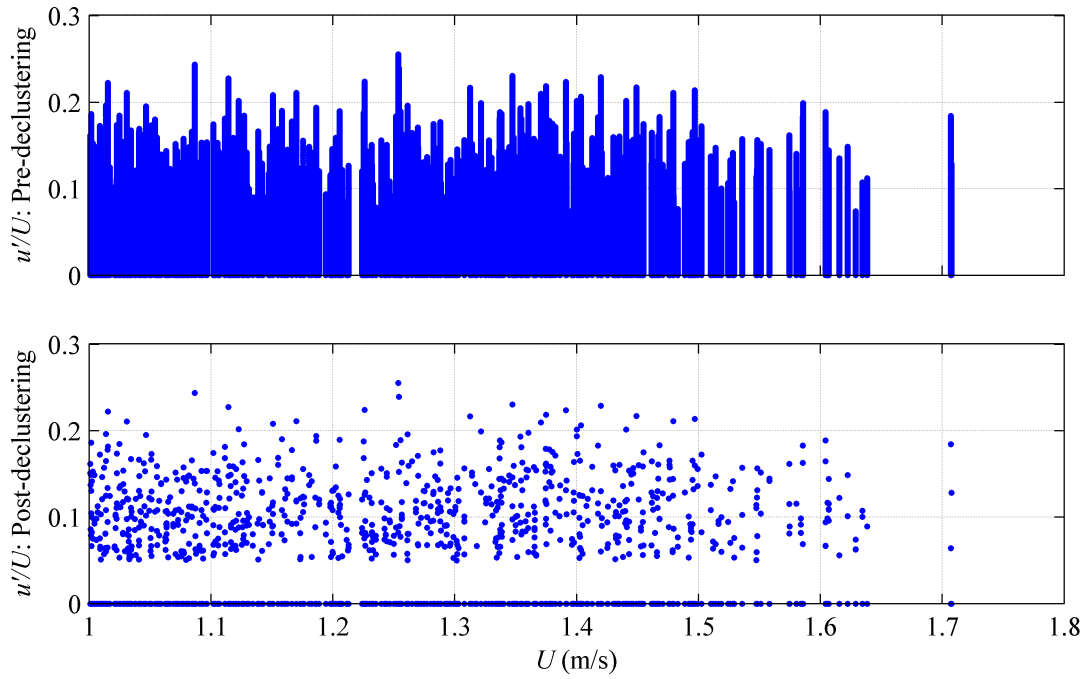

Figure 3.8: Declustering of normalised velocity fluctuations in the longitudinal direction versus the mean longitudinal flow speed: T_a = 4.0s, p = 0.05, r = 320s

3.6 Analysis of maximum velocity perturbations

3.6.1 Threshold selection

The selection of the threshold, x_t, to be used in the POT analysis was performed by assessing the stability of the distribution parameters for a range of potential threshold values. In particular, the stability of the values of the shape factor, ξ, and scale factor, σ, which govern the form of the GPD, was observed.

The values of the shape factor and scale factor are calculated by the bivariate optimization of the log-likelihood function of Equation 3.10 to a maximum for each value of x_t explored (Coles, 2001; Martins and Stedinger, 2000). In Equation 3.10, $i = 1, \ldots, k_n$ where k_n is the number of threshold exceedances, and $(1 + \xi y_i/\sigma) > 0$.

Using this technique, the variation of the values of these parameters can be seen to increase as the threshold, x_t, is increased. As previously discussed, setting the threshold too low can result in a bias in the GPD fit by values significantly less than the maxima. However, the accuracy of the model is reduced when a limited number of data points remain above a high threshold. The highest threshold which returns stable values of the shape and scale parameters was selected,

in a bias-variance trade-off. For the example shown in Figure 3.9, a threshold of $x_t = 0.13$ was selected.

$$l(\sigma, \xi) = \begin{cases} -k_n \cdot \log(\sigma) - (1 + 1/\xi) \sum_{i=1}^{k_n} \log(1 + \xi y_i/\sigma) \\ \qquad\qquad \text{when } \xi \neq 0 \\ -k_n \cdot \log(\sigma) - \sigma^{-1} \sum_{i=1}^{k_n} y_i \\ \qquad\qquad \text{when } \xi = 0 \end{cases} \tag{3.10}$$

A sample scatter plot of the perturbations over the acquisition time is presented in Figure 3.10. The selected threshold is indicated with a dashed black line.

3.6.2 Calculation of return level

For a data set of length M, the exceedance probability is defined by the parameter $\zeta = k_n/M$. As the same probability is denoted $\Pr\{X > x_t\}$, Equation 3.2 can then be simplified to the form of Equation 3.11 (Ceppi *et al.*, 2008).

$$\Pr\{X > x\} = \zeta \left[1 + \xi \left(\frac{x - x_t}{\sigma}\right)\right]^{-1/\xi} \tag{3.11}$$

It can be deduced that the return level x will be exceeded once every m_r observations, such that $\Pr\{X > x\} = 1/m_r$. Letting n_y represent the number of observations per year, the N_r-year return level can be calculated by Equation 3.12 (Coles, 2001; Della-Marta *et al.*, 2009).

$$x_{N_r} = \begin{cases} x_t + \frac{\sigma}{\xi}\left[\left(N_r n_y \zeta\right)^{\xi} - 1\right] & \text{when } \xi \neq 0 \\ x_t + \sigma \log\left(N_r n_y \zeta\right) & \text{when } \xi = 0 \end{cases} \tag{3.12}$$

Due to the limited duration of the available data set, the return period was limited to that of a single year such that $N_r = 1$. As equivalent data sets with increased duration become available from future site characterisation studies, this return period will be able to be extended.

Coles (2001) suggests that the error in ζ can be ignored in the analysis of the confidence intervals in the return levels due to its low uncertainty relative to the other model parameters. This allows the Equation 3.12 to be rearranged for σ to give an expression for the scale factor in

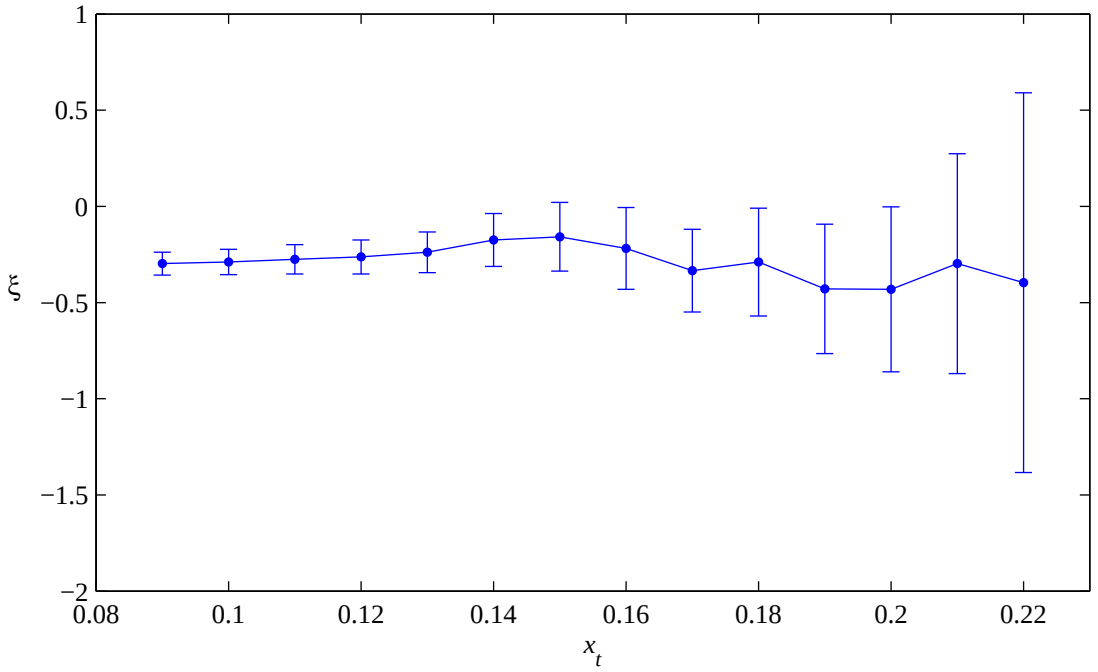

Figure 3.9: Stability analysis of GPD parameters with range of thresholds: T_a = 4.0s, p = 0.05, r = 320.

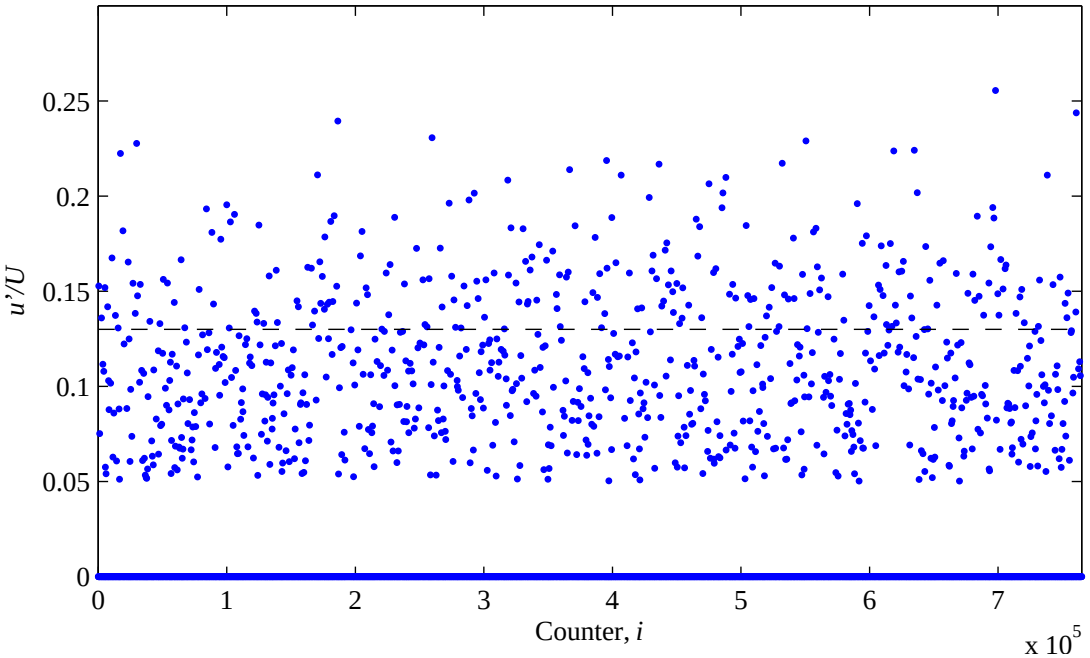

Figure 3.10: Example scatter plot of normalised velocity perturbations. The selected threshold is indicated with a horizontal dashed line: T_a = 4.0s, p = 0.05, r = 320.

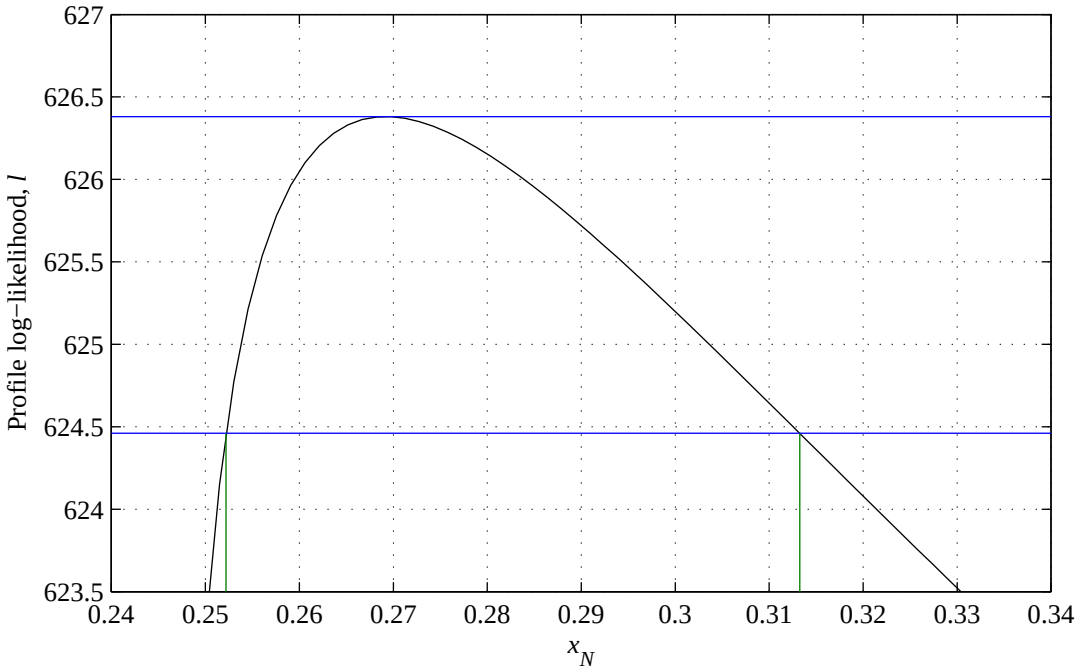

Figure 3.11: Representative calculation of log-likelihood confidence interval of return level: $T_a = 4.0$s, $p = 0.05$, $r = 320$s. The upper and lower confidence interval are indicated with a green vertical line.

terms of the return level, as shown in Equation 3.13.

$$\sigma = \begin{cases} \frac{\xi(x_{N_r} - x_t)}{(N_r n_y \zeta)^{\xi} - 1} & \text{when } \xi \neq 0 \\ \frac{x_{N_r} - x_t}{\log(N_r n_y \zeta)} & \text{when } \xi = 0 \end{cases} \tag{3.13}$$

By substituting Equation 3.13 into Equation 3.10 and maximising the resulting log-likelihood expression for ζ allows the log-likelihood profile to be plotted as a function of the return level, x_{N_r}. The resulting log-likelihood function for a representative case is shown in Figure 3.11.

The values of the 95% confidence interval in return level correspond to the x-ordinates where the log-likelihood function is equal to 1.92 less than the maximum value calculated. This value is calculated as half of the 95th quantile of the a chi-squared distribution, indicated with a blue horizontal line in Figure 3.11. Further details on the mathematical derivation and explanation of this method are given by Venzon and Moolgavkar (1988).

3.6.3 Statistical analysis program

The majority of the statistical analyses outlined in this paper were performed using the '*extRemes*' toolkit within the statistical software program *R* (R Development Core Team, 2009). This toolkit is an implementation of many techniques described by Coles (2001), and provides a graphical user interface to the '*ismev*' package. The National Center for Atmospheric Research (2007) provides more information about the capabilities of the toolbox.

3.7 Analysis results

3.7.1 Analysis parameters

Runs declustering was performed on the perturbation magnitudes using a declustering threshold of $p = 0.05$. The run length used for this analysis was defined by a duration of 10s. Due to the difference in sampling rate of the two instruments, this corresponded to a value of $r = 320$ for the analyses using ADV data, and $r = 20$ for the analyses using ADCP data.

A sensitivity study was performed to observe the influence of the run length parameter selection. The results of this study are shown graphically in the top plot of Figure 3.12 for the representative case of $T_a = 4.0$s and $p = 0.05$, with $x_t = 0.13$. The value of the return level was observed to be relatively constant, while the confidence intervals were seen to decrease slightly with increasing run length. Quantitatively, the return level shows a reduction of approximately 4% over the range of run lengths examined. The magnitude of the confidence interval decreases by approximately 38% over the same range.

The sensitivity of the one-year return level to the threshold selection for the POT analysis was also of interest. A similar study was performed to observe the variation in the return level as a function of threshold selection. The overall trends of the sensitivity study can be inferred from the effects of the threshold on the distribution parameters, shown in Figure 3.9. For example, the slight increase in return level when a threshold of $x_t \approx 0.14$ is used can be attributed to the slight increase in shape parameter, ξ, expected from Figure 3.9. However using the return level as the indicator of the sensitivity study provides a more meaningful quantification of the variation, than that obtained using the parameters which are used in its calculation.

The results of this analysis for the representative case of $T_a = 4.0$s, $p = 0.05$ and $r = 320$ are shown in the bottom plot of Figure 3.12. The return level varies by approximately 9% over the range of thresholds examined. Overall, the confidence interval of the return level is observed to increase with the threshold level. This is expected, as the amount of available data is reduced.

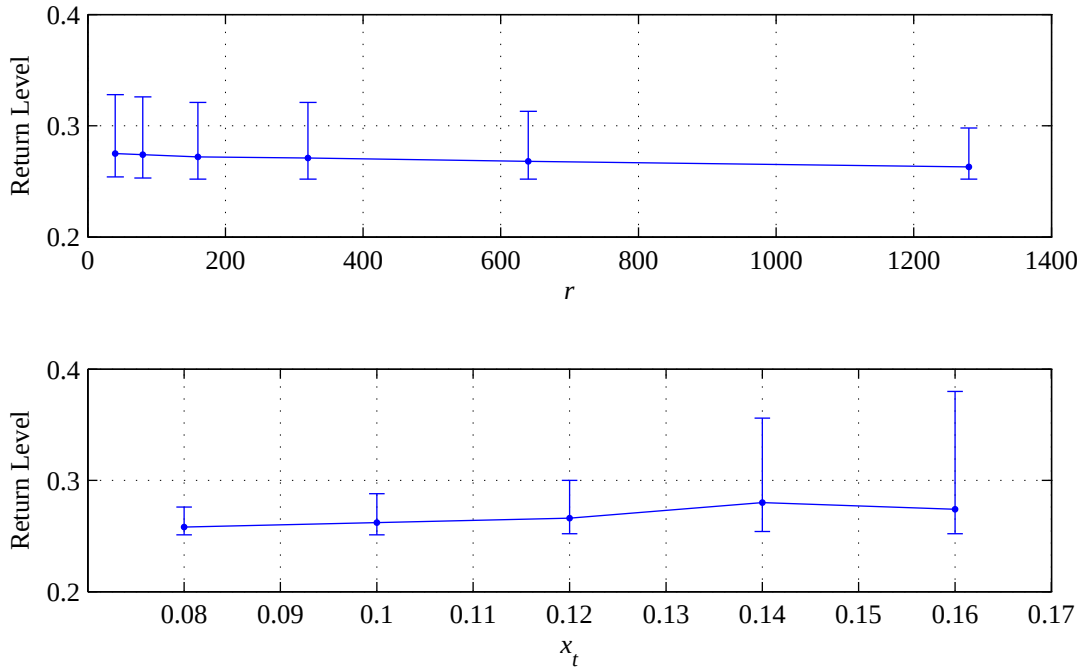

Figure 3.12: Stability analysis of one-year return level as a function of a) declustering run length, r, and b) threshold selection, x_t. These results are calculated for normalised flow perturbations measured by the ADV in the longitudinal direction: $T_a = 4.0$s, $p = 0.05$.

3.7.2 Diagnostics plots

The 'goodness of fit' of the resulting GPD model to the real data can be visualized in a number of useful diagnostic plots; the probability plot, quantile plot, density plot, and the return level plot (Coles, 2001). These plots are generated using functions available within the '*extRemes*' toolkit (The National Center for Atmospheric Research, 2007). The coordinates of the information presented in each plot are summarized in Table 3.3.

The probability and quantile plots represent a comparison between the empirical cumulative distribution function of $i/(k_n + 1)$ for $x_1 \leq x_i \leq \ldots \leq x_{k_n}$ and that of the GPD model, defined in Equation 3.14.

$$H(x) = 1 - \left[1 + \xi\left(\frac{x - x_t}{\sigma}\right)\right]^{-1/\xi} \tag{3.14}$$

When these two functions are well matched, both of these plots indicate the correlation with a linear scatter plot with a gradient of unity. The two plots both compare these two functions, but in differing ways, such that one may appear to demonstrate an acceptable fit while the

Table 3.3: Coordinates of Diagnostic Plots

Probability plot:	$\left\{\left(H\left(x_i\right), \frac{i}{k_n+1}\right) : i = 1, \ldots, k_n\right\}$
Quantile plot:	$\left\{\left(H^{-1}\left(\frac{i}{k_n+1}\right), x_i\right) : i = 1, \ldots, k_n\right\}$
Density plot:	(H, x)
Return level plot:	$\left(N_r, \left(x_t + \frac{\sigma}{\xi}\left[\left(N_r n_y \zeta\right)^{\xi} - 1\right]\right)\right)$

other does not. Firstly, the probability plot provides a direct comparison of the probability of occurrence of a perturbation of a specific magnitude. However, the quantile plot compares the perturbation magnitudes predicted by the two models over the range of probabilities of 0 to 1. In other words, the probability plot compares the probabilities predicted by the models for the range of perturbation magnitudes, and the quantile plot compares the perturbation magnitudes predicted by the models for the range of probabilities. In this way, these two plots present the same information on a different scale (Coles, 2001).

The density plot depicts a histogram of occurrences above discrete bands of perturbation magnitudes, normalised by the total number of threshold exceedances. In this way the GPD can be overlaid to observe how closely the model fits the distribution of the threshold excesses.

The return level plot shows the N_r-year return level as a function of return period, N_r, with associated 95% delta-method confidence intervals. An example is shown in Figure 3.15. Overlaid on this plot are the magnitudes of the velocity data points plotted against their expected return period. Because the data set being used is 17 days in duration, the greatest return period that can be plotted for a measured value is approximately $17/365 = 0.047$ years.

Note that the delta-method of confidence interval calculation used in this plot is different from the log-likelihood method introduced in §3.6.2. A key assumption of the delta-method is that the log-likelihood estimate is normally distributed for each return level (Coles, 2001). This results in the symmetrical confidence interval observed in Figure 3.15. In this plot the lower confidence bound suggests the non-physical phenomenon whereby the minimum expected value for the one year return level is less than the greatest measured value in a period significantly less than one year. This assumption of normality is not required for the log-likelihood method, which uses the log-likelihood function directly in the calculation of confidence interval, and is therefore generally accepted as providing more robust estimates of the standard error (Uusipaikka, 2009). The log-likelihood confidence interval incorporates the skew in variance which has the effect of excluding the perturbation magnitudes less than the maximum observed fluctu-

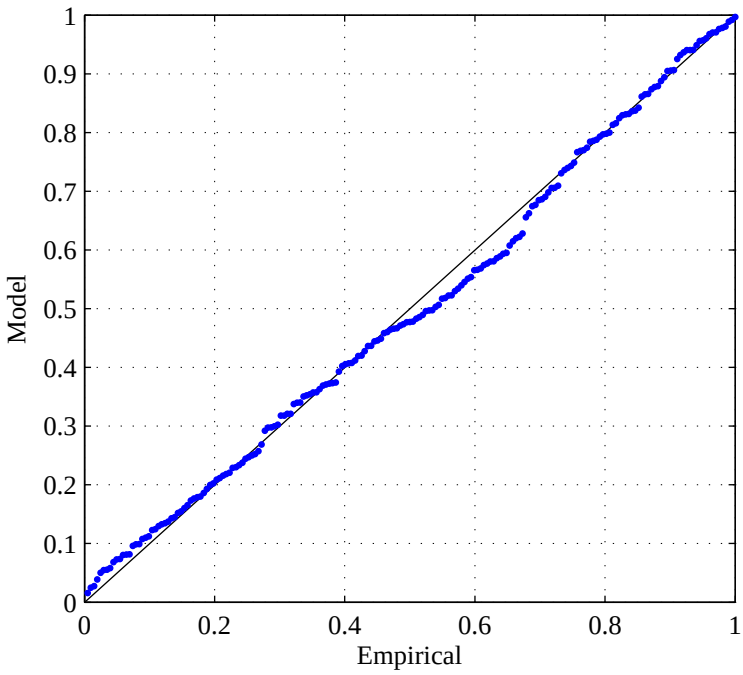

(a)

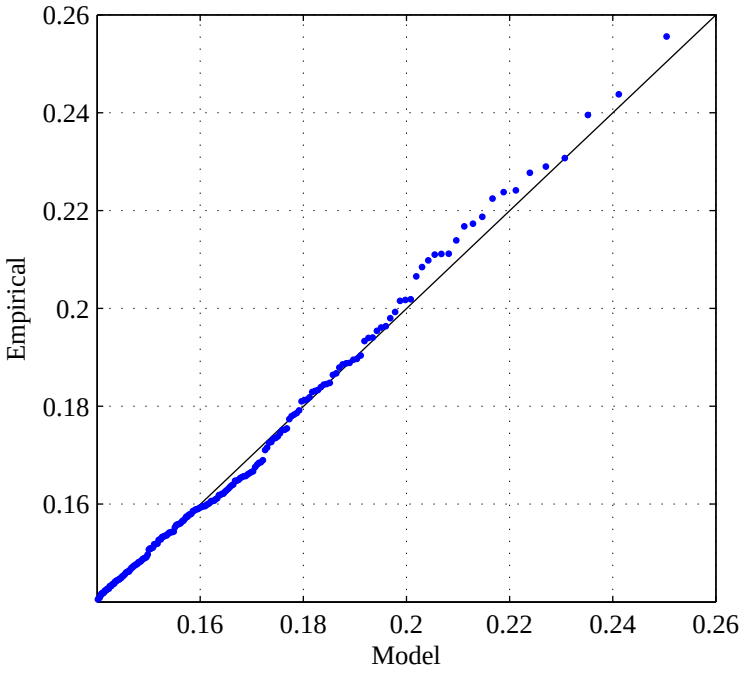

(b)

Figure 3.13: Diagnostic plots for GPD calculated for relative velocity perturbations measured using the ADV: T_a = 4.0s, x_t = 0.13, p = 0.05, r = 320.

ation. In this way the profile log-likelihood confidence interval offers a more realistic approximation of the expected errors and is used to calculate the confidence intervals of the maximum annual velocity perturbations in the extreme value analysis.

3.7.3 Return levels

The maximum relative velocity perturbations expected in a one-year return period were calculated for the range of averaging periods specified. The analysis was performed for the normalised longitudinal (u), transverse (v) and vertical (w) flow directions. The results of the one-year return level, with associated 95% log-likelihood confidence intervals are given in Figure 3.16.

The results obtained using the ADV data predict an annual maximum perturbation of 39% of the mean longitudinal flow speed for $T_a = 0.5$s, to within 95% confidence. This decreases to 29% for $T_a = 8$s. Identical results are obtained in the transverse direction using the ADV to within 1%. The use of ADCP data for the same analysis predicts relative longitudinal fluctuation of 89% when $T_a = 0.5$s, reducing to 46% when $T_a = 8$s. In the transverse direction, these values are seen to reduce slightly to 83% and 40%, when $T_a = 0.5$s and $T_a = 8$s, respectively.

In the vertical direction, the results of the extreme value analysis using the ADV data indicate a maximum annual relative velocity perturbation of 33% when $T_a = 0.5$s, again decreasing with an increasing averaging period. Unlike the horizontal flow perturbations, the analysis results obtained using the ADCP data indicate values less than that of the ADV for all averaging periods.

For the longitudinal direction, the length-scale averaging process was performed on the data, and the one-year return period calculated for the resulting time series. The results of this analysis for the range of averaging lengths considered is presented in Figure 3.17.

As with the time-scale averaging analysis, the results calculated using the ADV data are significantly less than those obtained using the ADCP measurements. At the effective averaging scale of $L_a = 1$m, the maximum annual relative velocity perturbations suggested in the ADV analysis is 36%, while the ADCP analysis results give a value of 90%. At the greatest averaging length-scale of $L_a = 8$m, these values calculated by the ADV and ADCP analysis are expected to decrease to 30% and 51%, respectively.

The magnitude of the one-year velocity perturbation is seen to decrease as the averaging time or length scale is increased. This is to be expected, as the averaging process decreases the variance

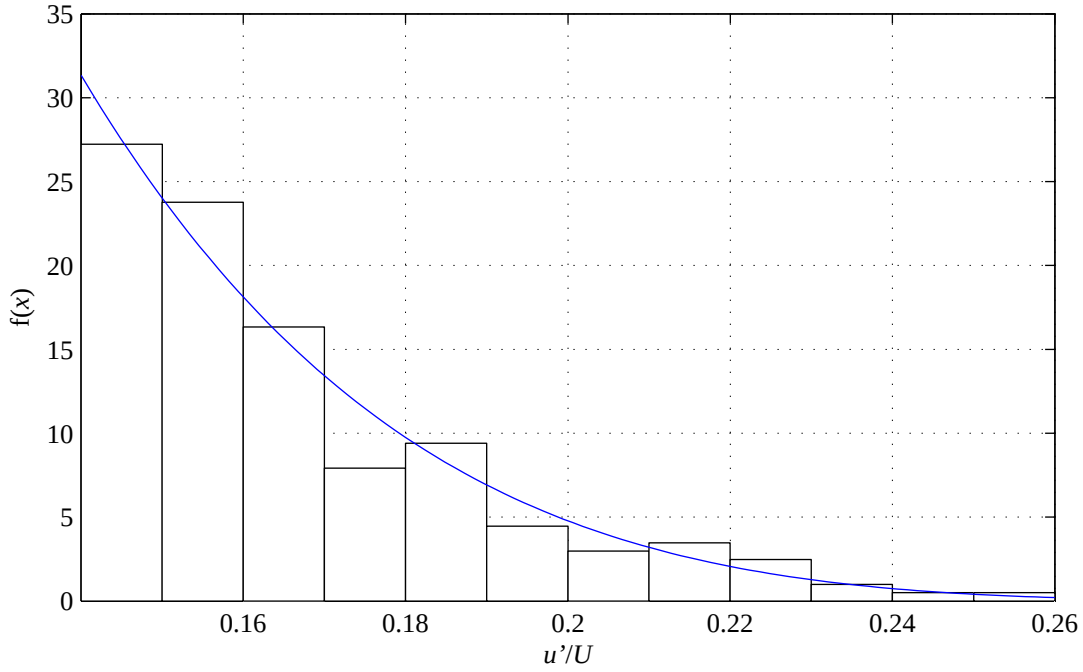

Figure 3.14: Diagnostic Plots for GPD calculated for ADV velocity perturbations: T_a = 4.0s, x_t = 0.13, p = 0.05, r = 320.

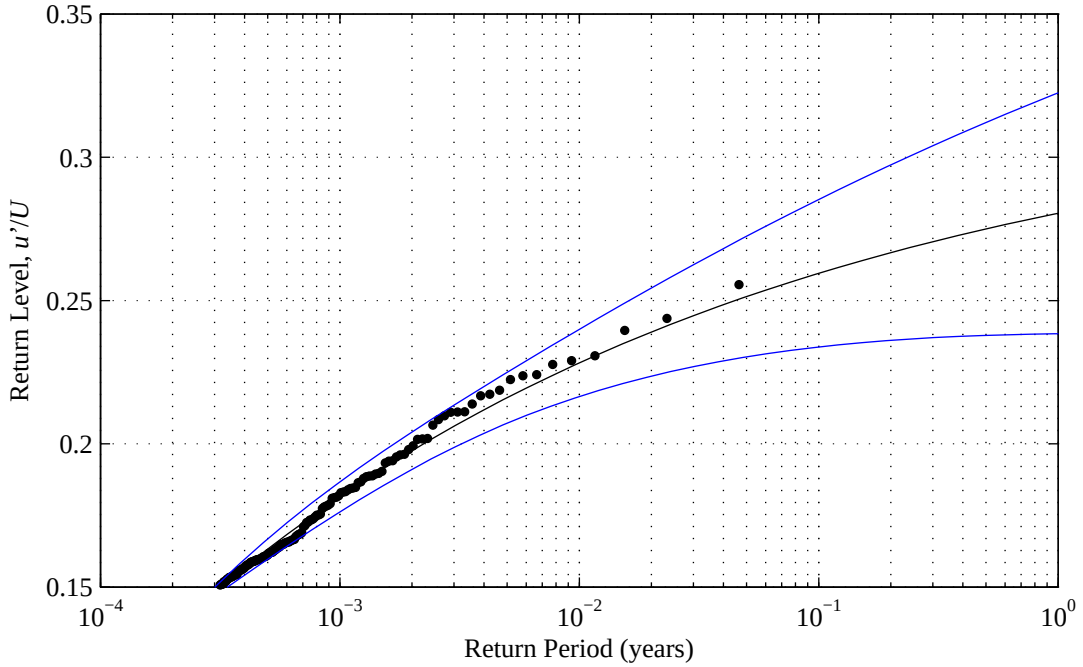

Figure 3.15: Sample Return Level plot for ADV perturbations: T_a = 4.0s, x_t = 0.13, p = 0.05, r = 320.

of the normalised velocity data set. The interpretation and comparison of the ADV and ADCP results are discussed in detail in §3.8.

3.7.4 Shape factor

The key similarity between all observations was the shape factor consistently being found to be a negative value. In accordance with Equation 3.2, the return level increases exponentially with the return period when $\xi > 0$, linearly when $\xi = 0$, and reaches an asymptotic limit when $\xi < 0$. In all extreme value analyses performed, $\xi < 0$, resulting in the asymptotic behaviour shown in Figure 3.15.

3.8 Discussion

3.8.1 Relative velocity perturbations in the horizontal direction

The results of the extreme value analysis using the ADCP velocity data are shown to significantly overestimate those derived from the ADV measurements for the normalised velocity perturbations in the horizontal direction. This is primarily due to the more significant Doppler noise in the ADCP measurement (Table 3.1). The maximum sampling frequency of the ADCP at 2Hz also contributes to the greater variance as fewer points are averaged for both the time and length scale analyses. With significantly less Doppler noise and greater sampling rates, the results of the analysis using the ADV data are taken as the benchmark of accuracy, and any discrepancy is attributed to these limitations of ADCP operation.

When the standard deviation of the velocity measurement is of interest, such as in the calculation of turbulence intensity, the distribution can be partially corrected for the standard error of the device as explained by Thomson *et al.* (2010). However, such a correction could not be implemented in this analysis where the individual instances of the velocity measurements were considered.

Both Figure 3.16 and Figure 3.17 show that the ADCP analysis significantly over-estimates the extreme value predictions beyond the confidence interval of the ADV analysis for all but the longest averaging scales in the horizontal directions. From this we can infer that the ADCP results are invalid with no statistical similarity to the ADV benchmark.

Doppler noise theoretically decreases as a function of $1/\sqrt{N_p}$, where N_p is the number of measurements used in the moving averaging, and this is responsible for the convergence of

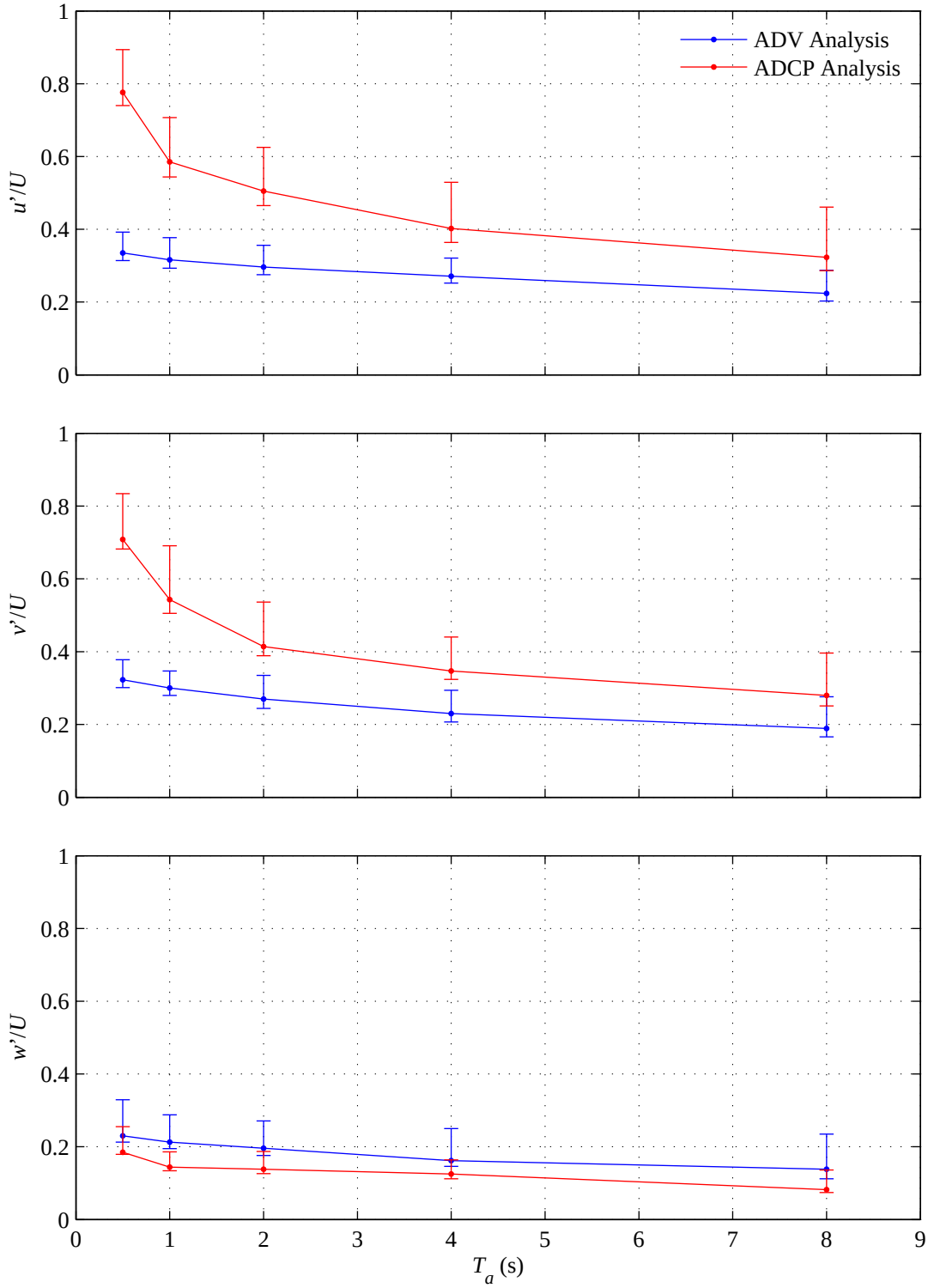

Figure 3.16: Effects of perturbation time-scale on the one-year velocity perturbation magnitude. The 95% confidence intervals calculated using the log-likelihood method are included.

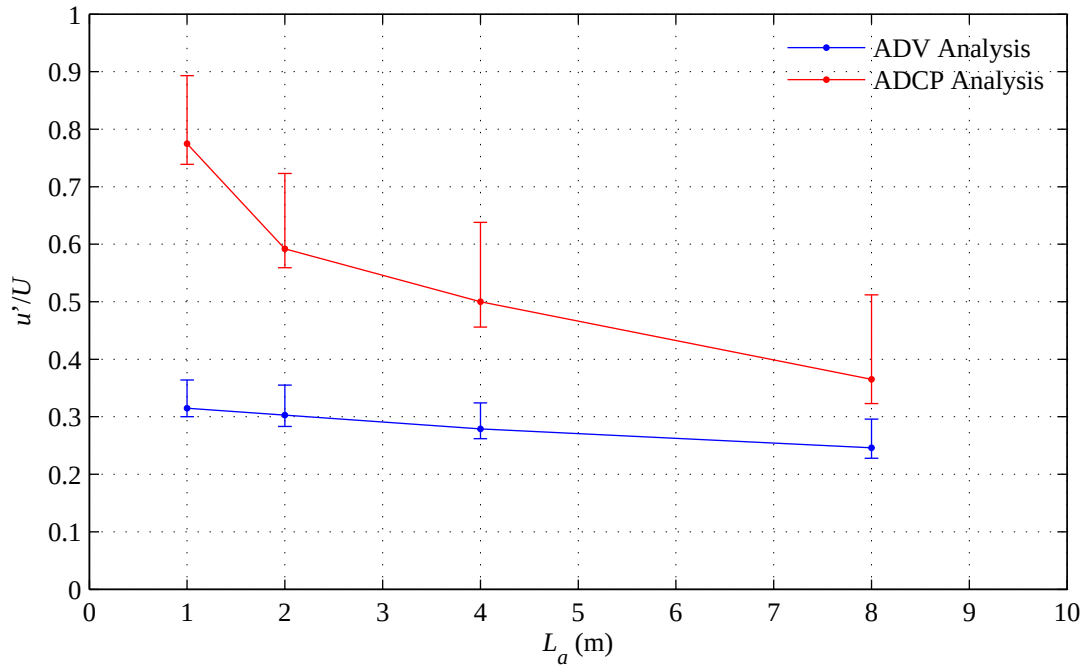

Figure 3.17: Effects of perturbation length-scale on the one-year velocity perturbation magnitude. The 95% confidence intervals calculated using the log-likelihood method are included.

results over longer time and length scales. The difference between the theoretical standard error of the ADCP and ADV is significant over all ensemble durations used in this analysis, as shown in Figure 3.18. While the averaging period of 8s results in a 75% reduction in Doppler noise relative to the 2Hz output ($N_p = 16$), this is still greater than that of the 32Hz ADV measurement without any averaging.

The increased range of the 95% confidence interval for the ADCP analysis is a result of having fewer data points available for the analysis, relative to the ADV. This is a result of both the lower ADCP sampling rates as well as fewer acquisition bursts per hour, as summarised in Table 3.1.

Interestingly, the differing beam configurations of the two devices act to decrease the velocity fluctuations of the ADCP relative to the ADV. As discussed in §3.3 the beams of an ADV are convergent to enable the velocity coordinates of a very small volume to be deduced. Conversely, the ADCP beams are directed in a diverging configuration. The underlying assumption of the ADCP is that the flow is homogeneous over the sample area, such that a velocity component measured by each beam in each different location can be transformed to calculate the velocity components of one location, notionally centralized above the ADCP device (RDI, 1996). As such, the velocity component measured in each bin is effectively averaged through the vector transformation process. Two beam velocities, transmitted from opposite sides the ADCP in-

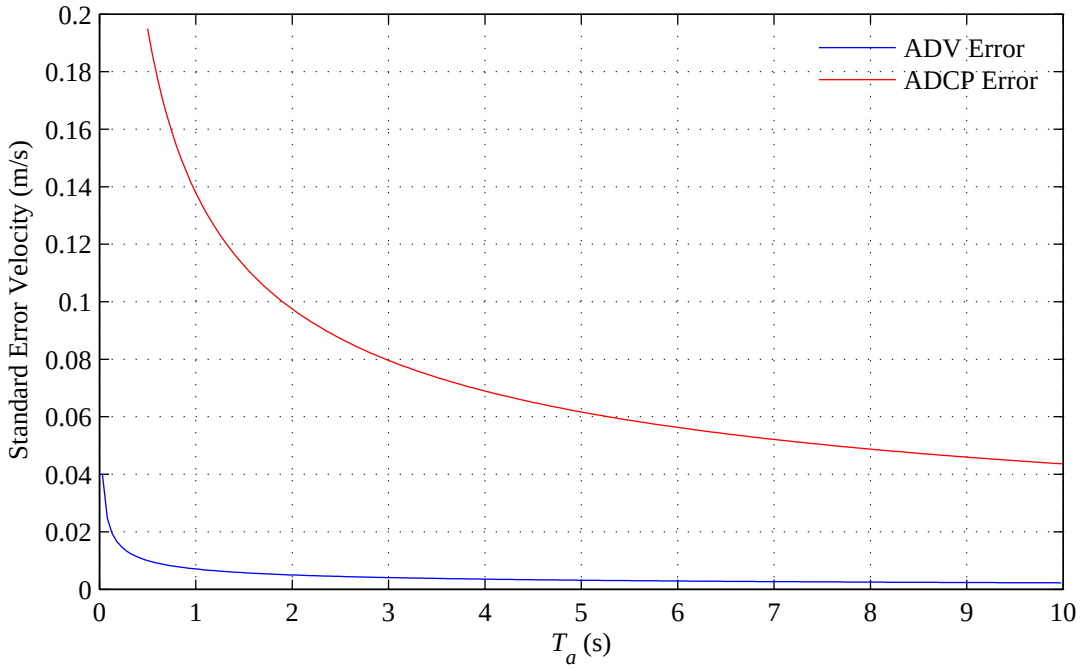

Figure 3.18: Influence of averaging period on theoretical standard error velocities due to Doppler noise for both the ADV and ADCP instruments used in the present analysis

strument, are used for the calculation of the horizontal velocity in the plane of the two beams. This has the effect of decreasing the measured velocity perturbations. In other words, without accounting for Doppler uncertainty, one would expect the ADV data to show stronger perturbations.

The range of results obtained in the analysis using length-scale averaging were very similar to those derived from time-scale averaging. The reason for this is that only values of $U \geq 1\text{m/s}$ were considered in the analysis, and the maximum mean flow speed recorded during the deployment was $U = 1.71\text{m/s}$. From Equation 3.9 it follows that the range of average periods corresponding to a particular averaging length is given by $0.59L_a \leq T_a \leq L_a$. As such, for the mean flow speeds available, the averaging length in meters and and averaging time period in seconds are similar.

3.8.2 Relative velocity perturbations in the vertical direction

The maximum expected relative velocity perturbations observed in the vertical direction were significantly less than those in the horizontal direction. The reason for such a result is a combination of flow characteristics and instrument alignment.

In a spectral analysis performed on the same data set as the present work, Thomson *et al.* (2012) identify three regions in the velocity spectra. At the lowest frequency the presence of large scale eddies are observed, and a Doppler noise floor is observed at the highest frequencies. In between these limits lies the inertial subrange where the spectra indicates isotropic energy cascade following the classical gradient of $f^{-5/3}$ (Taylor, 1937). Large scale eddies are suppressed in the vertical direction by the depth of the water column, which is a restriction not apparent to such flow perturbations in the horizontal direction. As such, for perturbation frequencies below the inertial subrange, the velocity perturbations are anisotropic. This observation can be used to explain the slight reduction in the maximum annual perturbations predicted by the ADV analysis, at the larger averaging periods.

However such anisotropic flow conditions are not expected at such high frequency perturbations as those represented by the shorter averaging periods. At such frequencies, a Doppler noise floor is observed in the horizontal flow direction which does not exist in the spectra of the vertical flow perturbations (Thomson *et al.*, 2012). The receivers of the Nortek Vector probe are angled at 30° off vertical and therefore the beam direction is more closely aligned in the vertical direction (Nortek AS, 2005). As such, the Doppler noise in this direction is lower than in the horizontal at the highest frequency fluctuations.

The beams of the ADCP are even more aligned with the vertical direction, at an angle of 20° off vertical (RDI, 1998). For the beam configuration of the RDI Workhorse Sentinel used to acquire the present data set, the vertical velocity time series is calculated using Equation 3.15 (RDI, 2010). In this equation, v_b represents the velocity in the direction of each of the four acoustic beams.

$$w = \frac{v_{b_1} + v_{b_2} + v_{b_3} + v_{b_4}}{4\cos(20°)} \tag{3.15}$$

This coordinate transformation effectively averages the vertical component of all four beam-wise velocity measurements. Even with the inadequacies of the instrument for high frequency measurements, this post-processing has the effect of significantly reducing the variance in the vertical velocity time series. As such the results of the maximum velocity perturbation using the ADCP data in the vertical direction are even less than those using the ADV. Again, this result is non-physical, but another limitation of the use of ADCP instruments for high frequency measurements. This effect is not so pronounced in the coordinate transformation to obtain horizontal velocity measurements, which uses only two beam velocities compared to the four used in the vertical case.

3.8.3 Duration of data set

The key limitation to this analysis is the length of data acquisition from both of the devices. Ideally, several years of data is required to perform the analysis for an extended return period and with a greater level of confidence.

However the present analysis offers useful indicators for expected velocity fluctuations, and a valuable starting point for ongoing analysis. With the recent increase of interest in instrumentation of tidally energetic sites for the application of tidal stream power, this may be a possibility in the future.

3.9 Chapter conclusions

This chapter presents an extreme value analysis of velocity perturbations at an energetic tidal site measured using both ADV and ADCP devices. The data set used was provided in a collaboration with the University of Washington and the Pacific Northwest National Laboratory, which allowed direct comparison between the measurements of an ADV and ADCP measurement bin at a location 4.8m above the seabed.

The extreme value analysis was performed by fitting a generalized Pareto distribution to exceedances of a specified relative velocity threshold. This POT methodology was selected as a means to make more efficient use of the limited data set than the classical GEV theory. The analysis was performed for the normalised velocity perturbations in the three orthogonal directions relative to the principal axis of the site: u'/U, v'/U and w'/U. The normalisation by the 64s mean longitudinal velocity was required in order to make the distribution of the velocity perturbation metric stationary throughout the tidal cycle. Due to the limitations in the duration of the data set, the return period of the analysis was selected as one year.

The data was filtered using a central moving average with a range of averaging durations from $T_a = 0.5$s to $T_a = 8$s. This process acts as a low-pass filter to remove higher frequency perturbations with periods greater than the averaging period. The results of the analysis performed using the ADV data predicted peak annual horizontal fluctuations of approximately 40% of the mean longitudinal flow velocity, to within 95% confidence. The anisotropy of the higher frequency perturbations is indicated by the lower peak fluctuation in the vertical direction. Longer averaging periods yielded lower return values as the higher frequency velocity perturbations (and Doppler noise) were filtered from the original data set.

The moving average filter was modified to average the velocity data in terms of a specified

length scale. This was implemented through the assumption that the velocity perturbations were of the frequency whereby they could be modelled as coherent motions advected at the mean flow speed. The results of this analysis indicated that a relative perturbation with a 1m length scale could be expected to be as high as 35%.

The results indicate large discrepancies between the measurements of the ADV, which are used as a benchmark, and that of the ADCP. This is primarily due to the increased Doppler noise of the ADCP readings in the horizontal direction, and the coordinate transformation process in the vertical direction. Such observations are important to recognize in a time when ADCP instruments are becoming increasingly popular for the measurement of flows in energetic tidal flows in the context of tidal stream power. While the assumptions required to measure the mean flow velocity are valid over long averaging periods, this data analysis highlights the risk of over-conservative design decisions if these instruments are used to quantify high frequency events in the time domain.

The limitations in the duration of presently available data for such an analysis have been identified. However this analysis provided useful indications of the potential magnitudes of the velocity perturbations within an energetic tidal flow. Such unsteady incident flow will result in appreciable dynamic drag loads on fastening structures installed in such conditions. The implications are perhaps greatest for the AGB concept, whereby the effective mass of the installation also becomes a dynamic quantity through the dependence of lifting surfaces subjected to the same flow conditions. The theoretical and experimental modelling of dynamic lift in response such unsteady flow conditions is investigated in the remainder of this thesis.

Chapter 4
Generating controllable velocity fluctuations using unsteady lift theory

4.1 Introduction

Unsteady structural responses due to dynamic flow conditions are important to a range of engineering applications, and generating such flow conditions in the laboratory enables the dynamic loads to be measured experimentally. In the context of AGB performance modelling, the dynamic lift of the hydrofoils in response to fluctuations in incident flow velocity is of paramount importance. Therefore controlling the behaviour of the time-varying fluid velocity in an experimental facility becomes a prerequisite challenge.

While some experimental methods elect to introduce relative motion between the fluid and structure by studying a moving body in a steady flow environment, this does not capture the effects of flow variations with length-scales less than that of the body. These effects constitute an important part of the diminishing aerodynamic admittance function[1] at high frequencies (Sears, 1941; Liepmann, 1952). In response, this chapter examines a laboratory set-up which will allow the user to generate pre-defined flow fluctuations in the longitudinal and vertical direction at a specific test location. This configuration has previously been shown to be effective in creating sinusoidal variations in vertical flow velocities (Tang *et al.*, 1996; Passmore *et al.*, 2001), however this chapter demonstrates the ability to reproduce an aperiodic predetermined velocity time series through the use of two oscillating lifting surfaces. Such a facility allows real tidal stream velocity measurements to be represented in a controlled environment to enable the improved experimental testing of unsteady response characteristics.

Finally, the theory of unsteady lift on a stationary lifting surface in response to longitudinal and vertical flow fluctuations is introduced. This theory is implemented in Chapter 6 in a comparison with the dynamic loads measured experimentally on a stationary wing in an unsteady velocity field.

[1] In unsteady aerodynamics, the admittance function describes the transfer function which relates the fluctuating velocity to the resulting unsteady loads in the frequency domain. The indicial admittance function refers to the force response to a step change in velocity conditions in the time domain.

The theory for generating controllable two-dimensional velocity time series, as developed in this chapter, has been reported in the Journal of Fluid Mechanics (Harding and Bryden, 2012c). The manuscript of this publication is included in Appendix B.

4.2 Review of experimental gust generation

The generation of unsteady incident flow conditions in aero/hydrodynamic experimentation has been a subject of wide research in response to its vast range of applications including both fixed and rotary wing flight, turbo-machinery and long span bridges. As a result, the task of generating dynamic inflow in laboratory experiments has seen a range of solutions over the past 50 years.

Perhaps the most elementary method is the introduction of static bluff bodies upstream of the test section to create large scale eddy structures in the flow. Examples of such configurations are the Counihan spires, roughness elements and turbulence generating grids (Lamson, 1957; Counihan, 1967). For such configurations, the magnitude of the flow fluctuations is governed by the geometry of the bluff bodies and the velocity of the flow. More recently, active turbulence generators have been developed to generate large scale turbulence using an upstream 'active grid' of many independently controlled flaps (Makita, 1991; Mydlarski and Warhaft, 1996).

A novel method of generating sinusoidal flow oscillations was designed by Holmes (1970) using flexible walls connected to a series of cams and springs. This apparatus was also used by Horlock (1974), and while it was able to generate a range of gust conditions and frequencies, an inherent fluctuation in the free-stream velocity was also observed.

The use of twin pitching lifting surfaces for the independent generation of oscillatory perturbations in longitudinal and vertical velocities was originally proposed by Ham *et al.* (1974) who describe a method which uses elliptical lifting surfaces with a jet slot in the trailing edge to alter the circulation about the foil in air. The direction of the jet is controlled by a cam in a round plenum at the aft of the lifting surface. Perturbations of up to 20% of the free-stream velocity of the air have been achieved using a similar method of gust generation (Jancauskas and Melbourne, 1980). Subsequently, pitching hydrofoils have been introduced to generate gusts in a single direction in wind tunnels (Tang *et al.*, 1996; Passmore *et al.*, 2001) and at high reduced frequencies in a water flume (Delpero, 1992; Horwich, 1993). A schematic diagram of the twin foil configuration used to generate longitudinal and vertical velocity perturbations is shown in Figure 4.1.

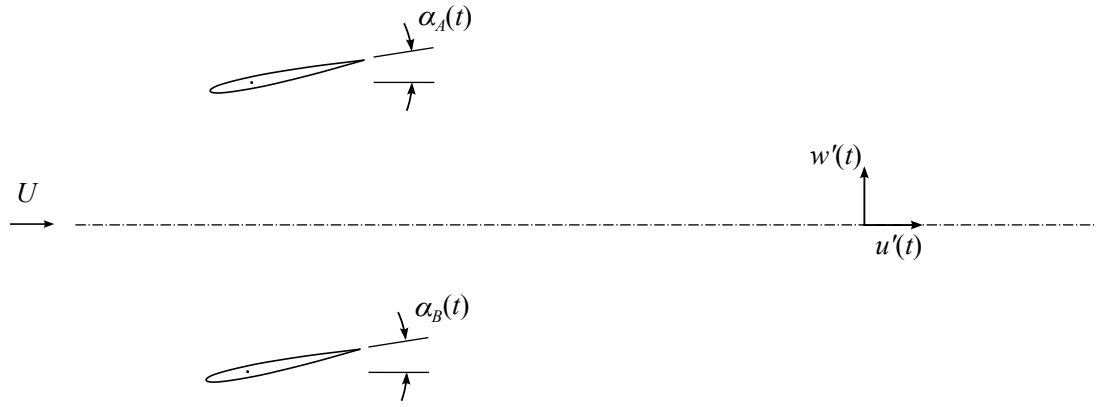

Figure 4.1: Schematic diagram of twin pitching foils to generate downstream velocity perturbations

The benefit of using two independently-controlled oscillating foils is that the perturbations can be generated in the longitudinal direction, x, and vertical direction, z, independently along the plane of symmetry between the foils. When the hydrofoil motion is harmonic, the motion of Foil A is denoted $\alpha_A = \alpha_0 e^{i\omega t}$ and that of Foil B is $\alpha_B = \alpha_0 e^{i(\omega t+\varphi)}$. If the two foils are oscillating in phase ($\varphi = 0°$), the longitudinal components of the induced velocity, u', cancel along the plane of symmetry between the two foils while the vertical components, w', are additive. When the foils are oscillating out of phase ($\varphi = 180°$), the w' components of the perturbations cancel along the plane of symmetry, and the u' components are additive (Ham *et al.*, 1974). A phase difference of $0° < \varphi < 180°$ will result in both a longitudinal and vertical perturbation, with relative magnitudes dependent on the phase.

This chapter presents a numerical model which allows the velocity perturbations to be calculated for a given time series of foil motions. This model is then manipulated to allow the reverse problem to be solved, such that the required time series of foil motions to generate a specified velocity time series can be calculated. The model is validated against existing experimental results, and the output of the reversed process is demonstrated for a range of combinations of longitudinal and vertical velocity fluctuations.

4.3 Quasi-steady circulation about a pitch-controlled hydrofoil

For incompressible attached flow over a fixed lifting surface, classical airfoil theory can be used to calculate the lift force per unit span of a hydrofoil through Equation 4.1. The Kutta-

Joukowski theorem relates the lift to the bound circulation of the lifting surface through the relationship $\Gamma_b = L/\rho U$.

$$L = \frac{1}{2}\rho U^2 C_L c \tag{4.1}$$

In the quasi-steady case, the lift coefficient, C_L, is a function of the instantaneous angle of attack, α, as shown in Equation 4.2. Here the lift-curve slope is defined as $C_{L\alpha} = \mathrm{d}C_L/\mathrm{d}\alpha$ and is constant for angles of attack less than the stall angle of the lifting surface.

$$C_L = C_{L\alpha}\alpha \tag{4.2}$$

If the lifting surface is allowed to pitch, the lift force on the foil and the bound circulation varies as a function of time. Lord Kelvin, representing the law of conservation of angular momentum, stated that the time rate of change of circulation around a closed curve is zero in an inviscid fluid (Thomson, 1869). This can be stated mathematically by Equation 4.3, where Γ_w represents the total circulation in the wake (Katz and Plotkin, 2001).

$$\frac{\mathrm{d}\left(\Gamma_b + \Gamma_w\right)}{\mathrm{d}t} = 0 \tag{4.3}$$

Considering a discretized vortex model, the change in the bound circulation over a discrete time step must be accompanied by a vortex with an equal and opposite circulation being released into the wake. The circulation released from the trailing edge of the foil into the wake at each time step is therefore $\Gamma_w(t) = \Gamma_b(t - \Delta t) - \Gamma_b(t)$, as shown in Figure 4.2.

4.4 Unsteady circulation about a pitch-controlled hydrofoil

In reality the lift coefficient does not instantaneously respond to a change in angle of attack to the value indicated by Equation 4.2, but rather increases to the quasi-steady value as the bound circulation develops (Garrick, 1938). The available literature and approaches to the computation of unsteady lift are applicable to a range of applications including aircraft (fixed wing and rotary wing) and turbo-machinery.

Seminal research on the topic was performed for the development of circulation about a wing

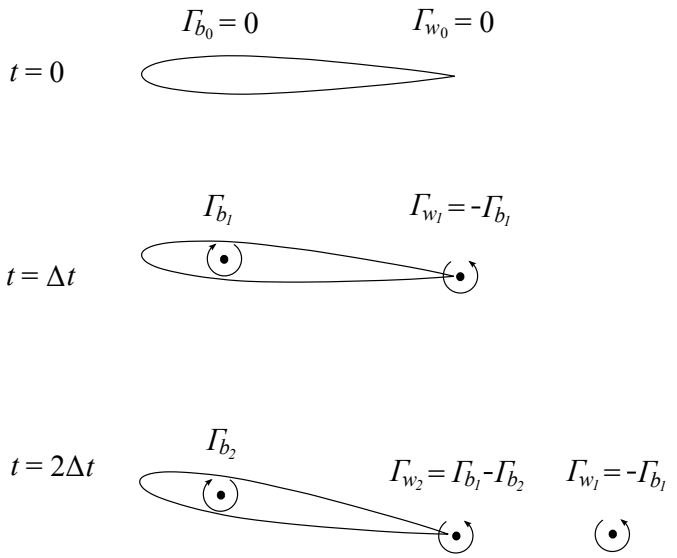

Figure 4.2: Discrete vortex model for a pitching lifting surface for the first two time steps. The vortex distribution over the chord length of the foil is represented as a single vortex at the quarter-chord location.

in response to step change in longitudinal velocity by Wagner[2] (1925). Later, Theodorsen (1935) explored the dynamic response of circulation about a sinusoidally pitching foil. A third fundamental case was explored by Küssner[2] (1936) who presented the growth of lift as a lifting surface penetrates into a step change in vertical velocity. These solutions are based on two-dimensional potential flow theory.

Other significant contributions to the theoretical understanding of unsteady lift were made by Sears (1941), Kemp (1952) and Horlock (1968).

The potential flow theories for unsteady lift can be divided into the two broad categories of frequency domain and time domain solutions. For the purpose of this analysis, the theoretical solutions to unsteady lift in the time domain have been used for the ease of calculation in response to an arbitrary velocity time series. Also the measure of forcing frequency becomes an ambiguous parameter when the longitudinal velocity is unsteady (Leishman, 2002).

In the time domain, the transient development of circulation about a foil in unsteady flow or undergoing unsteady motion itself can be accounted for by calculating the 'effective' angle of attack, α_e. This represents the equivalent quasi-steady angle of attack that provides the instantaneous lift coefficient experienced. The effective angle of attack can then be used in

[2] An explanation of the original German publication is presented in English by Garrick (1938)

the quasi-steady calculation of the bound circulation of the foil through the Kutta-Joukowski theorem.

The superposition of lift concept, explained by Jones (1938), describes how the circulation about a foil in general motion can be calculated by summing the step responses from each time step. For example, a step change in angle of attack results in a transient change in lift coefficient which develops to the quasi-steady value over time. The change in lift coefficient in response to subsequent changes in angle of attack during this settling time are combined in an additive manner to calculate the total change in lift coefficient. In this way, the unsteady lift of a foil undergoing an arbitrary pitch motion can be modelled in the time domain as the superposition of responses to a series of step changes in angle of attack.

4.4.1 Reduced frequency

The frequency of oscillation of the driving hydrofoils is expressed using the dimensionless value of 'reduced frequency', k, defined by Equation 4.4, where the angular frequency of the oscillations is defined as $\omega = 2\pi/T$.

$$k = \frac{\omega c}{2U} \tag{4.4}$$

This metric is proportional to the ratio of the chord length, c, to the length-scale of the perturbation given by UT.

4.4.2 Reduced time

The time domain solutions to unsteady aerodynamics are herein presented in terms of 'reduced time', defined by Equation 4.5 (Leishman, 2002).

$$s = \frac{1}{b}\int_0^t U \mathrm{d}t \tag{4.5}$$

This parameter can be considered as the distance travelled by the flow, normalised by the semi-chord, $b = c/2$. For a steady flow velocity, this expression can be simplified to $s = Ut/b$.

4.4.3 The Wagner function

The Wagner function, ϕ, describes the transient development of circulatory lift over an airfoil at a small angle of attack, instantaneously moving from stationary to a steady flow speed (Wagner, 1925; Garrick, 1938). This scenario is considered as being synonymous with a step change in angle of attack at a steady flow speed (Leishman, 2006). The resulting function modifies the geometric 'actual' angle of attack, α_a, in the calculation of the quasi-steady lift coefficient, as shown by Equation 4.6. The effective angle of attack can be expressed as $\alpha_e(s) = \alpha_a\phi(s)$. Applying thin airfoil theory on a two-dimensional lifting surface gives a theoretical lift curve slope of $C_{L\alpha} = 2\pi$.

$$C_L(t) = C_{L\alpha}\alpha_a\phi(s) \tag{4.6}$$

The exact solution to the Wagner function, $\phi(s)$, can be expressed in terms of Bessel functions of the first and second kind (Bisplinghoff *et al.*, 1996; Peters, 2008). However Jones (1940) presents a useful approximation of the function for a two dimensional wing in the exponential series of Equation 4.7. A comparison of the exact and approximate solution to the Wagner function is presented in Figure 4.3.

$$\phi(s) \approx 1.0 - 0.165e^{-0.045s} - 0.335e^{-0.300s} \tag{4.7}$$

Note that 50% of the final circulatory lift is achieved instantaneously, before gradually developing to 90% of the steady state value after the foil has traversed eight chord lengths.

4.4.4 The Küssner function

The Küssner function describes the growth of lift on a lifting surface as it penetrates into a vertical step gust. Defining the vertical gust with constant vertical velocity, w_0, the change in lift as a function of reduced time is defined by Equation 4.8 (Garrick, 1938). Here an apparent angle of attack is formed by the vertical velocity component such that $\alpha_a = w_0/U$. The effective angle of attack can then be expressed as $\alpha_e(s) = \alpha_a\psi(s)$.

$$C_L(t) = C_{L\alpha}\frac{w_0}{U}\psi(s) \tag{4.8}$$

As with the Wagner function, while an exact solution exists, the exponential approximation of

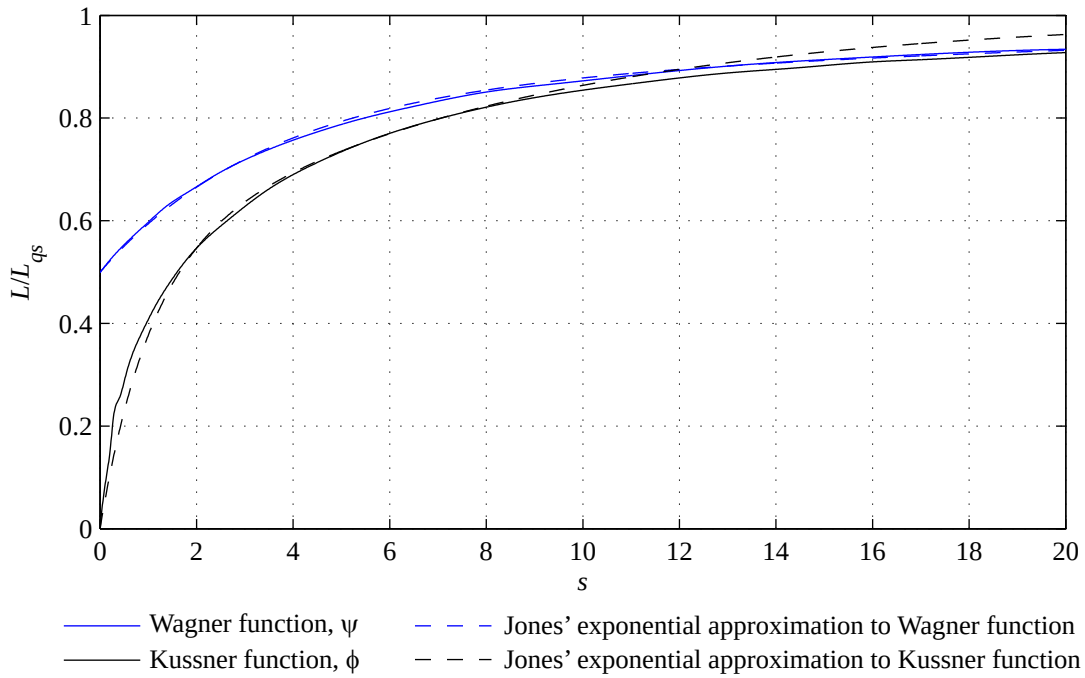

Figure 4.3: Küssner and Wagner functions with exponential approximations given by Jones (1940) for the development of circulatory lift.

Equation 4.9 is much more suitable to the following analysis (Bisplinghoff *et al.*, 1996). The exact solution and the exponential approximation to the Küssner function are compared with the Wagner function in Figure 4.3.

$$\psi(s) \approx 1 - 0.500^{-0.130s} - 0.500^{-s} \tag{4.9}$$

The Küssner function models the penetration phenomenon, where the effect angle of attack on the foil varies along the chord while it enters into the step gust. This explains why the $\psi(0) = 0$ as the wing begins to enter the gust, compared to the instantaneous value of $\phi(0) = 0.5$ for the Wagner function. The latter case is due to the entire chord being instantaneously subjected to a step change in angle of attack.

4.4.5 The Duhamel integral

Utilizing the principle of superposition of lift described earlier, the response to an arbitrary driving force can be calculated from a known indicial admittance function through the Duhamel integral (Bisplinghoff *et al.*, 1996). This integral allows the temporal response, $y(t)$, to a system

with an indicial admittance function, $A(t)$, under the generalized forcing function, $f(t)$, to be calculated by Equation 4.10 (Bisplinghoff *et al.*, 1996). Here τ is used as a time interval of integration.

$$y(t) = f(0)A(t) + \int_0^t \frac{\mathrm{d}f(\tau)}{\mathrm{d}\tau} A(t-\tau)\mathrm{d}\tau \tag{4.10}$$

When the forcing term is the effective lift coefficient such that $f(t) = C_{L\alpha}\alpha_e(s)$, and the indicial admittance function of either the Wagner or Küssner function is defined as $A(t) = \Omega(s)$, the unsteady effect on the circulatory term of the lift coefficient under arbitrary pitch motion can be described by Equations 4.11.

$$C_L(t) = C_{L\alpha}\alpha_e(s) \tag{4.11a}$$

$$\alpha_e(s) = \alpha_a(0)\Omega(s) + \int_0^s \frac{\mathrm{d}\alpha_a(\tau)}{\mathrm{d}\tau} \Omega(s-\tau)\mathrm{d}\tau \tag{4.11b}$$

The calculation of the unsteady lift coefficient is made more simple by using the exponential approximation of the Wagner and Küssner functions, which allows the 'recurrence solution' of the Duhamel integral to be implemented. If the indicial admittance term is expressed in the form of Equation 4.12, the effective angle of attack can be solved using the one-step recursive solution of 'Algorithm D-1' described by Equation 4.13 (Leishman, 2006).

$$\Omega(s) = 1 - A_1\mathrm{e}^{-b_1 s} - A_2\mathrm{e}^{-b_2 s} \tag{4.12}$$

$$\alpha_e(s) = \alpha_a(s) - X(s) - Y(s) \tag{4.13a}$$

$$X(s) = X(s-\Delta s)e^{-b_1\Delta s} + A_1\left[\alpha_a(s) - \alpha_a(s-\Delta s)\right] \tag{4.13b}$$

$$Y(s) = Y(s-\Delta s)e^{-b_2\Delta s} + A_2\left[\alpha_a(s) - \alpha_a(s-\Delta s)\right] \tag{4.13c}$$

Leishman (2006) presents Equation 4.14 to calculate the error for this approach, and recommends that the time increment of the solution be selected such that both $b_1\Delta s$ and $b_2\Delta s$ are less than 0.05.

$$\epsilon = 2 - \frac{b_1\Delta s}{1-e^{-b_1\Delta s}} - \frac{b_2\Delta s}{1-e^{-b_2\Delta s}} \tag{4.14}$$

4.4.6 Verification of unsteady lift calculation

To verify the approach described above, the response given by Equation 4.13 has been used to calculate the unsteady lift coefficient for two cases of variation in angle of attack. For this case, the Wagner function is used.

Firstly, a step change in angle of attack from $\alpha_a = 0°$ to $\alpha_a = 5°$ was simulated for a foil with a lift curve slope of $C_{L\alpha} = 2\pi$. The quasi-steady lift coefficient is calculated using the instantaneous angle of attack in Equation 4.2. This is compared with the effective lift coefficient, calculated by substituting Equation 4.13 into Equation 4.11a, in Figure 4.4a. This case represents the response to a single step change in angle of attack, which is the original scenario modelled by the Wagner function. Therefore, as expected, the result using the Duhamel integral agreed exactly with the input equation of Equation 4.7. This verifies the implementation of Algorithm D-1 to solve the Duhamel integral.

The angle of attack of the same foil was then simulated using an arbitrary time series constructed from five harmonic components. In this case, each time step represents a new step change in the angle of attack. The superposition of the time history of the motion is taken into account by the recursive solution of the Duhamel integral. Due to the transient development of circulation about an unsteady foil, a deficit can be seen between the quasi-steady and unsteady solutions, shown in Figure 4.4b. This plot demonstrates the flexibility of the solution which enables it to be used to calculate the unsteady lift coefficient for a wide range of motion time series.

4.5 Discrete vortex model of pitching hydrofoil wakes

A vortex model of the wakes of the twin pitching foils was used to calculate the induced velocity at a location on the plane of symmetry between them. This section describes the development of this model to calculate a velocity time series downstream of the foils for a known time series of foil pitch motion.

4.5.1 Induced velocity of a series of point vortices

A point vortex with circulation, Γ (m^2/s), acting at coordinates (x,y) can be shown to induce the radial and tangential components of velocity at point $P(X, Z)$ given in Equation 4.15. In this analysis a positive circulation is defined in the clockwise direction in the x-z plane, in accordance with the right-hand convention, as per Figure 4.5.

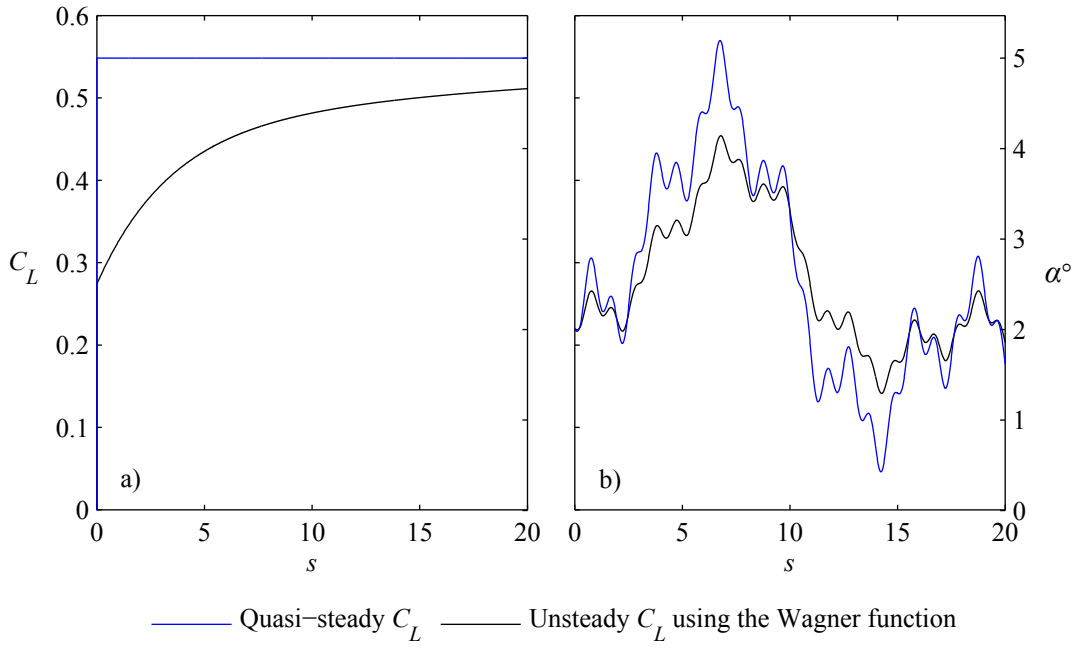

Figure 4.4: Comparison of quasi-steady lift coefficient to the effective lift coefficient resulting from the solution to the Duhamel integral using the Wagner function. The equivalent actual and effective angle of attack is shown on the adjacent axis. This comparison has been performed for a) a step change in angle of attack and b) an arbitrary fluctuation in angle of attack.

$$q_R = 0 \tag{4.15a}$$

$$q_\theta = \frac{-\Gamma}{2\pi R} \tag{4.15b}$$

The tangential component of induced velocity can be decomposed into Cartesian components given by Equation 4.16.

$$u' = -q_\theta \sin(\theta) \tag{4.16a}$$

$$w' = q_\theta \cos(\theta) \tag{4.16b}$$

Letting $\sin(\theta) = (Z - z)/R$ and $\cos(\theta) = (X - x)/R$, Equation 4.16 can be expressed by Equation 4.17, where $R^2 = (X - x)^2 + (Z - z)^2$.

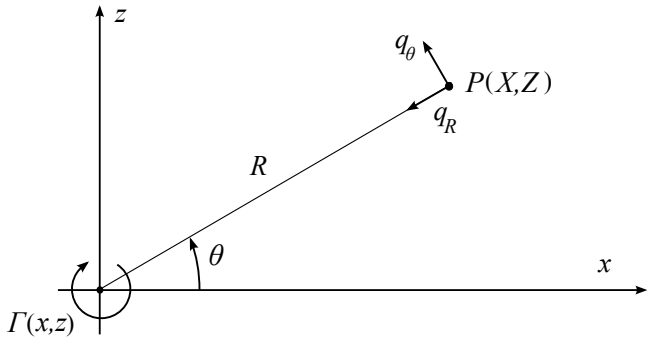

Figure 4.5: Schematic of notation used in potential flow model

$$u' = \frac{\Gamma\,(Z - z)}{2\pi R^2} \tag{4.17a}$$

$$w' = \frac{-\Gamma\,(X - x)}{2\pi R^2} \tag{4.17b}$$

4.5.2 Induced velocity of a single wake

The circulation in the wake of a single oscillating lifting surface in uniform flow is now considered. The following assumptions are made in the approached described in this section:

1. The lifting surface is modelled as a flat plate undergoing low angle pitch oscillations about the quarter chord location.
2. The vorticity shed to the wake from the trailing edge of the hydrofoil is advected along a horizontal line at the velocity of the free stream flow (planar wake assumption).
3. The location of the specified velocity time series is at a sufficient distance from the foils that the bound circulation is assumed to have negligible influence.
4. The Kutta condition applies at all times.
5. The wake vorticity is modelled as a two-dimensional situation.
6. The model is developed using an unbounded flow assumption.

Away from the bound vorticity at the oscillating foil itself, the wake is modelled as a sheet of discrete vortices. The single point model can be extended to calculate the velocity induced

by a series of point vortices at locations (x_j, y_j), where $j = \{1, 2, \ldots, M\}$. The combined influence of this series of point vortices can be solved for a range of locations (X_i, Z_i), where $i = \{1, 2, \ldots, N\}$, by summing the contributions to the induced velocity components from all the M point vortices. Letting $R_{ij}^2 = (X_i - x_j)^2 + (Z_i - z_j)^2$, this summation is shown in Equation 4.18.

$$u_i' = \frac{1}{2\pi} \sum_{j=i}^{M+i-1} \frac{\Gamma_j \left(Z_i - z_j\right)}{R_{ij}^2} \tag{4.18a}$$

$$w_i' = \frac{1}{2\pi} \sum_{j=i}^{M+i-1} \frac{-\Gamma_j \left(X_i - x_j\right)}{R_{ij}^2} \tag{4.18b}$$

The influence of the vorticity is inversely proportional to the distance to the point of influence, R. As such, the range of vortices included in the summation of the vortex model is not required to extend to infinity, but can be truncated to include a finite M points.

At each time step a vortex is shed from the pitching foil and is advected downstream at the constant free-stream velocity. As such, the time domain can be represented in the spatial domain where $\Delta x = U\Delta t$, as the self-induced velocity of the wake is neglected. In this way, the velocity time series at a single location can be solved in the spatial domain at a single instant in time, as shown in Figure 4.6.

4.5.3 Induced velocity of two parallel wakes

Introducing a second vortex series in parallel with the original allows the vertical and longitudinal flow velocity to be controlled independently. Defining the upper foil as Foil A and the lower as Foil B, the configuration of the twin oscillating foils is shown in Figure 4.7.

Recalling that the vorticity is defined as positive in the clockwise direction, it can be seen that the component of induced velocity in the longitudinal direction, u', is always negative from vortices in the wake of Foil A ($u_A' < 0$) and always positive from that of Foil B ($u_B' > 0$). As such, the magnitude of the perturbation in the longitudinal velocity is effectively controlled by the difference between the wake vorticity of Foil A and Foil B, such that u' is a function of $(\Gamma_B - \Gamma_A)$.

Furthermore, it can be seen that Foil A and Foil B have an additive effect on the induced velocity in the vertical direction, w'. The direction of this velocity is positive when $x > X$ and negative

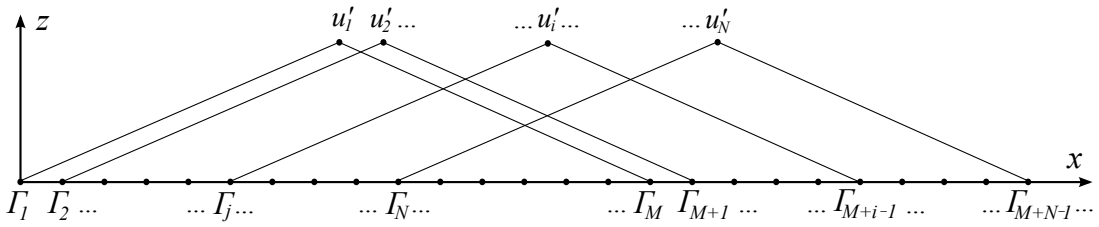

Figure 4.6: Schematic of vorticity notation for finite summation

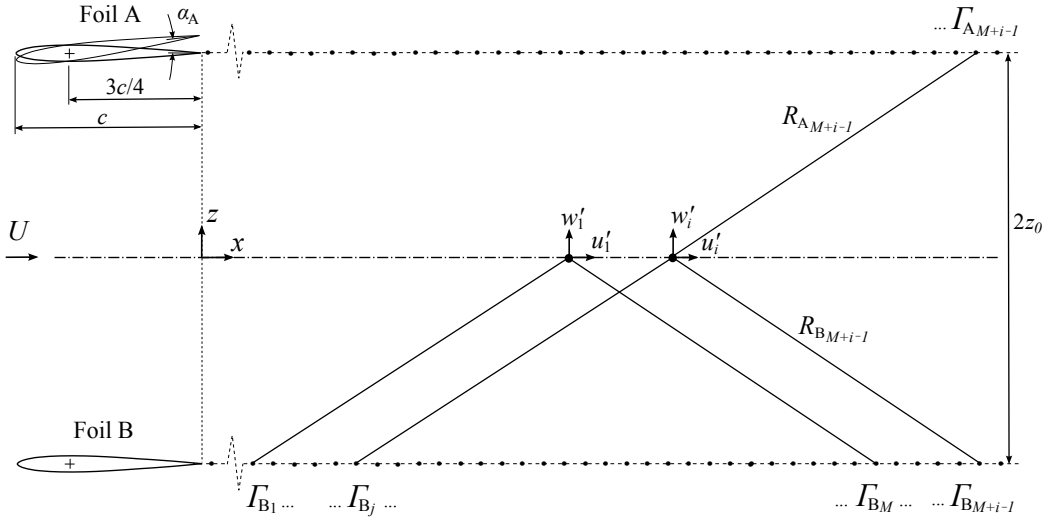

Figure 4.7: Schematic of velocity contributions from two parallel hydrofoils

when $x < X$. As such, the magnitude of the perturbation in the vertical velocity is effectively controlled by the sum of the wake vorticity of Foil A and Foil B, such that w' is a function of $(\Gamma_A + \Gamma_B)$.

The combined effect of Γ_{A_j} and Γ_{B_j} on the induced velocity at location i, is summarized by Equation 4.19.

$$u'_i = \frac{1}{2\pi} \sum_{j=i}^{M+i-1} \frac{\Gamma_{A_j}\left(Z_i - z_{A_j}\right)}{r_{ij}^2} + \frac{1}{2\pi} \sum_{j=i}^{M+i-1} \frac{\Gamma_{B_j}\left(Z_i - z_{B_j}\right)}{r_{ij}^2} \tag{4.19a}$$

$$w'_i = \frac{-1}{2\pi} \sum_{j=i}^{M+i-1} \frac{\Gamma_{A_j}\left(X_i - x_{A_j}\right)}{r_{ij}^2} - \frac{1}{2\pi} \sum_{j=i}^{M+i-1} \frac{\Gamma_{B_j}\left(X_i - x_{B_j}\right)}{r_{ij}^2} \tag{4.19b}$$

By locating the origin of the (x, z) coordinate system on the plane of symmetry between the two foils, the magnitude of the z-ordinate of circulation can be defined as half the vertical distance between the two foils, z_0, such that $z_{A_j} = z_0$, $z_{A_j} = -z_0$ and $Z_i = 0$.

Letting the effect of the configuration dimensions be summarised by the 'geometric influence factors' of $f_{ij} = z_0/2\pi\left[z_0^2 + (X_i - x_j)^2\right]$ and $g_{ij} = -(X_i - x_j)/2\pi\left[z_0^2 + (X_i - x_j)^2\right]$, Equation 4.19 can be expressed by Equation 4.20.

$$u'_i = \sum_{j=i}^{M+i-1} f_{ij}\left(\Gamma_{B_j} - \Gamma_{A_j}\right) \tag{4.20a}$$

$$w'_i = \sum_{j=i}^{M+i-1} g_{ij}\left(\Gamma_{A_j} + \Gamma_{B_j}\right) \tag{4.20b}$$

These equations can be expressed using the matrix notation of Equation 4.21.

$$\boldsymbol{u'} = \boldsymbol{f}\left(\boldsymbol{\Gamma_B} - \boldsymbol{\Gamma_A}\right) \tag{4.21a}$$

$$\boldsymbol{w'} = \boldsymbol{g}\left(\boldsymbol{\Gamma_A} + \boldsymbol{\Gamma_B}\right) \tag{4.21b}$$

The expanded form of these matrices, as implemented in the numerical model, is given in Equation 4.22.

$$\begin{bmatrix} u'_1 \\ u'_2 \\ u'_3 \\ \vdots \\ u'_i \end{bmatrix} = \begin{bmatrix} f_{1,1} & f_{1,2} & \dots & f_{1,M} & 0 & \dots & 0 & 0 & 0 \\ 0 & f_{2,2} & f_{2,3} & \dots & f_{2,M+1} & 0 & \dots & 0 & 0 \\ 0 & 0 & f_{3,3} & f_{3,4} & \dots & f_{3,M+2} & 0 & \dots & 0 \\ \vdots & \vdots & \vdots & \vdots & \vdots & \vdots & \vdots & \vdots & \vdots \\ 0 & 0 & \dots & 0 & 0 & f_{i,i} & f_{i,i+1} & \dots & f_{i,j} \end{bmatrix} \begin{bmatrix} \Gamma_{B_1} - \Gamma_{A_1} \\ \Gamma_{B_2} - \Gamma_{A_2} \\ \Gamma_{B_3} - \Gamma_{A_3} \\ \vdots \\ \Gamma_{B_j} - \Gamma_{A_j} \end{bmatrix} \tag{4.22a}$$

$$\begin{bmatrix} w'_1 \\ w'_2 \\ w'_3 \\ \vdots \\ w'_i \end{bmatrix} = \begin{bmatrix} g_{1,1} & g_{1,2} & \dots & g_{1,M} & 0 & \dots & 0 & 0 & 0 \\ 0 & g_{2,2} & g_{2,3} & \dots & g_{2,M+1} & 0 & \dots & 0 & 0 \\ 0 & 0 & g_{3,3} & g_{3,4} & \dots & g_{3,M+2} & 0 & \dots & 0 \\ \vdots & \vdots & \vdots & \vdots & \vdots & \vdots & \vdots & \vdots & \vdots \\ 0 & 0 & \dots & 0 & 0 & g_{i,i} & g_{i,i+1} & \dots & g_{i,j} \end{bmatrix} \begin{bmatrix} \Gamma_{A_1} + \Gamma_{B_1} \\ \Gamma_{A_2} + \Gamma_{B_2} \\ \Gamma_{A_3} + \Gamma_{B_3} \\ \vdots \\ \Gamma_{A_j} + \Gamma_{B_j} \end{bmatrix} \tag{4.22b}$$

4.6 Validation of vortex model

The spatial range of the summation, L, which includes M discrete vortices, must be large enough to capture all of the induced velocities from the wake. A sensitivity study was carried out for the required range, with the results summarized in Figure 4.8. In response to this analysis, the summation was made over the range of $L = 30c$ for the results presented in this chapter. Taking the point of interest as the central position of the integral range, the model was implemented to solve the velocity at coordinates of ($15c$,0) and the effect of the bound vorticity of the oscillating foils was ignored.

The implementation of the numerical model uses the same foil configuration as the experiments of Stapountzis (1982), where $z_0 = 1.1c$ and $c = 0.203$m.

A comparison with the experimental results presented by Stapountzis (1982) is made in Figure 4.9 for the case of two sinusoidally oscillating foils with a phase difference of $\varphi = 0°$. The metric of dimensionless gust intensity, $I_{g,w}$, is used to quantify the magnitude of the vertical velocity fluctuations in response to the sinusoidal motion of the oscillating foils and is given in Equation 4.23 Stapountzis (1982). Here w'_0 is the amplitude of the induced vertical velocity fluctuations and α_0 is the amplitude of the pitching motion.

$$I_{g,w} = \frac{w'_0}{U\alpha_0}, \tag{4.23}$$

The gust intensity varies as a function of reduced frequency. The numerical results show close

agreement with the experimental results which were available for the range of $0.05 \leq k \leq 0.52$.

The gust intensities diminish as $k \to 0$ as the circulation about the foil is shed so slowly that the strength of each vortex is low and the resulting induced velocities become negligible. The reduction in gust intensities as $k \to \infty$ is a result of the physical phenomenon of unsteady lift. As discussed in §4.4, the development of circulation about a pitching foil is a transient process. As the frequency of pitch oscillation is increased, the circulation about the foil has less time to develop resulting in an increasing deficit between the actual circulation about the foil and that given by quasi-steady lift theory (Ashley and Landahl, 1956). This effect is implemented in the numerical model through the indicial admittance response given by the Wagner function; however, experimental values were not available for frequencies greater than $k = 0.52$.

4.7 Foil motions for a desired velocity time series

The mathematical model can be inverted such that the foil motions required to generate a specified velocity time series can be calculated. This is referred to herein as the 'reverse' solution.

4.7.1 Pseudo-inversion of matrices

The primary challenge to solving the reverse problem is that the $i \times j$ matrices of $\boldsymbol{f}$ and $\boldsymbol{g}$ do not have a unique inverse. However, the pseudo-inverse of these matrices can be calculated using a 'least-square' best fit given by the Moore-Penrose method (Penrose, 1956).

Considering the general linear algebra problem $\boldsymbol{Ax} = \boldsymbol{B}$, a 'generalised inverse matrix' $\boldsymbol{J}$ may exist for matrix $\boldsymbol{A}$ as the solution to $\boldsymbol{AJA} = \boldsymbol{A}$. If $\boldsymbol{A}$ is an $i \times j$ rectangular matrix, the generalised inverse $\boldsymbol{J}$ will have the dimensions of $j \times i$ (Xue and Chen, 2008).

However it can be shown that the above criteria for $\boldsymbol{J}$ allows an infinite number of solutions, and so additional objective functions must be introduced. This is done by finding the least-squares solution to the original linear equation with the minimum Euclidian norm. Within a range of specified precision, a unique matrix of $\boldsymbol{K}$ can then be found. This matrix is called the 'Moore-Penrose pseudo inverse' of matrix $\boldsymbol{A}$, and is denoted by $\boldsymbol{K} = \boldsymbol{A}^{+}$ (Penrose, 1956; Hearon, 1968; Xue and Chen, 2008).

Applying the Moore-Penrose method to Equation 4.21 gives the required wake circulation to achieve a given velocity time series as Equation 4.24.

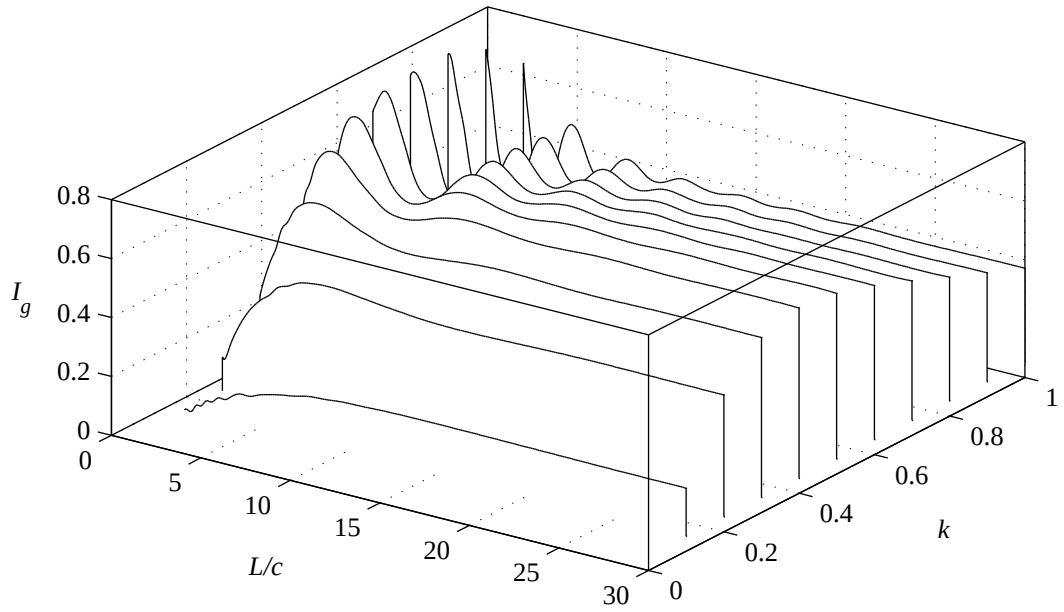

Figure 4.8: Sensitivity study for gust intensity, I_g, as a function of integral length, L, for a range of reduced frequencies, k.

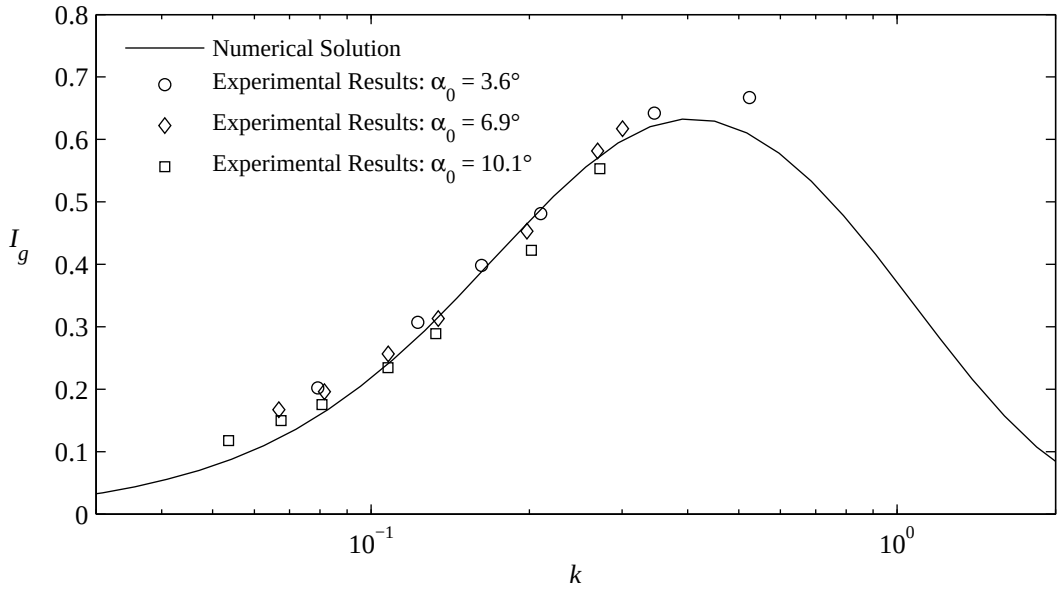

Figure 4.9: Comparison of numerical results using the method described in this paper with experimental results from Stapountzis (1982), for the case of in-phase sinusoidal foil oscillations at $Re = 4 \times 10^5$.

$$(\boldsymbol{\Gamma}_B - \boldsymbol{\Gamma}_A) = \boldsymbol{f}^+ \boldsymbol{u}' \tag{4.24a}$$

$$(\boldsymbol{\Gamma}_A + \boldsymbol{\Gamma}_B) = \boldsymbol{g}^+ \boldsymbol{w}' \tag{4.24b}$$

As the right hand sides of Equation 4.24 are known for a desired velocity time series and foil configuration, the circulation matrices on the left hand side can then be solved as simultaneous equations.

4.7.2 Calculation of foil motion from unsteady circulation time series

With a known circulation profile in the wake of each independent foil, the effective angle of attack can be found by combining the Kutta-Joukowski theorem, Equation 4.1 and Equation 4.11a, and rearranging for α_e. The result is given in Equation 4.25.

$$\alpha_e(s) = \frac{2\Gamma(s)}{UC_{L\alpha}c}, \tag{4.25}$$

Finally, Equation 4.13 is rearranged to calculate the required value of α_a with the single-step recursive solution in terms of α_e, shown in Equation 4.26.

$$\alpha_a(s) = \frac{\alpha_e(s) - \alpha_a(s - \Delta s)(A_1 + A_2) + X^*(s) + Y^*(s)}{1 - A_1 - A_2} \tag{4.26a}$$

$$X^*(s) = X(s - \Delta s)e^{-b_1 \Delta s} \tag{4.26b}$$

$$Y^*(s) = Y(s - \Delta s)e^{-b_2 \Delta s} \tag{4.26c}$$

4.7.3 Windowing of time series

Applying a windowing function to the velocity time series reduced instabilities in the solution of the pseudo-inverse. The implementation of the model in this chapter uses a Tukey window for this purpose (Tukey, 1967). The Tukey windowing filter used, $\zeta_T(x)$, is a tapered cosine window composed of a rectangular window with a magnitude of unity, with a cosine lobe at each end. This window is described mathematically by Equation 4.27, where r_T is the fraction of the time series modified by the cosine taper such that $0 \leq r_T \leq 1$ (Bloomfield, 2000).

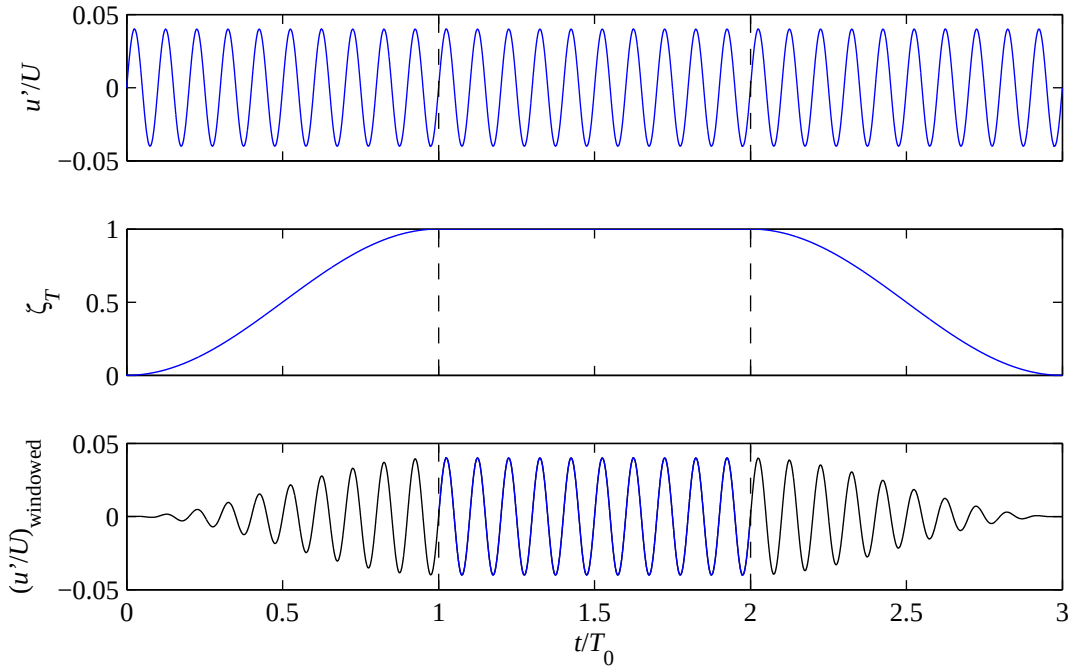

Figure 4.10: Representative plot of the process of windowing the velocity time series showing the repeating original time series (top), the windowing function (middle), and the resulting windowed velocity time series (bottom).

$$\zeta_T(x) = \begin{cases} \frac{1}{2}\{1 - \cos(2\pi x/r_T)\} & 0 \le x < r/2 \\ 1 & r/2 \le x < 1 - r/2 \\ \frac{1}{2}\{1 - \cos(2\pi(1-x)/r_T)\} & 1 - r/2 \le x \le 1 \end{cases} \tag{4.27}$$

It was found that using a value of $r_T = 2/3$ gave stable results. In order for such a window to be applied, the desired velocity time series of duration $T_0 = L/U$ was repeated three times and concatenated such that the duration was three times the original. The first original time series was therefore filtered by the increasing cosine taper, the second by unity and the third by the decreasing cosine taper. The second of the three original time series provided the unfiltered velocity time series and the stable solution of the circulation matrices. A representative plot of the process of windowing the velocity time series is demonstrated in Figure 4.10, showing the unaltered central third of the filtered velocity time series.

The need for such a filtering method is made clear by revisiting Equation 4.22. Considering the case of the vertical velocity perturbation only, one can see that the first value of w'_1 is calculated as the product of the first row of the $\boldsymbol{g}$ matrix and the circulation matrix. At both the beginning and end of the first row of the $\boldsymbol{g}$ matrix, the values approach zero. In order to find a value

of circulation which still allows the product to equal w'_1, a very large value of $(\Gamma_{B_1} + \Gamma_{A_1})$ is calculated. As this value is included in the calculation of subsequent values of w', the solution becomes unstable. By applying a window which reduces the time series to zero at the limits, the calculated values of circulation also become zero at the limits, and the solution is stable.

4.8 Results of reversed vortex model

The vortex model was used to calculate the required foil motions to produce a range of two-dimensional velocity perturbations with increasing complexity.

The results of the numerical model of the twin-oscillating foil configuration are summarized in Figure 4.11, which shows the outputs of four representative simulations to demonstrate the operating principle of the foil arrangement and to verify the inverse solution procedure. Figures 4.11a demonstrates the common situation of vertical velocity perturbations only, where the two hydrofoils are required to follow identical time series. Figure 4.11b illustrates the foil motion required to generate a oscillatory fluctuation in longitudinal velocity only, which is shown to be produced by sinusoidal foil oscillation with a phase difference of $\varphi = 180°$ as expected. Figure 4.11c illustrates the case of longitudinal and vertical flow fluctuations of equal magnitudes and a phase difference of $\varphi = 90°$. This represents the case where the effective angle of the incident flow is the greatest, which is the 'worst-case' combination of flow fluctuations in terms of generating the largest fluctuations in lift force on a foil. As such, the ability for this configuration of twin hydrofoils to be able to generate such a flow scenario in the laboratory is of special interest.

The novel contribution of this analysis is the ability to calculate the foil motion required to generate a desired velocity time series along the centreline. Figure 4.11d shows the case of arbitrary flow fluctuations in both longitudinal and vertical directions, and the corresponding calculated time series of the foil angles. This example demonstrates the flexibility of the numerical model as the required angular motion of the two foils is shown to be calculated for a time series with a range of driving frequencies as addressed in §6.7. This situation also demonstrates the capability of the twin-foil configuration to recreate a complex flow environment.

The frequency range of the velocity time series that can be produced is bounded by the approximate range of $0.06 \leq k \leq 1.9$ as shown in Figure 4.9. Outside of this range $I_g < 0.1$ and the relative velocity fluctuations become very small such that $u'/U < 1.7\%$ when $\alpha_0 = 10°$. It is also important to note that the steady Kutta condition used in the numerical model has been shown to be invalid at frequencies of $k > 2.0$ (Poling and Telionis, 1986). As such, the

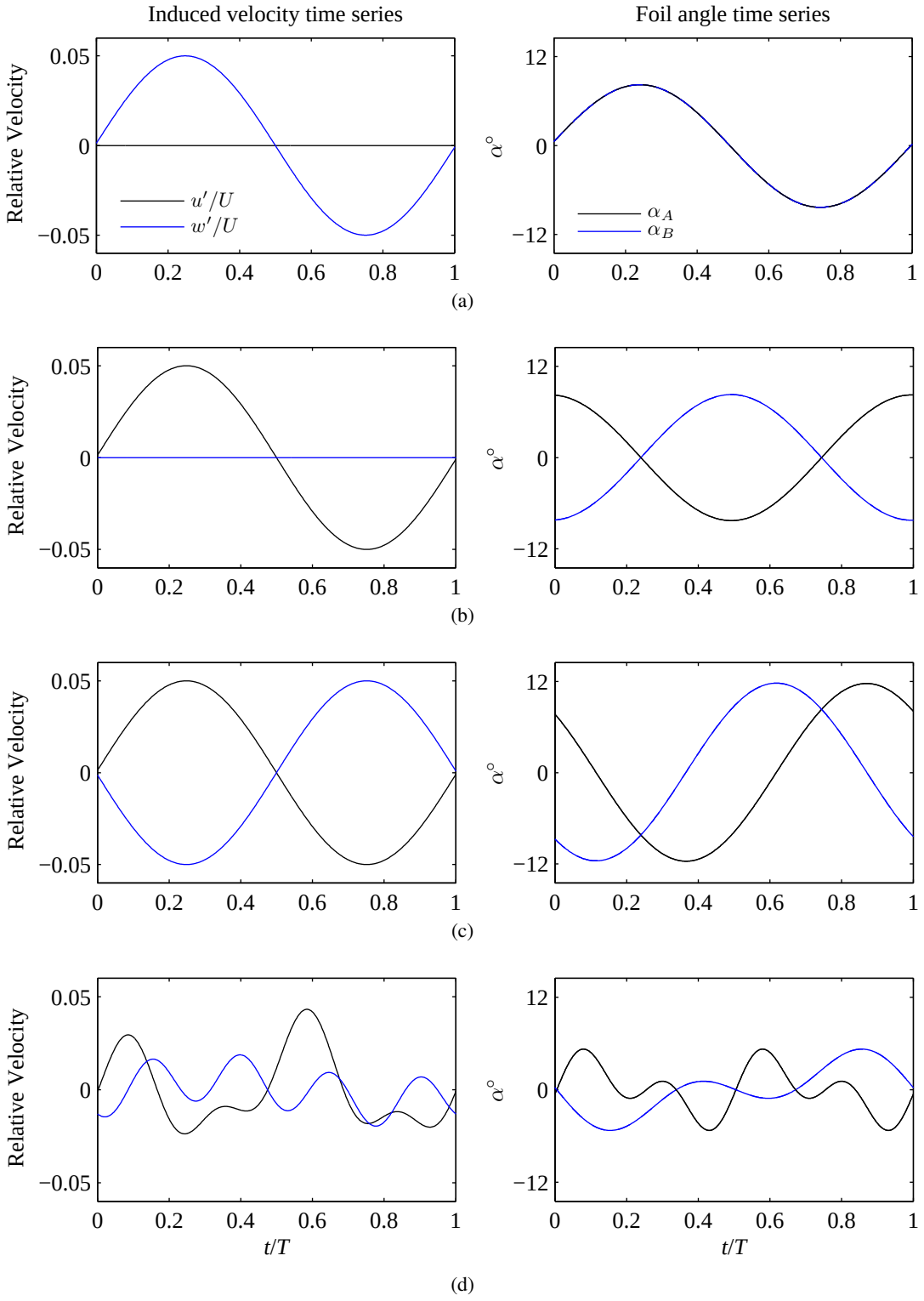

Figure 4.11: Representative results of the vortex model. The left column shows the time series of the desired velocity perturbations and the right column shows the required pitch motion of the two foils.

velocity time series is required to be band-pass filtered to within this frequency range prior to implementation in the numerical model in order to achieve realistic results.

4.9 Unsteady lift on a stationary hydrofoil

4.9.1 Introduction

The work discussed in this chapter up to this point has addressed the conditions of unsteady pitch motion of a foil in steady flow. This enabled the flow perturbations in the wake of twin pitching foils to be derived.

For the remainder of this chapter the theoretical influence of the resulting unsteady flow conditions on a stationary hydrofoil is examined. This scenario represents the operation of the AGB concept in dynamic flow conditions of an energetic tidal site.

In accordance with the theory of superposition of lift summarized by Jones (1938), a time domain solution has been derived to calculate the total lift on a two-dimensional hydrofoil in arbitrary flow perturbations in both the longitudinal (u') and vertical (w') directions. Two lift contributions are associated with each direction of velocity fluctuation. The first is derived from the circulation about the lifting surface, which is related to the flow velocity. A forcing term also results from the acceleration of the fluid flow in the direction of the lift force. This is herein referred to as the non-circulatory lift component.

In summary, the time-domain solution for unsteady lift presented in this chapter accounts for the following four forcing terms:

1. Circulatory lift contributions of unsteady longitudinal flow;
2. Circulatory lift contributions of unsteady vertical flow;
3. Non-circulatory lift contributions of unsteady longitudinal flow;
4. Non-circulatory lift contributions of unsteady vertical flow.

The calculation of each lift component is discussed in the following subjections.

4.9.2 Circulatory lift contributions of unsteady longitudinal flow

While several methods for the response to oscillatory free-stream velocity fluctuations have been suggested, a solution to the case of an arbitrary free-stream fluctuation is given by van der

Wall and Leishman (1994). For a stationary wing in unsteady flow, this theory can be expressed using the Duhamel integral in Equation 4.28, where ϕ represents the Wagner function.

$$L = \pi\rho uc\left(w_{3/4}(0)\phi(s) + \int_0^s \frac{\mathrm{d}w_{3/4}(\tau)}{\mathrm{d}\tau}\phi(s-\tau)\mathrm{d}\tau\right) \tag{4.28}$$

The lift contribution from the instantaneous longitudinal velocity is calculated in the absence of any onset vertical velocity component. As such, any component of the flow velocity which acts normal to the chord line is due to the angle of attack of the wing, or the rotational and translational motion of the wing itself. In the case of a fixed wing, the formula for the normal velocity at the three-quarter chord location is calculated as $w_{3/4}(t) = u(t)\alpha$ (Wagner, 1925; van der Wall and Leishman, 1994).

For further generalization of the theory, it is useful to present Equation 4.28 in terms of the lift coefficient as shown in Equation 4.29. This equation is derived using Equation 4.1, where the idealized value of $C_{L\alpha} = 2\pi$ assumed in Equation 4.28 has been substituted by the more general parameter of $C_{L\alpha}$. Equation 4.29 can be interpreted as the product of the lift curve slope and the effective angle of attack.

$$C_{L_1} = \frac{C_{L\alpha}}{u}\left(w_{3/4}(0)\phi(s) + \int_0^s \frac{\mathrm{d}w_{3/4}(\tau)}{\mathrm{d}\tau}\phi(s-\tau)\mathrm{d}\tau\right) \tag{4.29}$$

As explained in §4.4.5, the Duhamel integral in Equation 4.29 can be solved using a single-step recursive method when the exponential approximation of the Wagner function is used.

4.9.3 Circulatory lift contributions of unsteady vertical flow

For the case of vertical gusts convected at free stream velocity over a foil, the component of the flow velocity acting normal to the chord is denoted w_g. This normal velocity component is a characteristic of the flow which occurs independently of the free stream fluctuation. Ignoring the unsteady nature of the longitudinal velocity for this portion of the analysis, it can be shown that the normal velocity component is approximately equal to the vertical velocity component for small angles of attack, as $w_g = w' \cos(\alpha) \approx w'$.

Leishman (2006) presents the solution for the lift perturbation to an arbitrary normal velocity fluctuation. After replacing the idealized lift curve slope of 2π with the general term of $C_{L\alpha}$, the unsteady lift coefficient is described by Equation 4.30, where ψ represents the Küssner function shown in Figure 4.3.

$$C_{L_2} = \frac{C_{L\alpha}}{u}\left(w_g(0)\psi(s) + \int_0^s \frac{\mathrm{d}w_g(\tau)}{\mathrm{d}\tau}\psi(s-\tau)\mathrm{d}\tau\right) \tag{4.30}$$

As before, the exponential approximation to the Küssner function allows the recurrence solution to the Duhamel integral to be applied.

4.9.4 Non-circulatory lift contributions of unsteady longitudinal flow

A non-circulatory, or added mass component of lift is required to account for the acceleration of the flow in the immediate vicinity of the hydrofoil. For flow accelerations acting normal to foil, the resulting non-circulatory lift force is given by Equation 4.31, where the effective apparent mass can be shown to be equal to $M_a = \pi\rho c^2/4$ (Bisplinghoff *et al.*, 1996; Leishman, 2006).

$$L = -M_a\frac{\mathrm{d}w}{\mathrm{d}t} \tag{4.31}$$

The component of the longitudinal acceleration that is normal to the chord can be expressed as $\mathrm{d}w/\mathrm{d}t = \dot{u}\alpha$ for small angles of attack. For this case, the force can be shown to act through the mid-chord location ($s = 1$). Because the longitudinal velocity varies over the chord, at time s, the effective particle acceleration over the chord, $\dot{u}_e$, is calculated using the integral shown in Equation 4.32.

$$\dot{u}_e = \frac{1}{2}\int_{s-1}^{s+1} \dot{u}\mathrm{d}s \tag{4.32}$$

The combination of Equation 4.31 and Equation 4.32 can be rearranged in terms of the non-circulatory lift coefficient by given in Equation 4.33.

$$C_{L_3} = \frac{\pi c\dot{u}_e\alpha}{2u^2} \tag{4.33}$$

This result for the treatment of non-circulatory lift due to unsteady longitudinal flow agrees with that given by van der Wall and Leishman (1994).

4.9.5 Non-circulatory lift contributions of unsteady vertical flow

In a similar way to the added mass effects in longitudinal flow, the unsteady vertical flow also generates a non-circulatory lift component. Again, the fluctuating component of the vertical acceleration, $\dot{w}$, varies over the chord. The effective vertical acceleration component used in Equation 4.31, is calculated as the mean velocity fluctuation over the chord length, shown in Equation 4.34.

$$\dot{w}_e = \frac{1}{2}\int_{s-1}^{s+1} \dot{w} \mathrm{d}s \tag{4.34}$$

Equation 4.31 can be rearranged to give the non-circulatory lift coefficient due to an unsteady vertical velocity component shown in Equation 4.35.

$$C_{L_4} = \frac{\pi c \dot{w}_e}{2u^2} \tag{4.35}$$

4.9.6 Combination of lift contributions

Utilizing the principle of superposition of lift, the total forcing on the wing can be calculated as the sum of the individual responses in lift from the perturbation of each time step. As such, the total lift coefficient can be calculated by Equation 4.36.

$$C_{L,total} = \sum_{i=1}^{4} C_{L_i} \tag{4.36}$$

The total lift force is then able to be calculated using the standard equation for the lift on a wing of unit span, given by Equation 4.37

$$L_{total} = \frac{1}{2}\rho u^2 C_{L,total} c \tag{4.37}$$

4.10 Chapter conclusions

The use of two oscillating hydrofoils to generate arbitrary velocity fluctuations on the centreline of an experimental flume facility has been investigated. A numerical model has been developed to calculate these velocity fluctuations given the angular motion of the foils. This modelling

approach incorporates unsteady lift effects through the use of the Wagner function and uses a simplified vortex model to calculate the induced velocities between the hydrofoil wakes.

The discrete formulation of the numerical model facilitates the novel development of the inverse solution procedure, whereby the required foil motions to generate a desired velocity fluctuation time series along the centreline can be calculated. In this way, velocity perturbations can be created to reproduce a wide range of environmental conditions in the laboratory.

For the generation of oscillatory vertical velocity perturbations, gust intensities greater than $I_g = 0.1$ are expected to be achievable for a wide range of reduced frequencies, from $0.06 \leq k \leq 1.9$. The driving frequencies which give the maximum velocity fluctuations for a given α_0 are in the range of $0.4 \leq k \leq 0.6$ and are dependent on the geometry of the configuration. However it has been demonstrated that the combination of longitudinal and vertical velocity fluctuations is not limited to oscillatory motions but predetermined combinations of velocity perturbations at a point can be introduced through more complex motions of the two foils.

The chapter concludes by introducing the theory of unsteady lift on a lifting surface exposed to both longitudinal and vertical velocity perturbations. Through the superposition of the circulatory and non-circulatory lift effects, a combined lift coefficient is calculated for later comparison with experimental results presented in Chapter 6.

Chapter 5
Development of a two-dimensional velocity perturbation generator

5.1 Background

An experimental rig was developed to generate independent velocity perturbations in both the longitudinal and vertical flow directions based on the twin hydrofoil configuration introduced in Chapter 4. A third hydrofoil, instrumented with a load cell, was then installed downstream of the rig for the experimental measurement of the dynamic lift forces under a range of combinations of longitudinal and vertical flow perturbations. This apparatus was installed in the University of Edinburgh Circulating Water Channel, herein referred to as the 'flume'. A schematic of the set-up is presented in Figure 5.1.

Unless stated otherwise, all design and fabrication of the experimental apparatus discussed in this chapter were performed by the author.

Preliminary development of the experimental apparatus described within this chapter is reported in Harding and Bryden (2012a).

5.2 Acoustic Doppler velocimetry

In order to conduct repeatable experiments, the flow conditions in the experimental facility must be fully understood. This section summarizes the work performed on the flume to improve the distribution of the water velocity at the inlet, control the turbulence levels in a known way, and understand the resulting flow conditions.

An ADV was used to measure the three dimensional flow properties at a high spatial and temporal resolution while avoiding the need for extensive post-processing. In this study a Nortek Vectrino with the 'Plus' firmware and a down-looking cable probe was used. The Nortek Vectrino is capable of measuring the water velocity of a small sample volume in the directions of four converging acoustic beams. The operation of this device is similar to that of the three beam

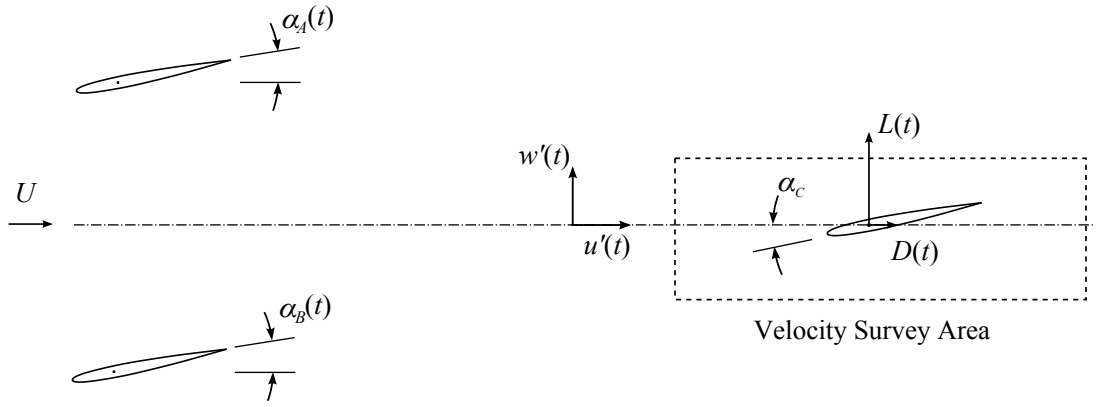

Figure 5.1: Schematic diagram of oscillating foils and downstream instrumented hydrofoil

Nortek Vector ADV described in §3.3.1, but with four acoustic beams to provide a level of redundancy. The resulting velocity vectors are then transformed to give the three dimensional particle velocity in the Cartesian coordinate system of (u,v,w).

As a pulse-coherent instrument, the operation of the Vectrino ADV is based on the calculation of the phase shift in the reflection of two acoustic pulses emitted from the transducer with a known time lag (Rusello, 2009). When the particle which the pulse is reflected off is moving away from the receiver, the time lag between the acoustic pulses is increased, as shown diagrammatically in Figure 5.2. In such a way, the component of the particle velocity in the direction perpendicular to the receiver arm can be calculated.

The various options available in the software controlling the Vectrino have been extensively investigated. This is the first time that such a thorough study has been carried out at the University of Edinburgh, and it has led to the development of a number of new experimental apparatus and procedures to be used in conjunction with the Nortek ADV.

5.2.1 ADV gantry system

In order to accurately and rapidly measure the flow in the flume at a variety of locations, a three degree of freedom gantry system was developed for the flume. This rig used a kinematic positioning system which allows the sample volume to be adjusted in 50mm increments in the longitudinal (x), transverse (y) and vertical (z) directions. The gantry system is shown in Figure 5.3. Detailed drawings of the gantry system are included in Appendix C.

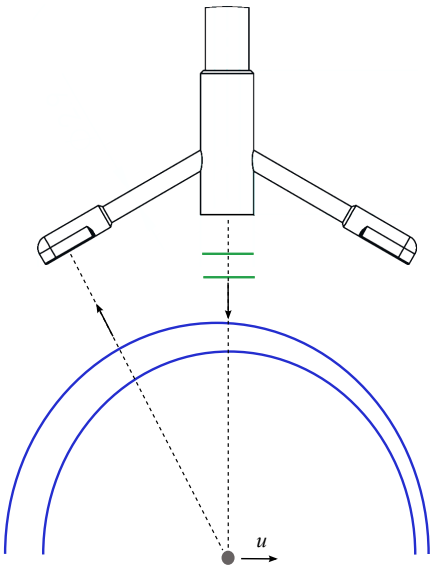

Figure 5.2: Transmitted (green) and reflected (blue) acoustic pulses of pulse-coherent ADV

5.2.2 Seeding methodology

The fundamental operating principle of acoustic Doppler velocimetry relies on the reflection of an acoustic pulse off suspended particles in the water. In order to measure a reflected signal of sufficient strength there must be sufficient suspended matter in the water column. Furthermore, because this method of measuring water velocity has the implicit assumption that the particles are moving with the same velocity as the water, the particles are required to have a density equal to that of water; in other words, they must be 'neutrally buoyant'. In this way no additional vertical velocity component is introduced by the particles rising or sinking.

As the flume is filled with fresh water with a very low concentration of solid particles, artificial particles must be added in a process known as 'seeding'. The seeding material used in the flume was glass micro-spheres with a mean diameter of 10μm. The variance of the density of this seeding material was reduced by allowing 10mL of seeding material to settle in 4L vessel of fresh water for 120s, and syphoning 2L of the suspended micro-spheres from a vertical location mid-way up the vessel. This settling time represents the approximate recirculation period of the flume which ensures that vertical drift of the syphoned particles will have a negligible effect on the vertical velocity measured by the ADV. The seeding material was added to the flume at the pump inlet over a period of 120s for even distribution through the water.

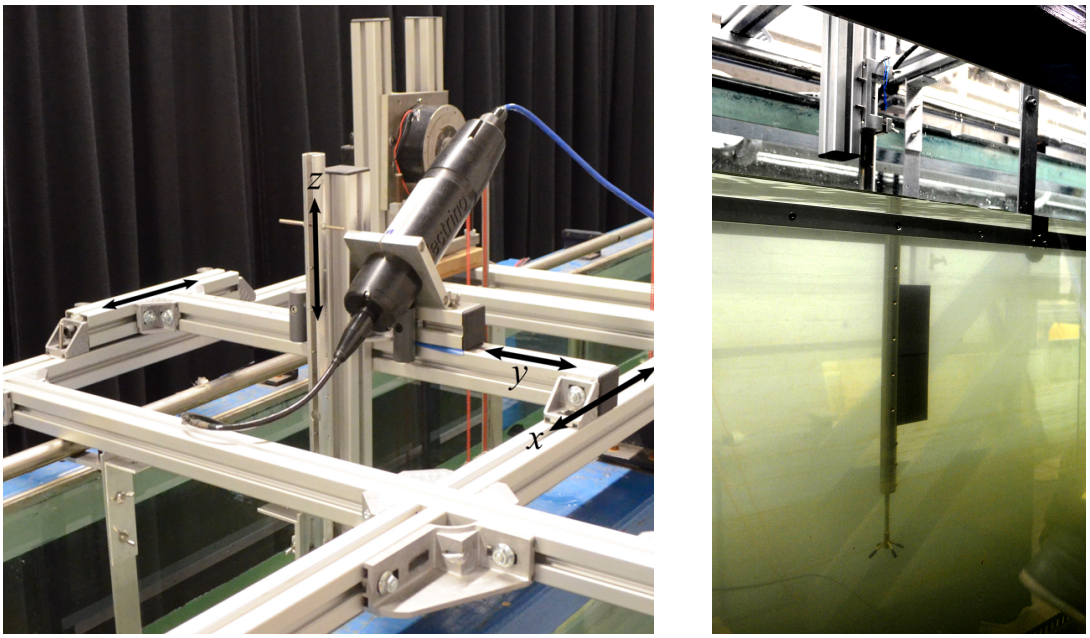

(a) Three degree of freedom gantry system mounted on the University of Edinburgh Circulating Water Channel

(b) ADV head protruding from gantry strut.

Figure 5.3: ADV gantry and associated coordinate system

5.2.3 ADV configuration settings

There is a range of settings available with the Vectrino which is designed to accommodate the various possible configurations of the instruments. A sensitivity study was performed on the key three parameters of the ADV operation to fully understand the effect of the transmit length, sampling volume and sampling frequency.

The transmit length corresponds to the duration of the acoustic pulses emitted by the transmitting transducer. The sample volume parameter describes the spatial resolution of the velocity measurement. The range of available sampling volumes is dependent on the selected transmit length. The sample volume is notionally a circular cylinder with a diameter of 6mm, and the 'Sample Volume' setting defines the cylinder length and is therefore herein referred to as the 'Sampling Length'. The orientation of this cylinder is the same as that described for the Nortek Vector ADV, shown in Figure 3.2a. The results of the sensitivity analysis performed using these parameters are presented in Table 5.1, in which the signal to noise ratio is denoted as SNR.

While the measured mean velocity was relatively constant for all combinations of transmit length and sampling length examined, the sampling volume was seen to have considerable influence on the standard error of the velocity measurement. For all values of the transmit length, it was observed that a very small sampling volume resulted in a relatively large standard

error in velocity and the value of this parameter causes the standard error to decrease. This can be explained by the fact that the spacial resolution of the measurement decreases with increased sample volumes. Hence, velocity fluctuations with length scales less than the spacial resolution are no longer captured. Conversely, it is known that decreasing the sample volume to the minimum of the range results in significant errors in the velocity measurement, resulting in a high standard error (Mathisen and Lohrmann, 2008). As such, the default parameters used in the subsequent experiments were a transmit length of 1.2mm and sample volume of 4.9mm.

The noise level of the measurement is positively related to the length of the time lag between the two pulses of a pulse pair. The duration of the time lag provides a limit on the maximum flow speed which can be measured, with a shorter lag being required to measure faster flows. Consequently, it is recommended that the slowest nominal velocity setting allowable for a particular situation be used to minimize noise in the velocity measurements. The nominal velocity range selected was ±0.3m/s, which is suitable for a vertical velocity range of ±0.27m/s and a horizontal velocity range of ±0.94m/s.

The internal sampling frequency of the Vectrino is a constant value and is dependent on the selected nominal velocity range (Lohrmann, 2006). While the maximum output sampling frequency is 200Hz, the internal ping rate is significantly greater than this. The setting labelled 'Sampling Frequency' is therefore more accurately described as the output frequency of the ensemble-averaged velocity values. The average number of points per ensemble is equal to f_i/f_s, where f_i is the internal sampling frequency or ping rate, and f_s is the selected sampling frequency. The internal ping rate for each nominal velocity range is presented in Table 5.3.

As discussed in §3.8.1, ensemble averaging of the signal acts to decrease the noise by a factor of $1/\sqrt{N_p}$ where N_p is the number of points in the ensemble (Nortek AS, 2005). It also has the effect of truncating the frequency range of the resulting spectrum as the Nyquist frequency is taken as $f_s/2$. To demonstrate this, the spectra of longitudinal velocity acquired at $f_s = 200$Hz is compared with the same data after an ensemble averaging with $N_p = 4$, and presented in Figure 5.4. The decrease in the calculated value of TI_u is due to the loss of energy above the frequency of $f_s/2N_p$ as a result of ensemble averaging. This observation can be extrapolated to infer that the selected sampling frequency decreases the maximum fluctuating frequency that we can observe in the data. The resulting values of TI_u for a number of sampling frequencies tested are presented in Table 5.2. The effect of aliasing is deemed to be negligible due to the relatively low energy content of the frequency components above the Nyquist frequency.

Table 5.1: Effect of transmit length and sampling volume on Vectrino velocity measurements for constant flow conditions

Transmit Length (mm)	Sampling Length (mm)	Frequency (Hz)	U (m/s)	TI_u (%)	90% Correlation Exceedance (%)	Mean Correlation (%)	Mean SNR (dB)
0.3	1.0	32	0.147	18.7	89.9	94.5	14.2
0.3	4.0	32	0.139	15.2	99.6	95.6	14.2
0.3	7.0	32	0.139	13.6	99.8	95.6	13.9
1.2	1.9	32	0.148	14.5	99.5	97.5	20.1
1.2	4.9	32	0.150	13.4	99.9	97.7	20.1
1.2	7.9	32	0.149	13.3	99.9	97.6	19.8
2.4	3.1	32	0.148	14.6	99.6	97.7	21.1
2.4	4.6	32	0.149	13.2	99.7	97.8	21.0
2.4	9.1	32	0.149	12.7	99.8	97.7	20.8

Table 5.2: Effects of sampling frequency on Vectrino velocity measurements for constant flow conditions

Transmit Frequency (mm)	Sampling Volume (mm)	Frequency (Hz)	U (m/s)	TI_u (%)	90% Correlation Exceedance (%)	Mean Correlation (%)	Mean SNR (dB)
1.8	7	8	0.147	12.0	99.0	96.9	20.0
1.8	7	16	0.149	12.4	99.8	97.4	19.9
1.8	7	32	0.149	13.1	99.9	97.6	19.8
1.8	7	64	0.149	13.1	99.9	97.7	19.8
1.8	7	128	0.148	14.2	99.8	97.5	19.7
1.8	7	200	0.145	15.8	99.5	97.3	19.7

Table 5.3: Internal sampling rate of Nortek Vectrino-Plus ADV (Lohrmann, 2006)

Nominal Velocity Range (m/s)	Internal Ping Rate, f_i (Hz)
0.03	426
0.10	667
0.30	1124
1.00	1754
2.50	1818
4.00	2564

5.2.4 Pulse-to-pulse interference

At some vertical locations above the flume floor, a sudden loss of correlation was observed, as shown in Table 5.4. This phenomenon, referred to as a 'weak spot', is explained by the existence of pulse-to-pulse interference observed over a vertical range of approximately 10mm (Rusello, 2010). This effect occurs when the reflection of one acoustic pulse from the flume floor arrives at the receiver at the same time as the reflection of a second acoustic pulse from the sample volume (Nylund, 2006).

The weak spot nearest to the flume floor (z = 200mm) is due to the pulse-to-pulse interference of the two coherent pulses in the pulse pair. The weak spot closer to (z = 550mm) can be understood as the interference between the leading pulse of two consecutive pulse pairs. Because this effect is dependent on the time lag between the pulse pairs, the vertical location of a weak spot is a function of the nominal velocity setting used. The location is also affected by the temperature effects on the speed of sound in water and the extent of the effect is altered by the composition of the reflective surface and the acoustic scattering caused by the water (Nortek AS, 2005).

5.3 Flume conditioning

Though the pump system in the recirculating water flume at the University of Edinburgh had been commissioned, the facility had never been fully calibrated. Preliminary experiments showed that significant modifications to the flow were required before the facility was suitable for the present work. As a result, a number of elements have been introduced to the flume by the author to improve control of the flow properties. The details of these installations are

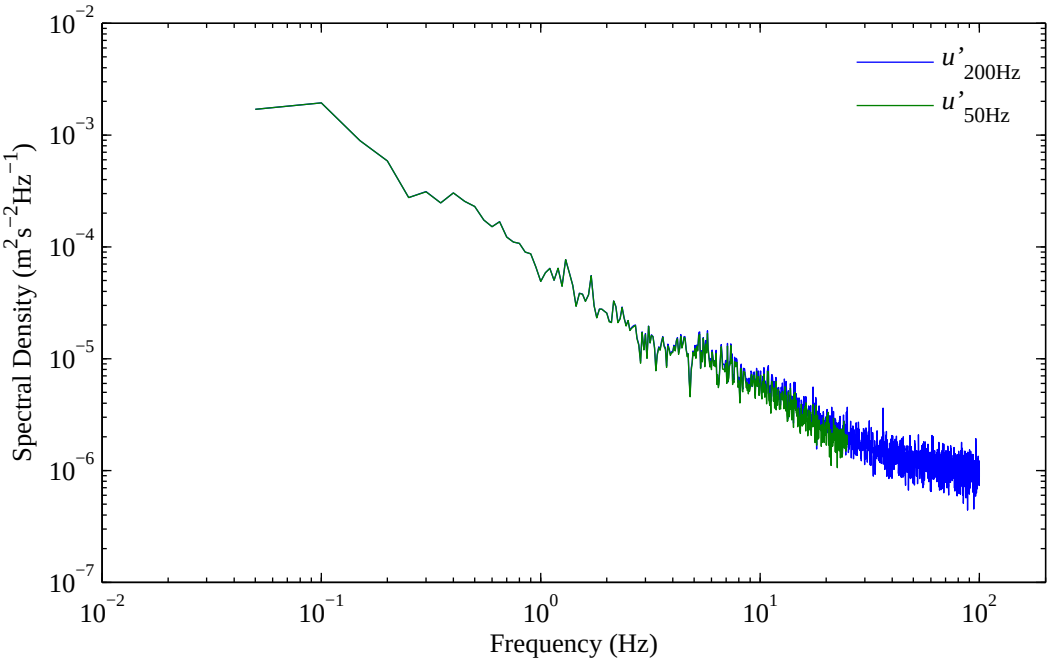

Figure 5.4: Effect of ensemble averaging on measured velocity spectra

described within this section. The resulting layout of the flume is presented schematically in Figure 5.5.

5.3.1 Turning vanes

Originally the return pipe of the recirculating pump system entered the flume in the upward direction at the upstream end of the facility. As such, the direction of the incoming water was vertical, when a horizontal flow direction was ultimately required. The result was a highly turbulent inlet condition, where a vertical jet of water was mixing vigorously at the upstream end of the flume, such that air was entrained into the flow and the resulting surface disturbances were unable to be dissipated within the length of the 22m flume.

The reasons for such violent mixing at the inlet can be broadly explained by two mechanisms. Firstly, the 1:9 expansion from the ⌀200mm circular inlet pipe to the nominal 400mm×700mm rectangular cross-sectional area of the flume induced large shear mixing. This is compounded by the uncontrolled redirection of the incoming water from a vertical to a horizontal direction.

One way to address these two issues was to design a set of turning vanes to distribute the incoming water evenly over the water column, while also redirecting the flow direction. As such the turning vanes are required to act as a diffuser and redirect the flow.

Table 5.4: Vertical profile of correlation statistics with weak spots identified with bold text (Nominal Velocity: 0.3m/s)

Distance from Flume Floor (mm)	Mean Correlation Coefficient (%)	Exceedance of 90% Correlation Coefficient (%)
50	97.6	99.9
100	97.6	99.9
150	96.9	99.9
200	**54.9**	**0.0**
250	97.6	99.9
300	96.6	99.9
350	97.7	99.9
400	97.2	99.8
450	97.5	99.7
500	97.5	99.8
550	**89.0**	**31.1**
600	97.3	99.7

The circular inlet pipe was divided into seven equal areas, using the geometrical analysis of Appendix D. The vanes then distributed approximately equal flow rates in each of the 100mm high horizontal bands spread vertically across the 700mm deep channel. The outer casing of the turning vanes was fabricated using sealed waterproof plywood, and the vanes were constructed out of 0.5mm stainless steel sheets. The fabrication and installation of the turning vanes in the flume are shown in Figure 5.6, and technical drawings of the final design are included in Appendix C.

5.3.2 Conditioning screens

Stainless steel mesh screens were added at regular intervals immediately downstream of the turning vanes to increase the rate of dissipation of large scale disturbances in the flow. It was found that larger spacing between adjacent screens increased the effectiveness of the flow conditioning.

The screens remove large scale turbulence from the flow by causing a greater pressure drop through the apertures where the velocity is greatest. Conversely, slower flow experiences a lower pressure drop. In this way the range of velocities downstream of each individual aperture is decreased. This acts to lower the turbulent mixing in the flow. The overall pressure drop

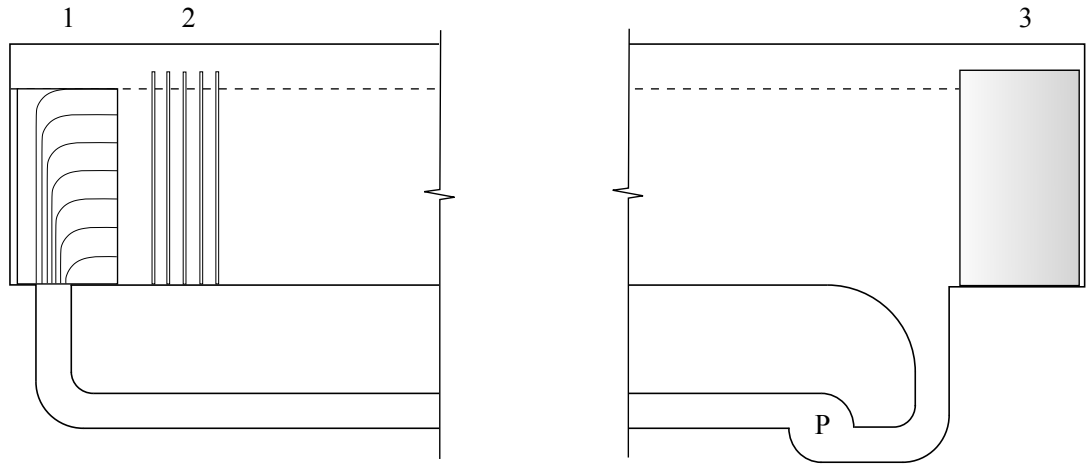

Figure 5.5: Schematic diagram of the flume layout and conditioning elements: 1) Turning vanes, 2) Conditioning screens, 3) Absorbing wedge. The nominal water level is indicated with a dashed line.

(a) Divisions of the turning vane inlet

(b) Completed turning vanes installed in the flume

Figure 5.6: Fabrication and installation of turning vanes in the flume

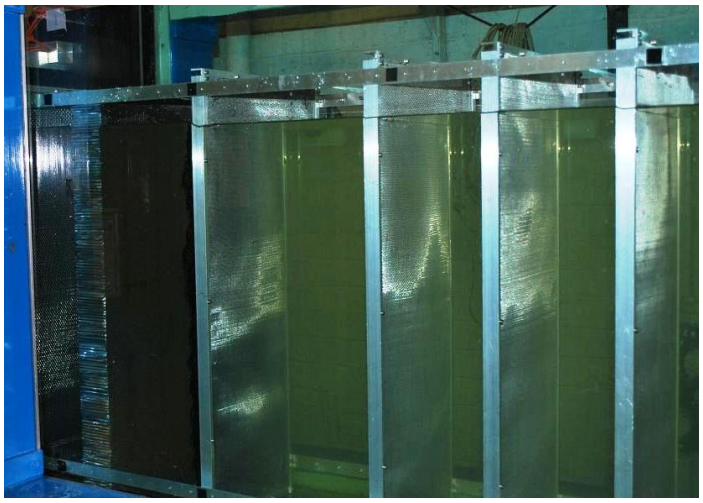

(a) Flow conditioning screens in cascading series at flume inlet

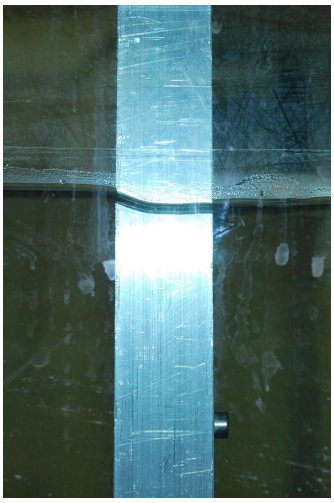

(b) Head loss through screen

Figure 5.7: Flow conditioning screens in the flume

through an individual mesh can be observed as a head loss, as shown in Figure 5.7b. The recirculating flow is driven by a centrifugal pump, and the flow speed was found to be relatively unaffected by the increased discharge pressure created by the screens.

The effects of individual and cascading series of screens were investigated in a series of 15 tests summarized by the test matrix of Table 5.5. Five minute velocity readings were taken in the cross-sectional centre of the flume for a number of distances from the inlet with each screen configuration. This allowed the natural dissipation rate of the turbulence to be observed. The longitudinal variation in turbulence for each screen configuration (SC) is shown in Figure 5.8.

As more screens where added at the inlet, a minimum turbulence intensity of $TI_u = 3\%$ was achieved. This corresponds to a standard velocity error of less than 5mm/s in flow where $U = 0.15$m/s. More information about the flow can be gained by examining the velocity fluctuations in the frequency domain. The spectra of the longitudinal and vertical velocity fluctuations are shown in Figure 5.9. This plot compares the energy in three representative tests; $U = 0.15$m/s with no flow conditioning ($TI = 13\%$), $U = 0.15$m/s with screen configuration 10 ($TI_u = 3\%$), and $U = 0$m/s.

The unconditioned flow showed an energy cascade which agreed with Kolmogorov's hypothesis where the spectral energy density is proportional to $f^{-5/3}$. However as screens are introduced to reduce the turbulence levels, this relationship is no longer visible. Both the longitudinal and vertical turbulence directions have been plotted to demonstrate the significantly higher noise level in the former due to the more oblique angle used in the calculation of this velocity from

Table 5.5: Test matrix of mesh screen configurations

Screen Configuration	Screen Spacing (mm)	Honeycomb	Screen Characteristics: Apertures per cm^2 × wire diameter (mm)							Beach
			3 × 0.9	6 × 0.9	16 × 0.56	30 × 0.25	40 × 0.35	90 × 0.25	200 × 0.25	
SC0										
SC1			✓							
SC2				✓						
SC3					✓					
SC4						✓				
SC5							✓			
SC6								✓		
SC11									✓	
SC7	5		✓	✓	✓	✓	✓	✓		
SC8	5		✓	✓	✓	✓	✓	✓		✓
SC9	5	✓		✓	✓	✓	✓	✓	✓	
SC10	20	✓		✓	✓	✓	✓	✓	✓	
SC12	20	✓		✓	✓	✓	✓	✓	✓	✓

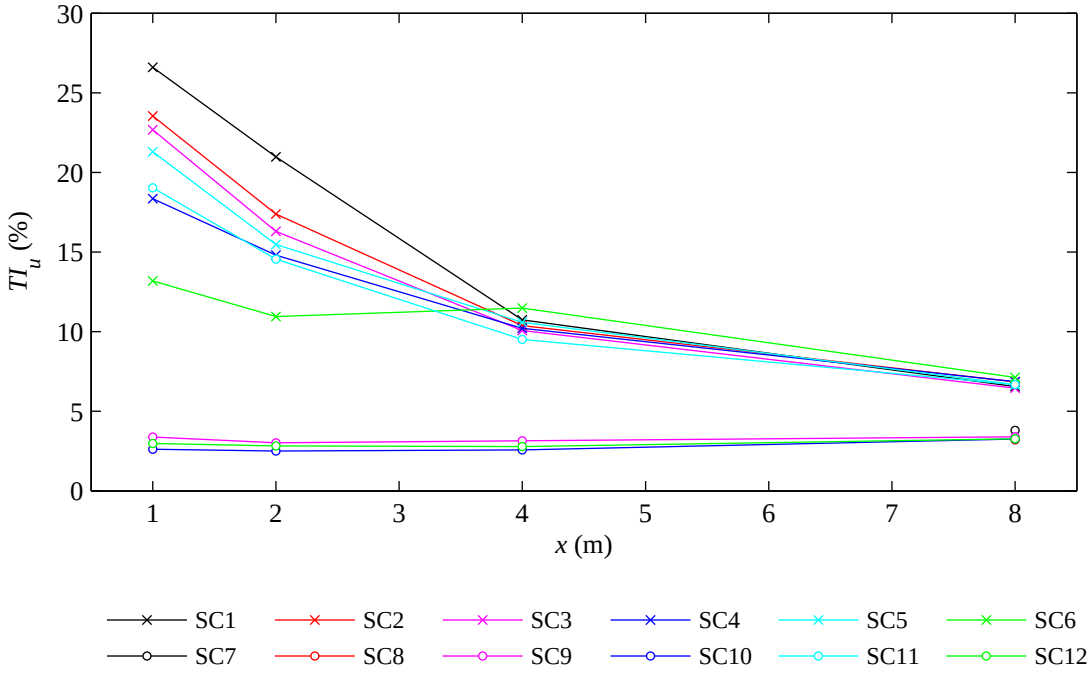

Figure 5.8: Turbulence intensity as a function of distance from downstream-most conditioning screen.

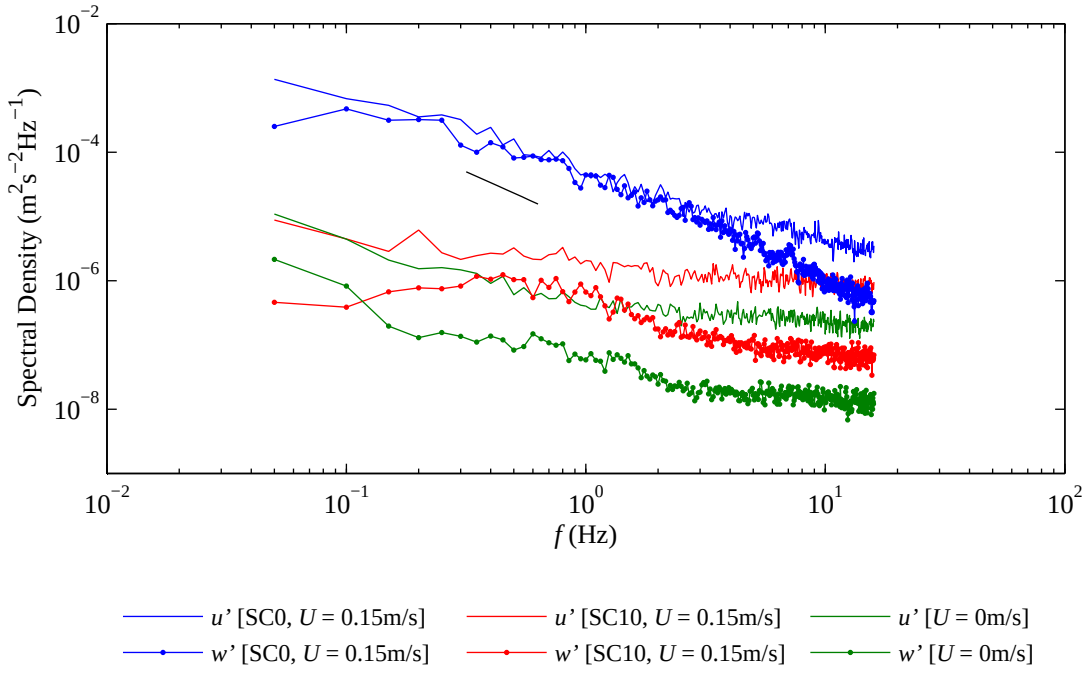

Figure 5.9: Spectral analysis of Vectrino output for different screen configurations and mean flow speeds.

the receivers which are orientated 30° from the horizontal. It was expected that the signal fluctuations from the velocity time series taken in stationary water would resemble white noise, however it can be seen that the acquired spectra deviate from this. This has been attributed to a number of phenomena including acoustic streaming; a process whereby a local current away from the transducer is created as result of the emitted acoustic pulse.

The screen configuration which resulted in the most steady flow was to use an aluminium honeycomb plate upstream of five mesh screens with decreasing porosity in the flow direction, as described by Table 5.6.

Table 5.6: Positions of final screen configuration

Screen Type	Screen Porosity (Apertures per cm^2)	Wire Diameter (mm)	Distance from Inlet (mm)
Honeycomb	3	-	200
Screen 1	16	0.56	400
Screen 2	30	0.25	600
Screen 3	40	0.35	800
Screen 4	90	0.25	1000
Screen 5	200	0.25	1200

After the installation of the turning vanes and conditioning screens, the vertical velocity profile was measured down the centre plane of the flume in 50mm increments at a location of 2m from the inlet. The vertical velocity profile was shown to vary by less than 4.5% down the depth of the channel. Similarly, a transverse velocity profile was measured across the flume in 50mm increments, at mid-depth at the same longitudinal location of 2m from the inlet. The variation in mean velocity across the width of the flume was measured to be less than 6.3%. Note that both velocity profiles were measured to within 50mm from the flume walls and floor due to limitations of the ADV operation near a solid boundary.

5.3.3 Absorbing beach

In order to dissipate any wave motion generated during start-up or operation of the flume, a porous beach installed downstream of the flume outlet. This addition to the facility was effective in absorbing larger scale flow variations which were not attenuated by the conditioning screens. It was observed that the addition of the beach resulted in a decrease in TI_u of approximately 0.5%.

5.4 Development of experimental test section

In order to allow closer comparison with existing theories, it was required that the flow within the test section was two-dimensional. As such, the effect of the transverse boundary layer profile across the flume must be minimised. The boundary layer was modelled according to Prandtl's one-seventh-power law for the development of turbulent boundary layers in conjunction with Kármán's momentum law. The development of the boundary layer thickness, δ, can be expressed as a function of the distance from the inlet, x, by Equation 5.1 (White, 2011).

$$\delta = \frac{0.16x}{Re_x^{1/7}} \tag{5.1}$$

The largest boundary layer is expected at the minimum flow speeds which was set at $U = 0.20\text{m/s}$. The experimental test section was designed to be installed at a location 2.0m from the inlet to the flume, where a boundary layer thickness of $\delta = 51\text{mm}$ is calculated at this speed. As such, the test section must be inset from the flume walls by at least this distance for the flow to be two-dimensional. To do this, 6mm thick polycarbonate sheets were used to create the test section away from the flume walls. A new boundary layer will of course develop within the test section. However, with the oscillating foils located 300mm from the leading edge of the test section walls, the reset boundary layer is calculated to be less than $\delta = 10\text{mm}$ by this location.

The assembled test section insert before and after installation in the flume is shown in Figure 5.10. The effect of the seeding material can be observed by the turbidity of the water in Figure 5.10b.

5.5 Installation of pitching hydrofoils

The hydrofoils used in the experiment have a NACA-0012 profile, with a chord length of 150mm and a span of 250mm. These were manufactured by rapid-prototyping methods using PA12 Polymer, with a water-proof surface finish for reduced absorption when submerged. This material was selected due its neutrally buoyant density which enabled a similar torque to be used when pitching in either direction. Each wing rotated about an 8mm diameter stainless steel shaft using two push fit polycarbonate bushes. The key dimensions of the foils are shown in the technical drawings of Appendix C.

The foils were manufactured to fit within the test section with a clearance of 3mm at either end. To locate the wings in position securely, the stainless steel shaft was machined to allow

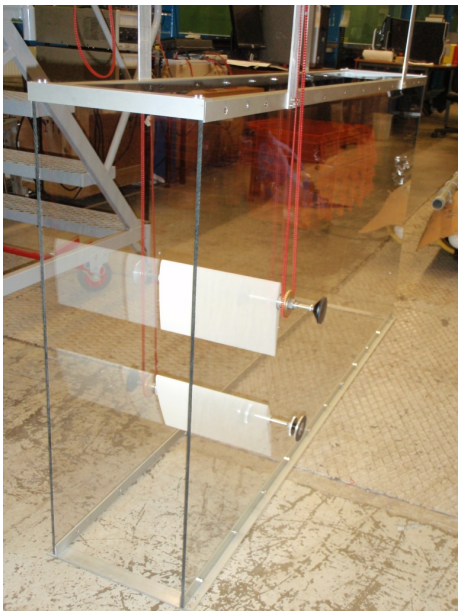

(a) Test section insert showing hydrofoils between 6mm polycarbonate walls.

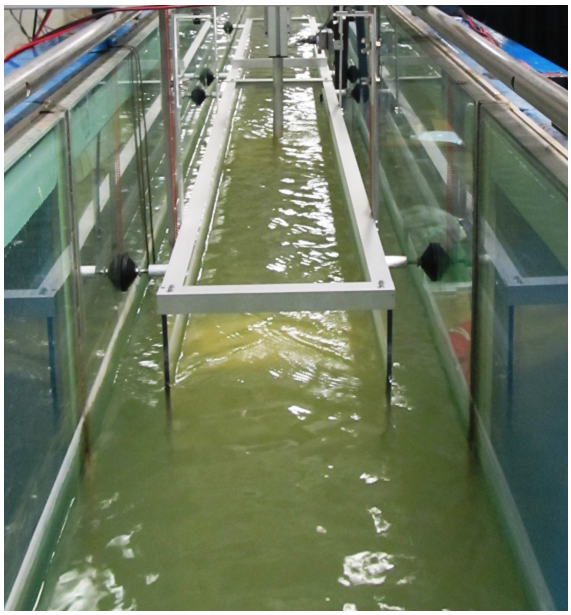

(b) Installed test section showing the seperation between the glass flume wall and the polycarbonate test section.

Figure 5.10: Experimental test section installation

threaded aluminium feet to be extended from one end. When the test section was fastened in position, the positioning foot was wound out of the shaft to push against the outer glass wall and fix the rotation axis of the foils.

Each hydrofoil was connected to an independent driving motor by a polyurethane timing belt reinforced with two 0.8mm diameter stainless steel cables, shown in Figure 5.11. The use of two independent driving motors for the two foils allows the phase difference between the foils to be defined by the user. The system was designed so that the belts were located outside of the test section to avoid disturbing the flow conditions, and so ran vertically down the outside of the polycarbonate walls. The torque was transferred from the pulley on the outside of the test section to the foil on the inside of the test section using a custom machined sheath connection for the pulley, which was then push fit into the foil.

Each DC brushless motor is fitted with a magnetic angular position sensor which allows the angle of attack of each foil to be controlled dynamically with a PID feedback loop. This feedback loop was programmed using the Field-Programmable Gate Array (FPGA) module of a National Instruments CompactRIO. The feedback control was executed using the inbuilt 1kHz clock, and the foil positions were recorded at a frequency of 50Hz. The position sensor set-up is shown in Figure 5.12.

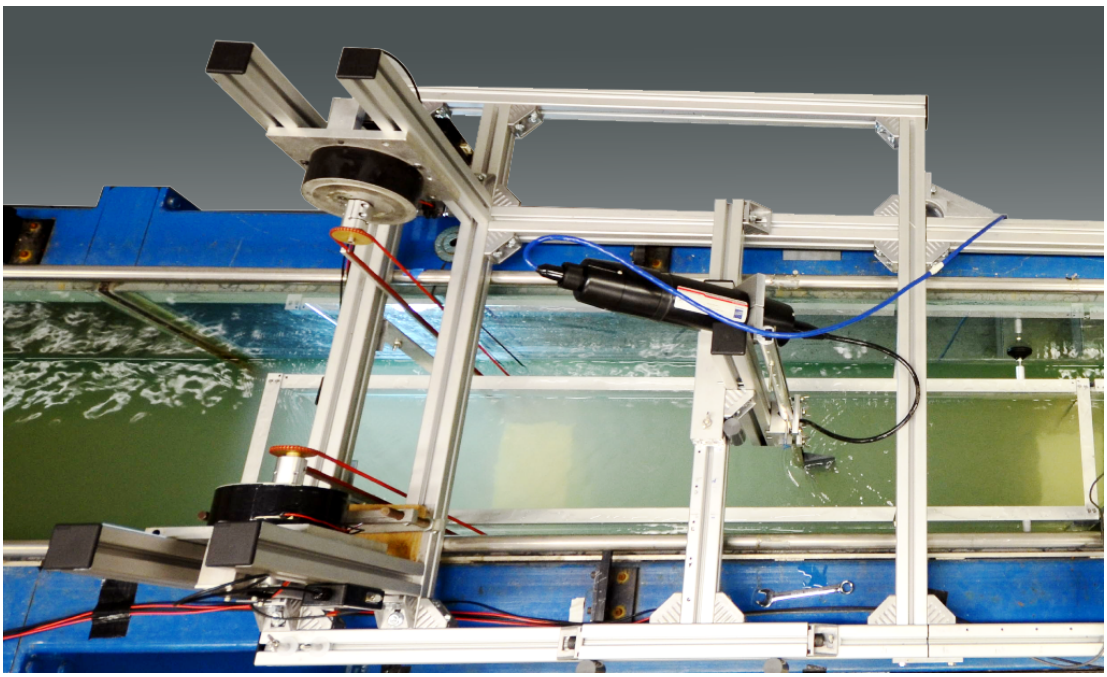

Figure 5.11: Driving motor rig on top of the recirculating water flume

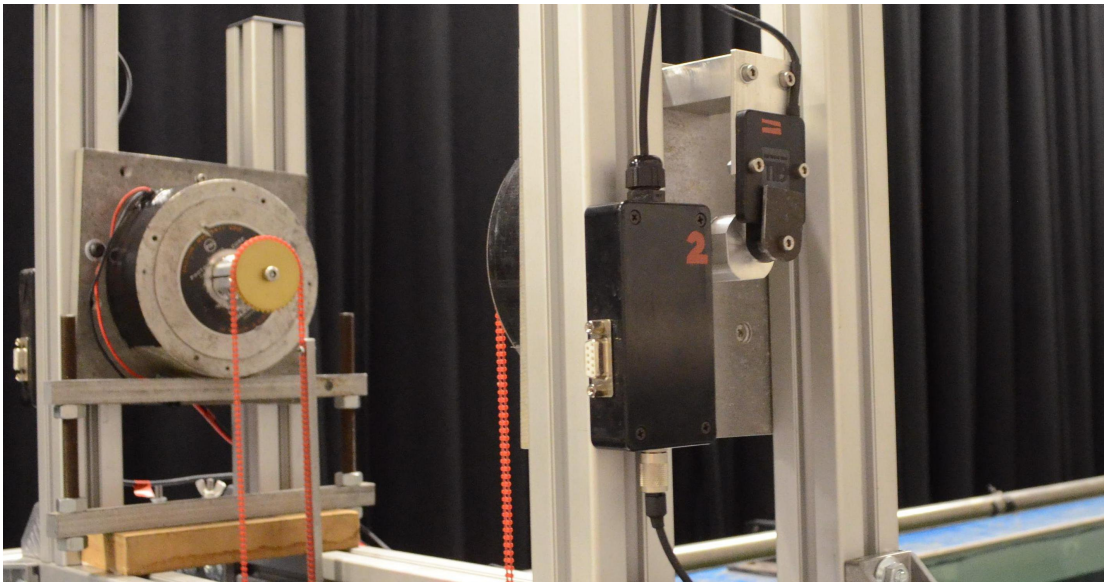

Figure 5.12: Position sensors mounted on motor shaft for position control

5.6 Installation of stationary hydrofoil

A third hydrofoil was installed in the test section which was fastened to a bidirectional load cell to measure the lift and drag forces. This foil was positioned on the plane of symmetry of the pitching foil system to measure the dynamic forces resulting from the unsteady incident flow. The relative location of the stationary hydrofoil is shown in Figure 5.1, within the 'Velocity Survey Area'. The foil geometry and construction were identical to those of the pitching foils, again with a 3mm clearance to the test section walls at either wing tip.

To allow the use of an existing load cell, developed by Goodfellow (2004), the stationary hydrofoil was connected to the load cell located on top of the flume by a 20mm square carbon fibre strut, as shown in Figure 5.13. Such an arrangement resulted in the hydrofoil being cantilevered from the vertical strut. The location of the net force on the wing was accounted for using a Wheatstone bridge circuit on both the top and the bottom of the load cell in both directions, to cancel the moment induced by the location of the force. This configuration required the use of 16 strain gauges. The signal to noise ratio was reduced by using an operational amplifier in the centre of each Wheatstone bridge arrangement.

During the experiments, this arrangement was prevented from measuring any drag on the strut by installing an isolating cover. An identical cover was installed on the opposite side of the test section to ensure symmetry of the flow.

The pitch of the stationary foil was fixed during each experiment, however the ability to alter the angle of attack of the foil between experiments was required. This was achieved by positioning the wing on a stainless steel shaft with an interface of two polycarbonate bushes. The angular position was fixed using a shaft locking mechanism which could be released from the top the of the connecting strut. The angle of attack was measured using a cable sensor mounted on the strut, which measured the vertical displacement of a known location aft of the pivot point. Because the cable sensor was spring loaded to tension the cable, this arrangement exerted a negative pitching moment on the foil. However, the tension force is referenced to the strut and so does not effect the measurement at the load cell itself.

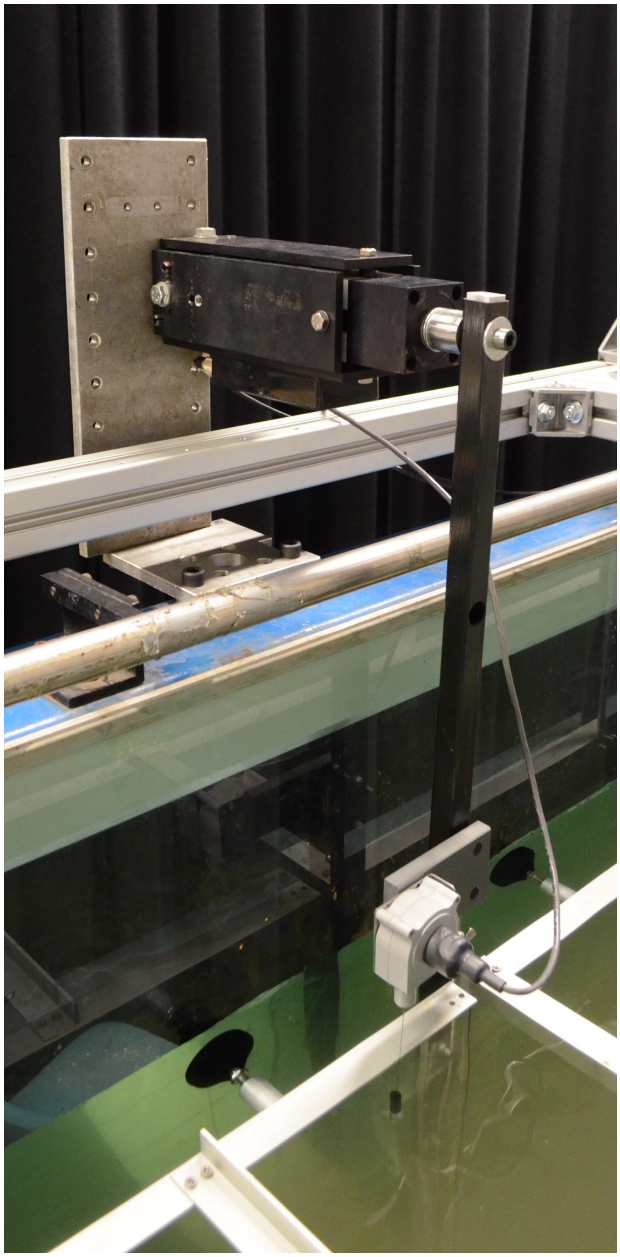

(a) Installed bidirectional load cell showing cable sensor mounted on vertical carbon fibre strut.

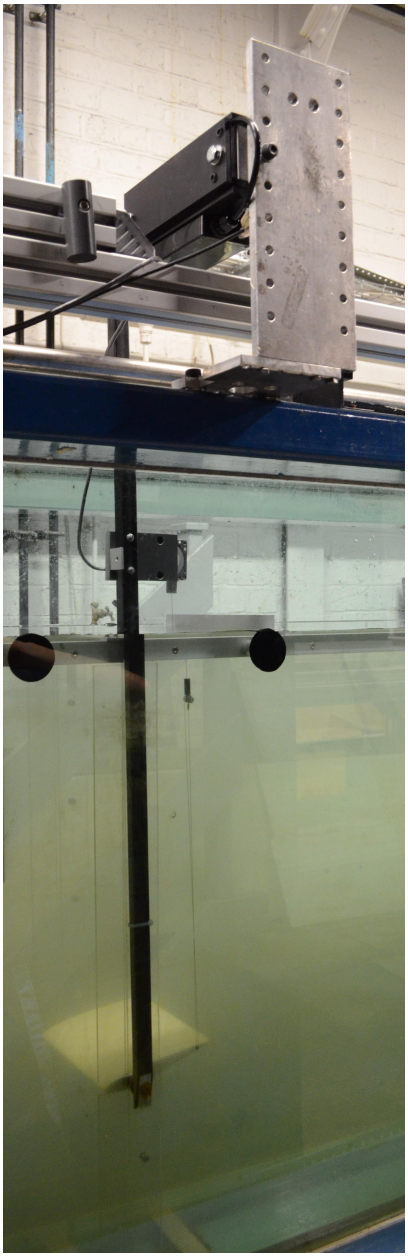

(b) Stationary hydrofoil mounted on vertical strut. The cable sensor attachment point can be seen near the trailing edge of the foil. The strut cover has been removed for clarity.

Figure 5.13: Installation of bidirectional load cell to measure the lift and drag of a stationary foil in unsteady flow.

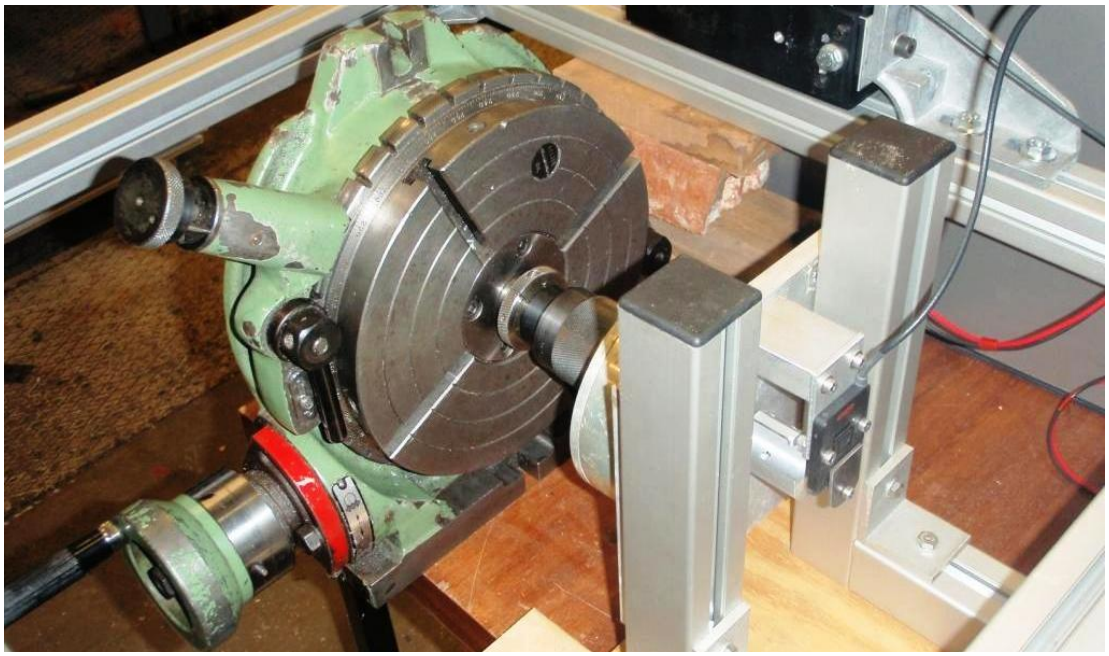

Figure 5.14: Calibration of magnetic angular position sensor using a dividing head

5.7 Calibration of sensors

5.7.1 Angular position sensors

Pitching foils

The angular position of the motor shaft was measured using '25mm Blade Sensors' manufactured by Gill Sensors. These used a magnetic activator to detect both translational and rotational motion without being in physical contact with the sensor. This configuration prevented deterioration of the sensor when being used to measure highly repetitive motions over a low angular range, making them suitable for the application of an oscillating foils. These sensors were calibrated by rotating the shaft of the driving motor with a dividing head, and measuring the voltage output of the sensor at 1.0° increments. The calibration apparatus is show in Figure 5.14 and the results are summarised in Table 5.7. A plot of the calibration process is presented in Figure E.1 in Appendix E.

Fixed foil

The angular position of the stationary hydrofoil, was measured using a retractable cable sensor fixed from the positioning strut to a location 90mm behind the pitch axis of the wing. The

relationship between the length of the cable and the voltage output of the sensor was calibrated using digital vernier callipers. The angular increment of the wing $\Delta\alpha$, could therefore be calculated from the change in length of the cable in millimetres, Δd_c, by the relationship $\Delta\alpha = \sin^{-1}(\Delta d_c/90)$. The relationship between the voltage signal and the angular position is shown to be linear for angles of attack less than $\alpha = 20°$ in Figure E.2 of Appendix E. The results of the calibration process are summarised in Table 5.7.

5.7.2 Force sensors

Offset voltage and sensor gains

The force sensor used to measure the lift and drag on the stationary wing was calibrated in both the F_x and F_z orientation by placing loads of known values at the wing attachment point. A greater number of increments were used to calibrate the -F_z direction which was used to measure the down-force of the wing and thus was the most critical direction of the load cell. The results of the calibration showed a linear relationship between force and voltage and the results plots are included in Figure E.3 of Appendix E.

Cross-talk

As forces in two perpendicular directions were being measured simultaneously, it is important that cross-talk is not apparent in the load cell. This was verified by attaching a load of 2.0N to the load cell and rotating it through 360° on a dividing head and taking the F_x and F_z force measurements at angular increments of 10°. After applying the offsets and gains established in the unidirectional tests, the force in the x-direction was plotted against that in the z-direction. In the case of zero cross-talk, such a plot forms a circle. The calibration results deviated slightly from the expected circular shape when the magnitude of the force in the x direction was equal to that in the z direction, however as the self-weight of the device is so much greater than the drag force of the wing, this observation is expected to be of negligible consequence. The graphical results of the cross-talk calibration are given in Figure E.4 in Appendix E.

Thermal drift of force transducer

When experiments were carried out for full days, the rate of thermal drift of the load transducer became significant when the load cell was not calibrated regularly. To observe the effect of thermal drift, the load cell was installed, with the wing attached, and the output signal acquired

Table 5.7: Summary of Calibration Data for Sensors

Sensor	Unit	Excitation Voltage (+V, -V)	Offset (unit)	Gain (unit/V)	Standard Deviation (unit)	Maximum Absolute Error (unit)
Gill Sensor 1	deg°	+5.00, 0.00	-32.66	13.61	0.12	0.18
Gill Sensor 2	deg°	+5.00, 0.00	-23.88	11.89	0.10	0.17
Cable Sensor	deg°	+5.00, 0.00	-641.87	181.06	0.06	0.09
Force Sensor (F_x)	N	+8.00, -8.00	-0.95	6.43	0.004	0.011
Force Sensor (F_z)	N	+8.00, -8.00	-2.96	5.68	0.010	0.029

at 1.0s intervals for one hour. The results of this experiment showed a thermal drift of 65mN/hr and 30mN/hr in the F_x and F_z, respectively.

5.7.3 Summary of calibration results

The results of the calibration procedures described in this section are summarized in Table 5.7.

5.8 Calculation of lift curve characteristics

Because the Reynolds Number of the experiments was limited by the test facilities, it was important to characterize the lift performance of the hydrofoils. To begin, the stationary foil was orientated to $\alpha = 0°$, by adjusting the pitch of the wing in the flow to generate no lift. From there, the angle of attack was increased in small increments, and the lift recorded at each angle of attack, to allow the lift curve to be plotted. The results of this analysis showed a lift curve slope of $\mathrm{d}C_L/\mathrm{d}\alpha = 1.32\pi$ and a stall angle of approximately 10°. These characteristics were measured for a low flow speed of Re = 3.8×10^4. These results are compared with experimental results at the similar Reynolds Number of Re = 4.0×10^4 performed by Althaus (1980) and presented in Miley (1982), with the results shown in Figure 5.15. The discrepancy in lift coefficient approaching stall could be explained by the 3mm gap between the wing tips and the edge of the test section, which introduced some variation from the purely two-dimensional results.

It was later decided that the experimental facility would be investigated at the maximum flow speed of the flume corresponding to Re = 5.8×10^4, though the lift curve characteristics were not measured. Experimental values of the lift coefficient were presented as a function of angle of

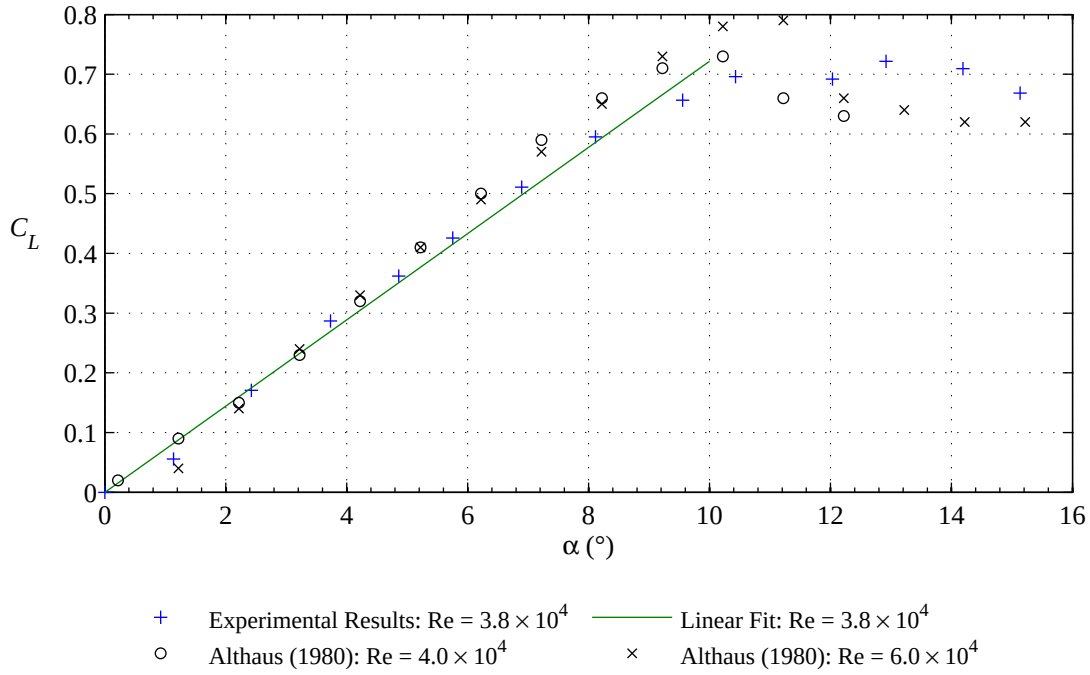

Figure 5.15: Lift curve of stationary NACA0012 hydrofoil measured at Re = 3.8×10^4

attack at the similar flow speed of Re = 6.0×10^4 by Althaus (1980), as presented in Figure 5.15. A 5.7% increase in the lift curve slope at Re = 6.0×10^4 relative to Re = 4.0×10^4 can be observed. This effect was neglected in the numerical calculations of the lift at the higher flow rates as it was considered to be within the range of experimental uncertainty, and a constant value of $dC_L/d\alpha = 1.32\pi$ was used for all numerical modeling.

5.9 System control and data acquisition

5.9.1 Overview

A control programme for the operation of the oscillating foil system was designed using LabVIEW 2010, developed by National Instruments. The host program was run on a dedicated Dell PC, with the PID feedback loop being run through the CompactRIO module to allow real time feedback at the internal clock frequency of 1kHz. Initial versions of the LabVIEW system control limited the foil motions to purely sinusoidal motions, but further development has facilitated the input of arbitrary motion paths defined by .csv files.

Calibrations of both the oscillating foil sensors and the load cell have been implemented into the

Figure 5.16: Front panel of LabVIEW control system and data acquisition programme.

LabVIEW control system. When these options are selected, the user received prompts to carry out each step of the respective calibration process. The calibration values are then calculated, displayed, and saved automatically.

The same LabVIEW programme was also developed to record the important outputs of the experiments with a time stamp. It was found that at higher acquisition frequencies, the data could not be saved at the desired rate or accuracy due to limitations in the computational performance. In response to this, a queuing system was developed into the data acquisition process to ensure that the rate of data saving did not interfere with the computational speed of other aspects of the program and feedback loop.

The graphical user interface of the host program is shown in Figure 5.16.

5.9.2 System inputs

The inputs to the LabVIEW programme are able to be entered through the graphical user interface to allow the rapid and intuitive configuration of the control and acquisition processes. The system inputs allow the user to specify the following parameters:

- Filepath to location of saved data
- Filepath specifying name of predefined foil motion
- Frequency of data acquisition (Hz)
- Save time series data of foil positions (Y/N)
- Save times series data of force on stationary foil (Y/N)
- Calibrate load cell (Y/N)
- Frequency of PID feedback loops (ms)
- PID gains for position feedback loop of pitching foils
- Masses used in the calibration of load cell
- Angular offset of pitching foils (deg°)
- Calibration constant for position sensor of pitching foils
- Angular gain specifying maximum angle of attach of pitching foils (deg°)

5.9.3 System outputs

The LabVIEW programme was developed to display a range of outputs to indicate the successful operation of the calibration, real-time control and data acquisition processes. The following outputs were displayed during the running of the LabVIEW programme for this purpose:

- Time series plot of desired foil motion
- Real-time plot of actual and desired foil motion
- Real-time plot of measured force on stationary foil
- Lift and drag force outputs of load cell (mV)
- Calibrated lift and drag forces on load cell (mN)
- Counter of number of data points acquired
- Counter of number of data points saved
- Successful saving operation check (Y/N)
- Real time location of pitching foils
- Real time error between desired and actual location of pitching foils
- Indicators of each stage of the load cell calibration process
- Offsets, gains and errors calculated in by the load cell calibration process

5.10 Chapter conclusions

This chapter describes the development of the experimental apparatus required for the implementation of the velocity perturbation generator described in Chapter 4.

A significant amount of time has been put into improving the recirculating water flume facility at the University of Edinburgh, prior to the development of the gust generation equipment. This work involved the design and fabrication of turning vanes and flow conditioning screens at the flume inlet and the installation of an absorbing beach at the downstream end. Extensive measurement and processing of the resulting flow velocities were carried out to fully understand the resulting flow fields, and to quantify the improvements.

The flow velocity was measured using a Nortek Vectrino ADV. A systematic study of the available configuration settings was performed before using this instrument. A kinematically located gantry system was designed to position the head of the ADV in know locations in the flow, and the importance of sufficient seeding of the flume was also recognised.

The development, design, fabrication and installation of the gust generation facility was carried out by the author. The final design included an inset test section within the flume walls to create a two-dimensional flow. Each of the two oscillating foils were driven using independent motor control to allow full flexibility of gust generation. The PID control system was implemented using the FPGA function of a CompactRIO device, configured using LabVIEW 2010. The control of the foil motions as well as the logging of relevant output parameters was performed through the graphical user interface of the host LabVIEW program. The thorough development of this customized interface with the experimental rig was beneficial for the accurate and efficient execution of the experimental agenda.

Chapter 6
Experiments in unsteady flow

6.1 Chapter introduction

This chapter describes the results of the experimental work performed on unsteady lift in a range of flow conditions.

To begin, the velocity field in the wake of the twin oscillating foils is characterised, and comparisons with the theoretical performance calculated in Chapter 4 are made. This process begins with the generation of single frequency sinusoidal oscillation in a single direction, before increasing the complexity of the foil motions to generate more complex two-dimensional flow perturbations.

The unsteady forces measured on the stationary wing subjected to a range of unsteady flow conditions are then presented. Again the incident flow conditions are varied at a single frequency and direction for preliminary tests before more complex flow conditions were generated. The measured forces are compared against those predicted by the unsteady theory introduced in §4.9.

The chapter concludes with a discussion of the results both in terms of the velocity fluctuations achieved and the forces measured.

6.2 Normalised velocity perturbation characteristics

6.2.1 Oscillation frequencies

In the initial phases of the flow characterisation, the driving foils were oscillated sinusoidally over a range of frequencies corresponding to the oscillation periods of $T = \{1, 2, 4, 8, 16, 32, 64\}$ s. These tests were carried out at two different Reynolds Numbers; $Re = 3.8 \times 10^4$ and $Re = 5.8 \times 10^4$. The dimensionless value of the reduced frequency is used in the results plots, with the conversion between the oscillatory period and the reduced frequency shown in Table 6.1 for convenience.

Table 6.1: Oscillatory period and reduced velocity conversion table

T (s)	k	
	$Re = 3.8 \times 10^4$	$Re = 5.8 \times 10^4$
1	1.86	1.31
2	0.93	0.65
4	0.46	0.33
8	0.23	0.16
16	0.12	0.08
32	0.06	0.04
64	0.03	0.02

6.2.2 Gust intensity

The metric of gust intensity, I_g, was first introduced in Equation 4.23, and is repeated in Equation 6.1. When the unit of radians is used for the angular amplitude of the oscillating foils, α_0, the resulting gust intensity is a dimensionless quantity.

$$I_{g,u} = \frac{u'_0}{U\alpha_0} \tag{6.1a}$$

$$I_{g,w} = \frac{w'_0}{U\alpha_0} \tag{6.1b}$$

For the case of variations in the longitudinal velocity, the amplitude of the velocity perturbations can be calculated as $u'_0 = \sqrt{2} \times u'_{RMS}$, where u'_{RMS} is the root-mean-squared value of the longitudinal velocity fluctuations. This was calculated as the square-root of the area under primary peak of a plot of the power spectral density (PSD) as a function of frequency (de Silva, 2000). This methodology, as suggested by Stapountzis (1982), mitigates the effects of the higher harmonic components of the velocity spectrum, as well as the fluctuations due to mechanical vibration and acoustic Doppler noise in the ADV measurements, which could otherwise cause an effective increase in the calculated gust intensity. The primary peaks of the PSD are shown in the representative plot of Figure 6.1 for both the u' and w' perturbations.

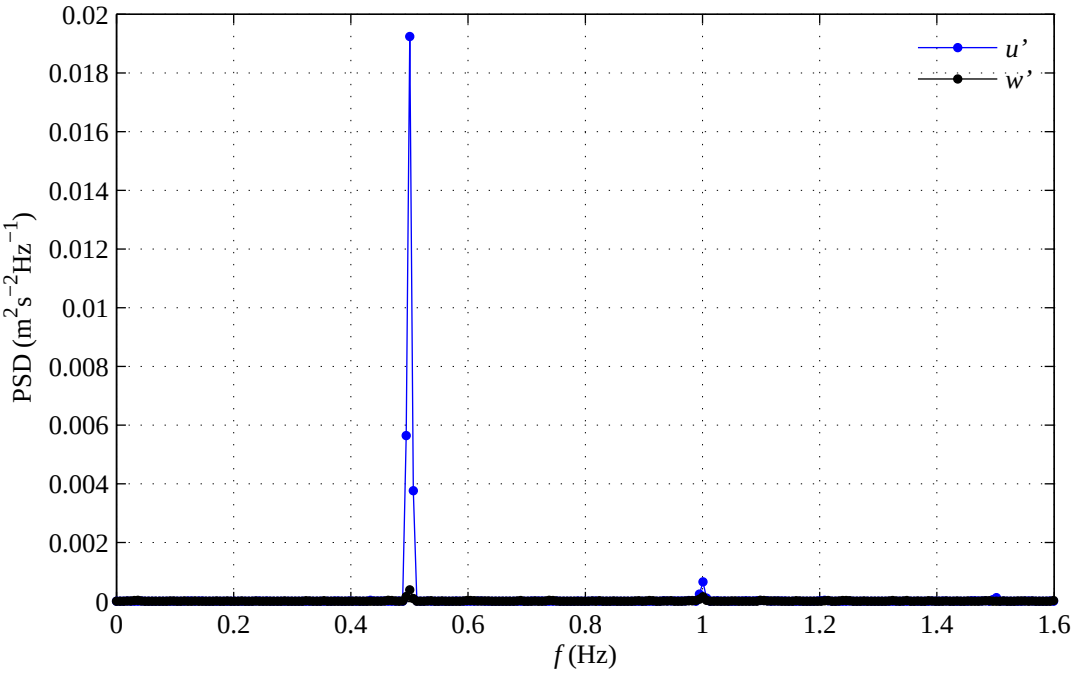

Figure 6.1: Power spectral density plot for the generation of longitudinal velocity perturbations: $\varphi = 180°$, $T = 2$s, $\alpha_0 = 6.0°$, $Re = 3.8 \times 10^4$.

6.3 Preliminary calibration of experimental setup

6.3.1 Nominal longitudinal location of velocity measurements

While the spatial range of the summation used in the theoretical solution was maintained at $L = 30c$ as discussed in §4.6, it was found that using the reduced value of $L = 14c$ modified the resulting velocity perturbations by <2%. As such, for practical purposes, the nominal longitudinal location of velocity measurements was selected as $x = 7c$, as the midpoint of this range of summation. Preliminary experiments supported this selection, indicating variations in measured gust intensities of less than 3% over the range of longitudinal positions of $4c \leq x \leq 10c$.

6.3.2 Duration of data acquisition

A stability analysis was performed in order to establish the duration of the data acquisition necessary to calculate the gust intensity reliably. To do this, velocity perturbations were recorded at a number of driving frequencies for an acquisition period of 300s. The gust intensity was then calculated using an incrementally increasing duration of the available data, up to the full acquisition period. The foil motion was initiated more than 60s prior to commencing any velocity

measurement to ensure that transient start-up effects were not recorded.

This analysis demonstrated that a steady state solution was reached by approximately 250s for all driving frequencies, and thus a conservative acquisition duration of 300s was used for all experiments. The results of this analysis are shown in Figure 6.2.

6.3.3 Transverse profile of velocity perturbations

Measurements were taken across the width of the test section to understand the transverse behaviour of the velocity perturbations away from the mid-plane of the flume. These were carried out in 50mm increments within the 250mm wide test section. A representative result of this procedure is shown in Figure 6.3.

The transverse profile shows that while the mean flow velocity is constant across the test section, the fluctuations reduce in magnitude nearer the test section walls. This is likely to be due to the sheer stresses near the wall influencing the circulation in the wake and is more pronounced for higher frequency oscillations.

In response to this observation, the velocity conditions generated for the force measurements on the stationary wing were recorded at the five lateral locations shown for each set of experimental parameters. The gust intensity results presented herein represent the velocity conditions measured in the centre plane of the flume to minimise wall effects. However, the resulting expected lift fluctuations were then computed by dividing the wing span into five sections across the span and calculating the forces experienced on each section. The total expected lift force was then calculated as the average of the forces calculated on the five span-wise sections.

The effects of the walls on the velocity perturbations is expected to decrease with a wider test section, however the current experiments were limited by the dimensions of the flume.

6.3.4 Calibration of gantry position

The location of the flume gantry was centred relative to the axis of symmetry of the oscillating foil system by carrying out a detailed velocity survey around the test section. The axis of symmetry of the oscillating foils is identifiable by the vertical position of the minimum velocity fluctuation, as indicated by Equation 4.18. The results of this survey are presented in Figure 6.4. Though these measurements were acquired in the absence of the stationary hydrofoil, the outline is shown with a white line for visualisation of the scale of the survey area.

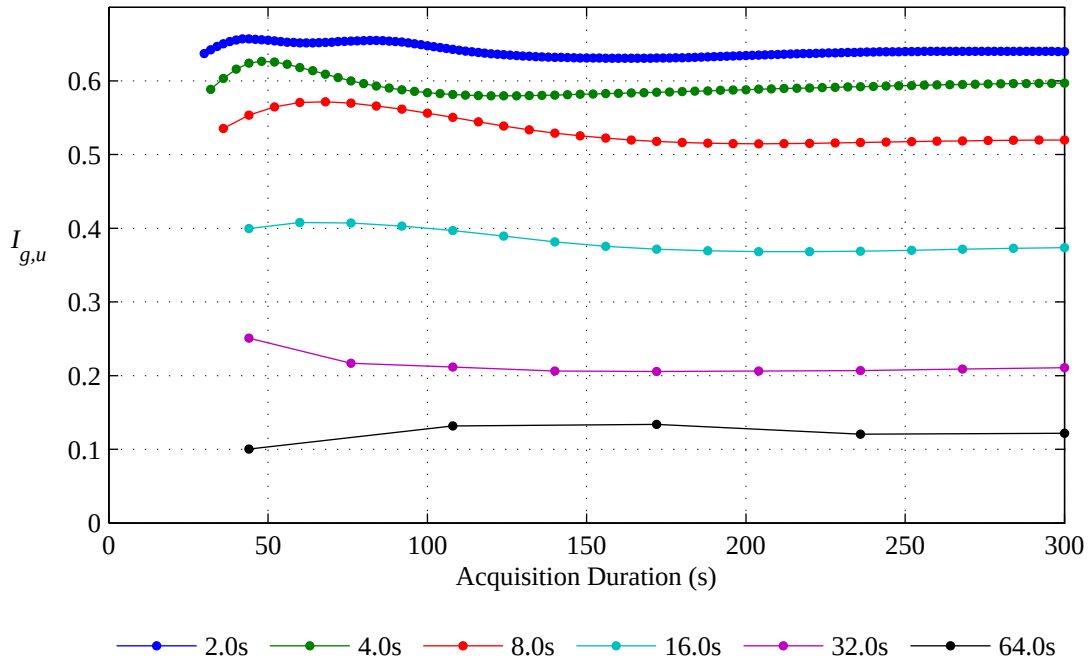

Figure 6.2: Transient response of $I_{g,u}$ with respect to the duration of data acquisition: $T = 2$s, $\alpha_0 = 6.0°$, $\varphi = 180°$, $Re = 3.8 \times 10^4$.

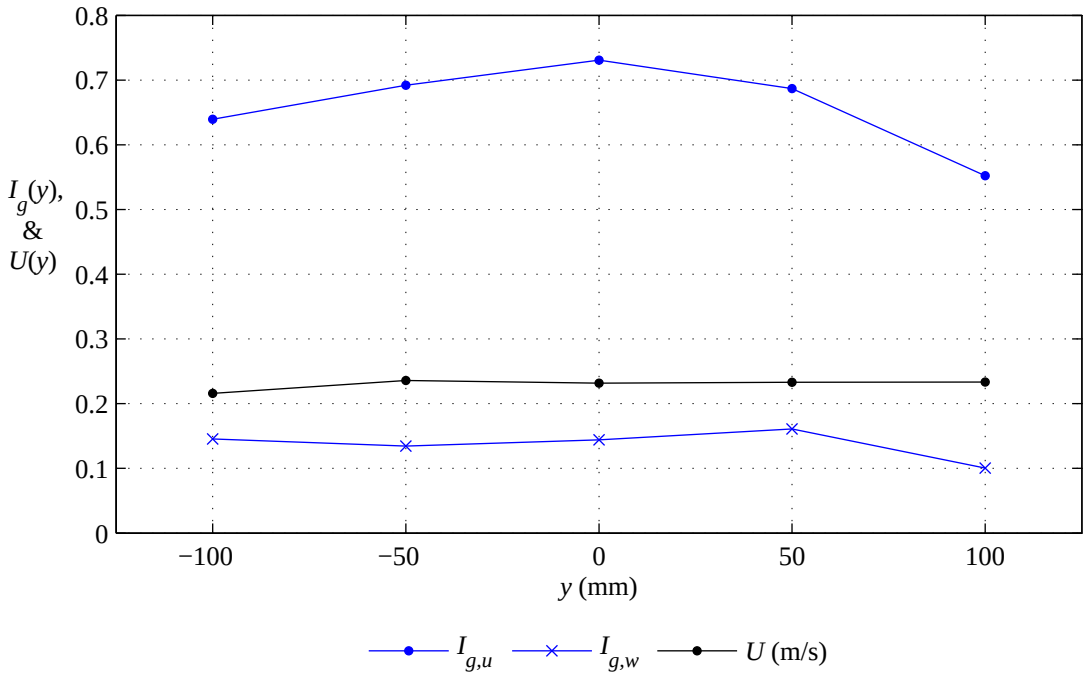

Figure 6.3: Transverse profile of gust intensity and mean flow velocity: $T = 2$s, $\alpha_0 = 6.0°$, $\varphi = 180°$, $Re = 3.8 \times 10^4$.

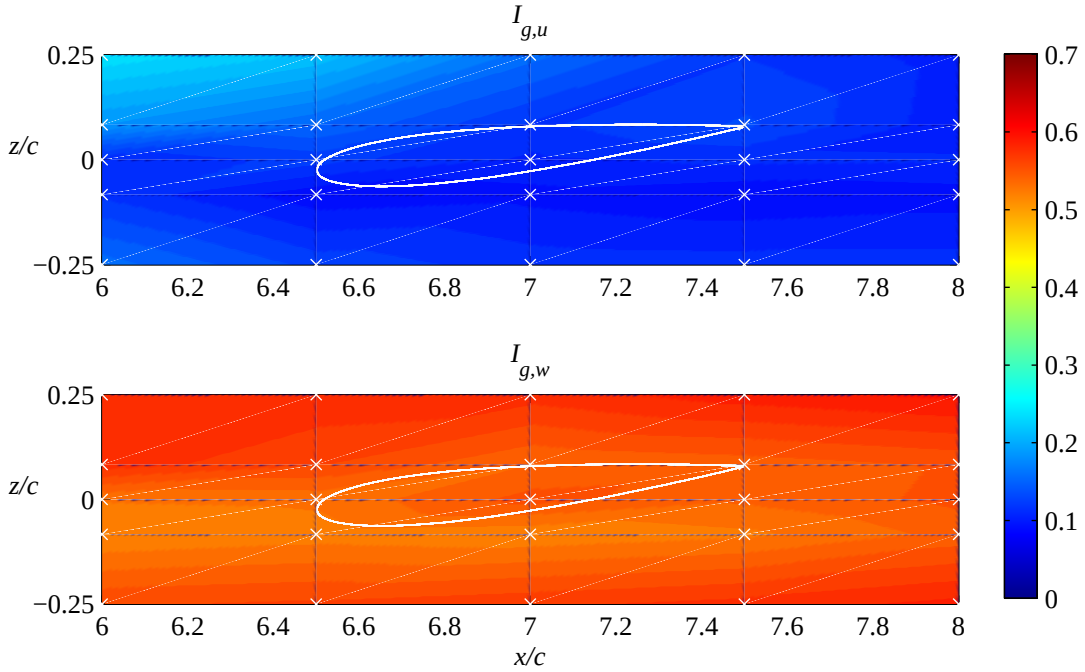

(a) Relative velocity fluctuations in the longitudinal and vertical directions for oscillations with phase difference of $\varphi = 0°$ and oscillation period of $T = 2$s.

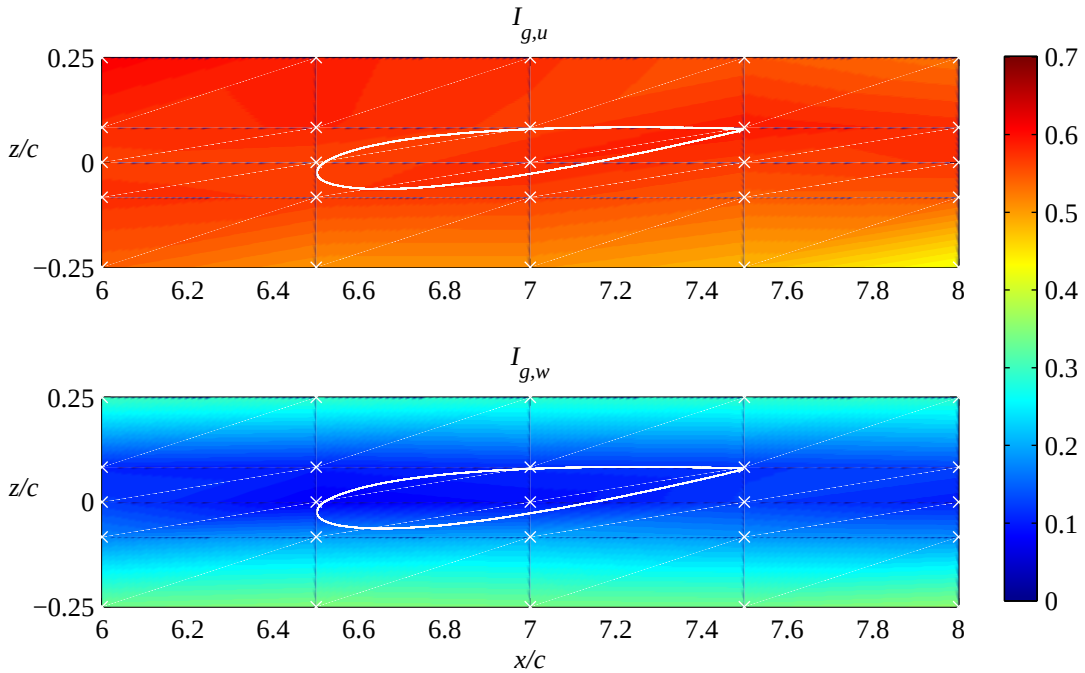

(b) Relative velocity fluctuations in the longitudinal and vertical directions for oscillations with phase difference of $\varphi = 180°$ and oscillation period of $T = 2$s.

Figure 6.4: Results of the velocity survey in the test section of the flume. Velocity measurements were taken at the locations indicated with a white cross.

While the oscillating foils produce relatively constant oscillations over the test section for the phase difference of $\varphi = 0°$ shown in Figure 6.4a, a vertical gradient in vertical velocity fluctuations is observed in Figure 6.4b when the phase difference is set to $\varphi = 180°$. The oscillation period of $T = 2$s shown in this calibration is at the high frequency end of the cases tested and the region of low vertical velocity fluctuation is shown to increase at lower oscillation frequencies.

6.3.5 Temperature effects

Temperature variation of the water in the flume can result from convective heat transfer towards room temperature, as well as temperature increases experienced as the flow passes through the pump.

The water temperature is particularly important when the flow speed is being measured using an acoustic sensor, as the speed of sound is a key parameter used in the calculation of the water velocity from the Doppler shift. The Nortek Vectrino is equipped with a thermometer in the probe to measure the water temperature at the time of measurement and instantaneously correct the value of the speed of sound used in this calculation. In such a way, the effects of temperature variations on the accuracy of the velocity measurement are accounted for.

A variation in water temperature also has the potential to alter the physics of the wake generated by the pitching foils through by altering the fluid viscosity. For each experiment the variation in water temperature was measured to be less than 3.0°C. This corresponds to a maximum variation in viscosity of 5.2%. This variation was deemed to introduce negligible variations in experimental conditions during each test.

6.4 Single frequency vertical velocity fluctuations

Velocity measurements were acquired at a location seven chord-lengths downstream of the oscillating foils along their centreline, with the two foils oscillating in phase such that $\varphi = 0°$, with an amplitude of $\alpha_0 = 6.0°$. The gust intensity was calculated for a range of pitching frequencies at $Re = 3.8 \times 10^4$ and $Re = 5.8 \times 10^4$, and the results are presented in Figure 6.5.

While reasonable agreement between the results and the theory is achieved at the high driving frequencies tested, a notable deviation from the theory is observed at the lower frequencies. Where the theory suggests that the velocity perturbations will reduced to effectively zero by $k = 0.01$, a steady state value of $I_{g,w} \approx 0.1$ is recorded. The theoretical values of gust intensity are derived from the assumption that the only phenomenon creating the velocity perturbation

is the circulation of the wakes behind the oscillating foils. However at the lower frequencies, where the wake circulation decreases, some velocity fluctuation is still measured. This can be explained by the non-circulatory phenomenon of the foils channelling the flow between them to introduce a vertical velocity component to the flow which is independent of the circulation in the wake, and thus dominates at the lower frequencies. This effect is expected to decrease by increasing the vertical spacing of the driving foils. This could not be verified in the present experimental facility due to the limiting depth of the flume.

6.5 Single frequency longitudinal velocity fluctuations

Velocity measurements were acquired at a location seven chord-lengths downstream of the oscillating foils along their centreline, with the two foils oscillating out of phase such that $\varphi = 180°$, with an amplitude of $\alpha_0 = 6.0°$. The gust intensity was calculated for a range of pitching frequencies, and the results are presented in Figure 6.6.

The shape of the frequency response predicted by the theory is clearly observed in the experimental results, with a peak gust intensity at $k \approx 0.6$. However, a clear offset in the gust intensity is observed. Again, this can be explained by a non-circulatory effect which is not included in the planar wake theory on which the predicted response is based. When oscillating out of phase, the proximity of the foils to each other results in a converging nozzle effect at one extreme of their motion, and a diverging nozzle effect at the other. This leads to a variation in the flow velocity in the wake along the centreline of the foils due to a phenomenon which is independent of the circulation in the wake. The magnitude of this effect is directly related to the relative change in cross-sectional area between the foils in the vertical plane during the peaks of their oscillatory motion, and so is expected to reduce with the foils proximity to each other.

6.6 Quadrature phase velocity fluctuations

The results of the numerical model developed in §4.8 have indicated that oscillatory longitudinal velocity perturbations can be generated out of phase with vertical velocity fluctuations of the same magnitude by oscillating the two hydrofoils with a phase difference of $\varphi = 90°$. This phase relationship is herein referred to as quadrature phasing.

Again, the achievable velocity perturbations are sensitive to frequency effects and the gust intensities calculated over a range of oscillation frequencies are presented in Figure 6.7. The experimental results show partial agreement with those predicted by the numerical model. In

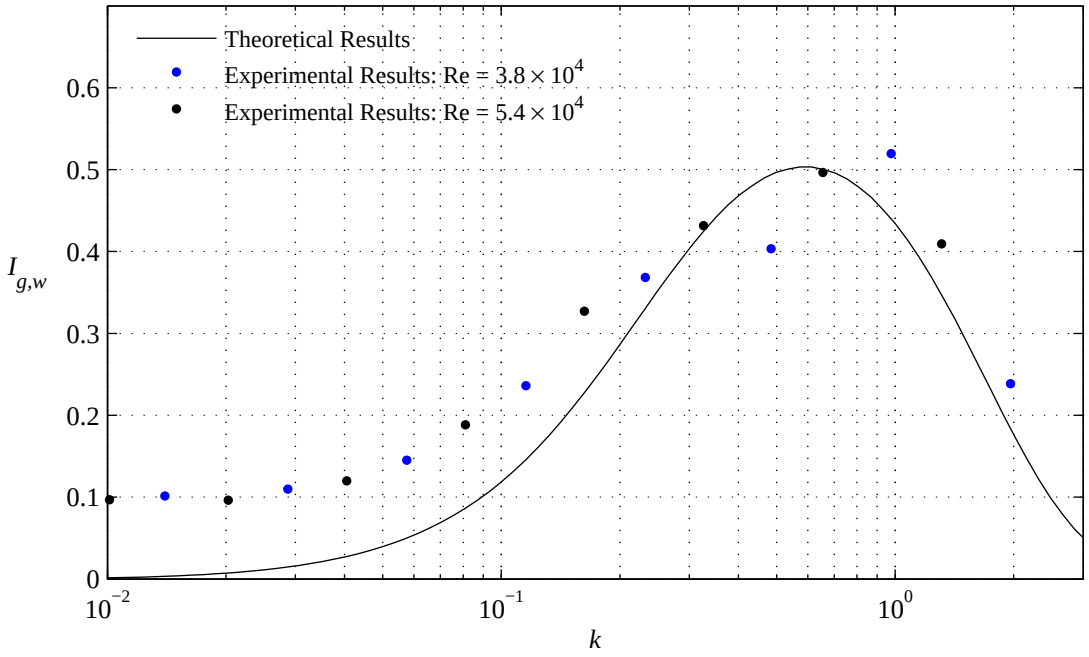

Figure 6.5: Results of the frequency effects on gust intensity for the generation of vertical velocity perturbations: $\varphi = 0°$, $\alpha_0 = 6.0°$

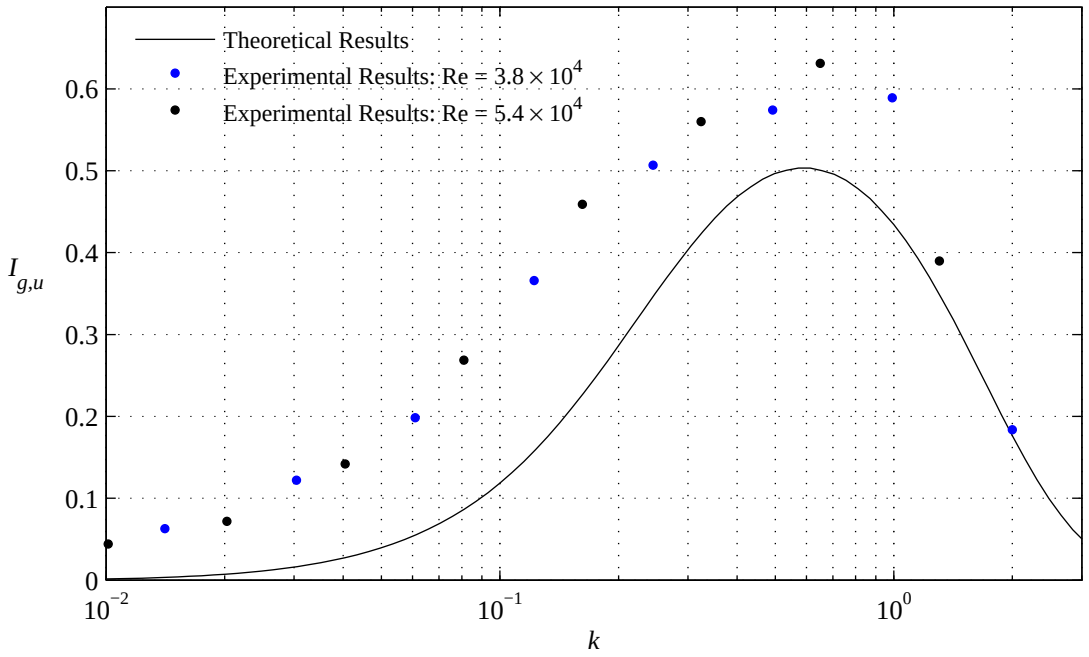

Figure 6.6: Results of the frequency effects on gust intensity for the generation of longitudinal velocity perturbations: $\varphi = 180°$, $\alpha_0 = 6.0°$

particular, the vertical perturbations show close agreement in the overall frequency response, while the longitudinal fluctuations are shown to reach a maximum at a significantly lower value of k than predicted by the model. At driving frequencies above $k \approx 0.3$ the measured longitudinal velocity perturbations were significantly less than those predicted by the numerical model. These experimental results are an anomaly which would required further experimentation to verify and explain.

The phase lag between the longitudinal and vertical velocity perturbations, ϕ_{uw}, was calculated using the cross-correlation of the two time series. The phase difference of the maximum cross-correlation is shown in Figure 6.8. The experimental results agreed approximately with the expected phase difference of $\phi_{uw} = 180°$. The key outlier in this analysis was at the driving period of $T = 2$s, which was the point of least agreement with the theory in the velocity perturbation analysis. This further indicates that additional testing in the range of $0.3 \leq k \leq 10$ is required.

While the frequency response of the gust intensity is a useful indicator of the magnitude of the velocity perturbation, it is also interesting to observe the response in the time domain. Figure 6.9 and Figure 6.10 show a comparison between the relative velocity perturbations expected by the model and those recorded in the experiments for two different oscillation frequencies. The experimental results presented are calculated as the mean of 20 oscillations, with the velocity measurements acquired at 200Hz.

The maximum oscillation period tested was $T = 1$s which showed large discrepancies between the experimental and theoretical gust intensities in the longitudinal direction. The results of this experiment are shown in Figure 6.9. While it can be seen that the relative longitudinal perturbations are less than those expected, this is predominantly observed in the time range of $0 \leq t \leq 0.4$. The averaged measured velocity is still observed to quantitatively agree with the expected results, with a phase difference of $\phi_{uw} = 174°$. The oscillation frequency which resulted in the closest agreement between the longitudinal and vertical velocity perturbations is plotted in the time domain in Figure 6.10. Though the magnitude of the measured velocity perturbations exceed those predicted by the theory, again a qualitative agreement is observed between the theoretical and experimental results.

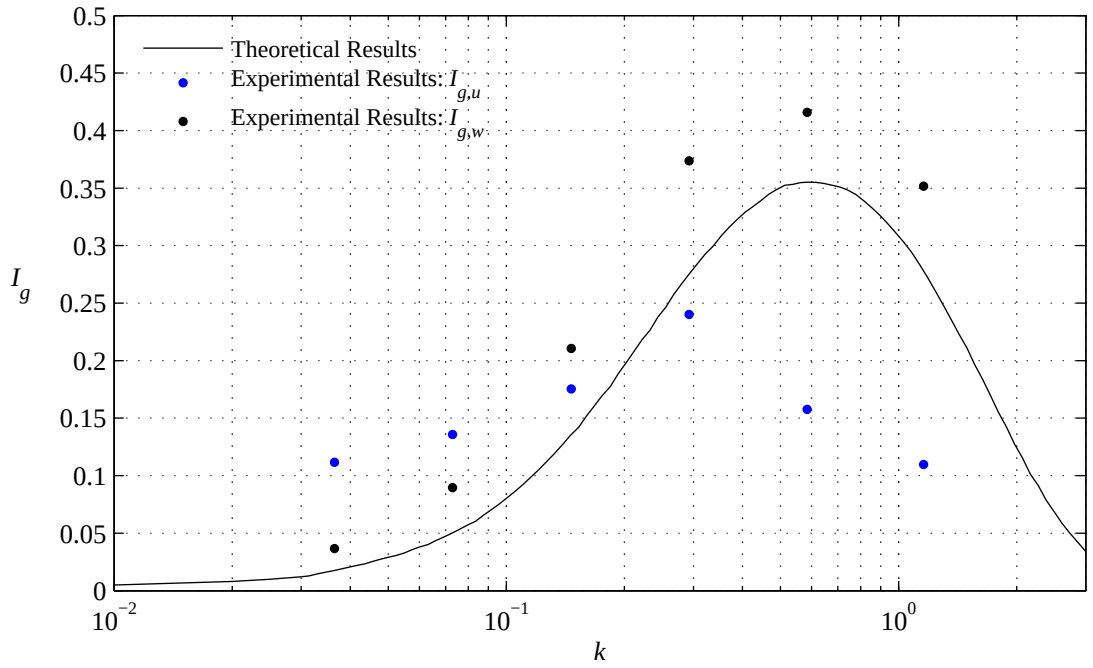

Figure 6.7: Results of the frequency effects on gust intensity for the generation of out-of-phase longitudinal and vertical velocity perturbations: $\varphi = 90°$, $\alpha_0 = 6.0°$, $Re = 5.8 \times 10^4$.

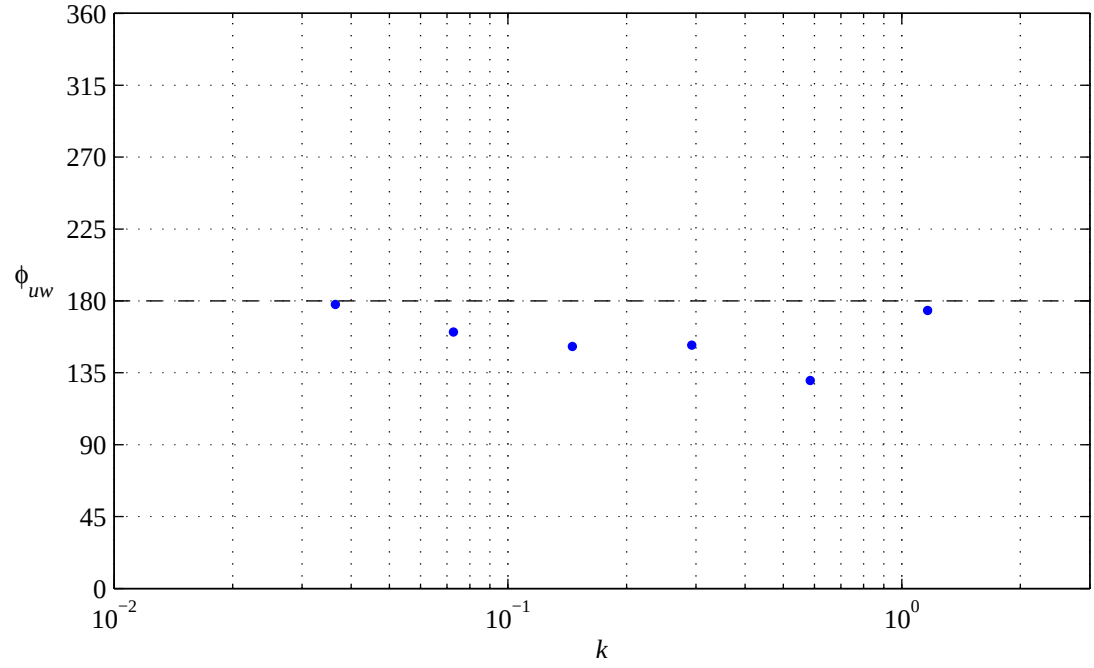

Figure 6.8: Results of the frequency effects on phase lag for the generation of out-of-phase longitudinal and vertical velocity perturbations: $\varphi = 90°$, $\alpha_0 = 6.0°$, $Re = 5.8 \times 10^4$.

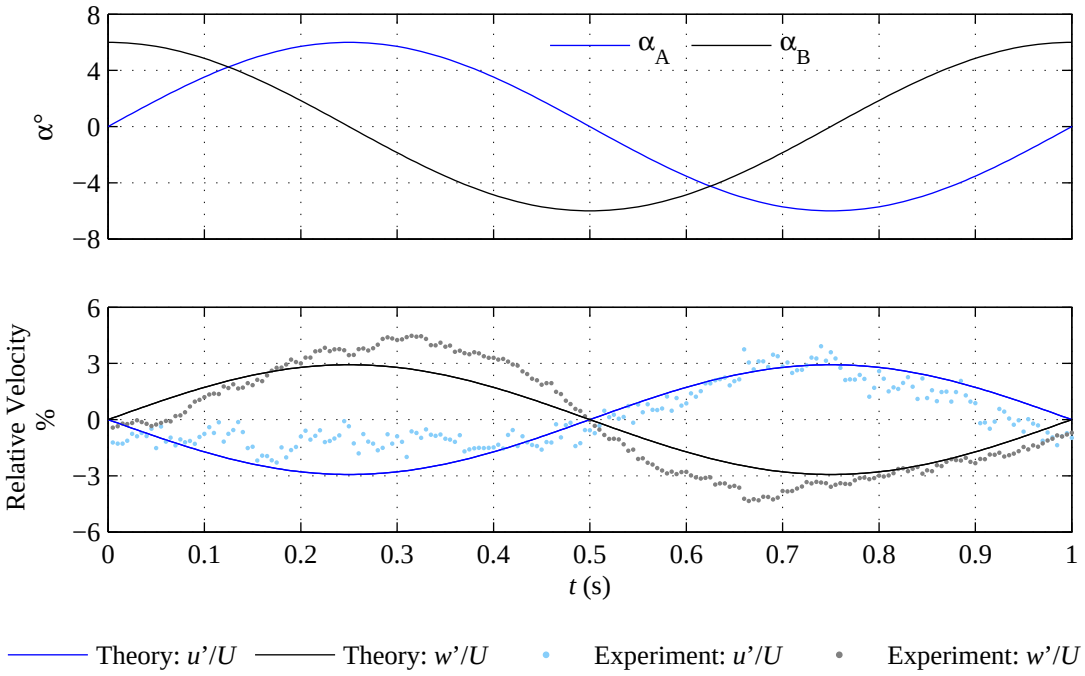

Figure 6.9: Representative plot of velocity time series generated by quadrature phasing of pitching foils: $\varphi = 90°$, $T = 1$s, $\alpha_0 = 6.0°$, $Re = 5.8 \times 10^4$.

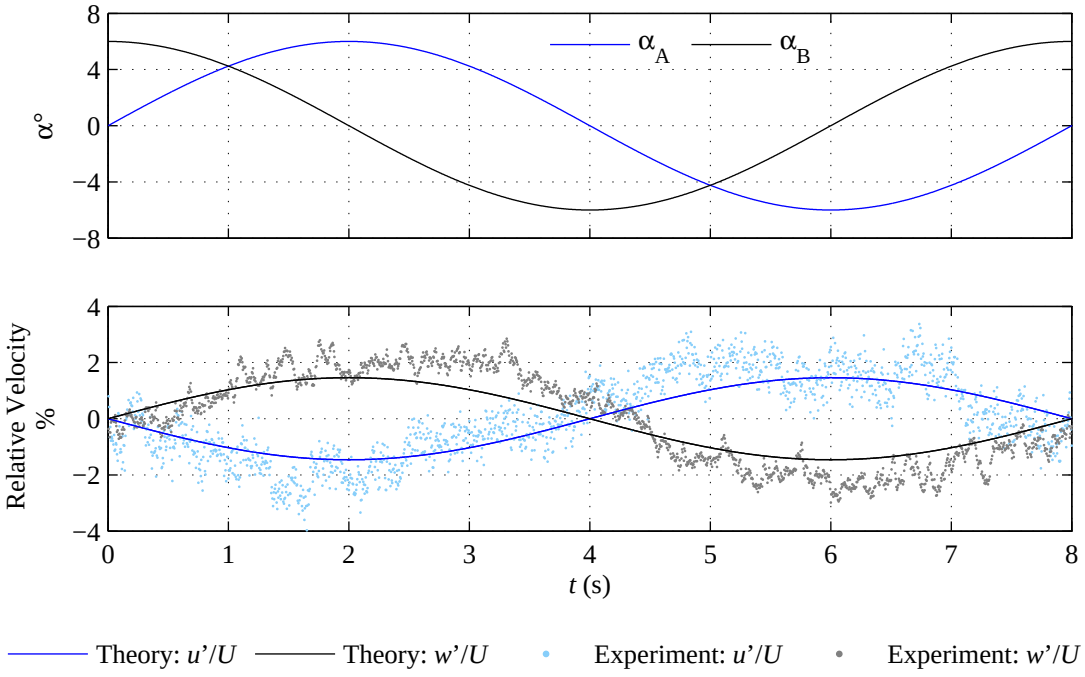

Figure 6.10: Representative plot of velocity time series generated by quadrature phasing of pitching foils: $\varphi = 90°$, $T = 8$s, $\alpha_0 = 6.0°$, $Re = 5.8 \times 10^4$.

6.7 Multiple frequency two-dimensional velocity fluctuations

6.7.1 Specification of foil motion with multiple frequency components

In order to demonstrate the flexibility of the configuration to generate user-defined velocity perturbations independently in both directions as shown in Figure 4.11d, a number of arbitrary foil motions were defined. A total of five arbitrary waveforms were specified, covering a range of frequency components, with the time series of the pitching foil motions being specified in Figure 6.11.

These arbitrary waveforms were developed in two different ways. Waveform 1 and Waveform 2 are defined using a number of frequency components to directly specify the motion path of the pitching foils. The resulting theoretical velocity perturbations were then calculated using the vortex model in the 'forward' direction. The frequencies of all the harmonics used to specify Waveform 2 are a half that of Waveform 1.

The remaining time series, defined by Waveform 3, Waveform 4 and Waveform 5, are calculated by specifying a desired two dimensional velocity perturbations with a number of frequency components and calculating the required foil motion to create these using the 'reverse' solution of the vortex model. The frequencies of all velocity perturbations of Waveform 4 and Waveform 5 are one-half and one-third that of Waveform 3, respectively.

The magnitude of the foil motions are defined in terms of α/α_0 such that the peak amplitude of the pitching motion can be adjusted by the pitch amplitude variable, α_0. Due to the linear theory used in the model, the resulting velocity perturbations will increase by the same factor. The range of pitch amplitudes implemented in the experiments for each waveform are summarised in Table 6.2.

All multiple frequency two-dimensional velocity fluctuation experiments were performed at flow speeds corresponding to $Re = 5.8 \times 10^4$.

6.7.2 Comparison of time series results

The pitching hydrofoils were driven to follow the predefined waveforms of Figure 6.11. The velocity perturbations were acquired for a period of 300s at the central transverse location. In post-processing, the time series were divided into shorter time series whose duration corresponded to the period of the respective waveform. These shorter time series were then averaged to yield the mean velocity response over one period of the waveform. The resulting velocity response is compared with the theoretical response for the case of $\alpha_0 = 6.0^\circ$ in Figure 6.12 and

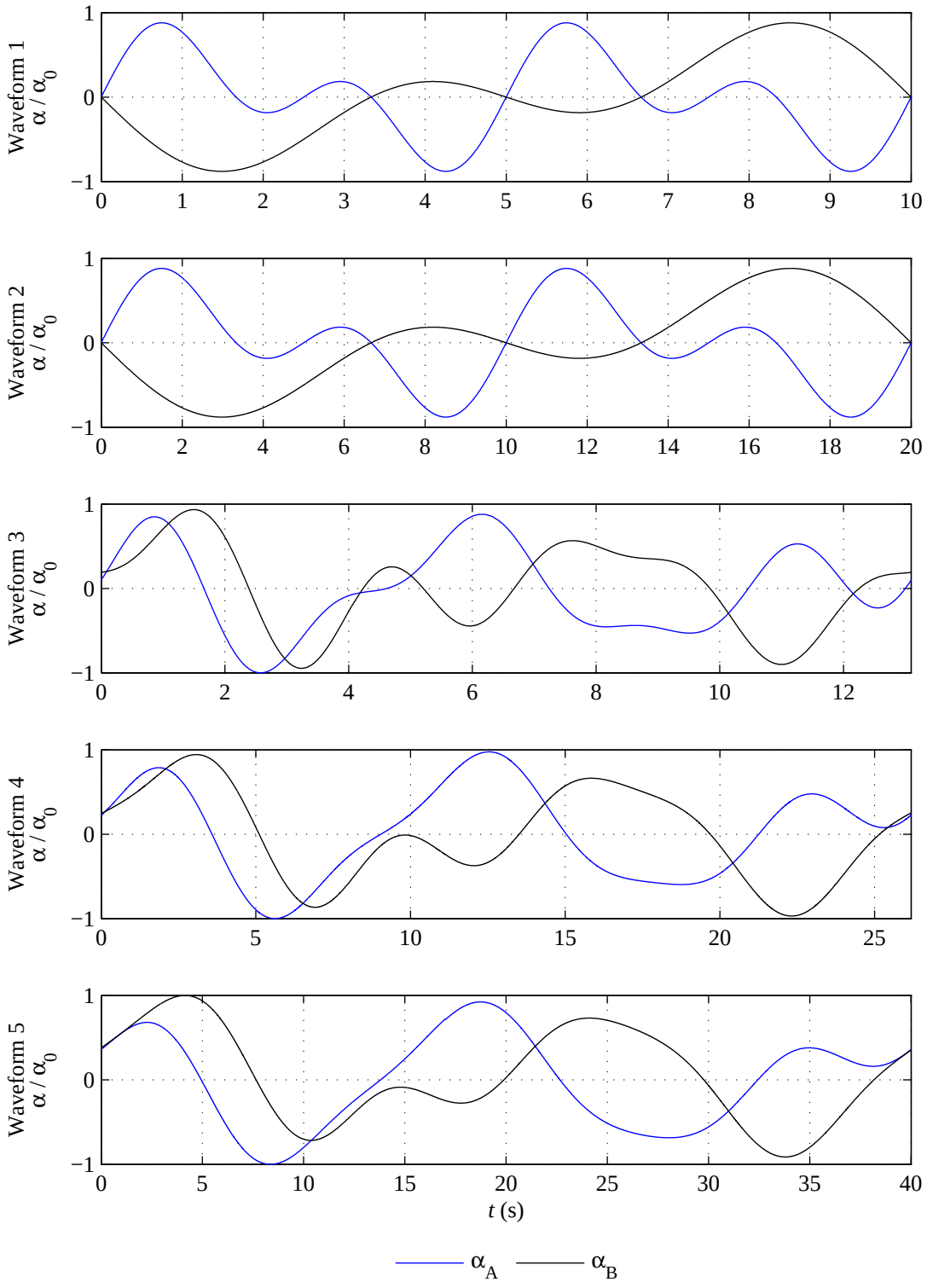

Figure 6.11: Time series of multiple frequency motion of pitching hydrofoils

$\alpha_0 = 10.0°$ in Figure 6.13. The frequency of this average response is displayed at the maximum ADV output frequency of 200Hz, and as such more measurement points are available for the longer duration waveforms. Note that no experimental values were collected for Waveform 5 at $\alpha_0 = 6.0°$.

The agreement between experimental measurements and theoretical prediction is generally good, with some discrepancies. Overall, the match between experimental and theoretical results is better for the longitudinal velocity perturbations than for the vertical direction. In the latter case, the experimental values are consistently lower than the theoretical results.

Waveform 1 shows very close agreement for both the case of $\alpha_0 = 6.0°$ and $\alpha_0 = 10.0°$, whereas Waveform 2 exhibits lower peak values in the measured response relative to the theoretical velocity perturbations. The opposite trend is observed from Waveform 3 to Waveform 5, where the agreement between the experimental and theoretical results improves with the decrease in frequency of the harmonic components used to define the velocity time series.

The spread of the experimental results is seen to be significantly greater in the longitudinal direction than the vertical direction. This can be attributed to the geometric configuration of the transducers in the Nortek Vectrino which are angled at 60° to the transmitted beam direction. This results in a higher accuracy reading in the vertical direction which is more aligned with the receivers than the longitudinal flow direction. This effect is particularly pronounced in dynamic flow conditions such as those generated in this experiment.

6.7.3 Velocity error analysis

To quantify the discrepancies between the measured and theoretical values, the RMS error of the measured velocity perturbation with respect to the theory was calculated for each value of α_0. In order for the RMS metric to be comparable for both the longitudinal and vertical

Table 6.2: Test matrix of multiple frequency foil motion

	$\alpha_0 = 6.0°$	$\alpha_0 = 10.0°$	$\alpha_0 = 12.0°$	$\alpha_0 = 14.0°$	$\alpha_0 = 16.0°$
Waveform 1	✓	✓	✓	-	-
Waveform 2	✓	✓	✓	-	-
Waveform 3	✓	✓	✓	✓	✓
Waveform 4	✓	✓	✓	✓	✓
Waveform 5	-	✓	✓	-	-

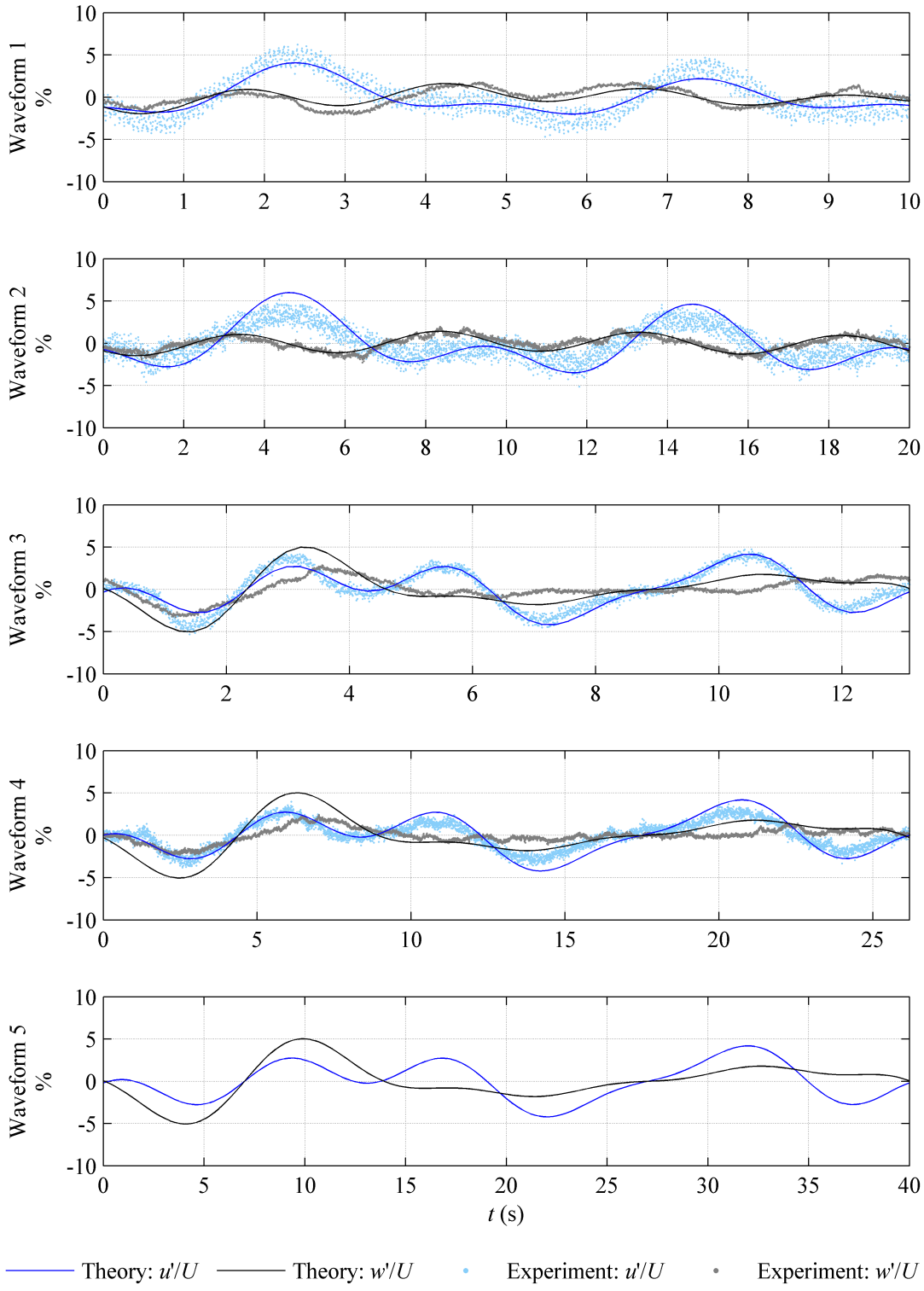

Figure 6.12: Multiple frequency velocity perturbation results: $\alpha_0 = 6.0°$

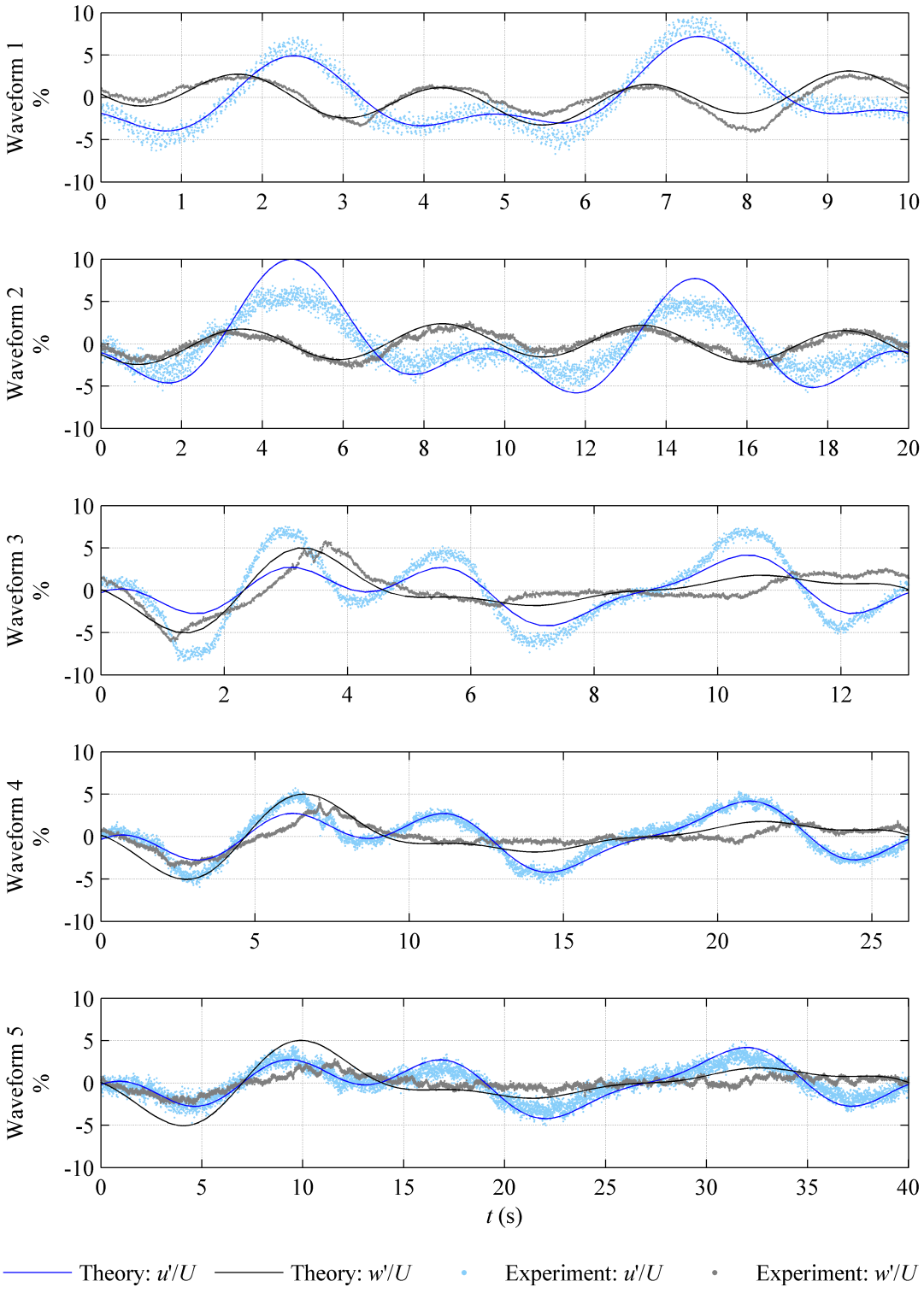

Figure 6.13: Multiple frequency velocity perturbation results: $\alpha_0 = 10.0°$

directions, a low-pass Butterworth filter was applied to the velocity time series. This removed the scatter of the measured points in the longitudinal direction in particular, which was due to the geometric configuration of the ADV as previously discussed.

The metric of the RMS error was calculated using the *absolute error* of the measured velocity time series with respect to the theoretical time series in each direction, as defined by Equation 6.2. Here the subscripts t and e represent theory and experimental results, respectively.

The *relative error* of the experimental time series with respect to the theoretical time series is often a useful parameter for error analysis. However, excessive values result when normalising the time series by values close to zero. By definition, this is the case for the velocity perturbations, and therefore relative errors have not been used in this analysis.

$$\delta\left(u'/U\right)_{RMS} = \sqrt{\left\langle\left(\frac{u'_e}{U} - \frac{u'_t}{U}\right)^2\right\rangle} \tag{6.2a}$$

$$\delta\left(w'/U\right)_{RMS} = \sqrt{\left\langle\left(\frac{w'_e}{U} - \frac{w'_t}{U}\right)^2\right\rangle} \tag{6.2b}$$

The results of this error analysis are shown in Figure 6.17. The amplitude of the pitching motion was observed to affect how well the theory predicts the measured velocity fluctuations, as the static stall angle of the foils was exceeded. At the lowest angular amplitude of $\alpha_0 = 6.0°$ the RMS errors for all multiple frequency waveforms tested was less than 0.3%. Recalling that the static stall angle of the NACA0012 hydrofoils used is approximately 10° at $Re = 5.8 \times 10^4$, it is expected that the linear lift theory will break down at angle of attack exceeding this. This is observed most clearly by the RMS error of Waveform 3, which shows a steady departure from the theoretical values at $\alpha_0 > 10°$. It is interesting to note that the other waveforms show a relatively constant RMS error in the range of 0.05% - 0.3% for $6.0° \leq \alpha_0 \leq 12.0°$.

Another informative method of observing the behaviour of the experimental results relative to the velocity perturbations expected by the theory is the plot the two time series against each other on set of Cartesian axes. In this way, a plot with a gradient of unity represents perfect agreement between the theory and measurements, and deviations from this can be used to identify the limits of the theory. These plots are presented in Figure 6.14 to Figure 6.16, for the representative cases of Waveforms 1-3.

The agreement between the theoretical and experimental velocity perturbation results was quantified using a linear regression analysis on the plots of Figure 6.14 to Figure 6.16. In particular,

the gradient of the linear fit, m, can be used to identify when the measured response is less than that predicted by theory ($m < 1$) or greater than the theoretical prediction ($m > 1$). The results of the linear regression analysis in response to the pitch amplitude are presented in Figure 6.18. For completeness, the gradient is defined by Equation 6.3, where c is a constant of the linear regression.

$$m_u = \frac{u_e - c_1}{u_t} \tag{6.3a}$$

$$m_w = \frac{w_e - c_2}{w_t} \tag{6.3b}$$

The gradient calculated using a linear regression analysis was shown to be relatively constant for the cases of Waveform 1 and Waveform 2 for the pitch amplitudes of $6.0^\circ \leq \alpha_0 \leq 12.0^\circ$. Considering all the values of α_0 for these three cases, the mean value of $m_u = 0.87$ and $m_w = 0.84$.

Other than Waveform 3 at $\alpha_0 \geq 12.0^\circ$, $m_w < 1$ was consistently calculated. As such, the predicted velocity perturbations consistently exceeded the measured values. However Waveform 3 shows an increase in both m_u and m_w as the pitch amplitude increases from $\alpha_0 = 6.0^\circ$ to $\alpha_0 = 16.0^\circ$. For these waveforms, it was found that $m_u < 1$ at low pitch angles which indicated that the theory was overestimating the longitudinal velocity perturbations in these cases. At the higher pitch angles, the gradient developed to values of $m_u > 1$, such that the measured velocity perturbations exceeded those predicted by the theoretical model.

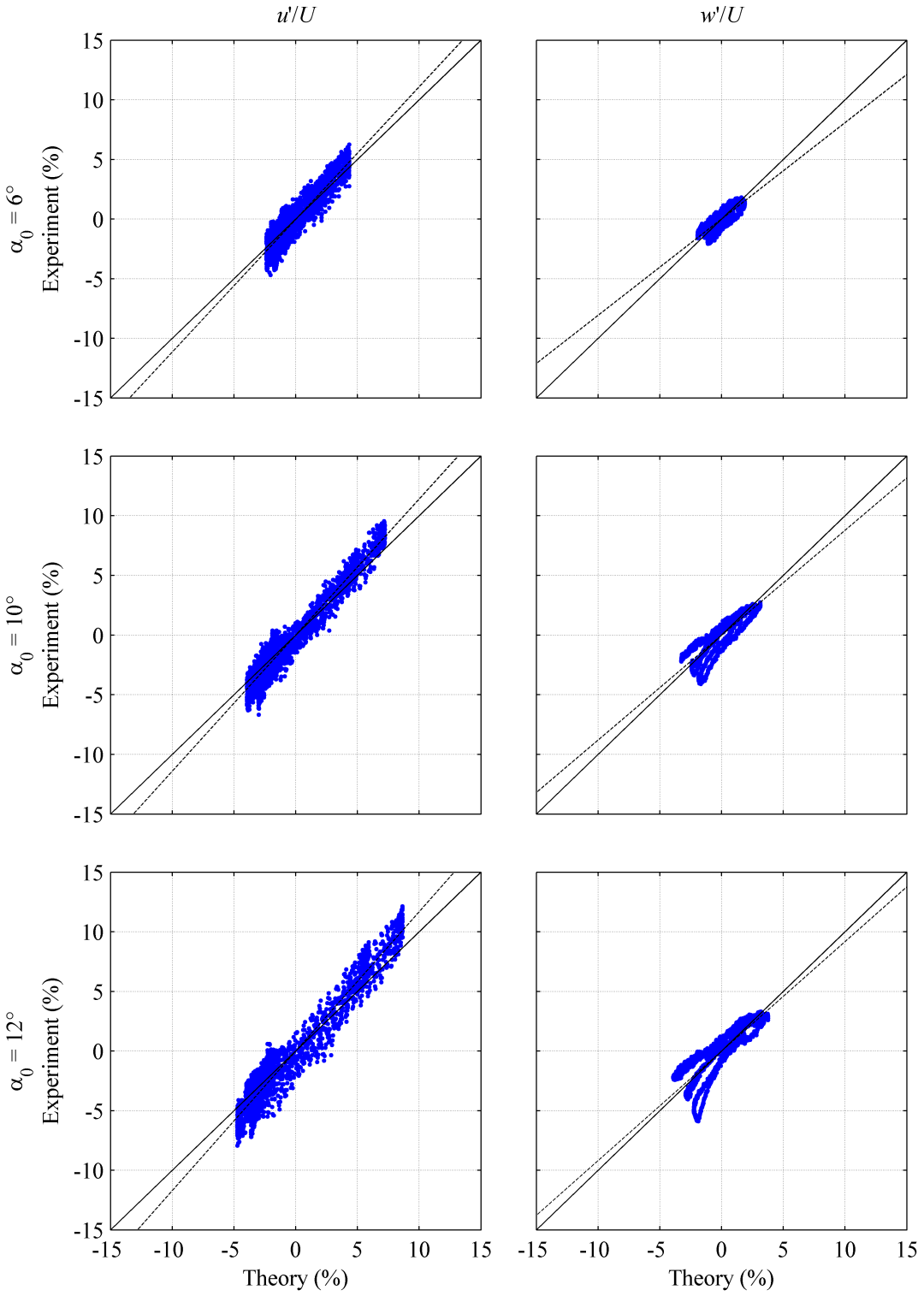

Figure 6.14: Scatter plot of theoretical and experimental results of Waveform 1. The solid line corresponds to a gradient of unity and the dashed line represents the gradient of the linear regression analysis.

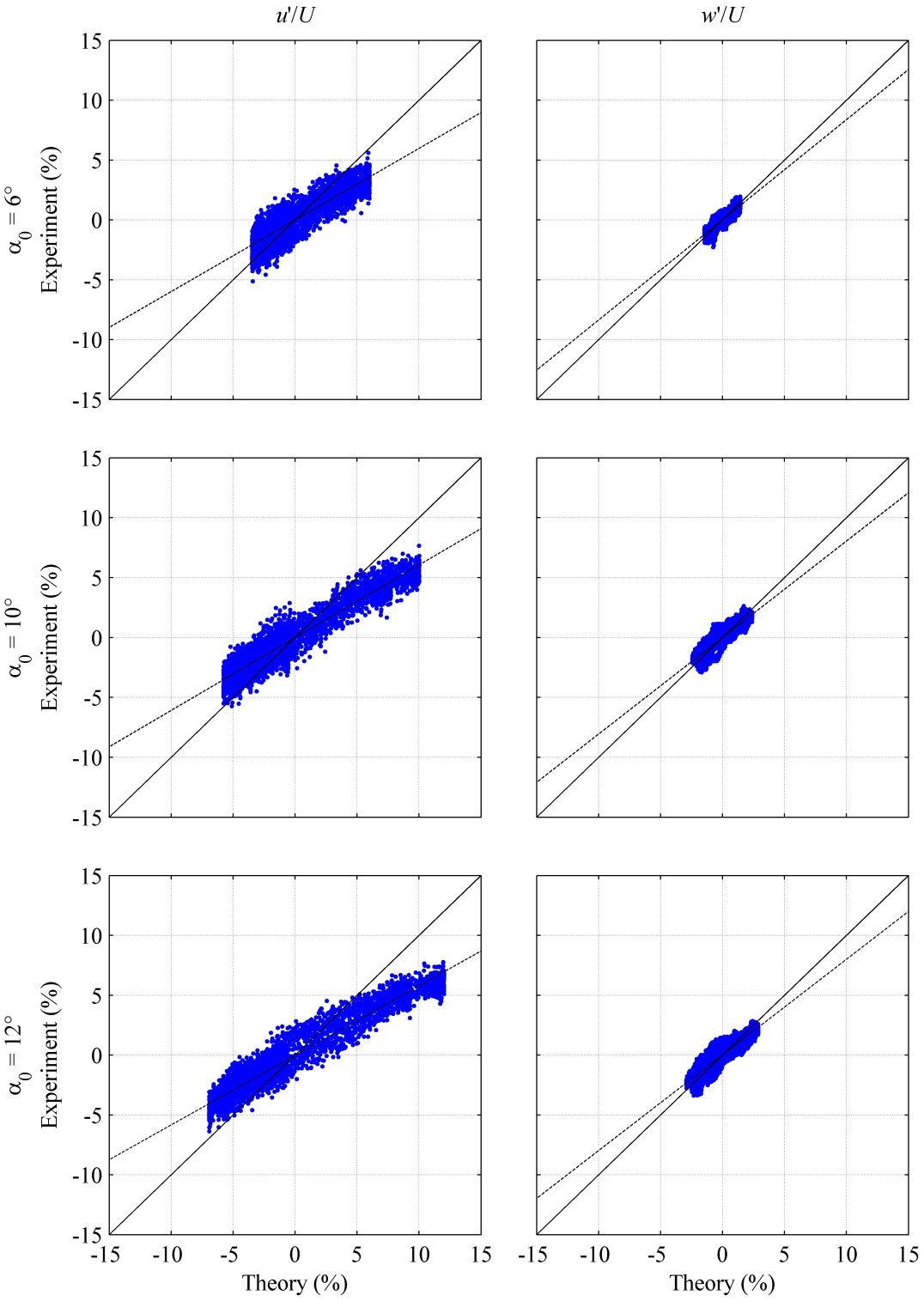

Figure 6.15: Scatter plot of theoretical and experimental results of Waveform 2. The solid line corresponds to a gradient of unity and the dashed line represents the gradient of the linear regression analysis.

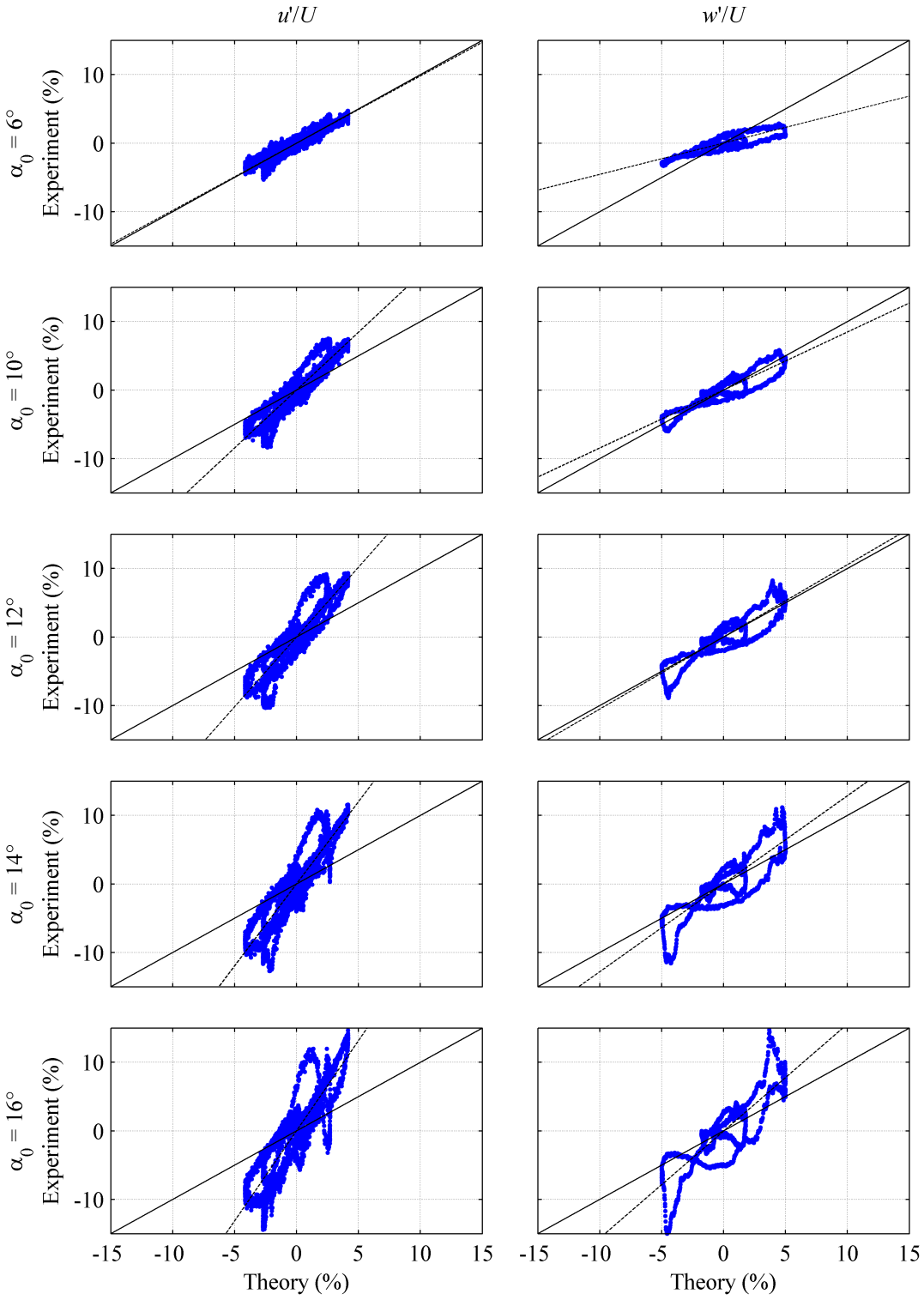

Figure 6.16: Scatter plot of theoretical and experimental results of Waveform 3. The solid line corresponds to a gradient of unity and the dashed line represents the gradient of the linear regression analysis.

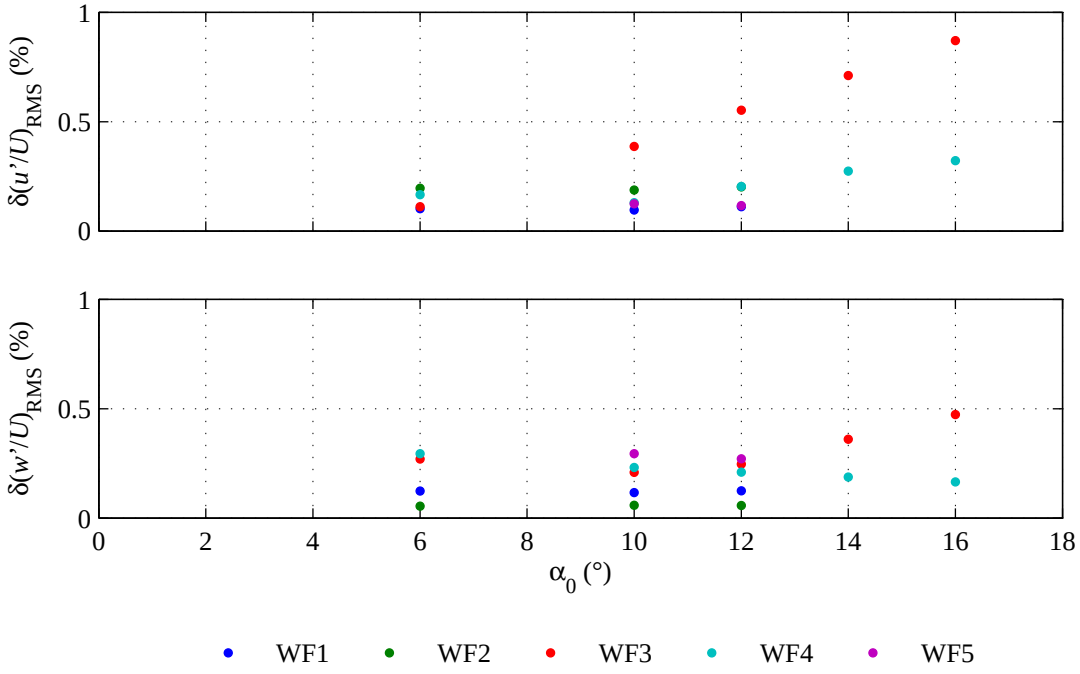

Figure 6.17: Experimental RMS errors for all waveform time series tested.

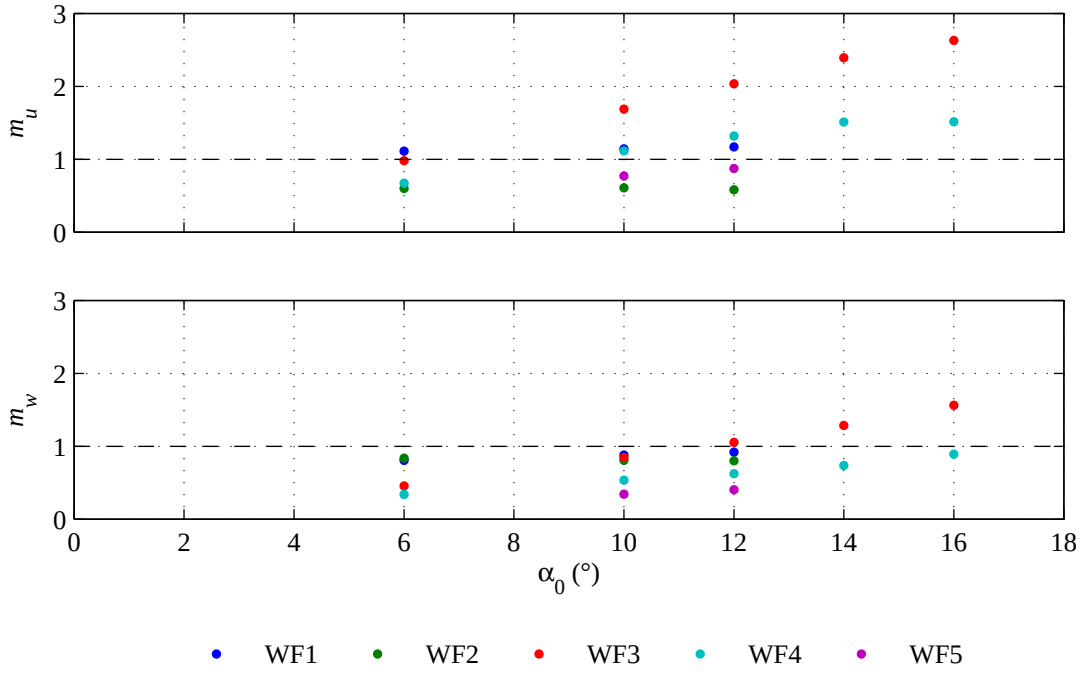

Figure 6.18: Results of linear regression analysis for all waveform time series tested.

6.8 Single frequency force fluctuations

The velocity response measured in the generation of single frequency flow perturbations was used to calculate the unsteady lift response expected on the stationary wing, using the unsteady lift theory described in §4.9.

These were then compared with the lift force measured experimentally by the load cell. This process is summarised by the flow diagram in Figure 6.19.

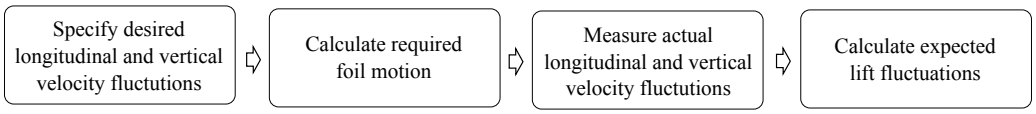

Figure 6.19: Flow diagram of numerical scheme for the generation of velocity fluctuations and calculation of expected resulting lift force.

The results presented in this chapter were measured at the maximum flow speed of $Re = 5.8 \times 10^4$ to maximise the lift forces, and consequently improve the signal to noise ratio of the analogue output of the load cell. The angle of attack of the stationary foil is denoted α_C, and is shown in the positive sense in Figure 5.1.

6.8.1 Vertical gusts

Vertical gusts were generated at a range of driving frequencies with a phase difference of $\varphi = 0°$ and a pitch amplitude of $\alpha_C = 6.0°$. The flow velocity was measured at five transverse locations at $y = \{-100, -50, 0, 50, 100\}$ mm from the vertical longitudinal plane of the flume. These measurements were averaged across the width of the test section at each time step to calculate the effective flow conditions experienced by the stationary wing. The resulting effective velocity time series was then used as the input to the numerical calculation of the unsteady lift described in §4.9 and compared with the measured values. To emphasise the significant deviation of unsteady lift from quasi-steady lifting theory, the quasi-steady lift was also calculated for each case. The comparison of the unsteady results with the quasi-steady results are presented in Figure 6.20. The results of the experimental and theoretical unsteady lift are repeated in Figure 6.21 with an adjusted vertical axis scale for clarity.

The transient development in unsteady lift is observed in the consistent lag of both the unsteady

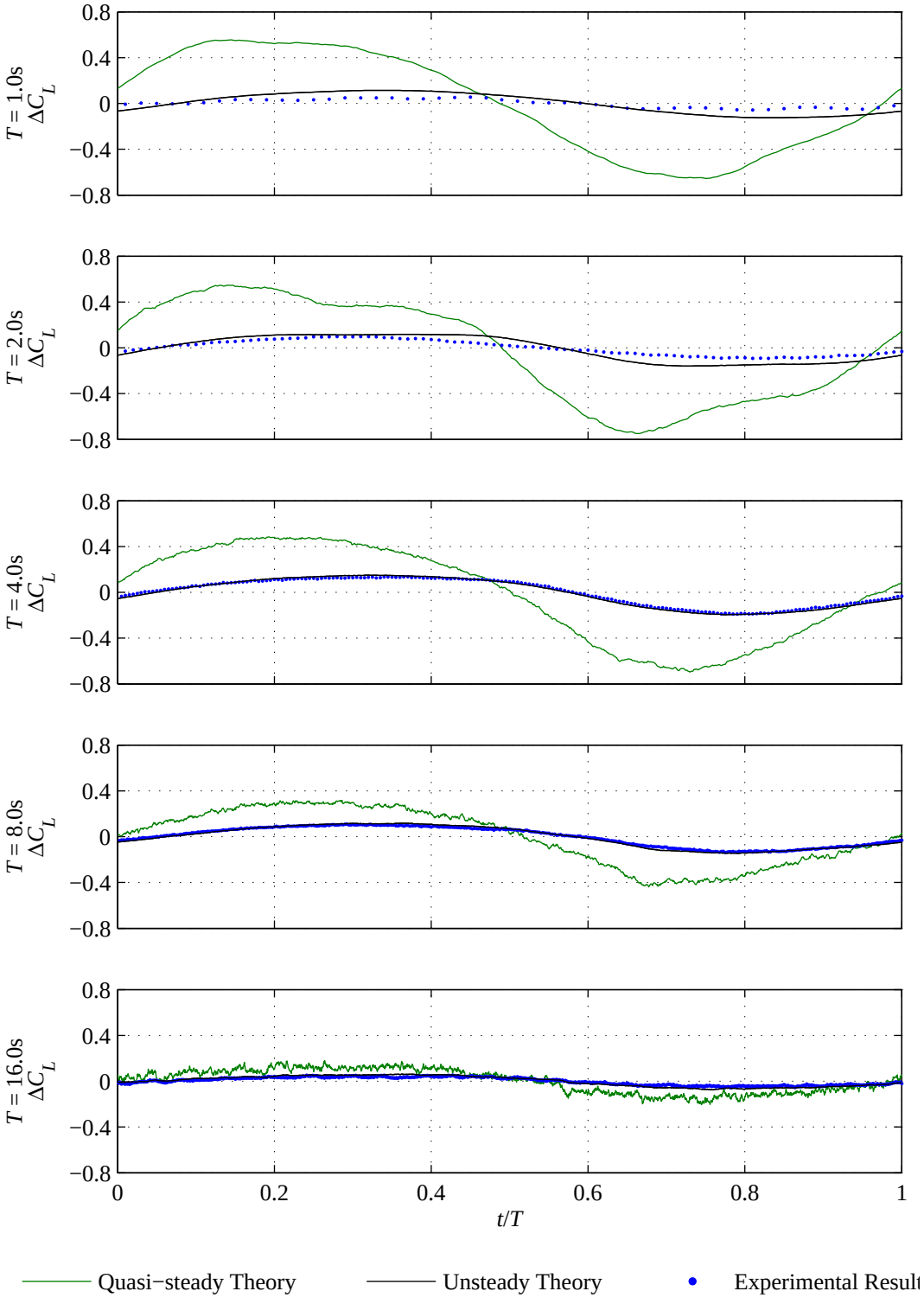

Figure 6.20: Comparison of quasi-steady and unsteady lifting theory with experimental results for a single frequency vertical gust

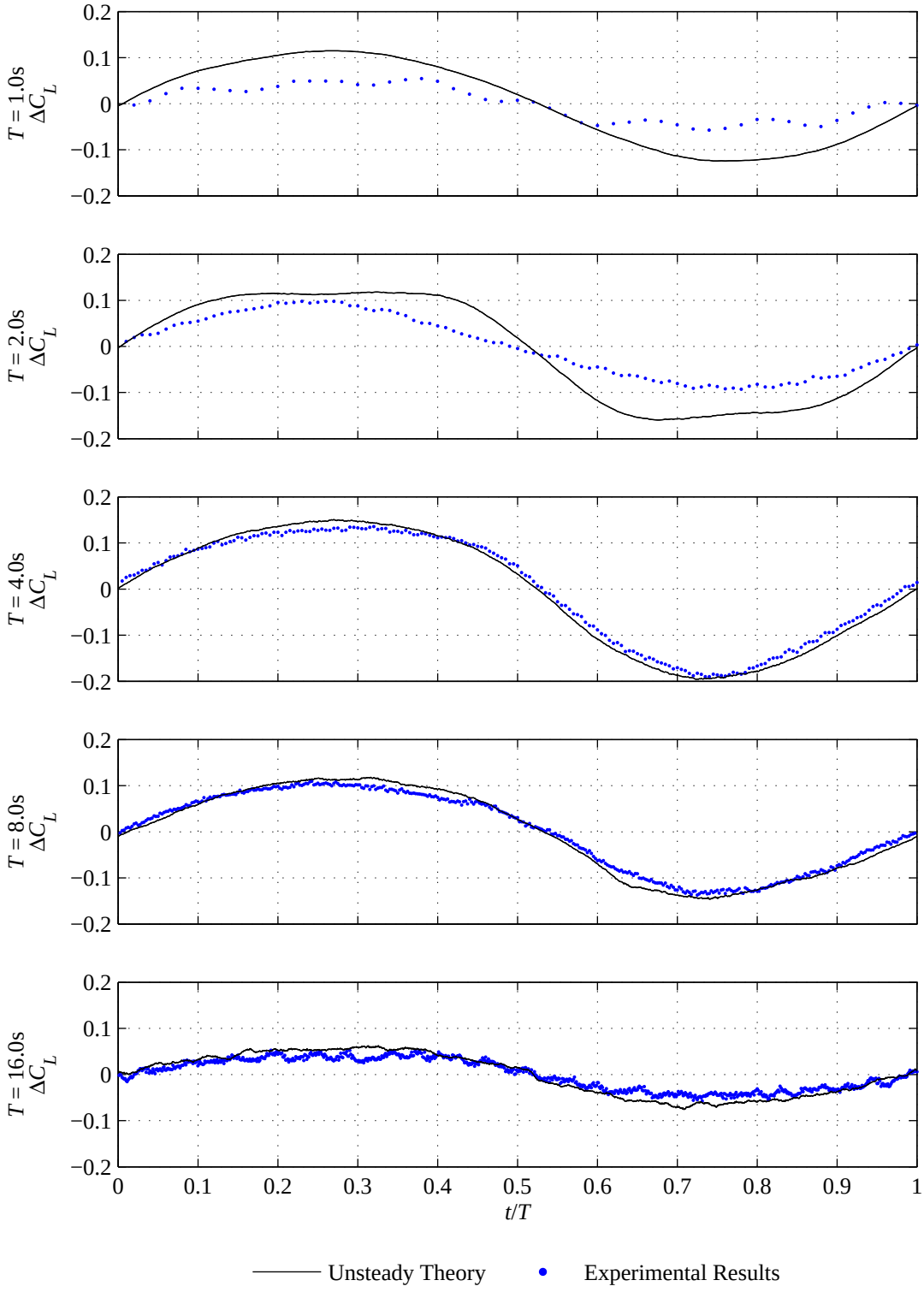

Figure 6.21: Experimental validation of unsteady lifting theory and experimental results for a single frequency vertical gust

and measured lift force, relative to the quasi-steady theory. This is in accordance to the Küssner function which describes how the circulation about a steady lifting surface develops in response to a step change in vertical velocity.

The magnitude of the change in lift coefficient is observed to decrease as the driving period of the pitching foils increases from $T = 1$s to $T = 16$s. This is due to the reduced magnitude of the vertical velocity perturbations at the lower frequencies as the circulation about the pitching foils is shed more slowly and the resulting induced velocities decrease.

The calculation of the expected lift using unsteady lifting theory closely agrees with the experimental results for the lower oscillation frequencies, shown in Figure 6.21. However large discrepancies were observed in the higher frequency gusts studied, with the amplitude of the theoretical fluctuation in lift being greater than twice of that measured for the lowest oscillation period of $T = 1$s.

6.8.2 Longitudinal gusts

Longitudinal gusts were generated at a range of driving frequencies with a phase difference of $\varphi = 180°$ and a pitch amplitude of $\alpha_0 = 6.0°$. In the same way as for the force analysis in the vertical gust, the velocity perturbations were measured at five transverse locations, and integrated across the width of the test section to calculate an effective velocity time series. The theoretical lift on the stationary wing was then calculated using both quasi-steady and unsteady lift theory, and compared against that measured experimentally.

The comparison of the unsteady results with the quasi-steady results are presented in Figure 6.22.

The primary difference in the force response to the longitudinal perturbations is the phase agreement between the quasi-steady and unsteady lift calculations. This contrasts with the phase lag of the unsteady lift theory relative to the quasi-steady lift theory for the vertical perturbation conditions. This can be explained by the difference in the indicial functions of Wagner and Küssner, used in the unsteady calculation of the circulatory component of lift for the longitudinal and vertical flow perturbations, respectively. The initial value of the Wagner function is $\phi(t = 0) = 0.5$, whereas the value of the Küssner function is $\psi(t = 0) = 0$, as shown in Figure 4.3. As such, 50% of the quasi-steady lift for a longitudinal gust is achieved instantaneously with the remainder of the lift developing with time.

Again the experimentally measured forces appear to be less than those calculated using the

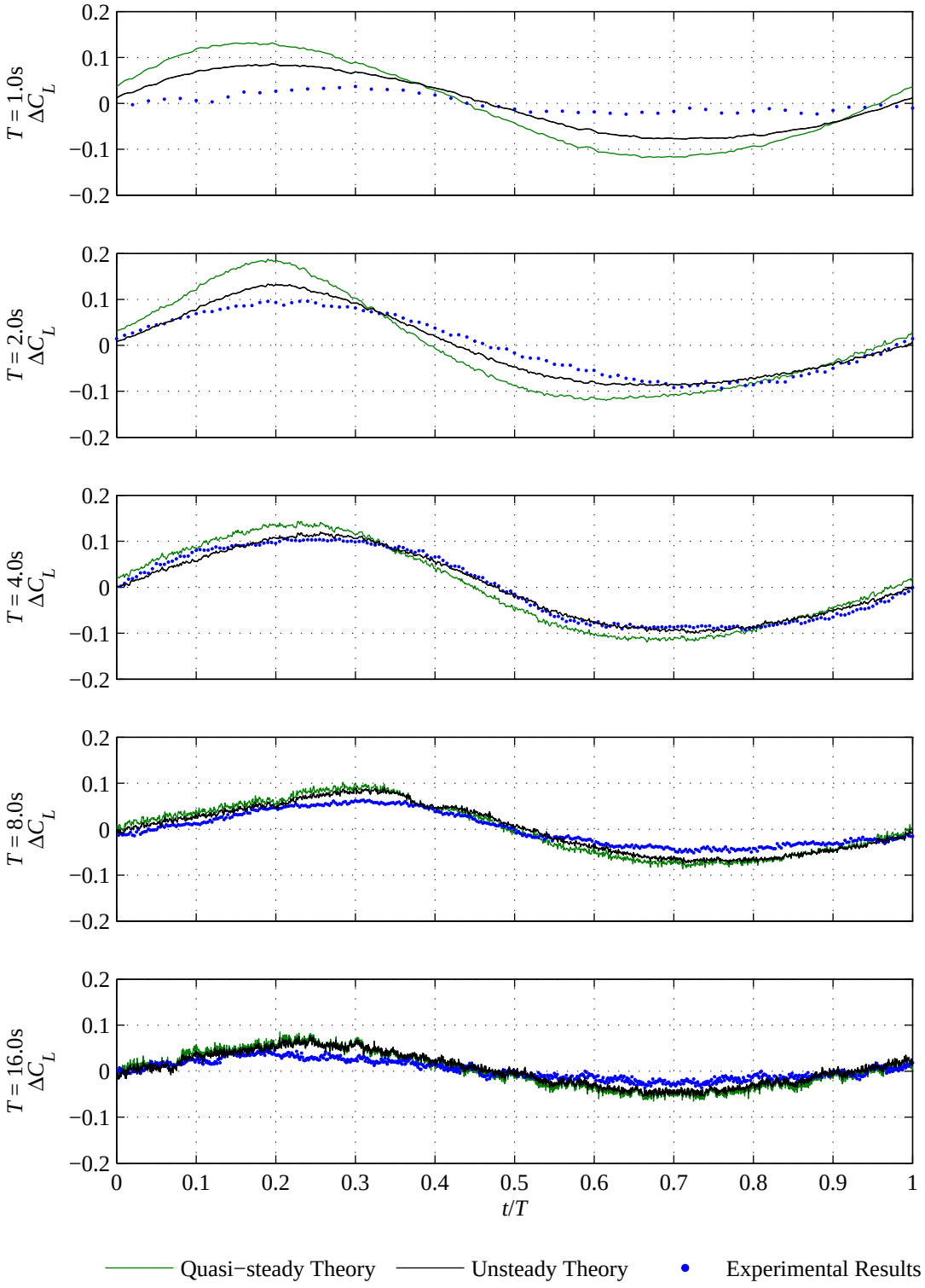

Figure 6.22: Comparison of quasi-steady and unsteady lifting theory with experimental results for a longitudinal gust

unsteady lift theory for all driving frequencies, with the difference being notably greater at the highest driving frequency tested ($T = 1$s).

6.8.3 Comparison of theoretical and experimental unsteady lift

The comparison between the theoretical and experimental unsteady lift results shown in §6.8.1 and §6.8.2 demonstrate close agreement at the lower oscillation frequencies. However increasing large discrepancies are observed as the oscillation frequency is increased.

One observed phenomenon which is likely to have contributed to this effect is the transverse profile of the velocity perturbations near the walls of the test section. As discussed in §6.3.3, the magnitude of the velocity fluctuations decreased at the edges of the test section due to the wall effects, and this effect became more pronounced as the oscillation frequency was increased. The behaviour of the velocity perturbations was not able to be measured to closer than 50mm from the flume walls on either side, equating to 25% of the flume width. As such, the velocity behaviour at the wing tips was not fully characterised in the area of lowest velocity fluctuations, which is likely to have resulted in some overestimation of lift force at the highest driving frequencies.

Furthermore, a reduction in measured lift may be caused by the three-dimensional effects induced by the clearance space between the wing tips and the walls of the test section. This results in wing tip effects which act to reduce the relative difference between the high and low pressure sides of the lifting surface. This causes a decrease in the measured lift relative to the two-dimensional conditions assumed in the theory. This effect is likely to become more pronounced at the higher frequencies when the rate of change in circulation about the stationary foil is greatest.

A further explanation of the discrepancy comes from a closer examination of the relative contributions of the circulatory and non-circulatory lift components. The peak circulatory lift component approaches the steady state value as the driving period of the velocity is reduced. Conversely, the contribution of the non-circulatory, or added mass, component is a function of the flow acceleration, and so increases as a function of oscillating frequency for a given perturbation magnitude. With the deviation of the experimental results from the theory occurring at the highest driving frequencies tested, it is logical to explore the non-circulatory effects in more detail.

The relative contributions of the circulatory and non-circulatory lift coefficients have been explored using the theoretical case of a single frequency vertical velocity perturbation in steady

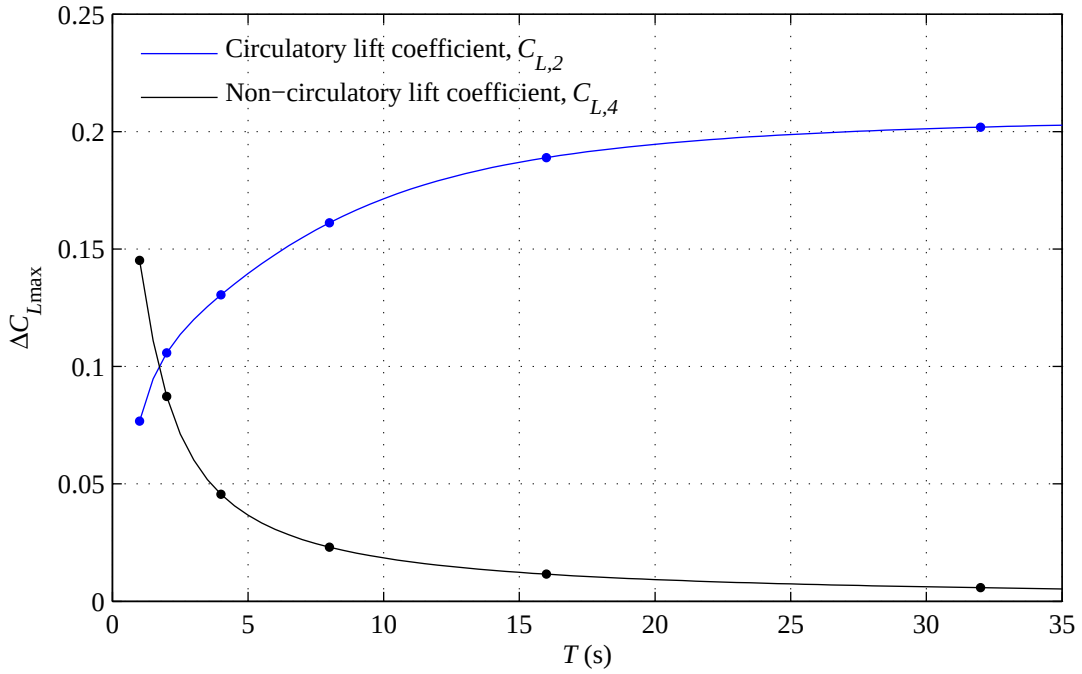

Figure 6.23: Comparison of circulatory and non-circulatory theoretical lift coefficients in response to single frequency vertical velocity perturbations with an amplitude of $|w| = 0.05U$ and period, T. The oscillation periods marked with a circle correspond to those tested in Figure 6.21

longitudinal flow, as investigated experimentally in §6.8.1. For this analysis, the amplitude of the vertical velocity perturbation was set at a constant value of $|w| = 0.05U$, and the influence of fluctuation period, T, was explored within a range to include all the results shown in Figure 6.21. The peak variation in lift coefficient attributed to both the circulatory and non-circulatory effects was calculated using the theory presented in §4.9, and the results are shown in Figure 6.23.

This theoretical case clearly shows that the added mass effects dominate the forces on the foil when $T = 1$s, and are of similar importance to the circulatory lift effects when $T = 2$s. Recalling the results presented in Figure 6.21, these cases correspond with the experiments whereby the theoretical lift coefficient exceeded the measured lift coefficient by the greatest amount. This suggests the overestimation of the effective apparent mass used in the non-circulatory lift calculation, assumed to be equal to $M_a = \pi\rho c^2/4$ (Bisplinghoff *et al.*, 1996; Leishman, 2006). This function represents the mass of a cylinder of fluid enveloping the lifting surface, with a diameter equal to the chord length. As this term has been shown to dominate the forces at the higher fluctuation frequencies examined, the results of the experiments presented herein suggest that an assessment of its appropriateness would form the basis of interesting future work.

6.9 Multiple frequency force fluctuations

The final aim of the experimental work was to verify the unsteady lifting theory under the conditions of combined vertical and stream wise velocity perturbations. Due to restrictions in access to the flume facilities, limited results were obtained for these flow conditions. Nevertheless, the dynamic force resulting from a single two-dimensional time series is examined in this section for completeness.

The flow conditions used for the analysis are generated through the pitching foil motion specified by Waveform 2 in Figure 6.11 which generated the velocity time series shown in Figure 6.12. The results of each component of lift, and the final combined lift coefficient are shown in Figure 6.24.

The predominant lift coefficient was $C_{L,2}$, corresponding to the circulatory lift term due to the vertical flow perturbations, though variations circulatory lift due to the longitudinal flow perturbations, $C_{L,1}$, were also apparent. For this particular velocity time series it is observed that the added mass effects are negligible due to the relatively low accelerations in both the longitudinal and vertical directions.

Agreement between the experimental and theoretical results was again achieved for the majority of the time series. As with the single frequency force measurements, the experimental results were observed to be lower than the theoretical unsteady lift calculations. This could be attributed to the aforementioned three-dimensional effects induced by the flume walls effects as well as the clearance between the wing tips and the walls of the test section.

Fluctuations in the force measurement were observed at a number of harmonics greater than the highest driving frequency of the pitching foils. The frequency where this was observed most clearly is at 2.19Hz. This is visible in the single frequency force results when $T = 16$s, particularly in Figure 6.21. One explanation for this phenomenon is an inherent mechanical resonance of the sensor-strut-foil system. The stationary foil configuration was designed to be a 'stiff' system, such that the resonance was significantly higher than the excitation frequency. The lowest resonance frequency observed is over twice the highest excitation frequency, however this phenomenon could be suppressed through the optimisation of the force measurement setup in future work.

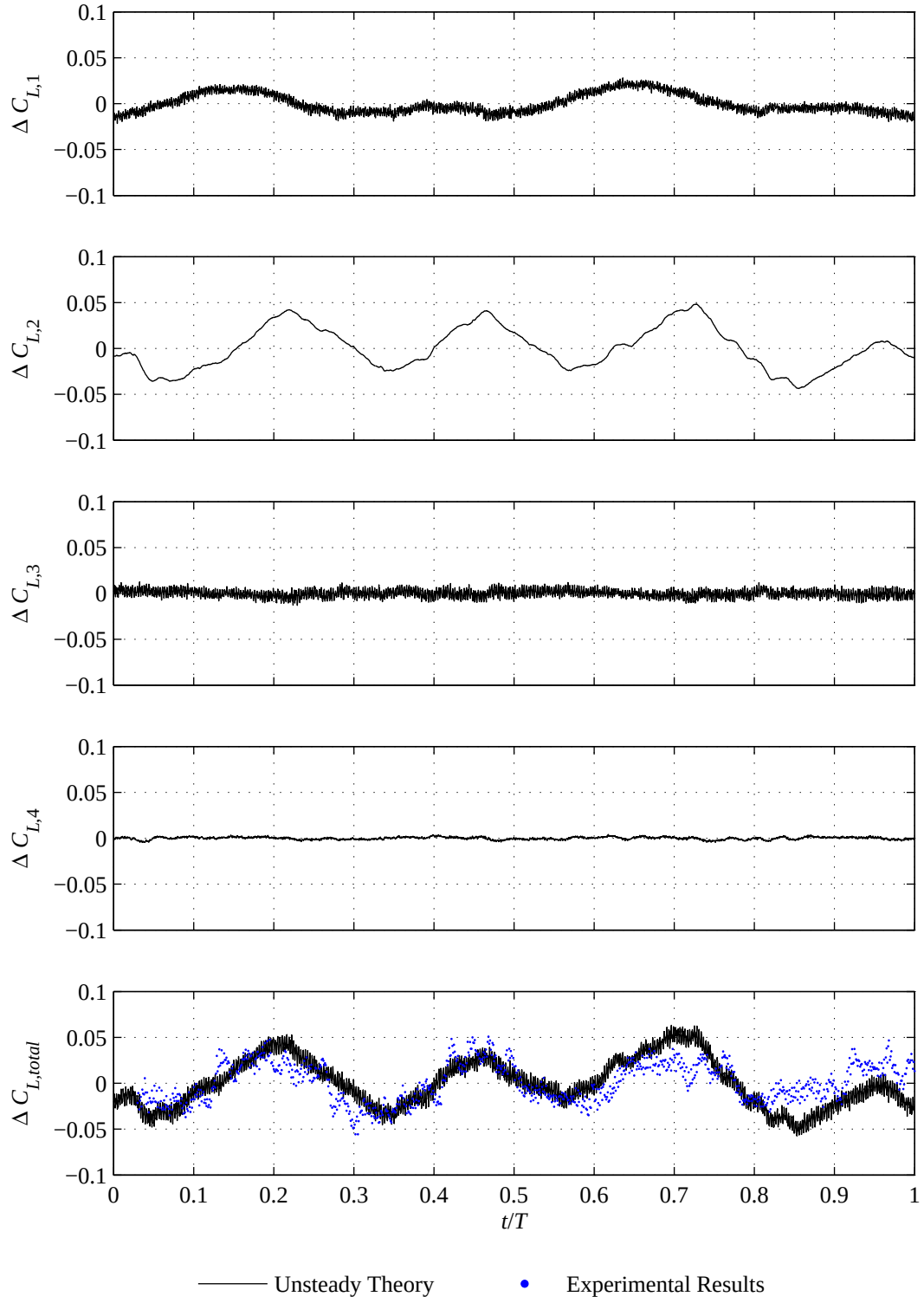

Figure 6.24: Experimental validation of unsteady lifting theory and experimental results for two dimensional velocity time series: $T = 20.0$s

6.10 Chapter conclusions

6.10.1 Overview

This chapter presents the results of the development of an experimental facility with the ability to introduce independent and controllable velocity perturbations in two dimensions in a recirculating water flume. This apparatus is designed to enable the study of dynamic loads in unsteady flow conditions for a range of applications. In this study a stationary hydrofoil has been used to demonstrate this ability, as the key component of the Active Gravity Base design.

6.10.2 Generation of unsteady velocity

To begin, the generation of single frequency, one-dimensional velocity perturbations was considered by driving the pitching foils at the same frequency, with a phase difference of $\varphi = 0°$ and $\varphi = 180°$ to generate velocity perturbations in the vertical and longitudinal directions, respectively. These tests were performed at two Reynold Numbers: $Re = 3.8\times10^4$ and $Re = 5.8\times10^4$.

The resulting gust intensities for both flow speeds demonstrated the same characteristic deviation from the theoretical gust intensity as the driving frequency was decreased. As previously discussed, this is likely to be due to the non-circulatory effects of the pitching hydrofoils. More specifically, a redirection of the water is observed in the case of the in-phase oscillation of the pitching foils, which is independent of the amount of vorticity in the wake. This resulted in an asymptotic gust intensity of $I_{g,w} \approx 0.1$ as $k \to 0$. A significant under-prediction of the longitudinal gust intensity was also observed when the pitching foils were driven out of phase for all but the highest driving frequencies. Again this can be attributed to the non-circulatory effect of the converging-diverging nozzle created between the two foils in this scenario. Both of these non-circulatory effects are expected to diminish as the relative spacing between the foils (z_0/c) is increased. This could not validated due to the constricting dimensions of the present experimental facility, but would be a useful study in future research.

Single frequency two-dimensional velocity perturbations were introduced by driving the pitching foils with quadrature phasing ($\varphi = 90°$). While the measured vertical velocity perturbations showed close agreement with the results predicted by the numerical model, the measured gust intensity characteristics of the longitudinal fluctuations exhibited significant discrepancies. Specifically, the frequency of the maximum gust intensity derived experimentally was lower than that of the peak response of the numerical model. The gust intensity was also significantly lower than the predicted response at driving frequencies greater than the frequency of maximum response. The phase difference between the vertical and longitudinal flow perturbations

was determined using a cross-correlation analysis, with expected phase difference expected to be $\phi_{uw} = 180°$. The measured phase differences ranged between $130° \leq \phi_{uw} \leq 178°$, with a mean of $\langle\phi_{uw}\rangle = 174°$.

To demonstrate the flexibility of the configuration, the motion of each pitching foil was defined by a position time series with multiple frequency components. Waveform 1 and Waveform 2 defined a motion path with two frequency harmonics for each foil. The expected velocity time series was then calculated from the foil time series using the numerical model in the forward direction. Waveform 3, Waveform 4 and Waveform 5 were calculated from by the numerical model in the reverse direction, to generate a pre-defined velocity time series with a number of frequency harmonics. The experimental results of this analysis showed qualitative agreement for the lower pitch amplitude of $\alpha_0 = 6.0°$, however greater discrepancies were observed in the velocity time series when the pitch amplitude was increased to $\alpha_0 = 10.0°$, which corresponded with the approximate angle of static stall. The mean RMS error the normalised velocity fluctuations was $\delta(u'/U)_{RMS} = 0.27\%$ and $\delta(w'/U)_{RMS} = 0.21\%$.

6.10.3 Measurement of dynamic loading on stationary wing

The key application of the pitching foil system is the experimental measurement of the dynamic response of bodies exposed to unsteady incident flows. To demonstrate this, the lift on a stationary hydrofoil instrumented with a load cell and positioned at a the mid-height between the two pitching foils was measured at the downstream location of $x = 7c$.

The symmetrical NACA0012 hydrofoil profile used was representative of those proposed in the design of an AGB. As such, the experimental forces measured on the hydrofoil were used to verify the predicted performance of the proposed unsteady lift calculations in dynamic inflow conditions within the context of the AGB design.

The experimental schedule began with the measurement of the lift force oscillations under a single frequency one-dimensional velocity fluctuation in the vertical direction. The significant deviation from quasi-steady lifting theory was demonstrated, particularly for high frequency flow perturbations. The unsteady lifting theory was also seen to overestimate the magnitude of dynamic lift response measured for the high frequency vertical perturbations. This could be attributed to three-dimensional effects caused by the presence of the flume walls as well as the clearance between the wing tips of the stationary foil and the walls of the test section. The important of the effective mass parameter used in the calculation of the non-circulatory lift component has also been explored. The lag in the development of the unsteady lift, relative to

the quasi-steady response was closely matched by the experimental results and is attributed to the use of the Küssner function in the unsteady lift calculation.

A comparison of theoretical and experimentally measured lift fluctuations was also performed for single frequency one-dimensional velocity perturbations in the longitudinal direction. The calculated unsteady lift assumes an initial value equal to 50% of the quasi-steady lift coefficient, as described by the Wagner function. This results in a closer agreement between the unsteady and quasi-steady results than for the case of vertical gusts, both in terms of amplitude and in terms of lag.

To conclude the experimental validation of the unsteady force analysis, the lift was measured on the stationary wing exposed to the two-dimensional velocity time series generated by the combination of pitch motions defined by Waveform 2. For this particular set of conditions, the circulatory lift in the vertical direction, $C_{L,2}$, exhibited the greatest fluctuation in lift, while the contribution of the circulatory lift due to the fluctuations in the longitudinal direction, $C_{L,1}$, was also observed. At the reduced frequencies of this particular time series, the added mass effects of $C_{L,3}$ and $C_{L,4}$ were seen to be negligible. The limited availability of the experimental facility reduced the range of velocity combinations explored. Further investigation in this area would therefore be of great interest.

Chapter 7

Conclusions

7.1 Contributions

The underlying context of this research was to develop the understanding of Active Gravity Base performance in unsteady flow conditions. Through this research, advancements were made in both the understanding of the tidal stream environment as well as laboratory scale testing of such an operating principle. In doing so, the present author believes that the contribution of this thesis also extend to inform the design of generic hydrodynamic components in a tidal turbine installation. Specifically, the results included herein may be useful inputs to the design specification of turbine blades as well as existing fasting techniques in energetic tidal sites.

7.1.1 Variations in tidal stream velocity

Preliminary considerations of the longitudinal and lateral stability of the AGB concepts prompted the analysis of the directionality of tidal flows with averaged hourly data from the waters of the northern United Kingdom. Though the correlation between the directionality and the flow energy may have been expected from experience, this relationship was quantified using the normalized ratio of eigenvalues of a principal component analysis (PCA) of 711 tidal records. It is believed that this study represents a progression in the understanding of tidal directionality. This analysis was published in Renewable Energy (Harding and Bryden, 2012b).

The analyses presented on the magnitude of high frequency velocity perturbations is a significant contribution to the understanding of the unsteady loads experienced by installations at energetic tidal locations. While spectral analyses are common, and bulk turbulence parameters such as Turbulence Intensity exist, such approaches result in the loss of information of the turbulent behaviour in the time domain. Specifically the peak fluctuations, which are key inputs to the mechanical design, are no longer able to be identified. Early stages of this analysis were published in the proceedings of the European Wave and Tidal Energy Conference (Harding *et al.*, 2011).

7.1.2 Generating two-dimensional velocity fluctuations in laboratory scale tests

The progress made in recreating a two-dimensional velocity time series for laboratory scale experiments is another important contribution of this research. The operating principle of twin pitching foils was adopted from existing studies, which used the configuration to generate one dimensional flow fluctuations at a range of discrete frequencies. The present work explored the ability to generate independent two-dimensional flow fluctuations through the relative motion of the pitching foils in a recirculating water flume. This was approached in the first instance by calculating the velocity perturbations expected from known foil motions, referred to herein as the 'forward solution'. The reverse solution was then developed to allow a desired velocity time series to be used as an input, and the required foil motion to generate this was then calculated. The development of this model was published in the Journal of Fluid Mechanics (Harding and Bryden, 2012c).

Experimental apparatus was designed, fabricated and installed by the present author to validate the theory developed in this thesis. The results of these experiment supported the theoretical calculations overall, with some discrepancies. In particular, the experimental results demonstrated the ability to generate two-dimensional velocity perturbations with both single and multiple frequency components. The present author is not aware of any other demonstration of this ability using the twin foil configuration.

7.2 Summary of conclusions

Conclusions specific to each chapter were presented throughout the thesis. The most important of these are reiterated below in order of chapter appearance.

A positive correlation exists between the available energy flux and directionality in the tidal flows of the Northern United Kingdom.

A conservative model of the flow velocity as a function of direction followed a Gaussian distribution. A directional analysis of the force and moments on an existing AGB geometry indicated that, under steady flow conditions, the lowest safety factor was associated with longitudinal slip.

The preliminary directional force analysis indicated that the lateral drag loads were low relative to those in the longitudinal direction. This was primarily due to the thrust force of the turbine which is aligned with the longitudinal direction.

Indicative magnitudes of maximum annual flow perturbations were predicted using a point-

over-threshold extreme value analysis. When a 0.5s moving average was applied to the data, instantaneous flow fluctuations in the longitudinal and transverse direction of up to 40% of the mean flow speed were predicted.

Anisotropic fluctuations were observed at the higher frequencies considered, with the measured vertical fluctuations consistently less than the horizontal fluctuations of the same effective timescales.

Tidal velocity measurements using an Acoustic Doppler Current Profiler (ADCP) were shown to be inadequate for use in such an analysis, when compared to the benchmark of the Acoustic Doppler Velocimeter (ADV) measurements.

An experimental facility was developed to generate controllable two-dimensional flow fluctuations at a specific location in a recirculating water flume. This was achieved through the use of two position-controlled pitching hydrofoils.

The interaction of the wake vorticity of each foil was used to induce independent longitudinal and vertical variations in the mean flow speed. The theoretical performance of the twin-foil configuration was developed using a planar wake vortex model and classical unsteady lift theory.

Initially the vortex model was developed to calculate the velocity perturbations on the plane of symmetry between the foils which resulted from a specified time series of foil motions. It was then developed to enable the 'reverse solution' to be solved. That is, the required foil motion time series to generate a desired velocity time series was able to be calculated.

The numerical model predicted that the twin foil configuration was able to generate significant flow fluctuations within the range of reduced frequencies $0.06 \leq k \leq 1.9$, with a peak gust intensity of $I_g = 0.5$.

An experimental validation of the theoretical model was performed using single frequency foil motions with phase angles of $\varphi = \{0°, 90°, 180°\}$. The experimental results for single frequency oscillations matched the theoretical predictions, with some offset error at low frequencies. This was predominantly attributed to non-circulatory effects which are not included in the numerical model, and result from the restrictive dimensions of the water flume.

The ability for the twin foil configuration to generate independent two dimensional velocity perturbations was also verified experimentally. Again, the experimental results agreed with the theoretical prediction for the majority of the time series.

The theoretical lift force on a stationary hydrofoil subjected to unsteady flow conditions was calculated using the superposition of the unsteady lift due to both the varying longitudinal and vertical velocity components. Each contribution was comprised of both a circulatory and non-circulatory lift term.

The lift force was measured on a stationary wing located in the unsteady flow conditions generated by the twin pitching foils. The experimental measured lift and the theoretically measured lift were compared for a number of single frequency flow oscillations, as well as a single two-dimensional, multiple frequency velocity time series. Again, overall the experimental values agreed with those predicted with the theory used. The discrepancies at high frequencies were attributed to the influence of the flume walls, the three-dimensional tip effects resulting from the clearance gap between the wing tips and the walls of the test section, as well as the effective mass parameter used in the calculation of the non-circulatory lift component.

7.3 Further work

This section highlights suggested paths of ongoing research. These are presented in order of appearance of the contributions described within this thesis.

7.3.1 Variations in tidal stream velocity

The statistical reliability of the extreme value analysis performed within Chapter 3 was limited by the duration of high frequency data acquired from energetic tidal sites. The duration of available data is expected to increase in the future, with the limitations of standard ADCP measurements becoming evident when high temporal and spatial resolution is required. It is anticipated that a data set of comparable quality to the original analysis with the duration of one year would greatly improve the accuracy of the extreme value analysis.

One technique to artificially increase the duration of available date is introduced by Peterka (1992), whereby a theoretical ‘super-station’ of data is made up of measurements from a number of separate, and theoretically independent acquisition stations. The use of such a methodology may be of benefit in the near future in the case of a number of relatively short duration data sets becoming available.

The application of the present extreme value analysis is limited to the effects of ambient turbulent flow conditions at a specific location. It is probable that these conditions are site specific. Quantifying the inter-site variation of the maximum flow fluctuations would be great interest

within the context of both the AGB performance and other aspects of tidal turbine design.

Due to the meteorological conditions during the acquisition of the present data set, the perturbation magnitudes measured neglect such influences as wave orbitals, wind driven flows and the effects of storm surge. It is expected that such factors may significantly influence the magnitude of the velocity fluctuations at other tidally energetic sites. As such, the addition of other drivers of unsteady flow velocities should be considered in future analysis. The magnitude of the 'worst-case' unsteady velocity therefore has the potential to significantly exceed that predicted by considering ambient turbulence alone.

With regard to the application of AGB performance, the maximum velocity perturbations may be expected to increase the effective angle of attack of the flow in such a way that dynamic stall is induced. The simultaneous decrease in lift and increase in drag associated with this phenomenon has the potential to result in failure of the foundation design. It is therefore of significant interest for future work to use the results presented in this thesis to examine this risk.

Another implication of the appreciable unsteady flow conditions is the generation of cyclic or fatigue loads on the structure supporting the lifting surfaces. Though the large area of the lifting surfaces enables a greater average down-force to be generated, the unsteady lift component is also appreciable. Consideration of fatigue failure in future consideration of the AGB concept is likely to be critical.

7.3.2 Generating two-dimensional velocity fluctuations in laboratory scale tests

In order to commission the apparatus developed to generate the flow perturbations, the experimental schedule began by generating the most elementary conditions of single direction and frequency perturbations. The necessity for this phase of the experiments reduced the available time to experiment with generating more complex flow conditions. Using the first phase of experiments presented in this thesis, the apparatus is now available for exploring the range of available parameters which were either defined or confined in the present oscillating foil system.

A number of uncertainties in the present experimental results were attributed to the proximity of the foils to each other and the boundaries of the test section. These factors were unable to be mitigated due to the dimensions of the available experimental facility. By increasing the depth of the test section, the vertical range of the the unbounded flow assumption would be increased, and the effect of the proximity of Foil A and to Foil B could be explored. By increasing the

width of the test section, the relative effect of the 3mm gap between the wing tip and the test section wall would be decreased, and the gradient of the transverse gust intensity profile is expected to be reduced. With these experimental limitations removed, further investigation into the appropriateness of the effective mass parameter used in the calculation of the non-circulatory lift component would be possible with the experimental configuration presented herein.

Acoustic Doppler Velocimetry, using the Nortek Vectrino ADV, was shown to be an efficient method of measuring the flow perturbations at high temporal and spatial resolution. However using such an instrument to survey the velocities over a wide area required a large number of measurements, with an incremental change in probe position. The velocity measuring technique of Particle Image Velocimetry (PIV) has the ability to measure the instantaneous velocity of the flow in a two-dimensional vector field. Though requiring significantly more post-processing than ADV, this optical method of velocity measurement would enable the visualisation of the flow behavior in the wake of the oscillating foil. This would allow the validity of the planar wake assumption used in the theoretical performance calculations to be observed.

The development of these experimental facilities for generating unsteady flow velocities is beneficial for exploring the dynamic loads experienced on a lifting surface, under controlled conditions. The use of such scaled tests are particularly informative in cases when experimentation using a full scale device prove to be logistically challenging and cost prohibitive. However the present author expects that the installation of a full scale instrumented lifting surface at a tidally energetic location will be required before any further commercialization of the AGB is attempted. The resulting time history of dynamic loads on a full scale lifting surface would prove invaluable for quantifying the variation in available down-force.

References

Abbott, I. and von Doenhoff, A. (1959), *Theory of Wing Sections: Including a Summary of Airfoil Data*, Dover Publications.

Ainsworth, D. and Thake, J. (2006), Final report on preliminary works associated with 1MW tidal turbine, Technical report, Department of Trade and Industry.

Althaus, D. (1980), Profilpolaren fur den modellflug, Neckar-Veriag, Villengen-Schwenningen.

American Petroleum Institute (2000), Recommended practice for planning, designing and constructing fixed offshore platforms.

API (2005), Design and analysis of stationkeeping systems for floating structures, Rev 3, American Petroleum Institute.

Ashley, H. and Landahl, M. (1956), *Aerodynamics of Wings and Bodies*, Dover.

Ashour, M. and Norris, G. (2000), Modeling lateral soil-pile response based on soil-pile interaction, *Journal of Geotechnical and Geoenvironmental Engineering*, 126(5), pp. 420–428.

Aubeny, C. and Murff, J. (2005), Simplified limit solutions for the capacity of suction anchors under undrained conditions, *Ocean Engineering*, 32(7), pp. 864–877.

Bahaj, A., Molland, A., Chaplin, J., and Batten, W. (2007), Power and thrust measurements of marine current turbines under various hydrodynamic flow conditions in a cavitation tunnel and a towing tank, *Renewable Energy*, 32, pp. 407–426.

Bang, S., Preber, T., Cho, Y., Thomason, J., Karnoski, S., and Taylor, R. (2000), Suction piles for mooring of mobile offshore bases, *Marine Structures*, 13, pp. 367–382.

Basset, C., Thomson, J., and Polagye, B. (2011), Estimating the acoustic impact of a tidal energy project, *Acoustic Society of America*, 129(4), pp. 2498–2498.

BBC (2010), Largest tidal power device unveiled, Accessed 15th August, 2012.
URL `http://www.bbc.co.uk/news/uk-scotland-highlands-islands-10942856`

Bisplinghoff, R., Ashley, H., and Halfman, R. (1996), *Aeroelasticity*, Dover Publications.

Black & Veatch Limited (2005), Tidal stream energy resource and technology summary report, Technical Report 4, Carbon Trust.

Bloomfield, P. (2000), *Fourier Analysis of Time Series: An Introduction*, Wiley-Interscience, New York, 2nd edition.

Boon, J. (2004), *Secrets of the Tide : Tide and Tidal Current Analysis and Predictions, Storm Surges and Sea Level Trends*, Horwood Publishing, 1st edition.

Bowditch, N. (1995), *The American Practical Navigator - An Epitome Of Navigation*, National Imagery And Mapping Agency, Maryland.

Bryden, I. (2006), The marine energy resource, constraints and opportunities, *Maritime Engineering*, 159, pp. 55–65.

BWEA (2007), Marine Renewable Energy, Accessed 15th August, 2012.
URL `http://www.bwea.com/marine/devices.html`

Carbon Trust (2011), Accelerating marine energy, Technical Report CTC797.

Ceppi, P., Della-Marta, P., and Appenzeller, C. (2008), Extreme value analysis of wind speed observations over Switzerland, *Arbeitsberichte der MeteoSchweiz*, 219, p. 43.

Clarke, J., Connor, G., Grant, A., Johnstone, C., and Ordonez-Sanchez, S. (2008), Contra-rotating marine current turbines: Performance in field trials and power train developments, in *10th World Renewable Energy Congress*.

Climate Change Act (2008), The Stationery Office, London.

Coles, S. (2001), *An Introduction to Statistical Modeling of Extreme Values*, Springer, 1st edition.

Cook, N. (1982), Towards better estimation of extreme winds, *Journal of Wind Engineering and Industrial Aerodynamics*, 9, pp. 295–323.

Counihan, J. (1967), An improved method of simulating an atmospheric boundary layer in a wind tunnel, *Atmospheric Environment*, 3(2), pp. 197–200.

Crowe, C., Elger, D., and Roberson, J. (2005), *Engineering Fluid Mechanics*, John Wiley & Sons, 8th edition.

Davison, A. and Smith, R. (1990), Models for exceedances over high thresholds, *Journal of the Royal Statistical Society. Series B (Methodological)*, 52(3), pp. 393–442.

de Silva, C. (2000), *Vibration: Fundamentals and Practice*, CRC Press, Boca Raton, Florida.

Della-Marta, P., Mathis, H., Frei, C., Liniger, M., Kleinn, J., and Appenzeller, C. (2009), The return period of wind storms over Europe, *International Journal Of Climatology*, 29, pp. 437–459.

Delpero, P. M. (1992), *Investigation of Flows Around a Two Dimensional Hydrofoil Subject to a High Reduced Frequency Gust Loading*, Master's thesis, Massachusetts Institute of Technology.

Divett, T., Vennell, R., and Stevens, C. (2009), Maximising energy capture by fixed orientation tidal stream turbines in time-varying off axis current, in *Proceedings of Australasian Coasts and Ports Conference*, 108, Wellington.

DNV (2011), Design of Offshore Steel Structures, General (LRFD Method): Standard DNV-OS-C101, Stiftelsen Det Norske Veritas.

Elgar, S. and Raubenheimer, B. (2001), Current meter performance in the surf zone, *Journal of Atmospheric and Oceanic Technology*, 18, pp. 1735–1746.

Emery, W. and Thomson, R. (1998), *Data Analysis Methods in Physical Oceanography*, Pergamom Press, 1st edition.

Energy Act (2004), The Stationery Office, London.

Fisher, R. and Tippet, L. (1928), Limiting forms of the frequency distribution of the largest of smallest member of a sample, in *Proceedings of the Cambridge Philosophical Society*, volume 24, pp. 180–190.

Fraenkel, P. (2006), Tidal & marine current energy, Franco-British Marine Energies Seminar, Le Havre.

Fraenkel, P. (2009), The UK SeaGen Project: Marine Current Turbines' experience, UK-Taiwan Workshopon Tidal Current Energy, Royal Society of Edinburgh.

Fuller, W. (1996), *Introduction to Statistical Time Series*, John Wiley & Sons, 2nd edition.

Garrick, I. E. (1938), On some reciprocal relations in the theory of nonstationary flows, Technical Report 629, NACA Tech. Report.

Gerwick, B. (1999), *Construction of marine and offshore structures*, CRC Press, 2nd edition.

Gilleland, E., Katz, R., and Young, G. (2010), Extreme value toolkit: Package 'extremes'. URL `http://cran.r-project.org/web/packages/extRemes/extRemes.pdf`

Gilli, M. and Këllezi, E. (2006), An application of extreme value theory for measuring financial risk, *Computational Economics*, 27, pp. 207–228.

Gooch, S., Thompson, J., Polagye, B., and Meggit, D. (2009), Site characterisation for tidal power, in *Oceans*, Biloxi, MI.

Goodfellow, P. (2004), *Investigation Into The Properties Of Adjacent Hydrofoils*, Master's thesis, School of Engineering, University of Edinburgh.

Goring, D. and Nikora, V. (2002), Despiking acoustic Doppler velocimeter data, *Journal of Hydraulic Engineering*, 128, pp. 117–126.

Gretton, G. (2009), *The hydrodynamic analysis of a vertical axis tidal current turbine*, Ph.D. thesis, The University of Edinburgh.

Gretton, G., Ingram, D., and Bryden, I. (2011), Results from blade element momentum and rans analyses of a practical full-scale horizontal axis tidal current turbine, in *EWTEC*.

Gumbel, E. (1958), *Statistics of Extremes*, Columbia University Press.

Ham, N. D., Bauer, P. H., and Lawrence, T. L. (1974), Wind tunnel generation of sinusoidal lateral and longitudinal gusts by circulation control of twin parallel airfoils, Technical Report 137547, NASA Contractor Report.

Harding, S. and Bryden, I. (2012a), Development of fixed hydrodynamic lifting surfaces to stabilise anchoring structures in energetic tidal flows, in *Proceedings of 31st International Conference on Ocean, Offshore and Arctic Engineering*, Rio de Janerio, Brazil.

Harding, S. and Bryden, I. (2012b), Directionality in prospective Northern UK tidal current energy deployment sites, *Renewable Energy*, 44, pp. 474–477.

Harding, S. and Bryden, I. (2012c), Generating controllable velocity fluctuations using twin oscillating hydrofoils, *Journal of Fluid Mechanics*, 713, pp. 150–158.

Harding, S., Thomson, J., Polagye, B., Richmond, M., Durgesh, V., and Bryden, I. (2011), Extreme value analysis of tidal stream velocity perturbations, in *Proceedings of the 9th European Wave and Tidal Energy Conference*, Southampton, England.

Harland and Wolff Licences Ltd (2001), Base design and foundation installation design feasibility study, Technical report, UK Dept for Business, Innovation and Skills (BIS).

Harris, R., Johanning, L., and Wolfram, J. (2004), Mooring systems for wave energy converters: A review of design issues and choices, in *Proceedings of the 3rd International Conference on Marine Renewable Energy*, heriot-Watt University, Edinburgh, UK.

Hearon, J. (1968), Generalized inverses and solutions of linear systems, *Journal of Research of the National Bureau of Standards - B. Mathematical Sciences*, 72B(4), pp. 303–308.

Hoerner, S. (1965), *Fluid Dynamic Drag*, Published by the author.

Hoffmans, G. and Pilarczyk, K. (1995), Local scour downstream of hydraulic structures, *Journal of Hydraulic Engineering*, 121, pp. 326–340.

Holmes, D. (1970), Experimental pressure distributions on airfoils in transverse and streamwise gusts, Technical report, University of Cambridge, Department of Engineering.

Horlock, J. (1968), Fluctuating lift forces on aerofoils moving through transverse and chordwise gusts, *Journal of Basic Engineering*, 90, pp. 494–500.

Horlock, J. (1974), An unsteady flow wind tunnel, *Aeronautical Quarterly*, 15, pp. 81–90.

Horwich, E. A. (1993), *Unsteady Response of a Two-Dimensional Hydrofoil Subject to High Reduced Frequency Gust Loading*, Master's thesis, Massachusetts Institute of Technology.

IEA (2012), Monthly electricity statistics: April 2012, Technical report, International Energy Agency.

Iskander, M., El-Gharbawy, S., and Olson, R. (2002), Performance of suction caissons in sand and clay, *Canadian Geotechnical Journal*, 39(3), pp. 576–584.

Jancauskas, E. and Melbourne, W. (1980), The measurement of aerodynamic admittance using discrete frequency gust generation, in *7th Australasian Hydraulics and Fluid Mechanics Conference*, Brisbane.

Jones, R. (1938), Operational treatment of nonuniform-lift theory, Technical Report 667, NACA Tech. Report.

Jones, R. (1940), The unsteady lift of a wing of finite aspect ratio, Technical Report 681, NACA Tech. Report.

Katz, J. and Plotkin, A. (2001), *Low-speed Aerodynamics: From Wing Theory to Panel Methods*, Cambridge University Press.

Kavazanjian Jr., E. (2006), A driven pile advantage: Batter piles, in *Piledriver*, Q4.

Kemp, N. (1952), On the lift and circulation of airfoils in some unsteady flow problems, *Journal of the Aeronautical Sciences*, 19, pp. 713–714.

Khan, M., Bhuyan, G., Iqbal, M., and Quaicoe, J. (2009), Hydrokinetic energy conversion systems and assessment of horizontal and vertical axis turbines for river and tidal applications: A technology status review, *Applied Energy*, 86, pp. 1823–1835.

Khan, M., Iqbal, M., and Quaicoe, J. (2008), River current energy conversion systems: Progress, prospects and challenges, *Renewable and Sustainable Energy Reviews*, 12, pp. 2177–2193.

Küssner, H. (1936), Zusammenfassender Bericht über den instationären Auftrieb von Flügeln, *Luftfahrtforschung*, 13, pp. 410–424.

Lamson, P. (1957), Measurements of lift fluctuations due to turbulence, Technical Report 3880, NACA Tech. Report.

LCICG (2012), Technology innovation needs assessment: Marine energy summary report, Technical report, Low Carbon Innovation Coordination Group.

Legrand, C. (2009), *Assessment for Tidal Energy Resource*, The European Marine Energy Centre, London.

Leishman, J. (2002), Challenges in modeling the unsteady aerodynamics of wind turbines, in *21st ASME Wind Energy Symposium and the 40th AIAA Aerospace Sciences Meeting*, Reno, Nevada.

Leishman, J. (2006), *Principles of Helicopter Aerodynamics*, Cambridge University Press, 2nd edition.

Liepmann, N. (1952), On the application of statistical concepts to the buffeting problem, *Journal of Aeronautical Sciences*, 19, pp. 793–800.

Lohrmann, A. (2006), Vector ping rate, Nortek AS Knowledge Center, Accessed 23rd November, 2012.
URL http://www.nortek-as.com/en/knowledge-center/forum/velocimeters/30181037

Makita, H. (1991), Realization of a large-scale turbulence field in a small wind tunnel, *Fluid Dynamics Research*, 8, pp. 53–64.

Maritime Journal (2008), Seagen successfully installed in northern ireland, Accessed 15th August, 2012.
URL http://www.maritimejournal.com/features101/marine-renewable-energy/seagen_successfully_installed_in_northern_ireland

Martins, E. and Stedinger, J. (2000), Generalized maximum-likelihood generalized extreme-value quantile estimators for hydrologic data, *Water Resources Research*, 36(3), pp. 737–744.

Mason-Jones, A., O'Doherty, D., Morris, C., O'Doherty, T., Byrne, C., Prickett, P., Grosvenor, R., Owen, I., Tedds, S., and Poole, R. (2012), Non-dimensional scaling of tidal stream turbines, *Energy*, 44(1), pp. 820–829.

Mathisen, M. and Lohrmann, A. (2008), Small vectrino sampling volumes, Nortek AS Knowledge Center, Accessed 2nd July, 2012.
URL http://www.nortek-as.com/en/knowledge-center/forum/velocimeters/159955427

McCann, G., Thomson, M., and Hitchcock, S. (2008), Implications of site-specific conditions on the prediction of loading and power performance of a tidal stream device, in *Proceedings of the 2nd International Conference on Ocean Energy*, Brest, France.

Microsoft Corporation (2012), Bing Maps - Admiralty Inlet, WA, Accessed 14th August, 2012.
URL http://www.bing.com/maps/

Miley, S. (1982), A catalog of low-Reynolds-number arifoil data for wind-turbine applications, Technical Report RFP-3387, Department of Aerospace Engineering, Texas A&M University.

Mori, N. (2009), MACE Toolbox, Accessed 25th November, 2012.
URL http://www.oceanwave.jp/softwares/mace/index.php?MACE%20Softwares

Mori, N., Suzuki, T., and Kakuno, S. (2007), Noise of acoustic Doppler velocimeter data in bubbly flow, *ASCE Journal of Engineering Mechanics*, 133(1), pp. 122–125.

Mraz, S. (2004), Plugging into the ocean, Accessed 10th February, 2011.
URL http://machinedesign.com/article/plugging-into-the-ocean-0916

Mydlarski, L. and Warhaft, Z. (1996), On the onset of high-Reynolds-number grid-generated wind tunnel turbulence, *Journal of Fluid Mechanics*, 320, pp. 331–368.

Myung, I. (2003), Tutorial on maximum likelihood estimation, *Journal of Mathematical Psychology*, 47, pp. 90–100.

NASA (2010), Induced drag coefficient, Accessed 3rd September, 2012.
URL http://www.grc.nasa.gov/WWW/k-12/airplane/induced.html

Neptune Renewable Energy Ltd (2012), Demonstrator design, Accessed 14th August, 2012.
URL http://www.neptunerenewableenergy.com/demonstrator-design/

Nortek AS (2005), *Vector Current Meter User Manual*, Rev. H.

Nortek USA (2012), The new and the old design of the nortek vector probe head, Accessed 23rd November, 2012.
URL http://williamlohrmann.com/hardware/VectorHeadComparison.html

Nylund, S. (2006), Weak spots, Nortek AS Knowledge Center, Accessed 16th October, 2012.
URL http://www.nortekusa.com/en/knowledge-center/forum/velocimeters/30180961

OpenHydro Group Ltd (2012a), Development: EMEC, Accessed 15th August, 2012.
URL http://www.openhydro.com/devEMEC.html

OpenHydro Group Ltd (2012b), Images, Accessed 14th August, 2012.
URL http://www.openhydro.com/images.html

Orme, J. and Masters, I. (2006), Analysis and comparison of support structure concepts for tidal stream turbines, in *Proceedings of World Maritime Technology Conference*.

Orme, J., Masters, I., and Griffiths, R. (2001), Investigation of the effect of biofouling on the efficiency of marine current turbines, in *Proceedings of MAREC 2001*.

ORPC (2011), TidGen Power System, Accessed 15th August, 2012.
URL http://www.orpc.co/orpcpowersystem_tidgenpowersystem.aspx

Owen, A. (2007), *The Application Of Low Aspect Ratio Hydrofoils To The Secure Positioning Of Static Equipment In Tidal Streams*, Ph.D. thesis, The Robert Gordon University.

Owen, A. and Bryden, I. (2005), Prototype support structure for seabed mounted tidal current turbines, *Proceedings of the Institution of Mechanical Engineers Part M: Journal of Engineering for the Maritime Environment*, 219(4), pp. 173–183.

Owen, A. and Bryden, I. (2009), Apparatus for controlling underwater based equipment, Patent Number US7611307, United States of America.

Palutikof, J., Brabson, B., Lister, D., and Adcock, S. (1999), A review of methods to calculate extreme wind speeds, *Meteorological Applications*, 6(2), pp. 119–132.

Passmore, M., Richardson, S., and Imam, A. (2001), An experimental study of unsteady vehicle aerodynamics, *Proceedings of the Institution of Mechanical Engineers, Part D: Journal of Automobile Engineering*, 215, pp. 779–788.

Penrose, R. (1956), On best approximate solutions of linear matrix equations, *Mathematical Proceedings of the Cambridge Philosophical Society*, 52(1), pp. 17–19.

Peterka, J. (1992), Improved extreme wind prediction for the United States, *Journal of Wind Engineering and Industrial Aerodynamics*, 41, pp. 533–541.

Peters, D. (2008), Two-dimensional incompressible unsteady airfoil theory - an overview, *Journal of Fluids and Structures*, 24, pp. 295–312.

Pickands, J. (1975), Statistical inference using extreme order statistics, *The Annals of Statistics*, 3, pp. 119–131.

Polagye, B., Epler, J., and Thomson, J. (2010), Limits to the predictability of tidal current energy, in *OCEANS 2010*, pp. 1–9.

Poling, D. and Telionis, D. (1986), The response of airfoils to periodic disturbances - the unsteady Kutta condition, *AIAA Journal*, 24(2), pp. 193–199.

Pope, S. (2000), *Turbulent Flows*, Cambridge University Press.

Prandle, D. (1997), The influence of bed friction and vertical eddy viscosity on tidal propagation, *Continental Shelf Research*, 17(11), pp. 1367–1374.

Previsic, M. (2005), Methodology for conceptual level design of tidal in stream energy conversion (TISEC) power plants, Technical report, Electric Power Research Institute and Mirko Previsic Consulting.

Previsic, M. (2006), System level design, performance, cost and economic assessment - Maine Western Passage tidal in-stream power plant, Technical report, EPRI.

Pugh, D. (1987), *Tides, Surges and Mean Sea-Level*, John Wiley & Sons Ltd.

R Development Core Team (2009), R: A Language and Environment for Statistical Computing, doi:ISBN3-900051-07-0, Accessed 21st January, 2013.
URL `http://www.r-project.org`

RDI (1996), *Acoustic Doppler Current Profiler: Principles of Operation - A Practical Primer*, Teledyne RD Instruments, California, USA, 2nd edition.

RDI (1998), Workhorse Acoustic Doppler Current Profiler Technical Manual, Technical Report P/N 957-6000-00, Teledyne RD Instruments.

RDI (2002), *WorkHorse Installation Guide*, Teledyne RD Instruments.

RDI (2010), ADCP Coordinate Transformation: Formulas and Calculations, Technical Report P/N 951-6079-00, Teledyne RD Instruments.

RDI (2012), Sentinel ADCP, Accessed 23rd November, 2012.
URL `http://www.rdinstruments.com/sen.aspx`

Richmond, M., Thomson, J., Durgesh, V., and Polagye, B. (2011), Inflow Characterization for Marine and Hydrokinetic Energy Devices: FY-2010 Annual Progress Report, Technical Report PNNL-19859, Pacific Northwest National Laboratory, Richland, WA.

Royston, P. (2007), Profile likelihood for estimation and confidence intervals, *The Stata Journal*, 7(3), pp. 376–387.

Rusello, P. (2009), A practical primer for pulse coherent instruments, Technical Report TN-027, Nortek AS.

Rusello, P. (2010), Weak spots, Nortek AS Knowledge Center, Accessed 16th October, 2012.
URL `http://www.nortekusa.com/en/knowledge-center/forum/velocimeters/30180961#1885903`

Rusello, P., Lohrmann, A., Siegel, E., and Maddux, T. (2006), Improvements in acoustic Doppler velocimetery, in *The 7th International Conference on Hydroscience and Engineering (ICHE-2006)*, Philadelphia, USA.

Salter, S. (1998), Proposal for a large, vertical-axis tidal-stream generator with ring-cam hydraulics, in *Proceedings of 3rd European Wave Energy Conference*, Patras, Greece.

Salter, S. (2009), Correcting the underestimate, in *Proceedings of the 8th European Wave and Tidal Energy Conference*, Uppsala, Sweden.

Sarpkaya, T. and Isaacson, M. (1981), *Mechanics of Wave Forces on Offshore Structures*, Van Nostrand Reinhold.

Sears, W. R. (1941), Some aspects of non-stationary airfoil theory and its practical application, *Journal of Aeronautical Sciences*, 8, pp. 104–108.

Smith, S. (2003), *Digital Signal Processing: A Practical Guide for Engineers and Scientists*, Elsevier.

Soukissian, T. and Arapi, P. (2011), The effect of declustering in the *r*-largest maxima model for the estimation of H_s-design values, *The Open Ocean Engineering Journal*, 4, pp. 34–43.

Stanton, B., Goring, D., and Bell, R. (2001), Observed and modelled tidal currents in the New Zealand region, *New Zealand Journal of Marine and Freshwater Research*, 35, pp. 397–415.

Stapountzis, H. (1982), An oscillating rig for the generation of sinusoidal flows, *Journal of Physics E: Scientific Instruments*, 15, pp. 1173–1176.

Stern, N. (2006), Stern review report on the economics of climate change: Summary of conclusions, Technical report, HM Treasury.

Strabo (1969), *The Geography of Strabo*, Harvard University Press.

Tang, D., Cizmas, P., and Dowell, E. (1996), Experiments and analysis for a gust generator in a wind tunnel, *Journal of Aircraft*, 33(1), pp. 139–148.

Tang, F. and Chen, D. (2012), Tidal flow patterns near a coastal headland, *World Academy of Science, Engineering and Technology*, 63, pp. 782–790.

Taylor, G. (1937), The statistical theory of isotropic turbulence, *Journal of Aeronautical Sciences*, 4, pp. 311–315.

Taylor, G. (1938), The spectrum of turbulence, in *Proceedings of the Royal Society of London. Series A, Mathematical and PhysicalSciences*, volume 164, pp. 476–490.

Tennekes, H. and Lumley, J. (1999), *A First Course in Turbulence*, The MIT Press.

Thake, J. (2005), Development, installation and testing of a large scale tidal current turbine, Technical report, IT Power.

The National Center for Atmospheric Research (2007), extRemes Toolkit, Accessed 15th January, 2013.
URL `http://www.assessment.ucar.edu/toolkit/`

Theodorsen, T. (1935), General theory of aerodynamic instability and the mechanism of flutter, Technical Report 496, NACA Tech. Report.

Thomson, J., Polagye, B., Durgesh, V., and Richmond, M. (2012), Measurements of turbulence at two tidal energy sites in Puget Sound, WA, *Journal of Oceanic Engineering*, 37, pp. 363–374.

Thomson, J., Polagye, B., Richmond, M., and Durgesh, V. (2010), Quantifying turbulence for tidal power applications, in *OCEANS 2010*, Seattle, Washington.

Thomson, W. (1869), On vortex motion, in *Transactions of the Royal Society of Edinburgh*, volume 25, pp. 217–260.

Tidal Generation Ltd (2010a), Advantage TGL, Accessed 15th August, 2012.
URL `http://www.tidalgeneration.co.uk/products/advantage-tgl/`

Tidal Generation Ltd (2010b), Gallery: Deployment & retrieval, Accessed 14th August, 2012.
URL `http://www.tidalgeneration.co.uk/gallery/?album=2&gallery=4`

Tukey, J. (1967), An introduction to the calculations of numerical spectrum analysis, in *Spectral analysis of time series*, Wiley, New York.

UKHO (1990), United Kingdom Hydrographic Office, Admiralty Chart No. 219, Western Approaches to the Orkney and Shetland Islands.

UKHO (1993), United Kingdom Hydrographic Office, Admiralty Chart No. 2249, Orkney Islands Western Sheet.

UKHO (1998), United Kingdom Hydrographic Office, Admiralty Chart No. 1954, Cape Wrath to Pentland Firth including the Orkney Islands.

Uusipaikka, E. (2009), *Confidence Intervals in Generalized Regression Models*, CRC Press.

van der Wall, B. and Leishman, J. (1994), On the influence of time-varying flow velocity on unsteady aerodynamics, *Journal of the American Helicopter Society*, 39(4), pp. 25–37.

Venzon, D. and Moolgavkar, S. (1988), A method for computing profile-likelihood-based confidence intervals, *Journal of the Royal Statistical Society. Series C (Applied Statistics)*, 37(1), pp. 87–94.

Wagner, H. (1925), Über die Entstehung des dynamischen Auftriebes von Tragflügeln, *Zeitschrift fur Angewandte Mathematik und Mechanik*, 5, pp. 17–35.

Wahl, T. (2003), Discussion of 'Despiking acoustic Doppler velocimeter data', *Journal of Hydraulic Engineering*, 129(6), pp. 484–487.

Walden, H. (1961), Comparison of one-dimensional wave spectra recorded in the German Bight with various 'theoretical' spectra, in *Ocean Wave Spectra*.

Walsh, T. (2012), BDN Maine, Eastport dedication celebrates emerging era of tidal generation, Accessed 14th August, 2012.
URL http://bangordailynews.com/2012/07/24/news/down-east/nations-first-underwater-tidal-turbine-dedicated-in-eastport/

Weissman, I. (1978), Estimation of parameters and large quantities based on the k largest observations, *Journal of the American Statistical Association*, 73, pp. 812–815.

White, F. (2011), *Fluid Mechanics*, McGraw-Hill, 7th edition.

Willis, M., Broudic, M., Haywood, C., Masters, I., and Thomas, S. (2013), Measuring underwater background noise in high tidal flow environments, *Renewable Energy*, 49, pp. 255–258.

Xue, D. and Chen, Y. (2008), *Solving Applied Mathematical Problems with MATLAB*, CRC Press.

Zhao, Z., Lian, J., and Shi, J. (2006), Interactions among waves, current, and mud: Numerical and laboratory studies, *Advances in Water Resources*, 29(11), pp. 1731–1744.

Appendix A
Technical Drawings of Active Gravity Base Design

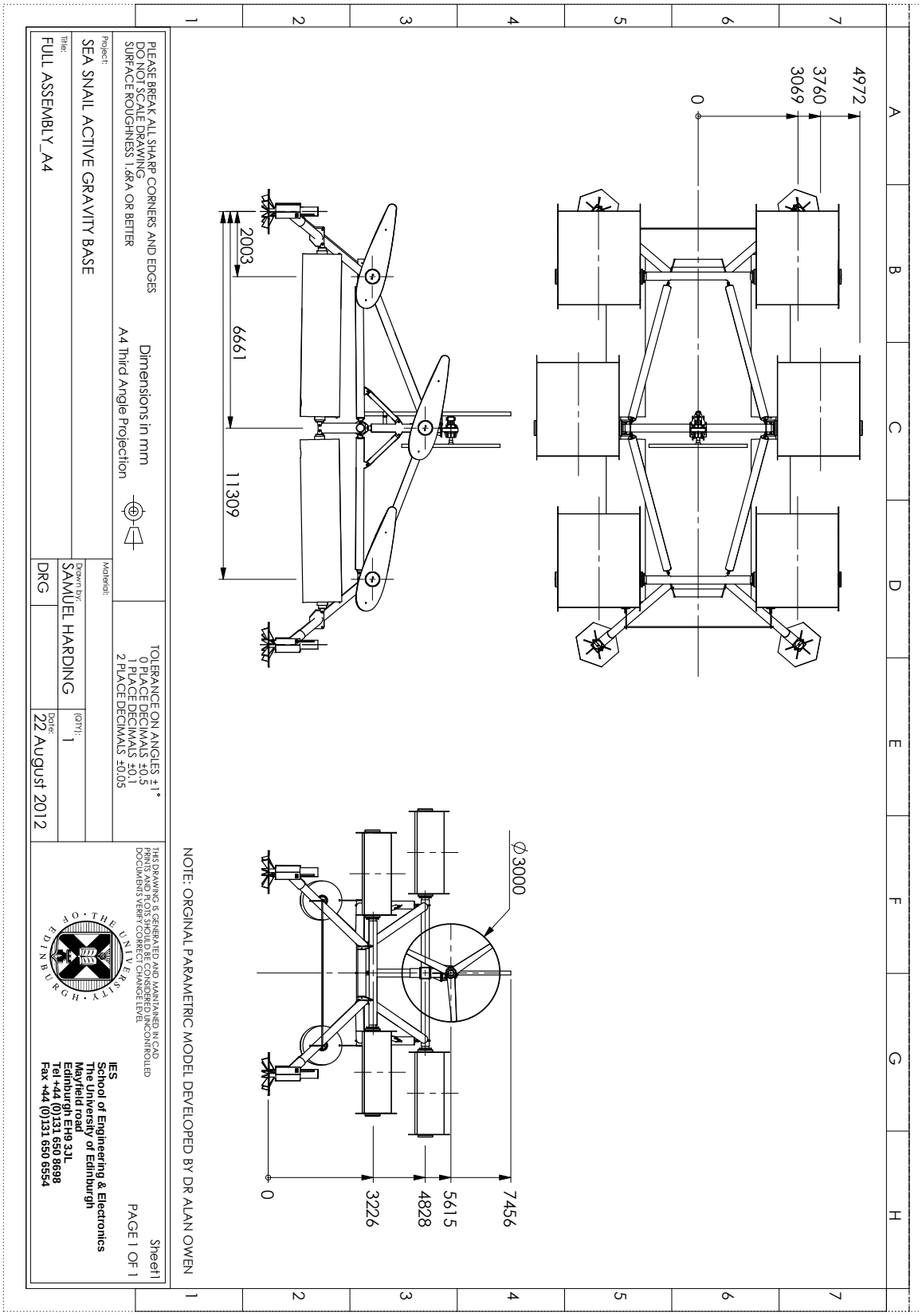
4972
3760
3069
0
2003
6661
11309
ϕ3000
0
3226
4828
5615
7456
NOTE: ORGINAL PARAMETRIC MODEL DEVELOPED BY DR ALAN OWEN
PLEASE BREAK ALL SHARP CORNERS AND EDGES
DO NOT SCALE DRAWING
SURFACE ROUGHNESS 1.6RA OR BETTER
Dimensions in mm
A4 Third Angle Projection
TOLERANCE ON ANGLES ±1°
0 PLACE DECIMALS ±0.5
1 PLACE DECIMALS ±0.1
2 PLACE DECIMALS ±0.05
Material:
Project:
SEA SNAIL ACTIVE GRAVITY BASE
Title:
FULL ASSEMBLY_A4
Drawn by:
SAMUEL HARDING
(QTY):
1
DRG
Date:
22 August 2012
THIS DRAWING IS GENERATED AND MAINTAINED IN CAD
PRINTS AND PLOTS SHOULD BE CONSIDERED UNCONTROLLED
DOCUMENTS VERIFY CORRECT CHANGE LEVEL
Sheet1
PAGE 1 OF 1
THE UNIVERSITY OF EDINBURGH
IES
School of Engineering & Electronics
The University of Edinburgh
Mayfield road
Edinburgh EH9 3JL
Tel +44 (0)131 650 8698
Fax +44 (0)131 650 6554

Appendix B
Journal of Fluid Mechanics Manuscript

J. Fluid Mech. (2012), *vol.* 713, *pp.* 150–158.
doi:10.1017/jfm.2012.442

Generating controllable velocity fluctuations using twin oscillating hydrofoils

S. F. Harding† and I. G. Bryden

Institute for Energy Systems, University of Edinburgh, Mayfield Road, Edinburgh EH9 3JL, UK

(Received 1 August 2012; revised 5 September 2012; accepted 5 September 2012;
first published online 16 October 2012)

An experiment apparatus has been previously developed with the ability to independently control the instantaneous flow velocity in a water flume. This configuration, which uses two pitching hydrofoils to generate the flow fluctuations, allows the unsteady response of submerged structures to be studied over a wide range of driving frequencies and conditions. Linear unsteady lift theory has been used to calculate the instantaneous circulation about two pitching hydrofoils in uniform flow. A vortex model is then used to describe the circulation in the wakes that determine the velocity perturbations at the centreline between the foils. This paper introduces how the vortex model can be discretized to allow the inverse problem to be solved, such that the foil motions required to recreate a desired velocity time series can be determined. The results of this model are presented for the simplified cases of oscillatory velocity fluctuations in the vertical and stream-wise directions separately, and also simultaneously. The more general case of two-dimensional aperiodic velocity fluctuations is also presented, which demonstrates the capability of configuration between the suggested frequency limits of $0.06 \leqslant k \leqslant 1.9$.

Key words: vortex flows, vortex streets, wakes/jets

1. Introduction

Unsteady structural responses resulting from dynamic flow conditions are important in a range of engineering applications, and generating such flow conditions in the laboratory enables the dynamic loads to be measured experimentally. Therefore, controlling the behaviour of the time-varying fluid velocity becomes a prerequisite challenge. Although some experimental methods elect to introduce relative motion between the fluid and structure by studying a moving body in a steady flow environment, this does not capture the effects of flow variations with length scales less than that of the body. These effects constitute an important part of the diminishing aero/hydrodynamic admittance function at high frequencies (Sears 1941; Liepmann 1952). In response, this paper examines a laboratory set-up that will allow the user to generate predefined flow fluctuations in the stream-wise and vertical direction along the centreline. This configuration has been shown to be effective in creating sinusoidal variations in vertical flow velocities; however, this paper demonstrates the ability to reproduce an aperiodic predetermined velocity time series through the use of two oscillating lifting surfaces. Such a facility allows full-scale velocity measurements to be reproduced in a controlled environment to enable the improved experimental derivation of unsteady response characteristics.

† Email address for correspondence: s.harding@ed.ac.uk

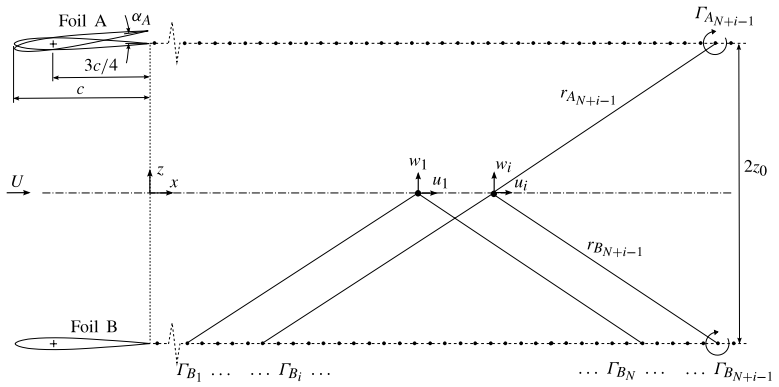

FIGURE 1. Schematic of velocity contributions from two parallel hydrofoils.

The use of oscillating lifting surfaces for the independent generation of oscillatory perturbations in longitudinal and vertical velocities was originally proposed by Ham, Bauer & Lawrence (1974), who describe a method that uses elliptical lifting surfaces with a jet slot in the trailing edge to alter the circulation about the foil in air. The direction of the jet is controlled by a cam in a round plenum at the aft of the lifting surface. Perturbations of up to 20 % of the free-stream velocity of the air have been achieved using a similar method of gust generation (Jancauskas & Melbourne 1980). Subsequently, pitching hydrofoils have been introduced to generate gusts in a single direction in wind tunnels (Tang, Cizmas & Dowell 1996; Passmore, Richardson & Imam 2001), and at high reduced frequencies in a water flume (Delpero 1992; Horwich 1993).

The benefit of using two independently controlled oscillating foils, shown in figure 1, is that the perturbations can be generated in the horizontal direction, x, and vertical direction, z, independently along the centreline between them. When the hydrofoil motion is harmonic, the motion of Foil A is denoted $\alpha_A = \alpha_0 e^{i\omega t}$, and that of Foil B is denoted $\alpha_B = \alpha_0 e^{i(\omega t+\theta)}$. If the two foils are oscillating in phase ($\theta = 0°$), the longitudinal components of the induced velocity, u, cancel along the centreline, and the vertical components, w, are additive. When the foils are oscillating out of phase ($\theta = 180°$), the w components of the perturbations cancel along the centreline, and the u components are additive (Ham *et al.* 1974). A phase difference of $0° < \theta < 180°$ will result in both stream-wise and vertical perturbations, with relative magnitudes dependent on the phase.

This paper presents a numerical model that allows the velocity perturbations to be calculated for a given time series of foil motions. This model is then manipulated to allow the reverse problem to be solved, such that the required time series of foil motions to generate a specified velocity time series can be calculated. The model is validated against existing experimental results, and the output of the reversed process is demonstrated for a range of combinations of vertical and stream-wise velocity fluctuations.

2. Mathematical model

The simplifying assumptions used in the approach described in this paper are:

(*a*) the aerofoils are flat plates undergoing small-angle oscillations about the quarter-chord location;

(*b*) the vorticity imparted to the wake from the trailing edge of the hydrofoil is convected along a horizontal line at the velocity of the free-stream flow (planar wake assumption);

(*c*) the location of the specified velocity time series is at a sufficient distance from the foils that the bound circulation is assumed to have negligible influence;

(*d*) the Kutta–Joukowski condition applies at all times.

2.1. *Circulation about a pitch-oscillating hydrofoil*

The transient development of circulation about a foil undergoing pitching motion is accounted for by calculating the 'effective' angle of attack, which can then be used in the quasi-steady calculation of the bound circulation of the foil through the Kutta–Joukowski theorem. The present analysis uses the non-dimensionalized time variable given by $s = 2Ut/c$, where U is the steady horizontal free-stream velocity, c is the foil chord length and t is the time. The relationship between the effective angle of attack for an oscillating foil, $\alpha_e(s)$, and the actual instantaneous angle of attack, $\alpha_a(s)$, can be described using the Duhamel integral (Bisplinghoff, Ashley & Halfman 1996; Leishman 2006):

$$\alpha_e(s) = \alpha_a(0)\phi(s) + \int_0^s \frac{\mathrm{d}\alpha_a(\sigma)}{\mathrm{d}\sigma}\phi(s-\sigma)\,\mathrm{d}\sigma, \tag{2.1}$$

where $\phi(s)$ represents the Wagner function for the response to an indicial change in angle of attack (Garrick 1938) and σ is the time variable of integration. When the indicial lift response is approximated by the form of $\phi = 1 - A_1\mathrm{e}^{-b_1 s} - A_2\mathrm{e}^{-b_2 s}$, (2.1) can be solved using the one-step recursive solution of Algorithm-D1 (see Leishman 2006, p. 461):

$$\alpha_e(s) = \alpha_a(s) - X(s) - Y(s), \tag{2.2a}$$

$$X(s) = X(s-\Delta s)\mathrm{e}^{-b_1\Delta s} - A_1[\alpha_a(s) - \alpha_a(s-\Delta s)], \tag{2.2b}$$

$$Y(s) = Y(s-\Delta s)\mathrm{e}^{-b_2\Delta s} - A_2[\alpha_a(s) - \alpha_a(s-\Delta s)]. \tag{2.2c}$$

For the Wagner function, Jones (1940) gives the values of $A_1 = 0.165$, $A_2 = 0.335$, $b_1 = 0.045$ and $b_2 = 0.300$.

Using the Kutta–Joukowski theorem, the instantaneous bound circulation per unit span for each foil is given by $\Gamma_b(s) = UC_{L\alpha}\alpha_e(s)c/2$, where $C_{L\alpha} = \mathrm{d}C_L/\mathrm{d}\alpha_e$ and C_L is the instantaneous quasisteady lift coefficient of the foil. The vorticity advected into the wake of the foils at each time step is $\Gamma(s) = \Gamma_b(s-\Delta s) - \Gamma_b(s)$.

2.2. *Contributions of twin hydrofoil wakes*

By locating the origin of the (x, z) coordinate system on the centreline between the two foils and applying a planar wake simplification, the magnitude of the z-ordinate of the wakes can be defined as half the vertical distance between the two foils, z_0, such that $z_{A_j} = z_0$ and $z_{B_j} = -z_0$.

From figure 1 it can be seen that the component of the induced velocity in the longitudinal direction by a clockwise vortex is always negative from Foil A ($u_A < 0$) and always positive from Foil B ($u_B > 0$). As such, the magnitude of the perturbation

in the longitudinal velocity is effectively controlled by the difference between the wake vorticity of Foil A and Foil B. Denoting the circulation per unit length of the wake as γ, the Biot–Savart law gives

$$u(X,t) = \frac{z_0}{2\pi}\int_0^\infty \frac{\gamma_B(x) - \gamma_A(x)}{(X-x)^2 + z_0^2}\,\mathrm{d}x, \tag{2.3}$$

where dx is a segment of the wake.

Furthermore, it can be seen that Foil A and Foil B have an additive effect on the induced velocity in the vertical direction. As such, the magnitude of the perturbation in the vertical velocity is effectively controlled by the sum of the wake vorticity of Foil A and Foil B, such that

$$w(X,t) = \frac{-1}{2\pi}\int_0^\infty \frac{(X-x)\,[\gamma_B(x) + \gamma_A(x)]}{(X-x)^2 + z_0^2}\,\mathrm{d}x. \tag{2.4}$$

3. Numerical model

3.1. *Discretization*

As the model is intended to use arbitrary time series of γ_A and γ_B, the solution to the vortex model is implemented in discrete form for ease of numerical integration. This is also shown to be beneficial when the reverse problem is addressed in § 3.2. Using the notation defined in figure 1, the combined effect of Γ_A and Γ_B on the induced velocity at location $(x_i, 0)$ can be calculated as a finite summation given by

$$u_i = \frac{z_0}{2\pi}\sum_{j=i}^{N+i-1}\left(\frac{1}{r_{ij}^2}\right)(\Gamma_{B_j} - \Gamma_{A_j}), \tag{3.1a}$$

$$w_i = \frac{-1}{2\pi}\sum_{j=i}^{N+i-1}\left(\frac{X_i - x_j}{r_{ij}^2}\right)(\Gamma_{B_j} + \Gamma_{A_j}), \tag{3.1b}$$

where $r_{ij}^2 = (X_i - x_j)^2 + z_0^2$.

The spatial range of the summation, L, which includes N discrete vortices, must be large enough to capture all of the induced velocities from the wake. A sensitivity study was carried out for the required range, with the results summarized in figure 2. In response to this analysis, the summation was made over the range of $L = 30c$ for the results presented in this paper. It was found that at ordinates of $x \geqslant 15c$ the perturbations induced by the wake vorticity were translationally independent. As such, the model was implemented to solve the velocity at coordinates of $(15c, 0)$, and the effect of the bound vorticity of the oscillating foils was ignored. The numerical model uses the same foil configuration as the experiments of Stapountzis (1982), where $2z_0 = 2.3c$ and $c = 0.203$ m.

Letting $\boldsymbol{f} = z_0/2\pi[z_0^2 + (X_i - x_j)^2]$ and $\boldsymbol{g} = -(X_i - x_j)/2\pi[z_0^2 + (X_i - x_j)^2]$, (3.1$b$) can be expressed in the form of a matrix product by

$$\boldsymbol{u} = \boldsymbol{f} \cdot (\Gamma_B - \Gamma_A)\,, \tag{3.2a}$$

$$\boldsymbol{w} = \boldsymbol{g} \cdot (\Gamma_A + \Gamma_B)\,. \tag{3.2b}$$

The time series of the velocity fluctuations can then be reconstructed using the assumption that the velocity fluctuations are being advected at the free-stream velocity.

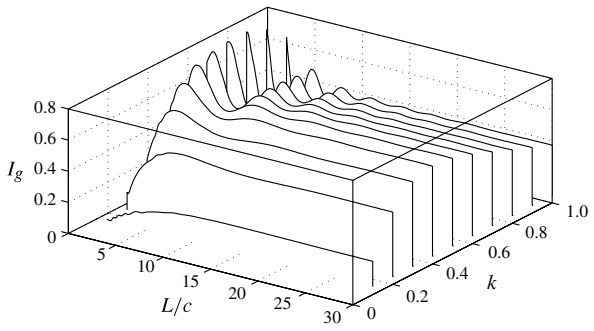

FIGURE 2. Sensitivity study for gust intensity, I_g, as a function of integral length, L, for a range of reduced frequencies, k.

3.2. *Foil motions for a desired velocity time series*

The mathematical model described in § 2.2 can be reversed, such that the foil motions required to generate a specified velocity time series can be calculated. Although the $i \times j$ matrices of $\boldsymbol{f}$ and $\boldsymbol{g}$ do not have a unique inverse, the pseudo-inverse calculated using a 'least-squares' best fit can be determined using the Moore–Penrose method (Penrose 1956). Denoting the pseudo-inverse of these matrices as $\boldsymbol{f}^+$ and $\boldsymbol{g}^+$, the required wake circulation to achieve a given velocity time series is calculated as

$$(\Gamma_B - \Gamma_A) = \boldsymbol{f}^+ \boldsymbol{u}, \tag{3.3a}$$

$$(\Gamma_A + \Gamma_B) = \boldsymbol{g}^+ \boldsymbol{w}. \tag{3.3b}$$

Applying a windowing function, such as a Tukey window, to the velocity time series reduced instabilities in the solution of the pseudo-inverse (Tukey 1967). The circulation matrices are then solved as simultaneous equations and (2.2*c*) can then be rearranged and solved for $\alpha_a(t)$.

4. Results

4.1. *Model verification*

The results of the numerical model of the twin oscillating foil configuration are summarized in figure 3, which shows the outputs of four representative simulations to demonstrate the operating principle of the foil arrangement, and to verify the inverse solution procedure. The top row (figure 3*a,e*) demonstrates the common situation of vertical velocity perturbations only, where the two hydrofoils are required to follow identical time series. The second row (figure 3*b,f*) illustrates the foil motion required to generate an oscillatory fluctuation in stream-wise velocity only, which is shown to be produced by sinusoidal foil oscillation with a phase difference of $\theta = 180°$, as expected. The third row (figure 3*c,g*) illustrates the case of stream-wise and vertical flow fluctuations of equal magnitudes and a phase difference of 180°. This represents the case where the effective angle of the incident flow is the greatest, which is the 'worst-case' combination of flow fluctuations in structural and aerospace applications such as long-span bridges and aerofoils. As such, the ability for this configuration of twin hydrofoils to be able to generate such a flow scenario in the laboratory is of special interest.

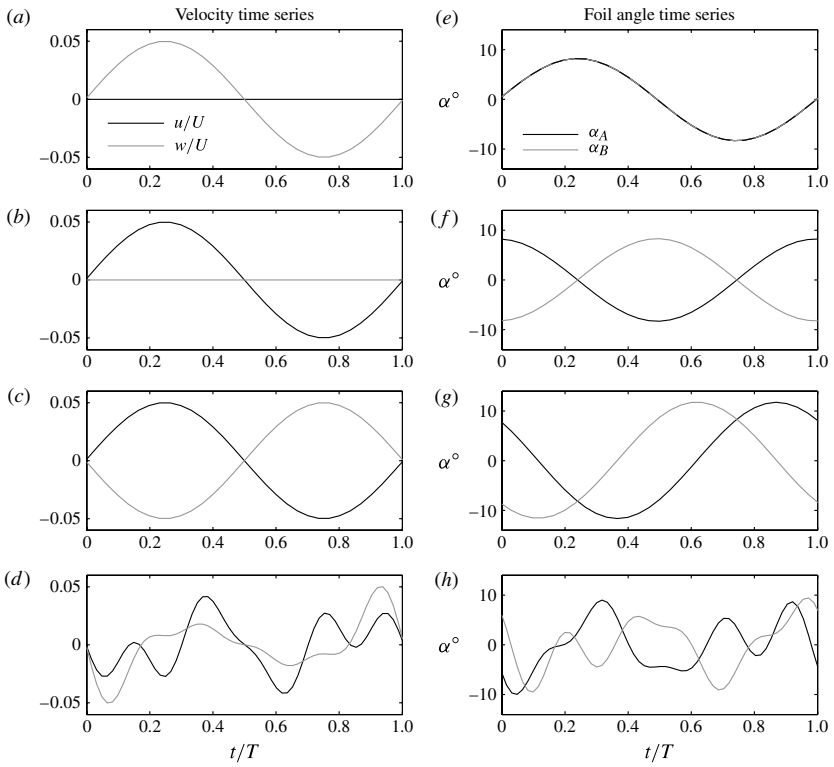

FIGURE 3. Representative results of the vortex model. The left column (*a–d*) shows the time series of the desired velocity perturbations and the right column (*e–h*) shows the corresponding time series of the angular positions of the foils required.

4.2. *Model validation*

A comparison with the experimental results presented by Stapountzis (1982) is made in figure 4 for the case of two sinusoidally oscillating foils with $\theta = 0°$. The metric of dimensionless gust intensity used to quantify the magnitude of the velocity fluctuations in response to the sinusoidal motion of the oscillating foils is given by (Stapountzis 1982)

$$I_g = \frac{w_0}{U\alpha_0}, \tag{4.1}$$

where w_0 is the amplitude of the vertical velocity fluctuations and α_0 is the amplitude of the foil pitching motion. The gust intensity varies as a function of reduced frequency, $k = \omega c/2U$, where ω is the driving frequency of the velocity fluctuation in radians per second. The numerical results show close agreement with the experimental results, which were available for the range of $0.05 \leqslant k \leqslant 0.67$.

The gust intensities diminish as $k \to 0$, as the circulation about the foil is shed so slowly that the resulting induced velocities become negligible. The reduction in

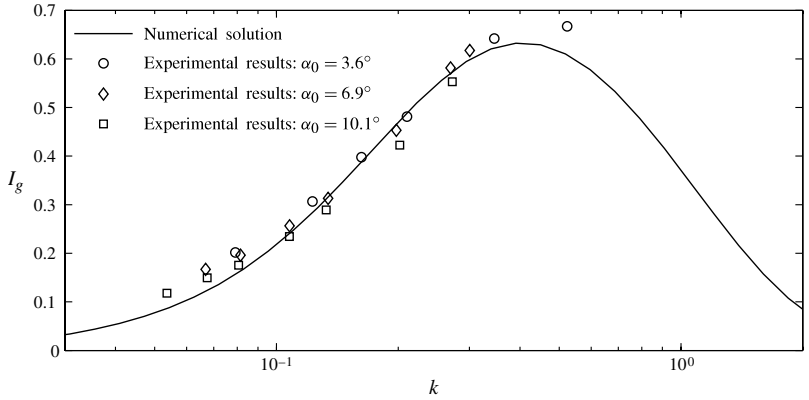

FIGURE 4. Comparison of numerical results using the method described in this paper with experimental results from Stapountzis (1982), for the case of in-phase sinusoidal foil oscillations at $Re = 4 \times 10^5$.

gust intensities as $k \to \infty$ is a result of unsteady lift theory, which accounts for the transient development of circulation about a pitching foil, as originally proposed Theodorsen (1935). As the frequency of pitch oscillation is increased, the reduced circulation about the foil has less time to develop, resulting in an increasing deficit between the actual circulation about the foil and that given by quasisteady lift theory (Ashley & Landahl 1956). This effect is implemented in the numerical model through the indicial response given by the Wagner function; however, experimental values were not available for frequencies greater than $k = 0.52$.

Experimental values are only available for comparison against the simplified case of in-phase oscillations of the foils.

4.3. *New results*

The novel contribution of this analysis is the ability to calculate the foil motion required to generate a desired velocity time series along the centreline. Figure 3(*d,h*) shows the case of temporally controlled flow fluctuations in both stream-wise and vertical directions, and the corresponding calculated time series of the foil angles. This example demonstrates the flexibility of the numerical model, as the required angular motion of the two foils is shown to be calculated for a time series with a range of driving frequencies. This situation also demonstrates the capability of the twin-foil configuration to recreate a complex flow environment. The frequency range of the velocity time series that can be produced is bounded by the approximate range of $0.06 \leqslant k \leqslant 1.9$, as shown in figure 4. Outside of this range, $I_g < 0.1$ and the relative velocity fluctuations become very small, such that $u/U < 1.7\,\%$ when $\alpha_0 = 10°$. It is also important to note that the steady Kutta condition used in the numerical model has been shown to be invalid at frequencies of $k > 2.0$ (Poling & Telionis 1986). As such, the velocity time series is required to be band-pass filtered to within this frequency range prior to implementation in the numerical model in order to achieve realistic results.

5. Conclusions

The use of two oscillating hydrofoils to generate arbitrary velocity fluctuations on the centreline of an experimental flume facility has been investigated. A numerical model has been developed to calculate these velocity fluctuations given the angular motion of the foils. This modelling approach incorporates unsteady lift effects through the use of the Wagner function and uses a simplified vortex model to calculate the induced velocities between the hydrofoil wakes.

The discrete formulation of the numerical model facilitates the novel development of the inverse solution procedure, whereby the required foil motions to generate a desired velocity fluctuation time series along the centreline can be calculated. In this way, velocity perturbations can be created to reproduce a wide range of environmental conditions in the laboratory.

For the generation of oscillatory vertical velocity perturbations, gust intensities greater than $I_g = 0.1$ are expected to be achievable for a wide range of reduced frequencies, from $0.06 \leqslant k \leqslant 1.9$. The driving frequencies that give the maximum velocity fluctuations for a given α_0 are in the range of $0.4 \leqslant k \leqslant 0.6$, and are dependent on the geometry of the configuration. However, it has been demonstrated that the combination of stream-wise and vertical velocity fluctuations is not limited to oscillatory motions, and predetermined combinations of velocity perturbations at a point can also be introduced through more complex motions of the two foils.

Acknowledgements

The authors wish to acknowledge Dr P. Johnson and Dr D. Forehand for their assistance in the development of the numerical model. S.F.H. wishes to acknowledge the Tertiary Education Commission of New Zealand for the funding of this research at the University of Edinburgh.

REFERENCES

ASHLEY, H. & LANDAHL, M. 1956 *Aerodynamics of Wings and Bodies*. Dover.

BISPLINGHOFF, R. L., ASHLEY, H. & HALFMAN, R. L. 1996 *Aeroelasticity*. Dover.

DELPERO, P. M. 1992 Investigation of flows around a two-dimensional hydrofoil subject to a high reduced frequency gust loading. Master's thesis, Massachusetts Institute of Technology.

GARRICK, I. E. 1938 On some reciprocal relations in the theory of nonstationary flows. *Tech. Rep.* 629. NACA Technical Report.

HAM, N. D., BAUER, P. H. & LAWRENCE, T. L. 1974 Wind tunnel generation of sinusoidal lateral and longitudinal gusts by circulation control of twin parallel airfoils. *Tech. Rep.* 137547. NASA Contractor Report.

HORWICH, E. A. 1993 Unsteady response of a two-dimensional hydrofoil subject to high reduced frequency gust loading. Master's thesis, Massachusetts Institute of Technology.

JANCAUSKAS, E. D. & MELBOURNE, W. H. 1980 The measurement of aerodynamic admittance using discrete frequency gust generation. In *7th Australasian Hydraulics and Fluid Mechanics Conference*. Brisbane. Institution of Engineers.

JONES, R. T. 1940 The unsteady lift of a wing of finite aspect ratio. *Tech. Rep.* 681. NACA Technical Report.

LEISHMAN, J. G. 2006 *Principles of Helicopter Aerodynamics*, 2nd edn. Cambridge University Press.

LIEPMANN, N. W. 1952 On the application of statistical concepts to the buffeting problem. *J. Aeronaut. Sci.* **19**, 793–800.

PASSMORE, M. A., RICHARDSON, S. & IMAM, A. 2001 An experimental study of unsteady vehicle aerodynamics. *Proc. Inst. Mech. Engrs Part D: J. Automobile Engineering* **215**, 779–788.

PENROSE, R. 1956 On best approximate solutions of linear matrix equations. *Math. Proc. Cambridge Philos. Soc.* **52** (1), 17–19.

POLING, D. R. & TELIONIS, D. P. 1986 The response of airfoils to periodic disturbances – the unsteady Kutta condition. *AIAA J.* **24** (2), 193–199.

SEARS, W. R. 1941 Some aspects of non-stationary airfoil theory and its practical application. *J. Aeronaut. Sci.* **8**, 104–108.

STAPOUNTZIS, H. 1982 An oscillating rig for the generation of sinusoidal flows. *J. Phys. E: Sci. Instrum.* **15**, 1173–1176.

TANG, D. M., CIZMAS, P. G. A. & DOWELL, E. H. 1996 Experiments and analysis for a gust generator in a wind tunnel. *J. Aircraft* **33** (1), 139–148.

THEODORSEN, T. 1935 General theory of aerodynamic instability and the mechanism of flutter. *Tech. Rep.* 496. NACA Technical Report.

TUKEY, J. W. 1967 An introduction to the calculations of numerical spectrum analysis. In *Spectral Analysis of Time Series* (ed. B. Harris). Wiley.

Appendix C
Technical Drawings

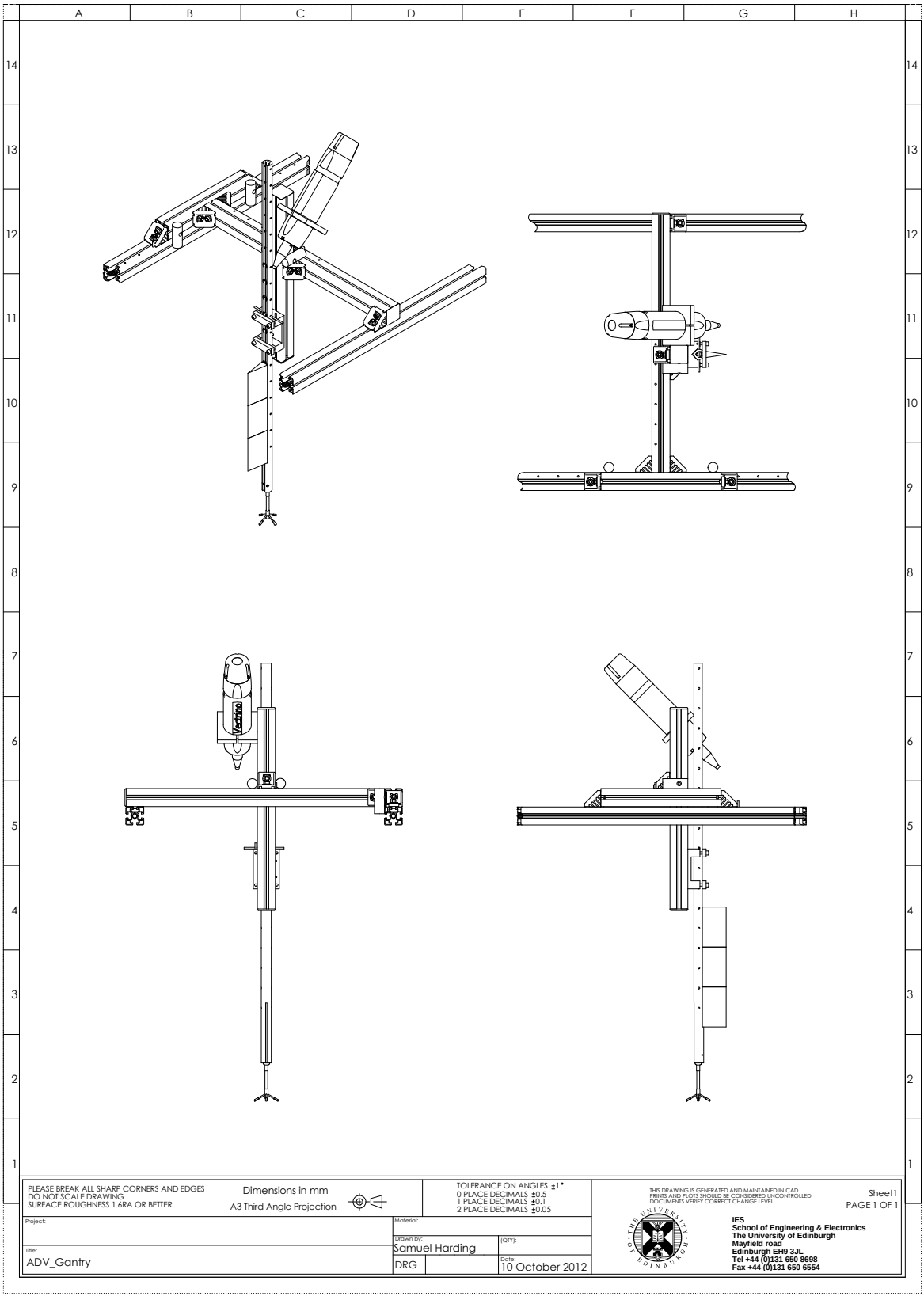

PLEASE BREAK ALL SHARP CORNERS AND EDGES
DO NOT SCALE DRAWING
SURFACE ROUGHNESS 1.6RA OR BETTER

Dimensions in mm
A3 Third Angle Projection

TOLERANCE ON ANGLES ±1°
0 PLACE DECIMALS ±0.5
1 PLACE DECIMALS ±0.1
2 PLACE DECIMALS ±0.05

THIS DRAWING IS GENERATED AND MAINTAINED IN CAD.
PRINTS AND PLOTS SHOULD BE CONSIDERED UNCONTROLLED
DOCUMENTS VERIFY CORRECT CHANGE LEVEL

Sheet1
PAGE 1 OF 1

Project:

Material:

Drawn by: Samuel Harding

(QTY):

Title: ADV_Gantry

DRG

Date: 10 October 2012

IES
School of Engineering & Electronics
The University of Edinburgh
Mayfield road
Edinburgh EH9 3JL
Tel +44 (0)131 650 8698
Fax +44 (0)131 650 6554

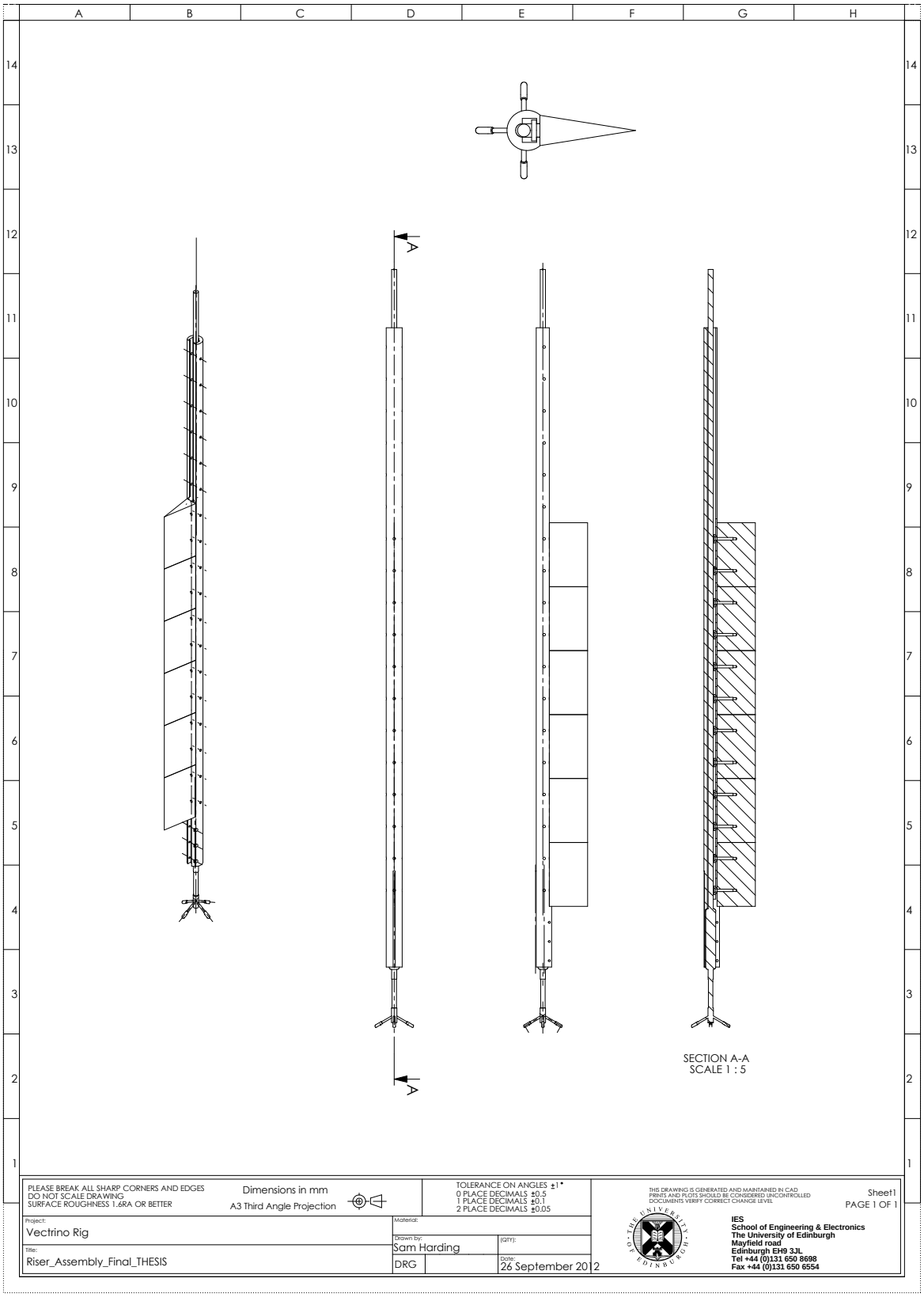

PLEASE BREAK ALL SHARP CORNERS AND EDGES
DO NOT SCALE DRAWING
SURFACE ROUGHNESS 1.6RA OR BETTER

Dimensions in mm
A3 Third Angle Projection

TOLERANCE ON ANGLES ±1°
0 PLACE DECIMALS ±0.5
1 PLACE DECIMALS ±0.1
2 PLACE DECIMALS ±0.05

THIS DRAWING IS GENERATED AND MAINTAINED IN CAD.
PRINTS AND PLOTS SHOULD BE CONSIDERED UNCONTROLLED
DOCUMENTS VERIFY CORRECT CHANGE LEVEL

Sheet1
PAGE 1 OF 1

Project: Vectrino Rig

Title: Riser_Assembly_Final_THESIS

Material:

Drawn by: Sam Harding

(QTY):

DRG

Date: 26 September 2012

IES
School of Engineering & Electronics
The University of Edinburgh
Mayfield road
Edinburgh EH9 3JL
Tel +44 (0)131 650 8698
Fax +44 (0)131 650 6554

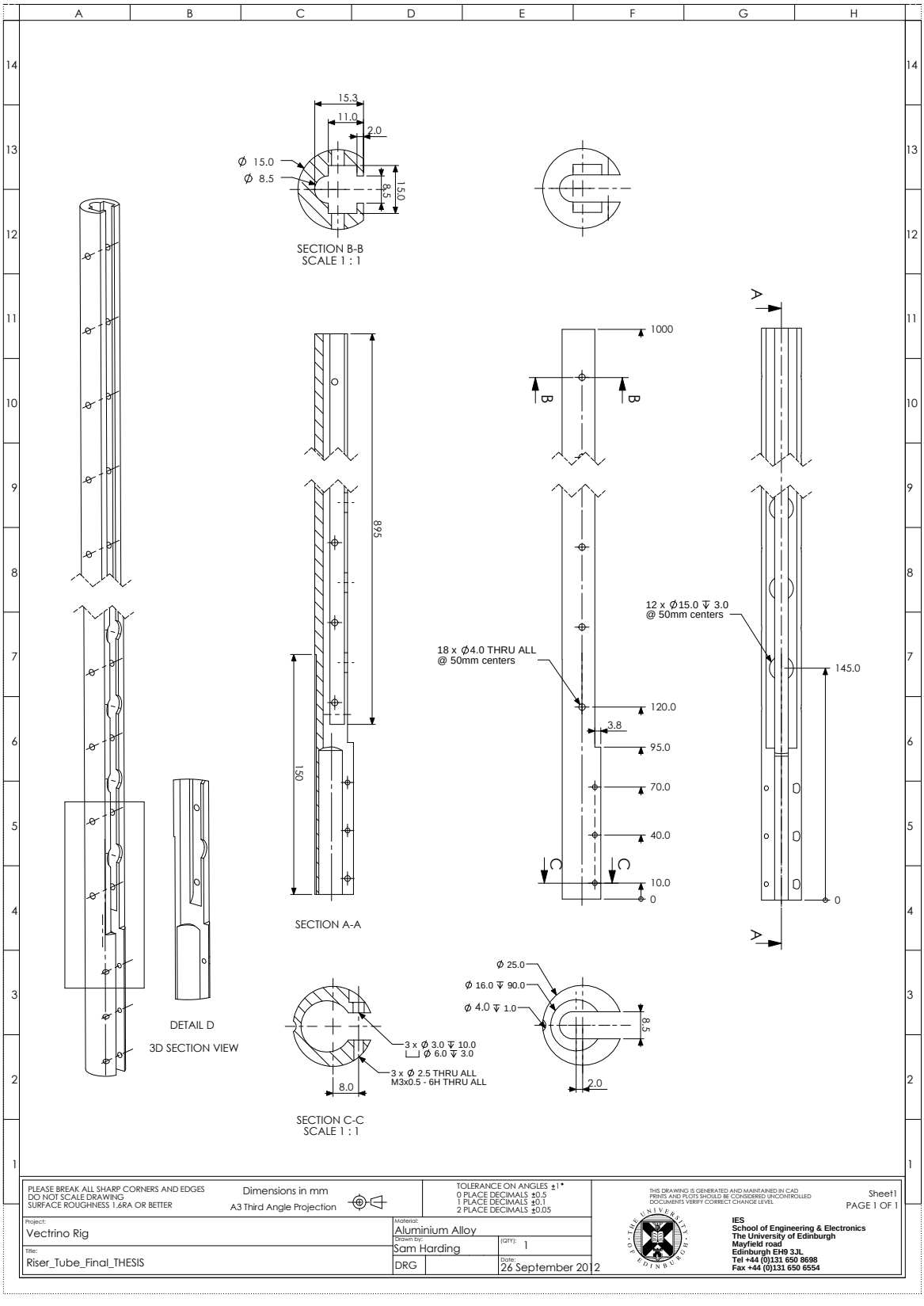
15.3
11.0
2.0
Ø 15.0
Ø 8.5
8.5
15.0
SECTION B-B
SCALE 1 : 1
1000
B
B
A
A
895
150
18 x Ø4.0 THRU ALL
@ 50mm centers
12 x Ø15.0 ↧ 3.0
@ 50mm centers
120.0
95.0
70.0
40.0
10.0
0
145.0
3.8
C
C
SECTION A-A
DETAIL D
3D SECTION VIEW
Ø 25.0
Ø 16.0 ↧ 90.0
Ø 4.0 ↧ 1.0
8.5
2.0
3 x Ø 3.0 ↧ 10.0
⌴ Ø 6.0 ↧ 3.0
3 x Ø 2.5 THRU ALL
M3x0.5 - 6H THRU ALL
8.0
SECTION C-C
SCALE 1 : 1
PLEASE BREAK ALL SHARP CORNERS AND EDGES
DO NOT SCALE DRAWING
SURFACE ROUGHNESS 1.6RA OR BETTER
Dimensions in mm
A3 Third Angle Projection
TOLERANCE ON ANGLES ±1°
0 PLACE DECIMALS ±0.5
1 PLACE DECIMALS ±0.1
2 PLACE DECIMALS ±0.05
THIS DRAWING IS GENERATED AND MAINTAINED IN CAD.
PRINTS AND PLOTS SHOULD BE CONSIDERED UNCONTROLLED
DOCUMENTS VERIFY CORRECT CHANGE LEVEL
Sheet1
PAGE 1 OF 1
Project:
Vectrino Rig
Material:
Aluminium Alloy
Drawn by:
Sam Harding
(QTY):
1
Title:
Riser_Tube_Final_THESIS
DRG
Date:
26 September 2012
IES
School of Engineering & Electronics
The University of Edinburgh
Mayfield road
Edinburgh EH9 3JL
Tel +44 (0)131 650 8698
Fax +44 (0)131 650 6554

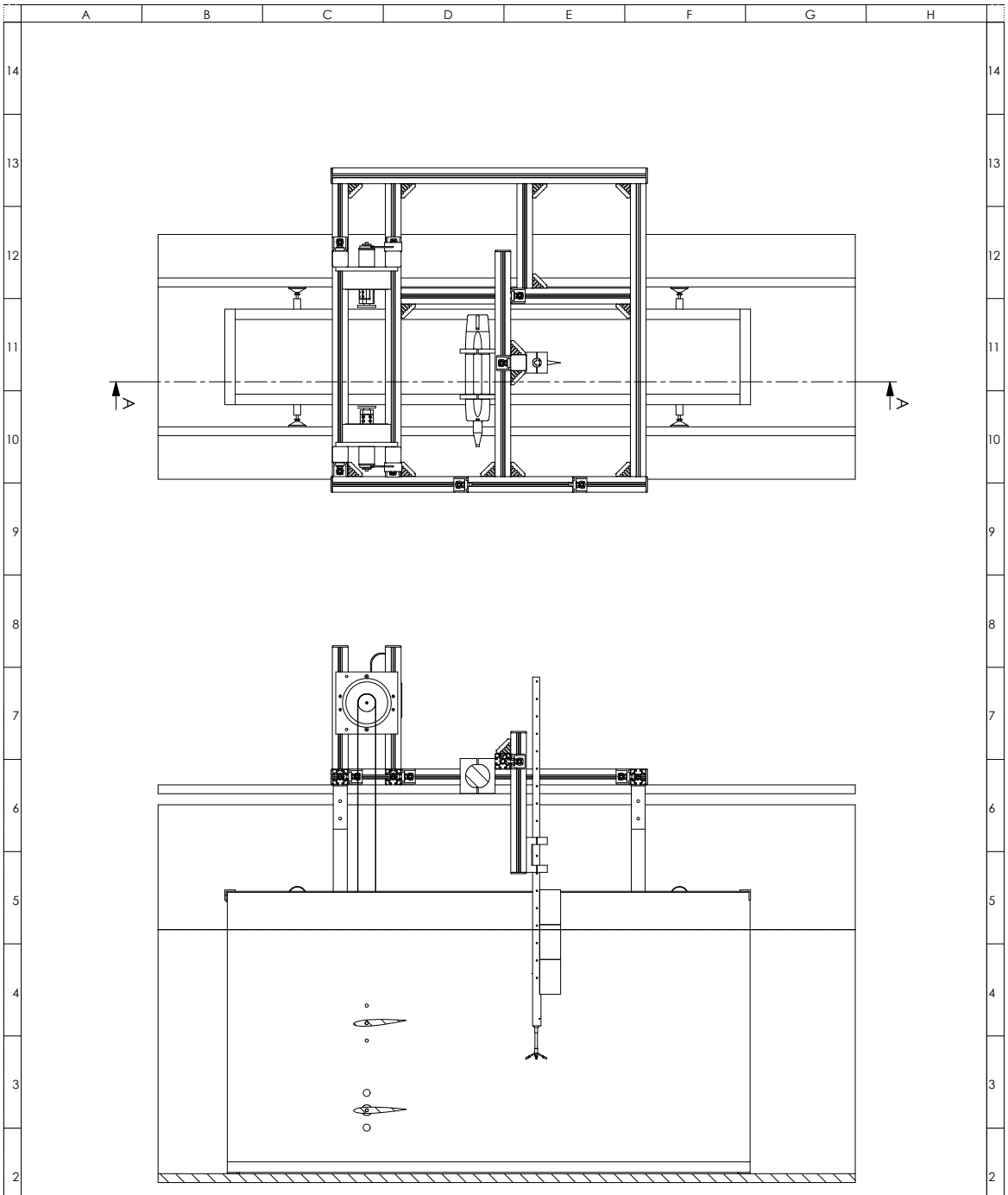

SECTION A-A

PLEASE BREAK ALL SHARP CORNERS AND EDGES
DO NOT SCALE DRAWING
SURFACE ROUGHNESS 1.6RA OR BETTER

Dimensions in mm
A3 Third Angle Projection

TOLERANCE ON ANGLES ±1°
0 PLACE DECIMALS ±0.5
1 PLACE DECIMALS ±0.1
2 PLACE DECIMALS ±0.05

THIS DRAWING IS GENERATED AND MAINTAINED IN CAD
PRINTS AND PLOTS SHOULD BE CONSIDERED UNCONTROLLED
DOCUMENTS VERIFY CORRECT CHANGE LEVEL

Sheet1
PAGE 1 OF 1

Project:

Material:

Drawn by: Samuel Harding

(QTY):

Title: Double_Foil_Rig_with_ADV

DRG

Date: 27 September 2012

IES
School of Engineering & Electronics
The University of Edinburgh
Mayfield road
Edinburgh EH9 3JL
Tel +44 (0)131 650 8698
Fax +44 (0)131 650 6554

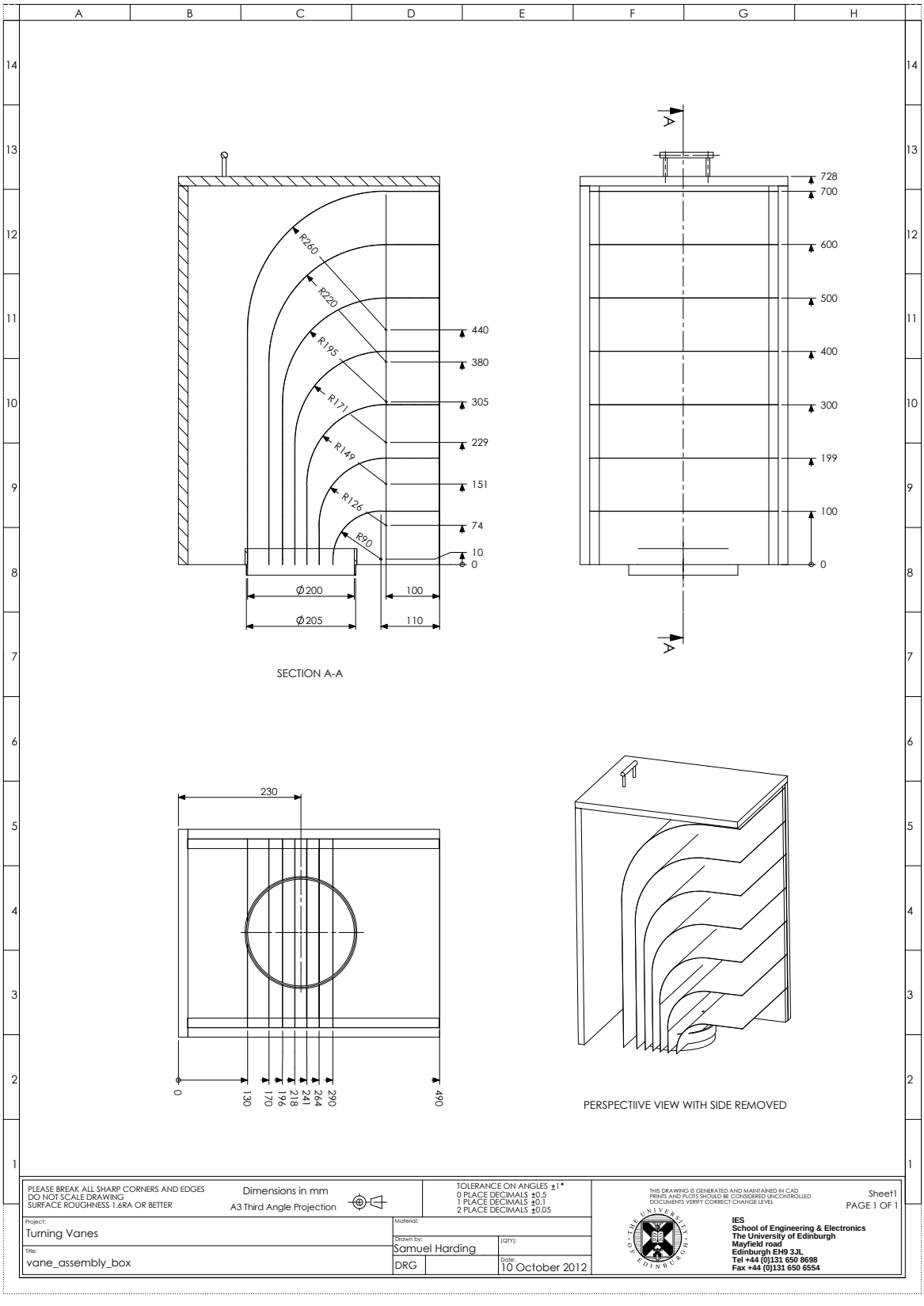
A
B
C
D
E
F
G
H
R260
R220
R195
R171
R149
R126
R90
440
380
305
229
151
74
10
0
Ø200
Ø205
100
110
728
700
600
500
400
300
199
100
0
SECTION A-A
230
0
130
170
196
218
241
264
290
490
PERSPECTIIVE VIEW WITH SIDE REMOVED
PLEASE BREAK ALL SHARP CORNERS AND EDGES
DO NOT SCALE DRAWING
SURFACE ROUGHNESS 1.6RA OR BETTER
Dimensions in mm
A3 Third Angle Projection
TOLERANCE ON ANGLES ±1°
0 PLACE DECIMALS ±0.5
1 PLACE DECIMALS ±0.1
2 PLACE DECIMALS ±0.05
THIS DRAWING IS GENERATED AND MAINTAINED IN CAD.
PRINTS AND PLOTS SHOULD BE CONSIDERED UNCONTROLLED
DOCUMENTS VERIFY CORRECT CHANGE LEVEL
Sheet1
PAGE 1 OF 1
Project:
Turning Vanes
Material:
Drawn by:
Samuel Harding
(QTY):
Title:
vane_assembly_box
DRG
Date:
10 October 2012
IES
School of Engineering & Electronics
The University of Edinburgh
Mayfield road
Edinburgh EH9 3JL
Tel +44 (0)131 650 8698
Fax +44 (0)131 650 6554

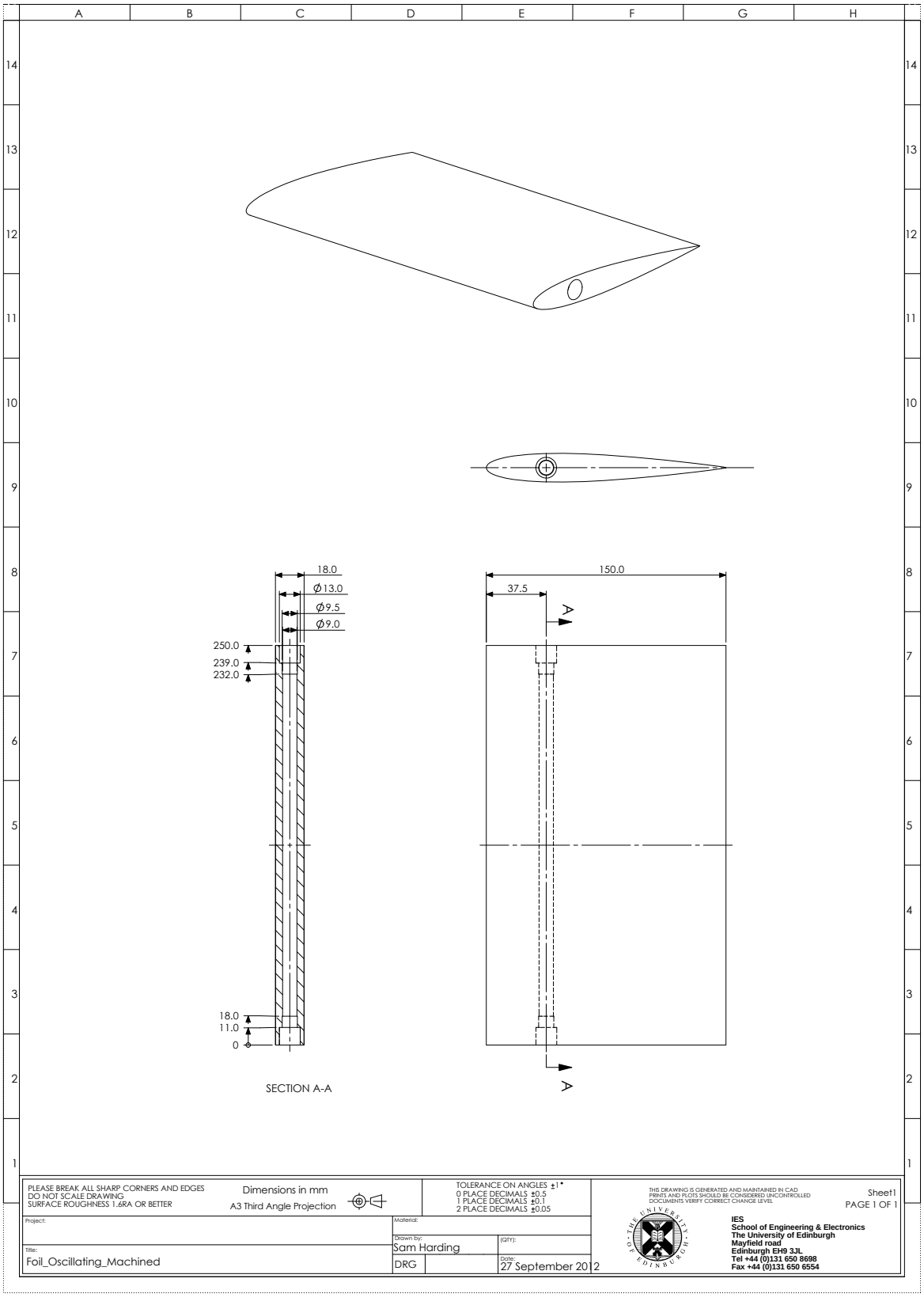
A
B
C
D
E
F
G
H
18.0
Ø13.0
Ø9.5
Ø9.0
250.0
239.0
232.0
18.0
11.0
0
150.0
37.5
A
A
SECTION A-A
PLEASE BREAK ALL SHARP CORNERS AND EDGES
DO NOT SCALE DRAWING
SURFACE ROUGHNESS 1.6RA OR BETTER
Dimensions in mm
A3 Third Angle Projection
TOLERANCE ON ANGLES ±1°
0 PLACE DECIMALS ±0.5
1 PLACE DECIMALS ±0.1
2 PLACE DECIMALS ±0.05
THIS DRAWING IS GENERATED AND MAINTAINED IN CAD
PRINTS AND PLOTS SHOULD BE CONSIDERED UNCONTROLLED
DOCUMENTS VERIFY CORRECT CHANGE LEVEL
Sheet1
PAGE 1 OF 1
Project:
Material:
Drawn by:
Sam Harding
(QTY):
Title:
Foil_Oscillating_Machined
DRG
Date:
27 September 2012
IES
School of Engineering & Electronics
The University of Edinburgh
Mayfield road
Edinburgh EH9 3JL
Tel +44 (0)131 650 8698
Fax +44 (0)131 650 6554

Appendix D
Geometric Analysis of Turning Vane Inlet

In order to divide the circular inlet pipe into N parallel sections of equal area, the solution to Equation D.1b must be found where $\{n < N/2 \cap n \in \mathbb{Z}\}$. The geometric parameters used in these equations are described diagrammatically by Figure D.1.

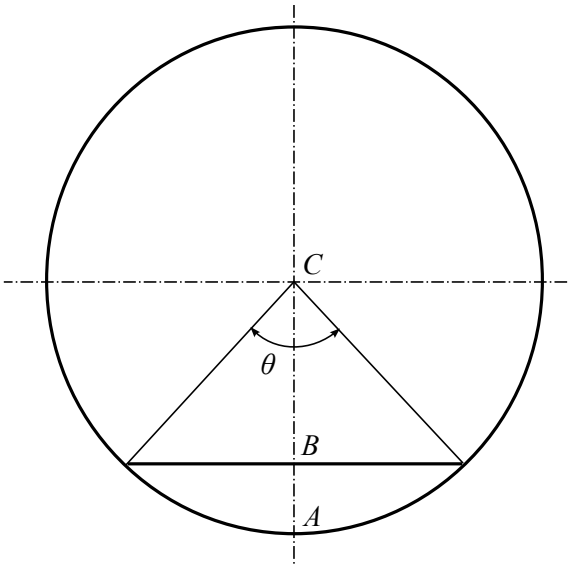

Figure D.1: Schematic of circular inlet pipe

$$\theta_n - sin\,(\theta_n) = 2n\pi/N \tag{D.1a}$$

$$\overline{AB}_n = \overline{AC}\,(1 - cos\,(\theta_n/2)) \tag{D.1b}$$

Note that by the definition of n, Equation D.1 can be only used to find the lengths of $\overline{AB}$ for one side of the circle (i.e. when $\overline{AB} < \overline{AC}$). The remaining distances can be calculated based on reflection of these values about the centerline. Also note that Equation D.1a must be solved for θ numerically before calculating the value of $\overline{AB}$ from Equation D.1b.

Appendix E
Experimental Calibration Plots

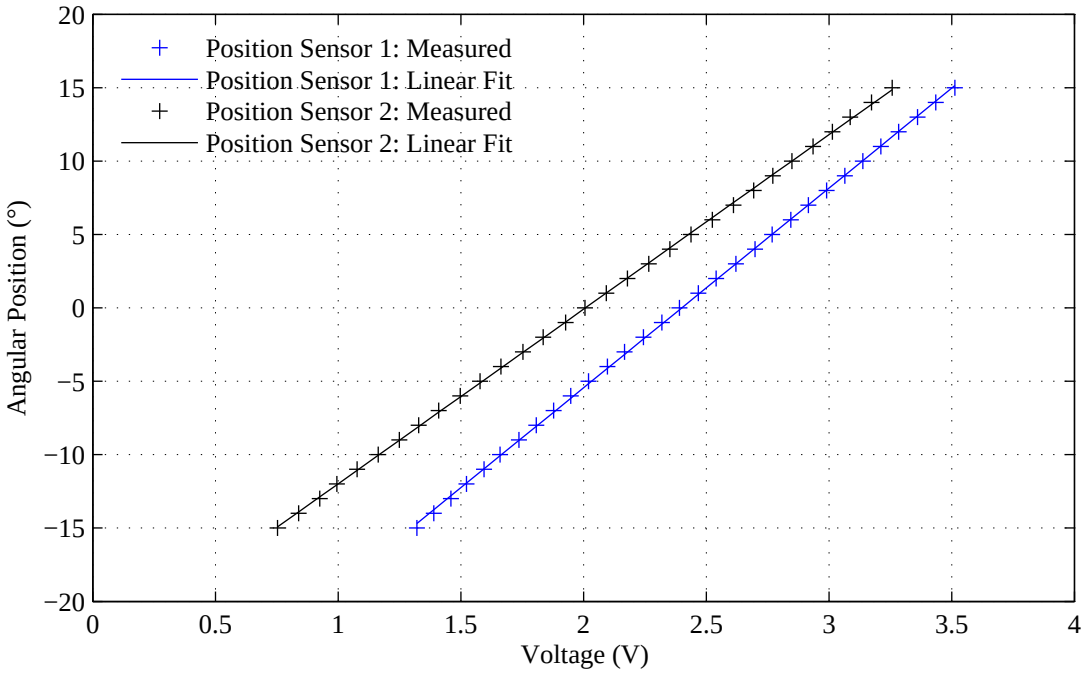

Figure E.1: Plot of calibration results for Gill Sensors

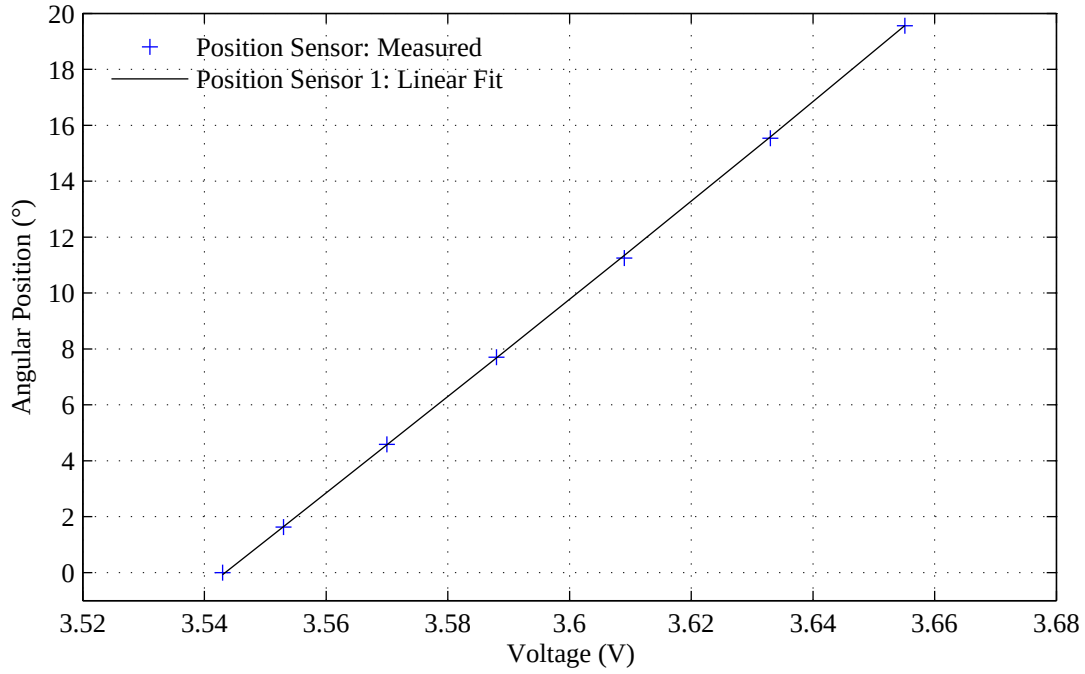

Figure E.2: Plot of calibration results for cable sensor

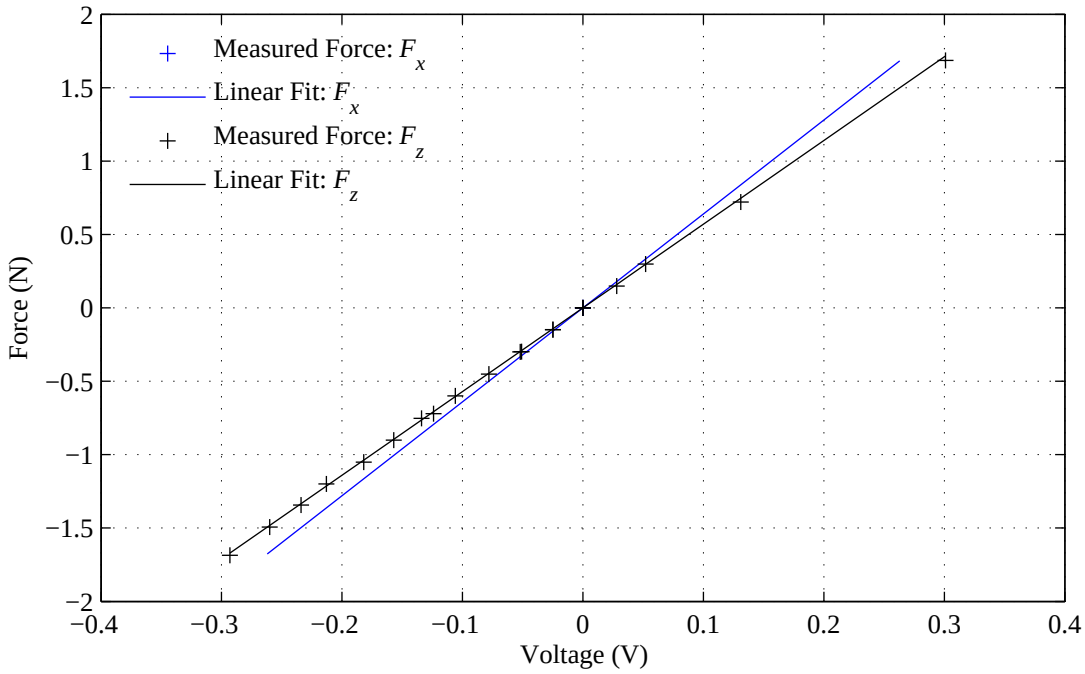

Figure E.3: Plot of calibration results for bi-directional force sensor

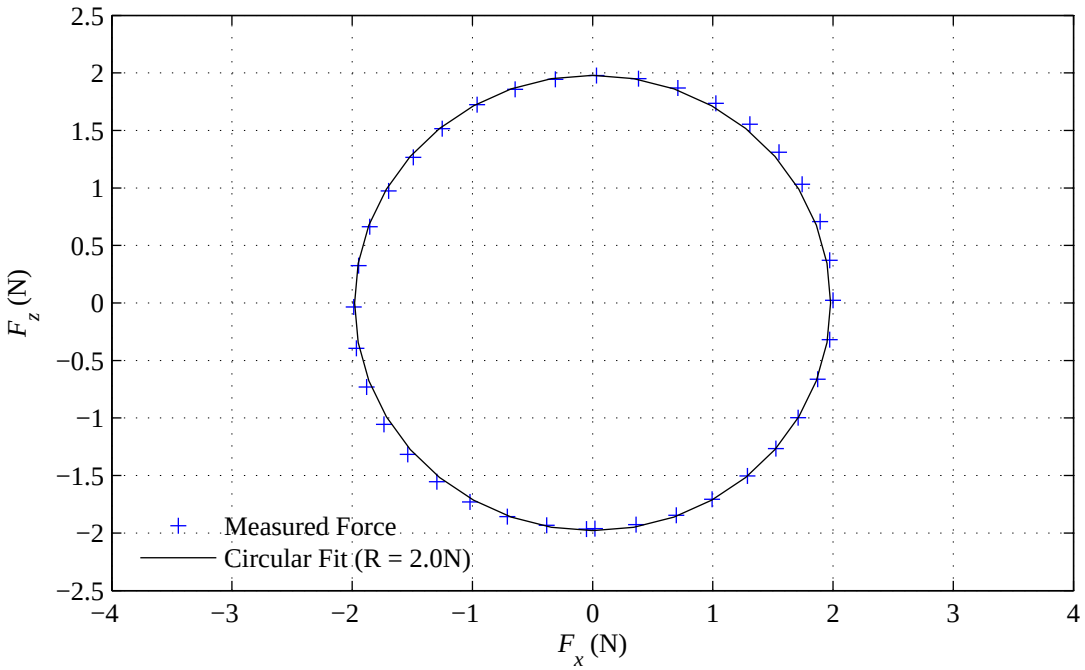

Figure E.4: Plot of cross-talk calibration results for bi-directional force sensor

Appendix F
Papers Published

International peer-reviewed journals

Harding, S. and Bryden, I., Generating controllable velocity fluctuations using twin oscillating hydrofoils, Journal of Fluid Mechanics, 713, 150-158, 2012.

Harding, S. and Bryden, I., Directionality in Prospective Northern UK Tidal Current Energy Deployment Sites, Renewable Energy, 44, 474-477, 2012.

International peer-reviewed conferences

Harding, S. and Bryden, I., Development of Fixed Hydrodynamic Lifting Surfaces to Stabilise Anchoring Structures in Energetic Tidal Flows, Proceedings of the 31st International Conference on Ocean, Offshore and Arctic Engineering (OMAE), July 1-6, 2012, Rio de Janeiro, Brazil.

UK peer-reviewed conferences

Harding, S., Thomson, J., Polagye, B., Richmond, M., Durgesh, V. and Bryden, I., Extreme Value Analysis of Tidal Stream Velocity Perturbations, Proceedings of the 9th European Wave and Tidal Energy Conference (EWTEC), September 5-9, 2011, Southampton, England.

Other publications

Gueydon, S. and Harding, S., Floating Wind Turbine Challenge, European Wind Energy Association, April 16-19, 2012, Copenhagen, Denmark.